UNIVERSITY OF LJUBLJANA
FACULTY OF MATHEMATICS AND PHYSICS
DEPARTMENT OF PHYSICS

Gregor Bavdek

STUDY OF STRUCTURAL AND ELECTRONIC PROPERTIES
OF THIN METALLIC AND ORGANIC FILMS

Doctoral thesis

ADVISER: assist. prof. Dean Cvetko

Kranj, 2006

UNIVERZA V LJUBLJANI
FAKULTETA ZA MATEMATIKO IN FIZIKO
ODDELEK ZA FIZIKO

Gregor Bavdek

ŠTUDIJ STRUKTURNIH IN ELEKTRONSKIH LASTNOSTI
TANKIH KOVINSKIH IN ORGANSKIH FILMOV

Doktorska disertacija

MENTOR: doc. dr. Dean Cvetko

Kranj, 2006

Abstract

In the last decade a growing attention is paid to the novel semiconducting organic layers with technologically useful optical, electronic and catalytic properties. Several organic materials have been already successfully used in production of photovoltaic devices, thin film transistors and organic light-emitting diodes. Nevertheless, they nowadays still express quite limited performances due to insufficient understanding of rather complicated mechanisms governing formation of organic layers, ordering processes, strength of interaction with the substrate and the corresponding physical properties of such interfaces. Studying of growth and ordering of various organic films on metallic and semiconducting substrates gives a challenging opportunity to get a closer insight into this processes and to optimize them in order to obtain high-performance technological devices.

In the present thesis I focus on the individual interface and film properties, growth mode and ordering of adlayers as a function of the system temperature, and the molecular alignment in three different organic/inorganic heterosystems. Particular emphasis is given to the study of ordering mechanism which crucially influences the charge carrier mobility inside the film and the charge carrier injection at the film-substrate interface, thus dictating the conduction properties of organic films and organic/inorganic heterojunctions. For investigation I have used various surface- and interface-sensitive experimental techniques, such as helium, electron and X-ray diffraction as well as X-ray photoelectron spectroscopy and X-ray near edge absorption.

Experimental analysis of the phases occurring in pentacene ($C_{22}H_{14}$) on Au(110) ultra thin film is presented. I study the film morphology at different deposition stages as seen by scattering of helium atoms and analyse the peculiar structure occurring at two different saturation phases with (3×6) and (6×8) periodicity, respectively. The phase diagram has been introduced, which has also been published in the J. Phys. Chem. B (see Appendix C). Pentacene molecules are found to organize in long correlated chains consistent of flat-lying side-by-side oriented molecules in the (3×6) phase. In the more dense (6×8) phase the spacing of these chains increases in order to accommodate in between a new kind of chain, where molecules line up head-to-head with the molecular planes perpendicular to the surfaces.

In copper phthalocyanine ($C_{32}H_{16}N_8Cu$, CuPc) on Au(110) heterosystem I find only weak film-substrate interaction, yet sufficient to lift the Au(110) missing row reconstruction. The presence of CuPc molecules induces a proliferation of Au(110) monoatomic steps, which on the other hand drive the molecular alignment in parallel well correlated CuPc chains with almost one-dimensional character of CuPc ordering. At the coverage of approximately 2/3 of monolayer, the film and the substrate both exhibits the (5×5) structure. Close to monolayer completion the Au substrate undergoes a "shallow" (1×3) reconstruction with an asymmetric unit cell relaxation. The CuPc film at the same time exhibits the (5×7) structure, with the molecules tilted by 32° to the surface. CuPc molecules are thus found to favor the adsorption with the molecular plane parallel to the locally exposed (111) microfacets of the Au(110) substrate, which are tilted by 35° to the substrate (110) plane. The study has been published in the J. Phys. Chem. B (see Appendix C).

The third presented system, 3,4,9,10-perylene-tetracarboxylic-dianhydride ($C_{24}H_8O_6$, PTCDA) on Ge(001), nicely shows the consequences of much stronger film-substrate interaction due to semiconductive nature of the substrate. When growing at low temperature ($\sim 170\,\mathrm{K}$), a disordered interface layer is surprisingly followed by orientationally well ordered film, which persists in the same morphology also when brought to room-temperature. When grown at room-temperature, however, the structure results in amorphous phase, consistent of the interface layer and randomly oriented large 3D islands. Nevertheless, the anomalous ordering at low temperature and the resulting uniform film unambiguously classifies PTCDA as the promising candidate in building organic semiconducting devices, whose high conductivity has already been observed for low-temperature grown films. The analysis of the PTCDA orientational growth is currently in preparation for publication.

The experimental work presented in this thesis has been carried out on the ALOISA/ HASPES beamline at the Elettra sinchrotron source in Trieste, which are part of the TASC laboratories under INFM-CNR, Italy.

Povzetek

V zadnjem desetletju je vse več pozornosti namenjene novim polprevodniškim organskim plastem s tehnološko uporabnimi optičnimi, elektronskimi in katalitskimi lastnostmi. Kar nekaj organskih materialov se je že izkazalo za uspešne pri izdelavi fotovoltaičnih elementov, tankoslojnih tranzistorjev in organskih svetlečih diod. Ti elementi pa imajo dandanes kljub vsemu še vedno dokaj omejene zmogljivosti. Glavni vzrok za to je pomanjkljivo razumevanje sicer dokaj zapletenih mehanizmov, ki sodelujejo pri nastanku organskih plasti, pri njihovem urejevanju in moči interakcije s substratom ter s tem vplivajo na fizikalne lastnosti stičnih plasti. Proučevanje rasti in urejevanja različnih organskih filmov na kovinskih in polprevodniških substratih ponuja natančnejši vpogled v te procese in omogoča njihovo optimizacijo, kar bi mogočilo izdelavo visokokvalitetnih tehnoloških elementov.

V tej disertaciji se osredotočam na lastnosti posameznih stičnih plasti in tankih filmov, na način rasti in urejevanje tankih plasti v odvisnosti od temperature ter na molekulsko orientacijo v treh različnih organsko/anorganskih heterosistemih. Poseben poudarek dajem proučevanju mehanizma urejevanja, ki ključno vpliva na mobilnost nosilcev naboja v filmu in prenos nosilcev naboja skozi organsko/anorganski heterostik. Za raziskave sem uporabljal različne površinsko občutljive eksperimentalne tehnike, kot so sipanje atomov helija, elektronov in X-žarkov ter rentgensko spektroskopijo in absorpcijo X-žarkov v bližini atomskih robov.

Najprej predstavim eksperimentalno študijo faz, ki se pojavijo v tankem filmu pentacen/Au(110). S sipanjem atomov helija sem raziskal morfologijo pri različnih stopnjah nanosa in analiziral neobičajno ureditev molekul pri dveh saturacijskih pokritostih, kjer sta prisotni fazi s periodičnostjo (3×6) in (6×8). Predstavil sem fazni diagram, ki je bil že objavljen v J. Phys. Chem. B (glej Dodatek C). Ugotovil sem, da se molekule pentacena v fazi (3×6) uredijo v dolge korelirane verige, sestavljene iz bočno staknjenih molekul, ki na površini ležijo (t.j. njihova molekulska ravnina je vzporedna s površino). V bolj gosti fazi (6×8) se razmik med verigami poveča, kar omogoči, da se mednje vrine strukturno povsem drugačna veriga, v kateri so molekule med seboj povezane vzdolž daljše osi in na površini stojijo pokonci (t.j. imajo molekulsko ravnino pravokotno na površino).

V heterosistemu bakrovega ftalocianina $(C_{32}H_{16}N_8Cu, CuPc)$ na Au(110) sem opazil sorazmerno šibko interakcijo filma s substratom, ki pa je kljub temu dovolj močna, da poviša rekonstrukcijo površine Au(110) z manjkajočimi vrstami. Prisotnost CuPc molekul inducira proliferacijo enoatomskih stopnic v substratu Au(110), kar po drugi strani povzroči, da se molekule CuPc uredijo v vzporedne dobro korelirane verige s skoraj enodimenzionalno naravo urejevanja. Pri pokritosti približno 2/3 monoplasti tako film kot substrat izkazujeta strukturo (5×5). V bližini izpolnitve prve monoplasti pride do rekonstrukcije Au substrata v "plitvo" (1×3) fazo z asimetrično relaksirano enotsko celico. Tanek CuPc film pri tem izraža strukturo (5×7), v kateri so molekule glede na površino nagnjene za 32°. Kot kaže, CuPc teži k adsorpciji, kjer je molekulska ravnina vzporedna z lokalno izpostavljenimi (111) mikropovršinami Au(110) substrata – te so namreč glede na (110) površino substrata nagnjene za 35°. Omenjena študija tankega filma CuPc/Au(110) je bila objavljena v J. Phys. Chem. B (glej Dodatek C).

V tretjem predstavljenem sistemu, 3,4,9,10-perilen-dianhidridu tetrakarboksilne kisline (PTCDA) na Ge(001), se zaradi polprevodniške narave substrata lepo kažejo posledice precej močnejše vezave filma na njegovo površino. Pri rasti pri nizki temperaturi ($\sim 170\,\mathrm{K}$) najprej nastane tanka neurejena stična plast, ki pa ji – presenetljivo – sledi orientacijsko dobro urejen film. Ta ohrani svojo morfologijo tudi, ko substrat segrejemo do sobne temperature. Za razliko od tega pri naparevanju PTCDA pri sobni temperaturi nastane popolnoma amorfna faza, ki jo sestavlja neurejena stična plast in pa naključno usmerjeni veliki 3D otoki. Anomalno urejevanje pri nizki temperaturi in nastanek uniformnega filma, katerega dobra prevodnost je bila že potrjena, pa kljub temu uvrščata PTCDA med obetavne materiale pri konstrukciji organskih polprevodniških elementov. V pripravi je več člankov, v katerih bodo objavljeni izsledki omenjenih raziskav PTCDA/Ge(001).

Eksperimentalno delo, ki ga predstavljam v tej disertaciji, je bilo opravljeno na žarkovni liniji ALOISA/HASPES na sinhrotronu Elettra v Trstu. Omenjena linija je del laboratorijev TASC, ki pripadajo italijanskemu CNR-INFM.

# Contents

Chapter 1

Introduction

For more than a decade now, organic materials are successfully entering the area of semi-conductors, sensors and photovoltaic devices. Due to their low cost, they are offered a challenging opportunity to play a role of the active material in the semiconductors as an alternative to more traditional inorganic semiconductors, such as Si, Ge and GaAs. Because of relatively low charge carrier mobility in the organic semiconductor layers, organics cannot (yet) rival the performance of the single-crystalline Si and Ge based devices, which have charge carrier mobilities about three orders of magnitude higher [1]. Consequently, the organic thin film transistors (OTFT) are currently not suitable for use in applications requiring very high switching speeds. They can, however, be competitive for existing or novel TFT applications requiring large-area coverage, structural flexibility and low-temperature processing. Such applications include switching devices for active-matrix flat-panel displays (AMFPDs) based on either liquid crystal pixels (AMLCDs) or organic light-emitting diodes (AMOLEDs). Although, at present, hydrogenated amorphous silicon (a-Si:H) is the most commonly used active layer in high-performing TFT backplanes of AMLCDs, the improvements in the efficiency of both, the OLEDs and OTFTs, could place the organic materials as a viable cost-effective alternative to the traditional a-Si:H.

For OTFTs to compete directly with a-Si:H TFTs, the former should exhibit device performance similar to that of the latter, i.e., field effect mobility $\mu = 1\,\mathrm{cm^2V^{-1}s^{-1}}$, and current modulation (or on/off ratio, $I_{\mathrm{on/off}}$) of 10^6 or higher at a maximum operating voltage of about 15 V or less. Additionally, they should be thermally stable and resistant to the prolonged exposure to ambient conditions. Despite of high technological expectations, organic materials, however, already make possible the applications that are not achievable using the entrenched technology, for example at the production of flexible AMFPD. Because of the high processing temperature used in a-Si:H TFTs (approximately 360 °C), it is not possible to fabricate AMLCD based on such TFTs on a transparent plastic substrate. Most OTFTs are, on the other hand, processed at or close to room temperature and therefore enable this technology which, in fact, complements the entrenched one instead of competing with it.

The intermolecular interactions in organic materials are generally dominated by weak van der Waals forces, which may be held responsible for the upper limit of charge carrier mobilities to fall between 1 and $10\,\mathrm{cm^2V^{-1}s^{-1}}$. The distance between nearest neighbour molecules is thus often too big to enable efficient overlap of molecular electronic states between adjacent molecules and appropriately good conductivity. In disordered organic semiconductors carrier transport takes place mainly by hopping between localized states,

with carriers scattered at every step. Hopping is assisted by phonons and the mobility increases with temperature, although it typically remains in the range of $\mu \ll 1\,\mathrm{cm^2V^{-1}s^{-1}}$. As a contrast, in inorganic semiconductors such as Si, Ge and GaAs, the atoms are held together with very strong covalent bonds, where charge carriers move as highly delocalized plane waves in wide bands and have a very high mobility at room temperature, reaching $\mu \approx 10^3\,\mathrm{cm^2V^{-1}s^{-1}}$. In this case, the mobility is limited by lattice vibrations (phononos) that scatter the carriers and thus it is reduced as the temperature increases. A very similar coherent band-like transport of delocalized carriers was however also observed as the prevalent transport mechanism in the single crystals of (organic) polyacenes (tetracene, pentacene) and PTCDA at very low temperatures $(1-4\,\mathrm{K})$. These planar molecules possess pronounced π-conjugated electronic system out of the molecular plane, enabling considerable $\pi - \pi^*$ orbital overlap along the stacking direction. Similar (high) mobilities as in the case of inorganic semiconductors were thus also reported for polyacenes. This behavior is rather impossible to observe in polycrystalline films when charge carrier transport through two or more grains is studied, because traps attributed to grain boundaries and other structural defects dominate transport.

In the case of planar molecules, such as polyacenes, large π-conjugation length along the long axis of the molecule and close molecular packing of the molecules along at least one of the short molecular axes (π-stacking) are two important conditions for high carrier mobility. These principles are also in operation in OTFTs based on polycrystalline vapor deposited pentacene thin films. The above claims are demonstrated by an example of pentacene growth on $\mathrm{SiO_2}$ at various substrate temperatures, shown in fig. 1.1. By grow-
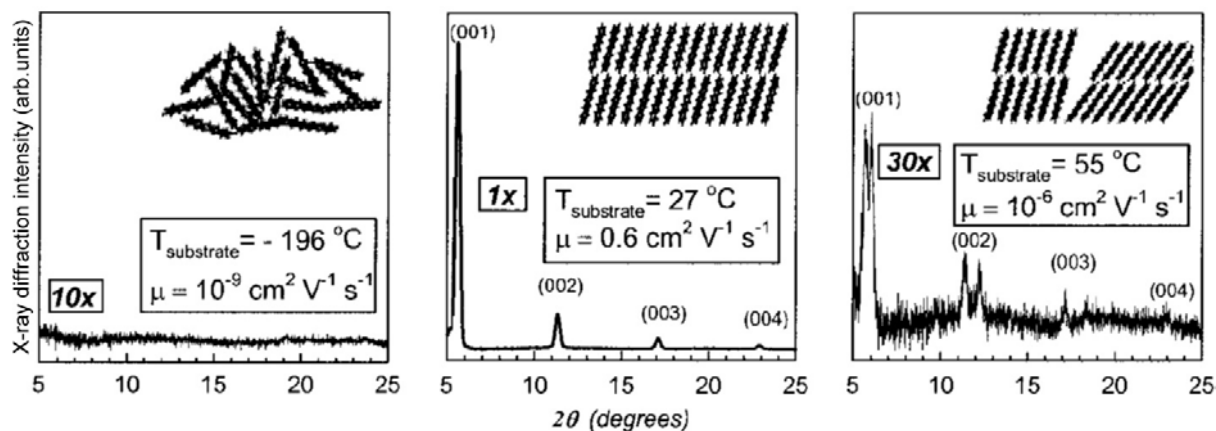
Figure 1.1: X-ray diffractograms, schematic representations of structural order, and field-effect mobilities corresponding to three different pentacene thin films. An amorphous phase (left), a single "thin-film phase" (middle) and a film consisting of two phases, the "thin-film phase" and the "single-crystal phase" (right) are shown. [1]

ing amorphous films of pentacene, which is achieved by keeping the substrate temperature close to $-196\,^{\circ}\mathrm{C}$ during deposition, a film that is practically insulating is produced. This is due to the fact that the overlap of the molecular orbitals of nearest-neighbour is very limited because of the disorder in the solid (fig. 1.1, left). When the substrate temperature is kept at room temperature during deposition, a highly ordered film is formed (as evidenced by X-ray diffraction) and the mobility measured at room temperature increases to $0.6\,\mathrm{cm^2V^{-1}s^{-1}}$ (fig. 1.1, middle). The structure of this thin film is different than the

structure of single crystals of pentacene, thus it has to be distinguished between the "thin-film phase" and the "single-crystal" phase of pentacene. When a mixture of the thin film phase and the single crystal phase is grown, the mobility is again very low, possibly due to the high defect concentration resulting from the coexistence of the two phases (fig. 1.1, right).

An important issue which is further addressed in the OTFT production is the local structure change in the organic layer due the presence of the metal, acting as the device electrode. Fig. 1.2 shows pentacene, grown on the SiO_2/Au heterojunction. On SiO_2, far
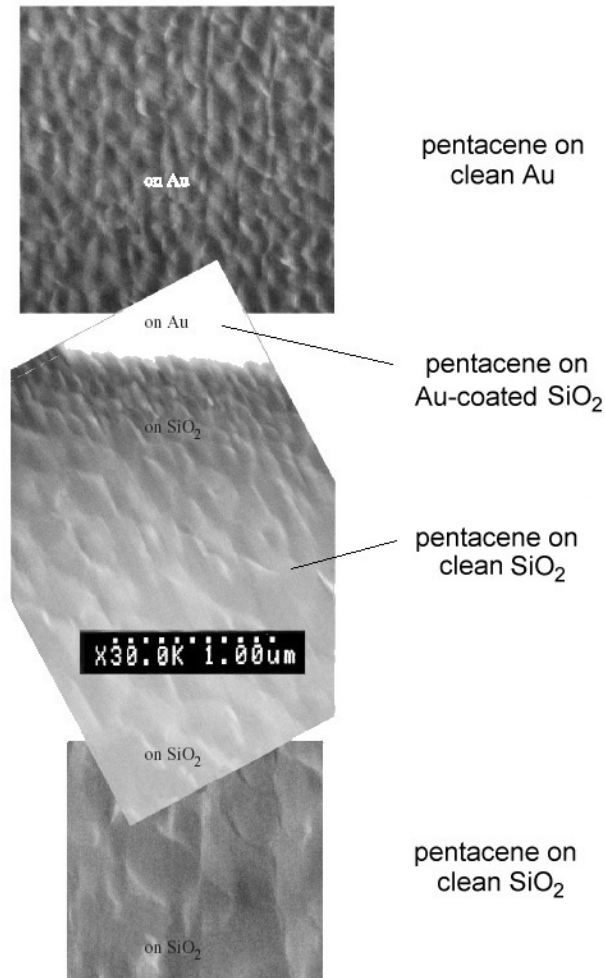
Figure 1.2: The scanning electron microscopy image of a pentacene thin film grown on SiO_2 and a Au electrode. The grain size is much smaller on Au (top) than on SiO_2 far from the Au edge (bottom). [1]

away from the Au edge, pentacene consists of quite large grains, with the size ranging from between 0.2 to 0.5 μm (fig. 1.2, bottom). On Au, the grain size is dramatically decreased as seen in the top of the same figure. Similarly small crystals are also observed on the SiO_2 in the vicinity of the Au. A transition region, where the grain size increases with increasing distance from the Au edge, can be nicely seen in the middle part of the figure 1.2. It is the morphology of the pentacene film in the region close to the electrode edge that causes the performance limitation of the TFT bottom contact. Right at the

edge of the Au electrode, there is an area with very small crystals and hence a large number of grain boundaries. Grain boundaries are high-volume and low-order regions that contain many morphological defects, which in turn are linked to the creation of charge carrier traps with levels lying in the band-gap. These defects can be considered responsible for the reduced performance of bottom contact pentacene TFTs. Knowledge about the morphology, present at the organic-metal interface, is therefore essential.

In the present work I address three different organic/inorganic systems, where morphology, strength of interaction with the substrate and the orientational ordering of the interface layer are the most relevant parameters concerning the substrate/film charge transport properties. The pentacene film structure as well as the growth mode on the Au(110) substrate is thoroughly studied in the present thesis in Chapter 5. A phase diagram with the morphologies corresponding to a certain temperature interval and coverage range is introduced, showing two highly stable long-range ordered saturation phases. The phase diagram and the XPS observations has been published in J. Phys. Chem. B (see Appendix C). In contrast with previously reported results on pentacene growth on Au(110) [2], no second layer formation is put to evidence. Instead, a stable phase with (6×8) periodicity has been observed with an interesting molecular configuration containing flat-lying and up-standing molecules, forming *"nanorails"*. The results of the present analysis has been presented on the ECOSS 2006 conference as well as on the SloNANO 2006 symposium (see Appendix C).

A copper phthalocyanine thin film formation has been studied as the prototypical system, where the molecular properties may be tailored by suitable choosing the central metal atom in the molecule. Metallophthalocyanines, M-Pcs, are planar or nearly planar organic molecules with a metal ion in the center. Along with other phthalocyanine derivatives, the chemically and thermally stable CuPc has wide applications in dye processing, spectral sensitization, chemical sensors, and optical data storage. These molecules exhibit interesting optical and electronic properties such as high photoconductivity, electroluminescence and a pronounced optical nonlinearity. Due to strong anisotropy of the optical and electrooptical properties of bulk M-Pcs, there is a large interest to grow ordered and highly oriented films with a well defined and stable phase. The transistor properties of phthalocyanines have received less attention presumably because of their low reported mobilities ($\approx 10^{-4}\,\mathrm{cm^2V^{-1}s^{-1}}$). Nevertheless, it was show that for CuPc high mobility of around $0.01\,\mathrm{cm^2V^{-1}s^{-1}}$ can be achieved by employing elevated substrate temperature during deposition, which affects directly the morphology of the film [3]. In case of metal substrates, the strong M-Pc-substrate interaction favors a planar adsorption geometry [4]. Ordered films with a close-packed molecular structure were observed on the Cu(111), Cu(100), Au(111), Au(110) and Ag(110) surfaces. On the Au(110) substrate, an interesting substrate-adsorbate interplay is observed, where not only the structure of the organic film is dictated but the reverse influence on the substrate structure is also pronounced. The disappearance of the clean Au two-fold substrate reconstruction and the appearance of a 3-fold periodicity in the presence of CuPc adlayer clearly evidences a strong substrate-adsorbate interaction [5]. Ordered chains of CuPc molecules are formed in the first layer, which represent a template for further multilayer growth. A detailed study of the copper phthalocyanine (CuPc) monolayer on Au(110) is presented in Chapter 6. The polarization dependent near edge X-ray absorption revealed, that the CuPc molecules are tilted by $\approx 32°$ relative to the surface. The substrate is found to express a shallow (1×3) missing row reconstructed phase, exhibiting an energy expensive rearrange-

ment of the Au(110) substrate with a large mass transport at the surface. The results of the presented analysis have been published in the J. Phys. Chem. B (see Appendix C).

The third investigated system, which is one of the most extensively studied compounds in the context of molecule electronic applications, is the perylene derivative 3,4,9,10-perylene-tetracarboxylic-dianhydride (PTCDA). The investigation of growth of organic van der Waals films on substrates of conventional semiconductors like Si, Ge and GaAs is of practical importance because of potential applications in hybrid organic/inorganic (OI) semiconductor structures [6]. It is also of fundamental interest, what structurally ordered interfaces can offer in terms of probing band alignment and charge carrier transport at OI heterojunctions. The PTCDA molecular ordering was widely studied in the means of electrical properties of organic-inorganic heterojunctions (OI-HJ) by Forrest et al. [7]. PTCDA is a planar molecule which crystallizes in the herringbone structure with significant π-interaction between the planar stacked sheets of molecules. By correlating charge carrier mobility with film growth conditions, the degree of stacking order can be inferred since μ is ultimately determined by the π-bond overlap between molecules in the stack. A typical PTCDA/Si OI device structure is shown in the fig. 1.3, left. The right
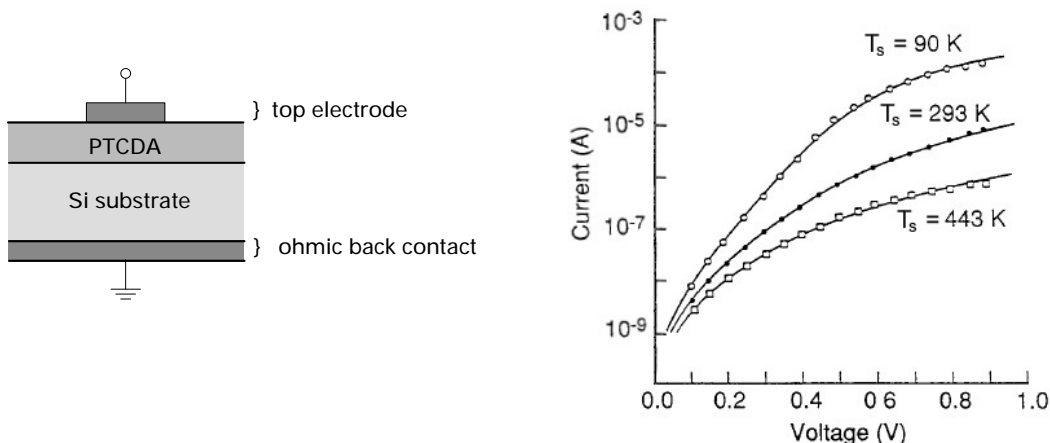
Figure 1.3: Structure of a typical OI-HJ device (left) and the forward-biased current-voltage characteristics for In/2000 Å PTCDA/p-Si devices, where the organic layer was deposited at different substrate temperatures, T_s (right). [7]

hand side of the same figure displays the forward biased $I - V$ characteristics for OI-HJ device with 2000 Å thick PTCDA films deposited at different substrate temperatures. For the sample with $T_s = 90$ K, the forward current has an exponential dependence on voltage due to charge diffusion across the OI heterointerface in the low bias voltage regime and then exhibits a roll off in current due to space-charge-limited current. For the sample with PTCDA deposited at $T_s = 443$ K, the forward current has no exponential dependence for the entire voltage range studied, indicating a low carrier mobility. From these dependences, the carrier mobility in the organic films decreases from 0.16 cm^{2}V^{-1}s^{-1} for the sample deposited at 90 K to $2 \cdot 10^{-4}$ cm^{2}V^{-1}s^{-1} for the sample deposited at 443 K, indicating a corresponding reduction in stacking order. The measurements of μ have been explained in terms of the thin-film structural properties. Due to the large π-orbital overlap along the stacking axis, charge (primarily holes for PTCDA) injected into the organic

films are transported along the stacking direction, giving rise to the high mobilities observed. In contrast, films deposited at elevated temperatures exhibit randomly oriented molecular stacks, which leads to a formation of grain boundaries. Due to negligible π-system overlap between the stacks, the carrier mobility is considerably reduced in the film (in some cases by almost 4 orders of magnitude). The structural properties and the molecular packing mechanism causes enormous anisotropies in both their conductive and dielectric properties. For example, the in-plane conductivity of orientationally ordered PTCDA films is found to be at least 6 orders of magnitude lower than the conductivity perpendicular to the film plane.

The strong influence of the substrate-adsorbate interaction on growth and ordering is reflected by the different types of growth observed for PTCDA on semiconductor surfaces. On Si(111) and GaAs(100), the beam deposition of PTCDA in vacuum leads to the formation of disordered structures with strong evidence for the molecular axes being oriented in a random fashion [8]. This observation is explained by a rather strong interaction between the PTCDA functional side groups with the substrate. For other less reactive passivated semiconductor surfaces, the formation of well ordered PTCDA adlayers has been reported for example, on Se:GaAs(110).

Interesting properties concerning growth and ordering as well as lack of the experimental data raised the motivation to study PTCDA on semiconductor substrate Ge(001). Highly reactive adsorption sites which result from the "dangling bonds" of the (001) truncated Ge surface are partially passivated through (2×1) reconstruction, thus offering a well suited substrate where PTCDA monolayer may serve as a template for further oriented growth in organic film. The analysis and results are presented in Chapter 7. They have already been presented in several conferences (see Appendix C) and are to be published soon as an autonomous scientific article. It was shown that at room temperature and above, the PTCDA/Ge(001) film consists of only wetting layer with the excess of the deposited material being gathered in the large 3D islands. On the other hand, at the temperature below 170 K, the disordered initial layer of PTCDA is followed by the orientationally well ordered organic film, which contains perfectly flat lying molecules, which are presumably packed as in the bulk PTCDA crystal. Moreover, in the PTCDA thin film the molecules persist well orientationally ordered even when brought to the room temperature, thus offering a viable route of thermally stable PTCDA films on semiconductor substrate.

Chapter 2

Thin film growth

Inorganic thin film growth by molecular beam epitaxy (MBE) and organic growth by molecular beam deposition (OMBD) have some similarities and some fundamental differences [12]. There are basically two types of epitaxy: when the deposition material is the same as the substrate and there is a one-to-one commensurate relationship between the particle positions in the deposited layer and the substrate, one speaks about *homoepitaxy.* When adsorbate material is different than the substrate, the process is called *heteroepitaxy.* In addition, when film lattice mismatch occurs with respect to the substrate, the substrate and the film appear to be incommensurate over any meaningful lattice length scale. Nevertheless, there can be a well-defined orientational relationship between the film and substrate lattice, resulting in azimuthal order with a preferred angle of orientation between the overlayer and the substrate. In this case the growth is termed as *quasiepitaxial.* If the substrate surface structure additionally dictates the morphology of the film, it is then said to be *substrate driven.*

In the inorganic MBE the adsorbates are usually single atoms or simple dimers that chemisorb on the surface. Atoms have an isotropic shape (sphere), thus the orientation of the adatom relative to the substrate or to other atoms is irrelevant for the strength of the interaction. Inorganic crystal growth relies on the rather strong covalent or ionic bond of the adsorbates to the substrate. As a contrast, organic molecules are large compared to atoms and are typically highly anisotropic, so the adsorption orientation crucially depends on the relative strength of the molecule-molecule and molecule-substrate interaction. In the organic molecular crystals, the prevalent interaction between the molecules is rather weak van-der-Waals-like dispersion force. The crystal growth mode depends on a delicate balance of the anisotropic interactions between the molecules, their neighbours, and the substrate. In the following sections, we first discuss general characteristics of the (inorganic) film growth and then enlighten the main differences, concerning growth and ordering of the organic films.

Depending on the bond strength, the adsorption includes charge transfer of the surface valence electrons to the unoccupied particle electronic states or v.v. It is tightly related to the geometrical structure of the system, i.e., adsorption site and bond length [13]. The adsorption strength depends on the specific pair of substrate-adsorbate species and may in some cases be high enough to cause structural changes of the substrate (such as surface reconstruction, observed in some noble and near-noble metals) or dissociation of the adsorbate (in case of molecules). The electronic states of the surface and the adsorbed

particle become in case of strong bonding considerably altered[1], as displayed in fig. 2.1. If the adsorbate electronic affinity level lies below the Fermi level of the substrate, the
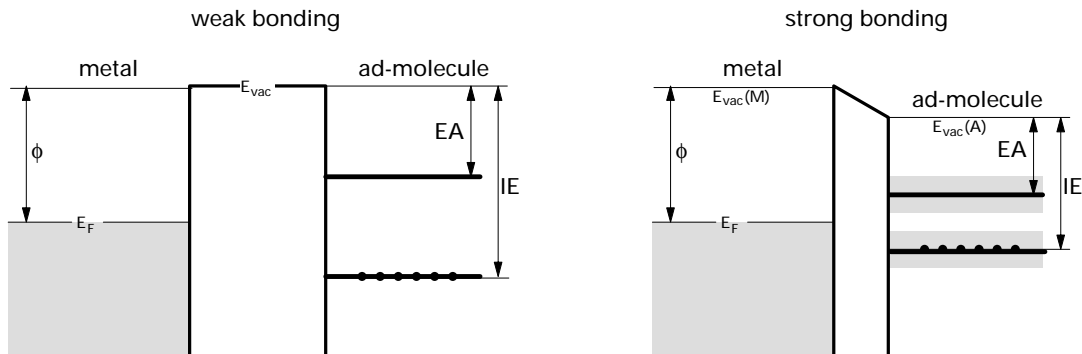
Figure 2.1: In case of weak adsorption, the molecular electronic levels remain almost intact (left), whereas they may alter significantly in the case of strong binding to the substrate (right), possibly giving rise to the change of the system work function. The Fermi level (E_F) and the substrate work function (ϕ), as well as the ionization energy (IE) and the electronic affinity (EA) of the adsorbate are also displayed.

charge moves from the adsorbate to the substrate. Analogously, if the adsorbate ionization energy lies above the substrate Fermi level, the charge moves in the opposite direction. In practice, charge transfer is often accompanied by the formation of an interface dipole barrier [10], which depends on the position of the adsorbate highest occupied and lowest unoccupied electronic levels relative to the substrate Fermi level. The formation of the dipole barrier furthermore leads to a change of the system workfunction.

2.1 Inorganic film growth by vapour condensation

In molecular beam epitaxy, the particles from the vapour phase adsorb on the substrate held at sufficiently low temperature. The driving force in epitaxial film growth is the vapour supersaturation of the evaporation material, which corresponds to the difference between the actual and the equilibrium vapour pressure, p and p_e, respectively. Accordingly, the substrate coverage $\Theta(p, T_s)$, where T_s is the substrate temperature, increases only in the nonequilibrium condition when $p > p_e(T_s)$, meaning that film growth from the vapour phase is a *nonequilibrium process*. For an ideal gas with pressure p at temperature

---

[1]The strength of the adsorption is usually expressed by the terms *chemisorption* and *physisorption*. By IUPAC definition [9], physisorption involves intermolecular forces (van der Waals forces) of the same kind as those responsible for the imperfection of real gases and the condensation of vapours, and which do not involve a significant change in the electronic orbital patterns of the species involved. The van der Waals binding energies are low, typically in the order of 10 to few 100 meV. In chemisorption, the forces involved are valence forces of the same kind as those operating in the formation of chemical compounds. The chemisorbed particles lie closer to the surface with respect to physisorbed ones (typically in the range of a few Å) and the binding energy ranges from ~ 0.5 up to around 10 eV. However, in case of large (e.g., organic) molecules, the evidence for the perturbation of the electronic states is practically always noticeable, although the binding energies might not be as high as in chemisorption. The terms physisorption and chemisorption are therefore less suitable in the field of organic films and will also be omitted in the present thesis.

T, the arrival rate (i.e., the deposition flux, F) of the particles on the surface unit area per unit time equals $F = p/\sqrt{2\pi mkT}$ [14], where m is the mass of the single gas particle and k the Boltzman constant. This creates single particles on the substrate with number density $n(t)$ on a surface with N_0 sites per unit area, so that the single-particle concentration is $c = n(t)/N_0$. The particle then diffuses over the surface until it is involved in one of the following processes (see fig. 2.2): reevaporation, nucleation in 2D or 3D clusters, capture by existing clusters or capture at lattice defects, e.g., steps. Each of these processes is
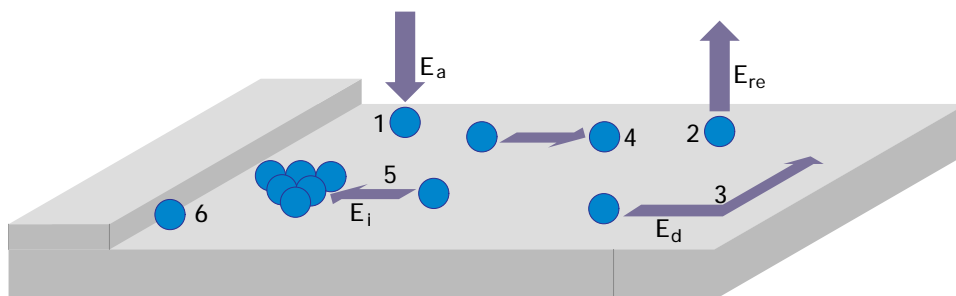
Figure 2.2: The elementary processes on the surface: adsorption (1), reevaporation (2), surface diffusion (3), nucleation of cluster (4), capture by existing cluster (5) and capture at lattice defects (6). The adsorption binding energy (E_a) and the thermal activation energies for re-evaporation, surface diffusion and binding energy to the cluster (E_{re}, E_d, E_i, respectively) are also shown.

governed by a characteristic time, which itself depends on a single-particle concentration, c, and total coverage, Θ. The characteristic times of the processes, which are *thermally activated* (e.g., surface diffusion and re-evaporation), turn to be controlled by the corresponding activation energy and the characteristic surface vibration (attempt) frequency. For example, the surface (lateral) diffusion occurs via hopping, which is characterized by a time $\tau_h = \nu_0^{-1} e^{E_d/k_B T_s}$. Here E_d is the surface diffusion activation energy, whose typical value is around $0.5\,\text{eV}$ [15], and ν_0 the attempt frequency, $\nu_0 = 2kBT/2\pi h \approx 10^{13}\,\text{s}^{-1}$. The hopping time is furthermore tightly related to the single particle diffusion constant,
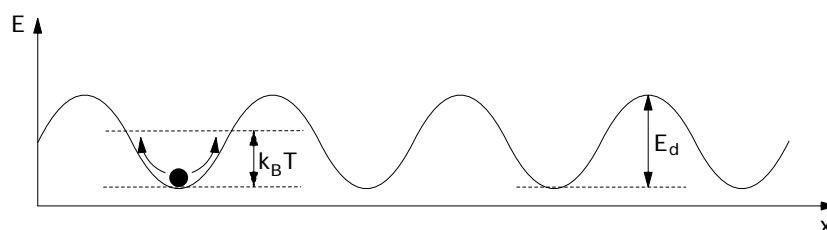
Figure 2.3: The surface diffusion depends on the ratio between the thermal energy ($k_B T$) and hopping activation energy (E_d).

D_s. It is related to the characteristic hopping time τ_h as $D_s = a^2/\tau_h$, where a is the surface lattice constant. For a given time τ, before a single particle gets involved in one of the surface processes (except diffusion), the mean free path l of a particle can then be obtained from $l^2 = D_s\tau$.

The MBE growth can be viewed as a competition between two processes – disordering through (random) deposition and ordering (smoothening) through diffusion, that may

occur on widely separated time scales. In terms of thermodynamics, one speaks about the *equilibrium growth*, when smoothening dominates disordering during the deposition, and equilibrium growth morphology is achieved at any point of growth.

In heteroepitaxial systems, the structure of the evaporated material is usually different from the structure of the substrate. Depending on the substrate wetting and the elastical deformations, which arise from the mismatch of the substrate and adsorbate lattice parameters, three different growth modes of thin films are distinguished. The equilibrium shape of the growing clusters is related to different mechanisms of nucleation. They can be thermodynamically characterized in the terms of surface and interfacial free energies. Let γ^S and γ^F be the free energies of the substrate and film, respectively, and γ^{SF} the interfacial free energy between the substrate and the film. If a deposited material wets the substrate, a 2D or layer-by-layer (Frank-van der Merwe) growth may occur[2], as displayed in fig. 2.4, left. In this case every consecutive layer starts to grow after the completion
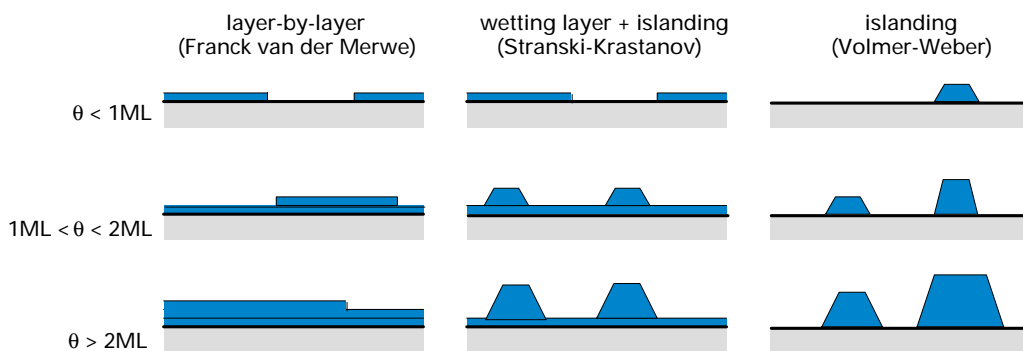

Figure 2.4: Three possible types of film growth in heteroepitaxy.

of the previous one. It is energetically favorable to distribute the film uniformly over the surface, $\gamma^S \geq \gamma^F + \gamma^{SF}$. When on the other hand the adsorbate doesn't wet the substrate, the islands are nucleated and continue to grow as domes, i.e., 3D (Volmer-Weber growth). The energetic relationship in this case reads as $\gamma^s < \gamma^F + \gamma^{SF}$. A third possible growth mode (Stranski-Krastanov) includes a combination of the former two: the substrate is first wet with one or more monolayers, which are then followed by the 3D islands. The cohesion forces inside the overlayer get overwhelmed by the accumulated elastic energy due to strain. Hence, at a certain (early) deposition stage, the growth mode switches from layer-by-layer to island regime.

2.2 Organic film growth

In contrast to atoms, organic molecules have a shape with a pronounced anisotropy, which leads to a number of new aspects and effectively introduces a new dimensionality in film growth [8]. Probably the most fundamental difference in growth between atomic and organic systems is that organic molecules are "extended objects" and thus have *internal degrees of freedom* [16]. The *orientational degrees of freedom* may lead to orientational domains, which are additional source of disorder (see fig. 2.5). In addition, they are

---

[2]By minimizing the surface area, layer-by-layer growth mode represents the equilibrium growth in homoepitaxy.
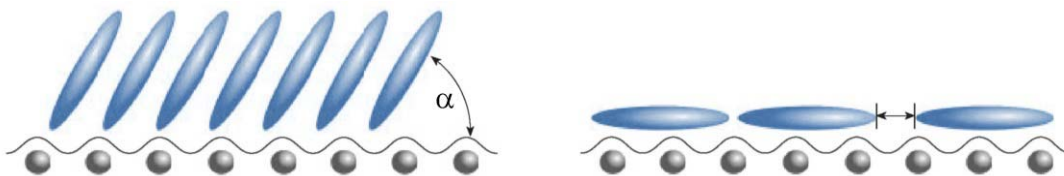
Figure 2.5: Orientational degrees of freedom may lead to orientational domains (left), representing additional source of disorder. Molecules are mostly larger than the unit cells of (inorganic) substrates, thus leading to translational domains (right), which causes smearing-out of the corrugation of the substrate potential experienced by adsorbate.

not included in conventional growth models and can therefore give rise to qualitatively new phenomena, such as the change of the molecular orientation during film growth. Even without considering such transition during growth, the distinction between the films composed of flat-lying molecules and those built-up of up-standing molecules is important and obviously only possible for molecular systems. The *vibrational degrees of freedom* can on the other hand have an impact on the interaction with the surface as well as the thermalization upon adsorption and the diffusion behavior.

The molecule-molecule and molecule-substrate interaction potential is generally different from the case of atomic adsorbates and van-der-Waals-like interaction is more important in organic systems. The response to the substrate lattice strain is usually different, i.e., more strain can potentially be accommodated. In the systems, where the accumulation of strain leads to a *critical thickness* (before the growth mode changes), this thickness can be greater for "softer" materials. The diverse interactions with the substrate and the corrugation of the potential are sometimes discussed in terms of "van-der-Waals epitaxy" and "quasi-epitaxy" [7]. The presence of van-der-Waals-like interactions implies that the relevant temperature scales (for evaporation from a crucible and also for diffusion on the substrate) are usually lower. It should be emphasized, however, that the total interaction energy of a molecule (integrated over its contact area with a surface) can be substantial and comparable to that of strongly interacting (chemisorbing) atomic adsorbates. Nevertheless, in terms of interaction energies per atom, those of the organic molecules considered here are usually weaker. Since we are concerned with closed-shell molecules and van-der-Waals-type crystals, there are no dangling bonds at the organic surface, and thus the surface energies are usually weaker than for inorganic substrates. Importantly, however, if the surface of the substrate is strongly interacting, this results in limited diffusion and thus the evolution of well-ordered films is hindered.

The size of the molecules and the associated unit cells are furthermore greater than that of typical (inorganic) substrates. The effective lateral variation of the potential is thus smeared out, i.e., averaged over the size of the molecule, making the effective corrugation of the substrate as experienced by the molecule weaker than for atomic adsorbates. The size difference of the unit cells of adsorbate and substrate also implies that there are more translational domains (see fig. 2.5). Moreover, organics frequently crystallize in low-symmetry structures, which can again lead to multiple translational and orientational domains, which are both a source of disorder, in addition to those known from inorganic systems (e.g., vacancies).

Generally, most of the above claims directly or indirectly impact the interactions and

thus also the barriers experienced during diffusion. Thus, not only the static structure, but also the growth dynamics exhibit differences compared to inorganic systems.

The position of a single molecule is no longer uniquely determined by three coordinates defining its center of mass; in fact, three angles defining the orientation of the molecules have to be given additionally. Moreover, molecules are usually nonrigid, they are rather soft, and can deform when brought into contact with substrate or even in the molecular bulk. For many organic molecules there is not a unique bulk structure, so the *polymorphism* is rather a rule than an exception. The presence of different polymorphs indicates the presence of different types of arrangements for a given molecule with sometimes pronounced differences in molecular packing but with very similar lattice energies. Some of these polymorphs are metastable and show irreversible phase transitions to the thermodynamically more stable structure, in other cases different stable structures exist that exhibit reversible phase transitions among them. Frequently, it is observed that particular polymorphs depend on the way the single crystals are grown.

To model and control organic thin film growth from the vapour phase, it is necessary to adapt the conventional models for inorganic molecular beam epitaxy so that these major differences are incorporated. The high mismatch of the organic overlayer relative to the inorganic substrate produces strain in the interface layers which may result in the relaxation of the epitaxial structure at a critical thickness, thereby generating periodical defects. Central questions in this respect concern the molecular orientation at interfaces, ordering properties including the geometric structure, thin film growth mechanisms, and the chemical interaction. The molecular orientation and geometric structure at the interface as well as the chemical interaction in the first layer determine the growth mode of thin films. It is perhaps to ambitious to derive a complete set of general rules for describing the growth of organic molecules on solid substrates, since the experimental databasis is still rather small and, unlike in the case of metal-on-metal deposition, currently there is no thorough theoretical framework available to describe and analyse the deposition of molecular thin films on rigid surfaces. In spite of that, in most cases the structure of the deposited films has been studied for a particular molecule/substrate combination.

Considering that the main interest in organic thin films is due to potential application in molecular electronics, the studied molecules are mainly π-conjugated aromatic systems with near to planar structure, which exhibit promising electronic properties. When brought into contact with solid substrates, in addition to being distorted, molecules form a bond to the support, the strength of which can vary over a rather large range of values. In the simplest case, only rather weak but always present dispersion forces appear, which give rise to van der Waals type interaction. On reactive substrates, the possibility of covalent bond formation has to be considered, possibly accompanied by (partial) dissociation of the molecule. The chemical interaction at the interface determines the electrical, electronic and perhaps optical properties. The interaction at the interface may give rise to a charge exchange or polarization and hence influences the direction and size of the interface dipole, the position of the charge neutrality level and the relative positions of the occupied and unoccupied bands. These parameters determine the electronic structure at the molecular semiconductor/metal contact interface. Benzene based organic molecules generally bond to the surface in the way to maximize the overlap of the surface d-electrons with the π-electronic system of the molecule. For device applications, this is an important property because the precise electronic structure at the substrate-molecule interface is important to understand the efficiency of charge injection from the electrical contacts

in the molecular semiconductor. Further growth of the film and the molecular packing, which is conditioned by the structure of the wetting layer and its interaction with the substrate, defines the film charge carrier transport, which is significant in the construction of electronic devices. In case of the planar aromatic molecules, a large π-conjugation length along the long axis of the molecules and close molecular packing of the molecules along at least one of the short molecular axes (π-stacking) are two essential conditions for high carrier mobility (see 2.6). It was reported, for example, that by growing pentacene
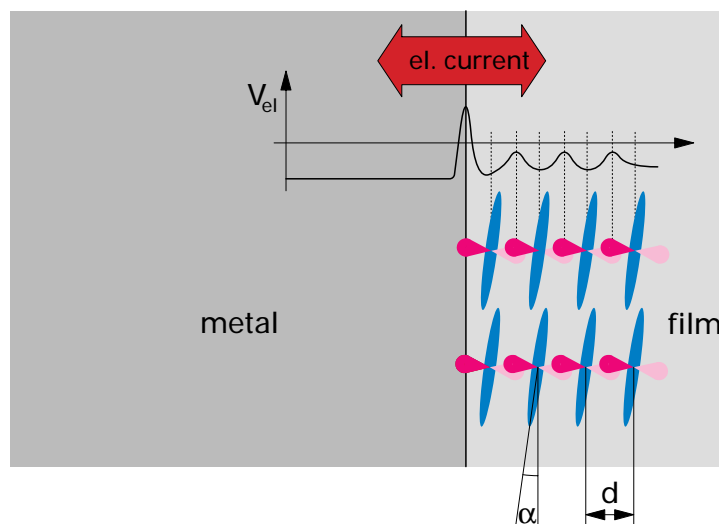
Figure 2.6: The charge injection at metal-film interface and the conduction properties inside the film crucially depend on the overlap of the electronic states. The parameters of the overlap are the intermolecular distance and the molecular packing.

overlayer on SiO_2 substrate [11], which is kept at the temperature close to $77\,K$ during deposition, produces an amorphous film that is practically insulating. This is due to the fact that the overlap of the molecular orbitals is very limited because of the disorder in the solid. On the other hand, when the substrate is kept at room temperature during deposition, a highly ordered film is deposited, and the measured mobility is $0.6\,cm^2/Vs$.

The lack of the experimental data together with the absence of a comprehensive theoretical basis on one side and high technological relevance on the other side, make nowadays the investigations of organic semiconducting thin films and their interfaces with various substrates one of the most challenging field of material physics.

Chapter 3

Near Edge X-ray Absorption Fine Structure

In NEXAFS, *Near Edge X-ray Absorption Fine Structure*, we measure the X-ray absorption near the excitation edge of a certain atomic shell. The electron from a localized inner shell is excited to one of the unfilled molecular states, followed by the de-excitation through emission of a fluorescent photon or an Auger electron. When exciting the atom's core shells, Auger emission is amongst most probable processes. In this two-stage process, an electron from higher orbitals gets ejected by taking over the energy of the electron which relaxes to the core level, as displayed in fig. 3.1, right.
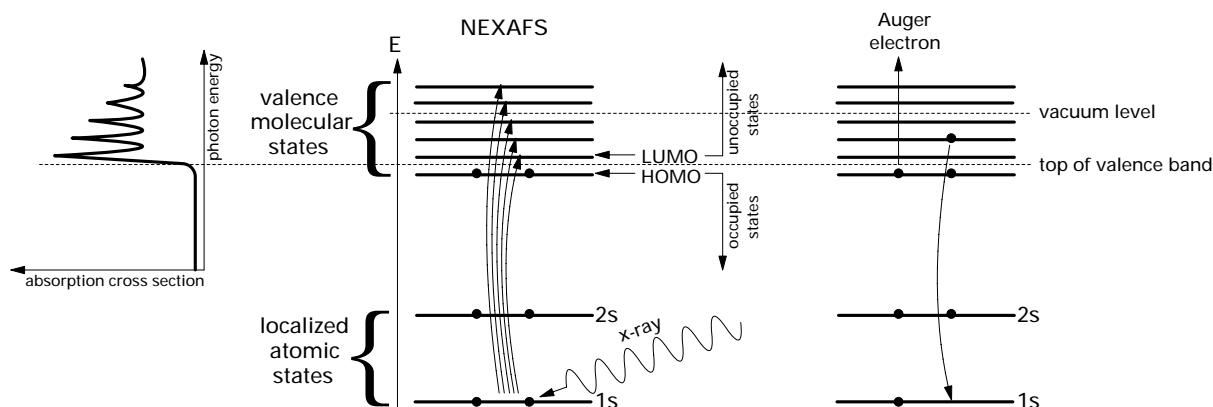
Figure 3.1: The mechanism of NEXAFS (middle), a corresponding X-ray absorption spectrum (left) and Auger emission (right).

The X-ray absorption can be measured either directly by monitoring the attenuation of the X-ray intensity passing through the sample, or indirectly by observing the intensity of some secondary process, e.g., Auger emission or X-ray fluorescence[1].

Since X-ray absorption depends on the initial core-level and final unoccupied electron states the corresponding absorption spectrum reveals both, different initial atomic chemical states and molecular final states. By sweeping the X-ray photon energy over the

---

[1]There are other de-excitation mechanisms, involving multiple electron excitations and low energy electron emission that can be monitored by total yield emission or even by measuring the electron drain current from the sample.

ionization edge, the NEXAFS signal effectively maps the unfilled molecular states. The transition is furthermore conditioned by the symmetry of the source and target orbital. Thus, when using polarized X-rays, the non-ionizing transitions may exhibit angular dependence, i.e., *linear dichroism*. Since the symmetry of orbitals dictates the directions of bonds, one can determine, with the linearly polarized X-rays, the orientation of the bonds and consequently molecular orientation in space. In the field of molecular film growth this is a very useful method for inspecting the geometry of the adsorbed molecules.

In the following, the basic principles of NEXAFS, the theory of X-ray absorption mechanism followed by the molecular orbital theory are briefly discussed. Using elementary group theory, the NEXAFS transition selection rules are introduced together with their application in molecular geometry determination from the angular dependence of X-ray absorption. The typical content of the NEXAFS spectra is also discussed followed by the standard procedures for NEXAFS data analysis.

3.1 The mechanism of X-ray absorption

The cross section of the X-ray absorption follows from the Fermi's "Golden Rule" for the transition probability per unit time P_{if} from a state $|i\rangle$ to a state $\langle f|$ [17]. By introducing a harmonic time-dependent perturbation $V(t) = \bar{V}e^{i\omega t}$, we start with:

$$P_{if} = \frac{2\pi}{\hbar}\left|\langle f|\bar{V}|i\rangle\right|^2 \rho_f(E), \tag{3.1}$$

where $\rho_f(E)$ is the energy density of the system's final states. In order to obtain the total X-ray absorption cross section at a given photon energy we have to sum over all shells with binding energies lower than $\hbar\omega$. However, since we are mainly interested in the partial absorption cross section of inner shells and since all electrons in the outer shells have a smooth cross section in the range of the inner-shell excitation energies, we will neglect the underlying cross section contribution from the outer shells.

The inner shell excitation is produced by an electromagnetic wave with the electric field vector $\mathbf{E}$. Using the Coulomb gauge [18] the corresponding vector potential $\mathbf{A}$ is given by

$$\mathbf{E} = -\frac{1}{c}\frac{\partial \mathbf{A}}{\partial t}. \tag{3.2}$$

In the form of a plane electromagnetic wave with wave vector $\mathbf{k}$, frequency ω and polarization unit vector $\boldsymbol{\epsilon}$, the vector potential is written as

$$\mathbf{A} = \boldsymbol{\epsilon}A_0\cos\left(\mathbf{kx} - \omega t\right) = \boldsymbol{\epsilon}\frac{A_0}{2}(e^{i(\mathbf{kx}-\omega t)} + e^{-i(\mathbf{kx}-\omega t)}). \tag{3.3}$$

The wave vector is related to the frequency and wavelength as $|\mathbf{k}| = \omega/c = 2\pi/\lambda$. Since we are only interested in absorption, the second exponential term which represents photon emission will be omitted in further calculations. It is clear from eq. (3.2) and eq. (3.3) that $\mathbf{A}$ and $\mathbf{E}$ are collinear in space and their magnitudes are related by $E_0 = A_0\omega/c$. The perturbative term in eq. (3.1), which represents the interaction of a spinless particle of charge $-e$ and mass m with an electromagnetic field [19] can now be written as

$$V(t) = \frac{e}{mc}\mathbf{A}\mathbf{p}, \tag{3.4}$$

where $\mathbf{p} = \sum \mathbf{p}_i$ is the sum of the linear momentum operators of the individual electrons.

Combining equations (3.4) and (3.3) with the "Golden Rule" (equation 3.1), we obtain the transition probability per unit time:

$$P_{if} = \frac{\pi e^2}{2\hbar m^2 c^2} A_0^2 \left| \langle f | e^{i\mathbf{kx}} \boldsymbol{\epsilon} \mathbf{p} | i \rangle \right|^2 \rho_f(E). \tag{3.5}$$

For $\mathbf{kx} \ll 1 \Rightarrow |\mathbf{x}| \ll \lambda/2\pi$, where λ is the wavelength of the X-rays and — $\mathbf{x}$ — the estimation of the K-shell diameter, the equation can be simplified by retaining only the first term in the expansion. By doing this we confine to the *dipole approximation*. In our case, for the excitation of the carbon K-shell at $\hbar\omega = 284\,\text{eV}$ the wavelength is $\lambda/2\pi = 7.0\,\text{Å}$. We can estimate $|\mathbf{x}|$, characterizing the K-shell diameter of the carbon, from the Bohr radius $a_0 = 0.53\,\text{Å}$ and the atomic number Z as $|\mathbf{x}| \approx 2a_0/Z = 0.18\,\text{Å}$. The dipole approximation is obviously well satisfied.

To obtain the X-ray absorption cross section, defined as the number of electrons excited per unit time divided by the number of incident photons per unit time per unit area,

$$\sigma = \frac{P_{if}}{F_{ph}}, \tag{3.6}$$

we need first to find the photon flux F_{ph}, associated with the plane wave in eq. (3.3). It is given by the energy flux of the electromagnetic field [18] divided by the photon energy:

$$F_{ph} = \frac{E_0^2 c}{8\pi\hbar\omega} = \frac{A_0^2 \omega}{8\pi\hbar c}. \tag{3.7}$$

The final result for the X-ray absorption cross-section in dipole approximation is then

$$\sigma = \frac{4\pi^2\hbar^2}{m^2} \frac{e^2}{\hbar c} \frac{1}{\hbar\omega} \left| \langle f | \boldsymbol{\epsilon} \mathbf{p} | i \rangle \right|^2 \rho_f(E). \tag{3.8}$$

Here $\langle f |$ and $| i \rangle$ are exact many-electron wavefunctions of the system. A great simplification in calculating the cross-section can be done when working in the single-particle approximation [20]. We assume that primary excitation of "active" electron is rapid with respect to the relaxation time of other "passive" electrons. This allows the separation of initial and final wavefunction into an "active" single-electron part and a "passive" multi-electron part. We get $| i \rangle = \phi_i \Psi_i^{N-1}$, where ϕ_i is an orbital from which an electron is excited, and $\langle f | = u_f \Psi_f^{N-1}$, where u_f is the wavefunction of the excited electron and Ψ^{N-1} is the properly anti-symmetrized determinant of the remaining $N-1$ electrons. The cross-section accordingly becomes

$$\sigma \propto \left| \langle u_f | \boldsymbol{\epsilon} \mathbf{p}_1 | \phi_i \rangle \langle \Psi_f^{N-1} | \Psi_i^{N-1} \rangle \right|^2, \tag{3.9}$$

where $\mathbf{p}_1$ is the momentum operator of the "active" electron. Higher-ordered terms which are associated with excitations of one or more of the "passive" electrons are omitted. The second term in eq. (3.9) represents the overlap integral between the passive $(N-1)$-electron wavefunctions in the initial and final states. It is close to but less than 1 and reflects the intensity lost from the "main" one-electron transition by multi-electron excitations.

We notice that the absorption cross section crucially depends only on the product $\langle f | \boldsymbol{\epsilon} \mathbf{p} | i \rangle$. Putting photon polarization vector in front of the bracket, we get the remaining

term $\langle f|\mathbf{p}|i\rangle$, which is the *matrix element* of the dipole transition expressed in momentum space. To make use of the symmetry data of initial and final electron states, we move to coordinate space, considering operator equivalent

$$\mathbf{p} = -i\hbar\nabla = \frac{im(E_f - E_i)}{\hbar}\mathbf{r}. \tag{3.10}$$

By using *dipole operator* $\boldsymbol{\mu}$ instead of $\mathbf{r}$, where $\boldsymbol{\mu} = e\mathbf{r}$, we write the final expression for the dipole matrix element

$$D_{if} = \langle f|\boldsymbol{\mu}|i\rangle. \tag{3.11}$$

When studying particular molecular transitions in the present thesis we will always refer to this result[2]. The *transition intensity*, I_{if}, additionally depends on the X-ray polarization direction $\boldsymbol{\epsilon}$ and is according to eq. (3.8) expressed as

$$I_{if} \propto \left|\langle f|\boldsymbol{\epsilon}\boldsymbol{\mu}|i\rangle\right|^2 = \left|\boldsymbol{\epsilon}\langle f|\boldsymbol{\mu}|i\rangle\right|^2 = \left|\boldsymbol{\epsilon}D_{if}\right|^2. \tag{3.12}$$

3.2 Molecular orbital theory

The intramolecular electronic transitions can be efficiently explained by introducing the *molecular orbital theory* [17, 21, 22]. Accordingly, when two atoms are kept at small mutual distance, the electron trajectories rearrange due to presence of additional charge and the electrons are said to be found in *molecular orbitals*. They are distributed between the two atoms and if the total energy of the system lowers, they produce a chemical bond.

As in case of atoms, molecular orbitals are represented by the electronic wave functions. The corresponding electronic charge density is then obtained by taking the square of the molecular orbital (i.e., electronic wave function). In case of single and double chemical bonds, only s and p atomic orbitals are involved in formation of molecular orbitals (MO). When two atomic orbitals have the same relative sign in the region of overlap and the electron density concentrates in the center between the two nuclei (fig. 3.5, left), the σ-bond occurs.

The energy level of the corresponding MO is lower than the energy of each separate atomic level, which stabilizes the system. The most common realizations of σ-bond are shown in fig. 3.3.

When two atomic orbitals with the opposite sign overlap and the electron density is concentrated on the line passing through the two nuclei, the central region is void of electron density and a nodal surface occurs, separating the electron density (fig. 3.2, right). The resulting repulsion leads to *antibonding* sigma interaction, where the corresponding MO level lies higher in energy than separate atomic levels, thus destabilizing the system (fig. 3.4).

---

[2]Speaking of transitions to bound states and the intensities of resonances, *optical oscillator strength f* is sometimes introduced, which is related to the X-ray absorption cross section according to $\sigma(E) = C\frac{df}{dE}$, where $C = 2\pi^2 e^2\hbar/mc$. Since f is the energy integral of the cross section, the oscillator strength is a measure of the intensity of the resonance $f = \frac{2}{m\hbar\omega}|\langle f|\boldsymbol{\epsilon}\mathbf{p}|i\rangle|^2$. The oscillator strengths for bound state transitions can be converted to cross sections by introduction of a bound state energy density of final states, $\rho_b(E)$: $\sigma(E) = Cf\rho_b(E)$. In a cross-section versus energy graph the height of a bound state resonance is given by σ and the width by $1/\rho_b$. The oscillator strength is then equal to the area of the resonance peak.
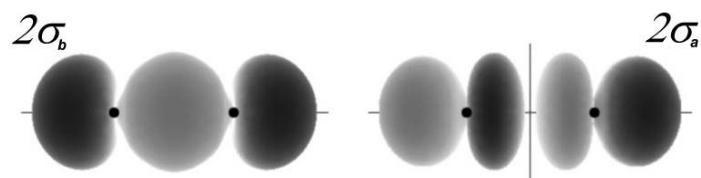
Figure 3.2: The electron density distribution around two atoms (represented by black dots) in the case of σ-bonding (left) and σ-antibonding (right) molecular orbital. The relative sign of the corresponding wave functions is illustrated by dark and light shade, respectively.
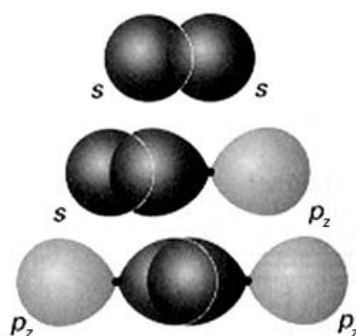
Figure 3.3: Various possibilities of realizing the σ-bond.
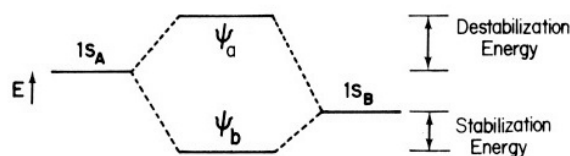
Figure 3.4: The energy of bonding and antibonding orbitals between two nuclei.

In case of double bond, the collinear σ-bond is accompanied by π-bond. The electron density in π-orbital is concentrated in the central region above and below the line connecting the two nuclei, (fig. 3.5, left). In case of the opposite relative sign of electronic

Figure 3.5: The electron density distribution around two atoms in the case of π-bonding (left) and π-antibonding (right) molecular orbital. The relative sign of the corresponding wave functions is illustrated by dark and light shade, respectively.
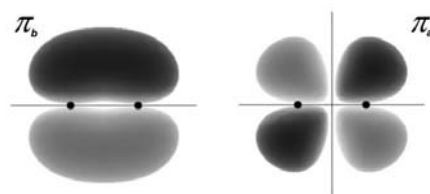
orbitals there is a nodal plane with no electron density between the two nuclei above and below the connecting line and the π-antibonding orbital is produced (fig. 3.5, right). Note that the molecular π-bond orbital can only be formed by overlapping two p-type atomic orbitals (fig. 3.6), while the σ-bond orbital can occur by combining any pair of atomic orbitals.
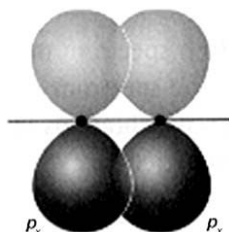
Figure 3.6: Realization of the π-bond.

Molecular orbitals can either be symmetric or antisymmetric with respect to inversion of space through the center of molecule. Orbitals are thus given a second label g (*gerade*), indicating even, and u (*ungerade*) indicating odd inversion symmetry. Examples of gerade and ungerade σ and π orbitals are shown upon fig. 3.7. A brief inspection of spatial
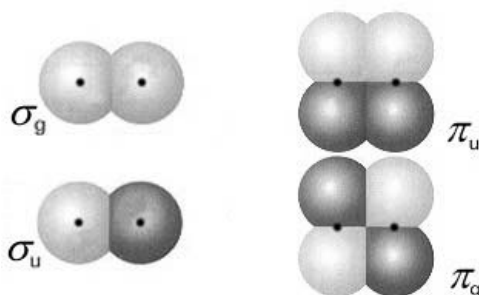
Figure 3.7: σ and π molecular orbitals that are symmetric and antisymmetric upon inversion of space.

symmetry of the orbitals on figures 3.2 and 3.5 shows that σ_b and π_a are symmetric (g) while σ_a and π_b are antisymmetric (u).

The overlap of two atomic orbitals does not always form a molecular orbital. In our approximation, where we construct the molecular orbitals from the linear combination of the atomic orbitals (the $LCAO$ method), several principles have to be considered. One is that in order for two atomic orbitals to mix, they must have the same symmetry about the internuclear axis. The symmetry of the newly arised molecular orbital is also the same. If the atomic orbitals don't possess the same symmetry, there is no bonding interaction. The atomic orbital is unaffected by the presence of the other atomic orbital, so they are regarded as nonbonding. Besides the correct symmetry, in order to form a bond, the two atomic orbitals need to be similar in energy. Combining the orbitals of very different energies leads to only small interaction and the stabilization (and destabilization) energy of the molecular orbital decreases.

The number of obtained molecular orbitals is equal to the number of the given atomic orbitals. Filling the molecular orbitals with electrons is subject to the same rules as for

atomic ones: electrons enter the lowest orbital available, the maximum number of electrons in an orbital is 2 (Pauli exclusion principle) and electrons spread out before pairing up (Hund's rule). Electrons first enter the lowest orbital available and the maximum number of electrons per molecular orbital is 2. Energetically the lowest unoccupied molecular orbital will be abbreviated as LUMO, the second lowest LUMO+1 and so on. The unoccupied molecular orbitals are by convention marked with asterisk, e.g., σ^*, π^*. Right beneath the LUMO lies the energetically highest occupied molecular orbital, HOMO. Occupied orbitals under HOMO are denoted as HOMO-1, HOMO-2 etc.

3.3 Transition selection rules

We make use of the group theory to estimate the matrix element of a certain electron transition in the molecule. Only zero and non-zero results will be distinguished, referring to forbidden and allowed transition.

As defined in eq. (3.11) the matrix element is evaluated by integrating the product of initial and final wave function together with the operator for dipole transition,

$$D_{if} = \langle f|\boldsymbol{\mu}|i\rangle = \int \Psi_f^* \boldsymbol{\mu} \Psi_i d\mathbf{r}. \tag{3.13}$$

If the product $\Psi_f^* \boldsymbol{\mu} \Psi_i$ is antisymmetric along at least one of the coordinate axis the integral is equal to zero, meaning that the transition is forbidden. It is thus necessary to know the parity of each factor.

According to the group theory, every molecular orbital must form a basis for some irreducible representation of the point group of the molecule (PGOM), i.e., must transform as one of the irreducible representations of the PGOM. The orbital electronic transition is then allowed if the triple direct product of the representations

$$\Gamma(D_{if}) = \Gamma(\Psi_f) \times \Gamma(\mu) \times \Gamma(\Psi_i) \tag{3.14}$$

contains the totally symmetric irreducible representation of the PGOM. In practice, one must examine whether the triple product of characters for a certain symmetry operation is totally symmetric. The allowed transitions follow from a general rule, which forbids transitions between two states of the same inversion symmetry. Hence $g \to g$ and $u \to u$ transitions are forbidden, since the dipole operator is antisymmetric upon inversion and thus the direct product of initial and final states must be ungerade, too.

3.4 Polarization dependence

The polarization dependence of the intensity of a particular resonance can be derived quite generally from the expression for the transition intensity in eq. (3.12) and is based on the concept that bonds and associated MOs in molecules are highly directional. It is assumed that we use linearly polarized X-ray light, where the direction along which the photons are antisymmetric is determined by the unit vector of polarization, $\boldsymbol{\epsilon}$.

The initial state $|i\rangle$ is to a very good approximation represented by the atomic $1s$ wavefunction of the excited atom in the molecule. It is spherically symmetric and can thus be represented by the function $|i\rangle = R_{1s}(r)$. In one-electron model, the final molecular

state of the transition can be represented by a corresponding *linear combination of atomic orbitals (LCAO)* [23]. Despite of being a rough simplification, the LCAO is one of the simplest, yet successful way to mathematically construct the electron wave functions in molecules. It assumes that the molecular orbitals ϕ_i are expanded in a basis set of N atomic orbitals χ_l according to

$$\phi_i = \sum_{l=1}^{N} a_{il}\chi_l, \tag{3.15}$$

where a_{il} are the weights of the individual atomic orbitals in the LCAO expansion. The further derivation is for simplicity confined to atoms from the second row in periodic system. The final state wavefunction can thus be written as a linear combination of atomic $1s$, $2s$ and $2p$ states:

$$|f\rangle = g|1s\rangle + a|2s\rangle + b|2p_x\rangle + c|2p_y\rangle + d|2p_z\rangle. \tag{3.16}$$

Here the coefficients g, a, b, c, d give the weight of the atomic orbitals in the LCAO expansion. Expressing the atomic wavefunctions in spherical coordinates one gets

$$|f\rangle = gR_{1s}(r) + aR_{2s}(r) + R_{2p}(r)(b\sin\vartheta\cos\varphi + c\sin\vartheta\sin\varphi + d\cos\vartheta), \tag{3.17}$$

where $R_{1s}(r)$, $R_{2s}(r)$ and $R_{2p}(r)$ represent the radial part of wavefunctions. The position vector $\mathbf{r}$ in the dipole operator is expressed in the same coordinate representation, $\mathbf{r} = r(\hat{\mathbf{e}}_\mathbf{x}\sin\vartheta\cos\varphi + \hat{\mathbf{e}}_\mathbf{y}\sin\vartheta\sin\varphi + \hat{\mathbf{e}}_\mathbf{z}\sin\vartheta)$, where $\hat{\mathbf{e}}_\mathbf{x}$, $\hat{\mathbf{e}}_\mathbf{y}$ and $\hat{\mathbf{e}}_\mathbf{z}$ are the unit vectors along axes of the coordinate system. The vector matrix element is now obtained by integration:

$$\langle f|\boldsymbol{\mu}|i\rangle = \langle f|e\mathbf{r}|i\rangle = R\frac{4\pi}{3}(b\hat{\mathbf{e}}_\mathbf{x} + c\hat{\mathbf{e}}_\mathbf{y} + d\hat{\mathbf{e}}_\mathbf{z}), \tag{3.18}$$

where $R = \int R_{1s}(r)R_{2p}(r)r^3dr$ is the radial part of the matrix element. Thus, according to equation (3.18), for K-shell excitation, the vector matrix element points in the same direction as the p-component in the final state orbital on the excited atom. For final state we now consider the σ^* and π^* orbitals of two double bonded atoms. We orient the coordinate system so that the σ^* orbital and therefore the internuclear axis, lies along the z-axis, and the π^* orbital lies along x-axis. (Another π^* orbital in case of triple bonding would point along y-axis.) The orientation of the X-ray polarization unit vector $\boldsymbol{\epsilon}$ is specified by spherical angles θ and ϕ. The polarization dependence of resonance intensity associated with the σ^* molecular orbital final state is then given by

$$I_{if}(\sigma^*) \propto |\boldsymbol{\epsilon}\cdot\hat{\mathbf{e}}_\mathbf{z}|^2 \propto \cos\theta^2. \tag{3.19}$$

The σ^* resonance intensity is greatest for $\boldsymbol{\epsilon}$ *along* the internuclear axis and vanishes when $\boldsymbol{\epsilon}$ is perpendicular to it. The polarization dependence of the resonance associated with the π^* orbital is correspondingly given by

$$I_{if}(\pi^*) \propto |\boldsymbol{\epsilon}\cdot\hat{\mathbf{e}}_\mathbf{x}|^2 \propto \sin\theta^2\cos\phi^2 \propto \sin\theta^2. \tag{3.20}$$

The π^* resonance has the opposite angular dependence from σ^*. Equations (3.19) and (3.20) describe the origin of the linear dichroism in the NEXAFS angular spectra. Both types of resonances are therefore very helpful in defining the bond and furthermore molecular orientation in space.
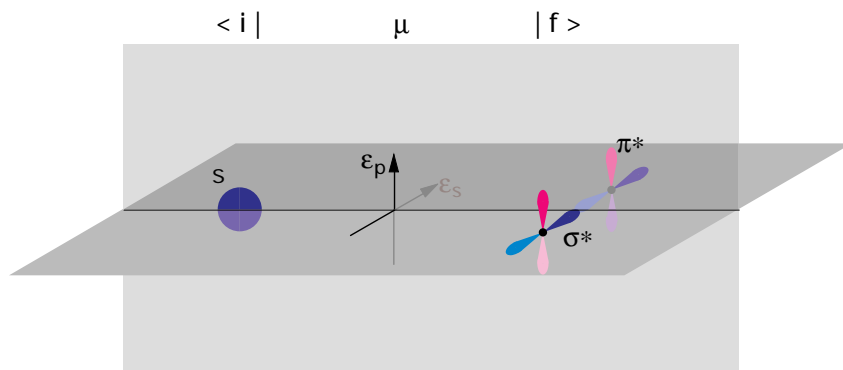
Figure 3.8: Spatial orientations of σ^* and π^* orbitals in four classes of molecules.

The following graphical example, shown in fig. 3.8 should explain the possibility for a certain transition, depending on the photon polarization. The initial state s is symmetric on reflection through both planes and is therefore of character $\Gamma_h(s) = \Gamma_v(s) = 1$. The p-polarized photon is symmetric on vertical and antisymmetric on horizontal plane, $\Gamma_v(\boldsymbol{\epsilon_p}) = 1$ and $\Gamma_h(\boldsymbol{\epsilon_p}) = -1$. The characters of s-polarized photons are reversed. The final molecular state is represented by the model of double bond on the right-hand side of the figure. Its σ^* bond is antisymmetric on the vertical plane and symmetric on the horizontal one, $\Gamma_v(\sigma^*) = -1$ and $\Gamma_h(\sigma^*) = 1$. The π^* bond characters are reversed with respect to σ^* ones. The determination of the transition probability is now straightforward: the transition to σ^* molecular state is allowed for s-polarized and forbidden for p-polarized photon, which follows from

$$
\begin{aligned}
\Gamma_v(\sigma^*) \times \Gamma_v(\boldsymbol{\epsilon_s}) \times \Gamma_v(s) &= -1 \times -1 \times 1 = 1 &\Rightarrow& \quad \text{allowed,} \\
\Gamma_v(\sigma^*) \times \Gamma_v(\boldsymbol{\epsilon_p}) \times \Gamma_v(s) &= -1 \times 1 \times 1 = -1 &\Rightarrow& \quad \text{forbidden.}
\end{aligned}
\tag{3.21}
$$

The same dependence follows for the product of the characters which correspond to the horizontal plane. The transition to π^* molecular state has reversed probability:

$$
\begin{aligned}
\Gamma_h(\pi^*) \times \Gamma_h(\boldsymbol{\epsilon_p}) \times \Gamma_h(s) &= -1 \times -1 \times 1 = 1 &\Rightarrow& \quad \text{allowed,} \\
\Gamma_h(\pi^*) \times \Gamma_h(\boldsymbol{\epsilon_s}) \times \Gamma_h(s) &= -1 \times 1 \times 1 = -1 &\Rightarrow& \quad \text{forbidden.}
\end{aligned}
\tag{3.22}
$$

We now examine the particular spatial orientation of π^* and σ^* systems in the molecules. Depending on the number and mutual orientation of either s or p orbitals, the molecular orbital "sum" can either point in a specific direction and is thus of *vector* type or it spans a plane, being of *plane* type. The schematic illustrations of most common orbital configurations are displayed in fig. 3.9. In the case of single, double or triple bond, the two atomic s orbitals form a simple σ^* bond, which points parallel to the internuclear axis. The p orbitals in double bond, on the other hand, extend perpendicularly to the σ^* bond, thus making the sum pointing in an arbitrary direction perpendicular to it. In the case of triple bond, the p orbitals sum in the spatially degenerate π^* system around the internuclear axis, thus spanning a plane. Similarly, in the benzene ring the in-plane s orbitals span the plane of σ^* system. The π^* system, however, remains essentially concentrated below and above the ring plane, thus retaining the vector nature.
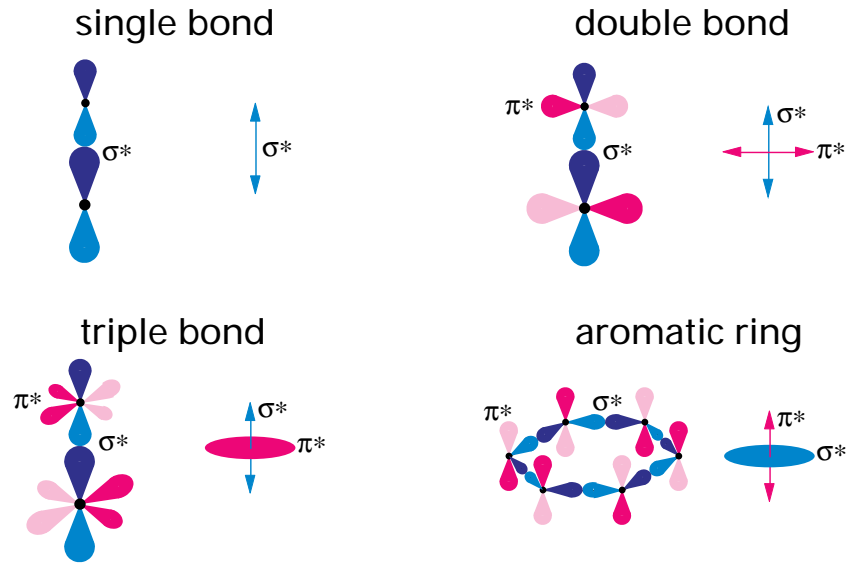
Figure 3.9: Spatial orientations of σ^* and π^* orbitals in four classes of molecules. The double arrows (planes) denote the directions (planes) along which the certain orbital system is antisymmetric.

3.5 Molecular orientation relative to the substrate

When determining the molecular orientation relative to the substrate, one fixes the coordinate system to the surface rather than to the molecule. The absorption geometry for the vector type of orbital is shown in fig. 3.10, left. As derived in sec. 3.4 and according

Figure 3.10: Coordinate system with the corresponding geometry of *vector* (left) and *plane* σ^* or π^* orbital on the surface.

to the notation in fig. 3.10, the angular dependence of the σ^* or π^* vector orbital changes as $I_v \propto \cos^2 \delta$, where δ is the angle between the X-ray polarization vector and vector orbital. Expressing the same projection with angles, defined in coordinate system of the surface one gets

$$I_v \propto (\cos\theta\cos\alpha + \sin\theta\sin\alpha\cos\phi)^2. \tag{3.23}$$

The absorption intensity of σ^* or π^* plane orbitals is on the other hand obtained by integrating eq. (3.19) over all azimuthal angles in a plane with normal **P**. This yields the intensity of the plane orbital to change as $I_p \propto \sin^2 \zeta$. Passing into the surface coordinate

system as shown in fig. 3.10, right, the same intensity becomes

$$I_p \propto 1 - (\cos\theta\cos\gamma + \sin\theta\sin\gamma\cos\phi)^2. \qquad (3.24)$$

As seen in equations (3.23) and (3.24), the angular dependence of the resonance explicitly depends on the azimuthal orientation ϕ of the molecule relative to the substrate. We have to consider now a large number of molecules on the substrate. In the presence of well ordered surface with a certain shape of corrugation, the adsorption geometry is strongly affected which leads to the formation of the domains with equivalent molecular orientation. In case of high surface symmetry, the azimuthal dependence relative to the substrate can even get lost completely. In any case, however, the NEXAFS signal averages over all present configurations, which consequently simplifies the corresponding expressions. Two most useful cases will be considered in the following discussion, i.e., substrate with twofold and higher symmetry.

In case of twofold symmetry, we don't distinguish between the two groups of molecules with orbital tilt α and $-\alpha$ (γ and $-\gamma$ for plane orbitals). The cross-term in eq. (3.23) containing $\cos\phi$ vanishes upon averaging over the two adsorption geometries, and the equation for the vector orbital simplifies into

$$I_v \propto \cos^2\theta\cos^2\alpha + \sin^2\theta\sin^2\alpha\cos^2\phi. \qquad (3.25)$$

Similarly, the eq. (3.24) for plane orbital simplifies into

$$I_p \propto 1 - \cos^2\theta\cos^2\gamma - \sin^2\theta\sin^2\gamma\cos^2\phi. \qquad (3.26)$$

When the substrate possesses higher symmetry, e.g., threefold or fourfold, we assume no preferential orientation of the molecules and the absorption signal averages over all azimuthal angles ϕ. This yields the intensity of the vector orbital

$$\begin{aligned} I_v &\propto \cos^2\theta\cos^2\alpha + \frac{1}{2}\sin^2\theta\sin^2\alpha \\ &\propto \cos^2\theta(1 - \frac{3}{2}\sin^2\alpha) + \frac{1}{2}\sin^2\alpha. \end{aligned} \qquad (3.27)$$

By averaging over ϕ for plane orbital one gets

$$\begin{aligned} I_p &\propto 1 - \cos^2\theta\cos^2\gamma - \frac{1}{2}\sin^2\theta\sin^2\gamma \\ &\propto \frac{1}{2}[\cos^2\theta(1 - 3\cos^2\gamma) + 1 + \cos^2\gamma]. \end{aligned} \qquad (3.28)$$

3.6 Properties of the experimental NEXAFS spectra

The particularly simple symmetry and the localized nature of the $1s$ initial state greatly favors the study of the K-shell excitations. Since the K-shell excitation occurs on a particular atom due to spatial localization of the $1s$ initial state, it is the local symmetry of the molecular orbital final state on the excited atom which determines whether the transition is allowed. Accordingly, the final state wavefunction could only be of $l = 1$ nature in the coordinate system of the excited atom. In the center-of-mass *molecular* coordinate system, however, all l-values are allowed.

An important quantity in the discussion of K-shell excitation is the *1s ionization potential (IP)* defined as the minimum energy necessary to excite an electron from a $1s$ shell to the continuum of states above the vacuum level (VL). The ionization potential $IP(i)$ associated with a particular electron i or *binding energy* $E_b(i)$ is expressed as the difference between the exciting photon energy $h\nu$ and the kinetic energy of the photoelectron:

$$IP(i) = E_b(i) = h\nu - E_{kin}. \tag{3.29}$$

When metallic substrates are used, the photoelectron binding energy typically refers to the Fermi level and the ionization potential equals to the sum of electron binding energy and the metal workfunction.

As the excitation energy (i.e., photon energy) approaches the ionization potential the bound state cross section merges into continuum cross section through ever closer-spaced atomic Rydberg states. In the presence of bonds to hydrogen atoms, Rydberg states are accompanied by hydrogen-derived antibonding $C - H^*$ orbitals, which also occur close to vacuum level. The mechanism of exciting the electrons from the atomic core shell into molecular σ^* and π^* orbitals are shown on fig. 3.11, right. Here we have assumed that
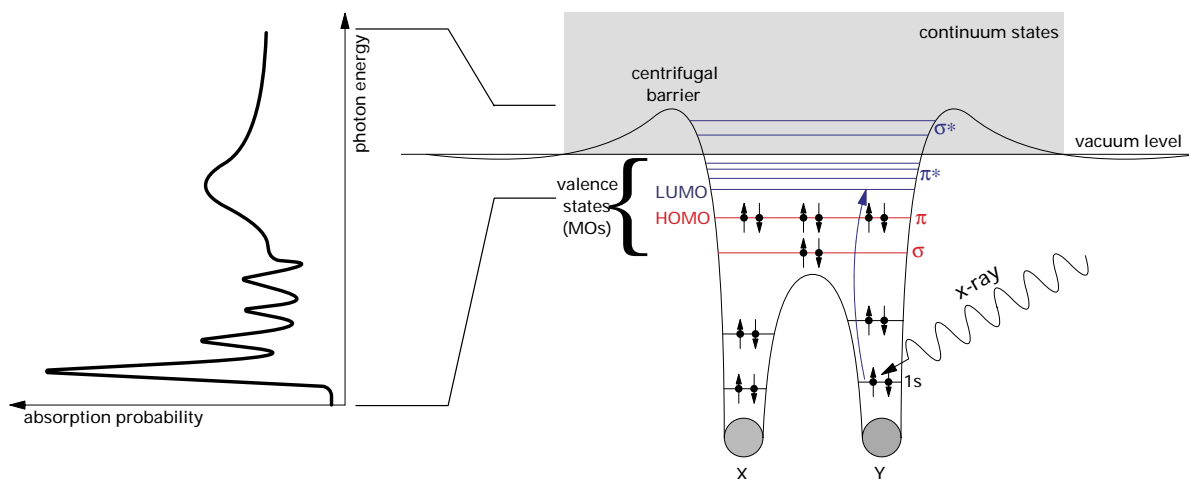

Figure 3.11: The mechanism of K-shell excitation in the system with two bound atoms (right) and the corresponding photoelectron spectrum (left).

transitions of $1s$ core electron to all empty states are allowed, and ignored the multi-electron excitations. We have Rydberg states below and continuum states above the vacuum level, E_v. As illustrated, the lowest unoccupied molecular orbital (LUMO) for two bound atoms is usually a π^* orbital with a σ^* orbital at higher energy. Of course, π^* orbital is only present in spectra of double-bonded atoms. For the neutral molecule these states typically lie above the vacuum level, while in ionized atom the π^* state is pulled below E_v due to attenuated screening of the core positive charge[3]. In the core-hole excited molecule there is an upward (smaller binding energy) relaxation shift of the $1s$ orbital and a downward shift of the outer orbitals because of the increased attractive Coulomb potential created by the core hole. In fact, in all known K-shell spectra of low-Z molecules the π^* resonance, if present, is the lowest energy structure and its energy position falls below the vacuum level.

---

[3]Features below the IP are sometimes called *Feshbach resonances*.

In σ^* resonances, the excited electron gets trapped above the IP in quasi-bound σ^* states[4]. They are confined with the potential barrier arising from the centrifugal part ($\propto l(l+1)/r^2$) in the effective potential which becomes positive for large l. The centrifugal term is small for K-shell excitations of an atom ($l = 1$) but may dominate for the K-shell excitations of a molecule because relative to the center of the molecule large l-values are present in the wavefunction of an excited electron. The σ^* resonances are only trapped in certain directions, e.g., along the internuclear axis for the resonance. The energy width of the σ^* resonance is related to the lifetime of the quasi-bound electronic state. Because of the increasing decay probability of the electron to continuum states, σ^* resonances become broader the higher they lie in the continuum, thus having asymmetric line shape with a tailing towards higher energy. Significant asymmetrical broadening additionally occurs as a consequence of the vibrational motion of atoms in the molecule due to variation in internuclear distance. Since the X-ray absorption process is fast compared to the vibrational motion, the NEXAFS spectrum is a sum of "snapshot" spectra of molecules at different stages of their vibrational cycle, as shown in fig. 3.12. Taking into account that σ^* orbitals are directed along the internuclear axis between two atoms, the asymmetric broadening is absent for π^*-type resonances.
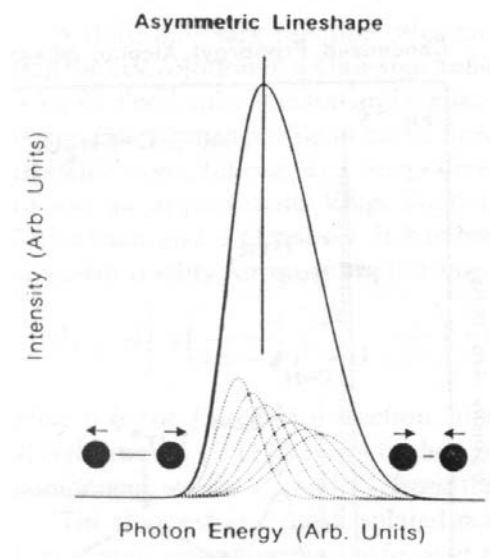
Figure 3.12: Origin of the asymmetry of σ^* shape resonances.

Several step-like features can also appear in the NEXAFS spectra. They are basically the result of a core level electron being excited to a continuum or quasi-continuum of final states, e.g., to the smooth density of states. At the IP, corresponding to the threshold for transition to continuum of unbound free states, a step-like increase in X-ray absorption is expected, producing the background of the same shape in the NEXAFS spectra. In the presence of adsorbate, the ionization potential of the substrate can be considerable shifted with the respect to the clean substrate because of altered workfunction.

Additionally, the step at FL may occur due to transitions to the densely spaced unfilled electronic states of the metallic substrate above the Fermi level, which mix with molecular

---

[4]The σ^* transitions belong to so called "shape resonances", because the excited state is stabilized against immediate decay by a hump in the potential shape as shown on fig. 3.11, left.

states. One would expect that Fermi edge is the lowest energy feature in the NEXAFS spectrum of a molecule, since all states below the FL of the metal should be filled in the ground state and thus no empty final states should be available below the FL. This argument is incorrect, however, because the transition energies are determined by final state effects and not by the ground state properties. As discussed earlier, the π^* resonance energy is conditioned almost exclusively by the arrangement of the $1s$ and LUMO levels and intra-molecular core hole screening. This energy is nearly identical for either free or strongly adsorbed (chemisorbed) molecules. The $1s$ electron binding energy relative to the FL of a molecule bonded to the surface, however, depends on the strength of core hole screening by the metallic electrons. In the photoemission case the molecule is ionized and the photoelectron itself does not contribute to the screening of the core hole. During non-ionizing excitation, on the other hand, the molecule remains neutral and the core hole stays effectively screened also by the excited electron. The screening by metal electrons is thus small or non-existent.

The height of a FL step depends on the strength of hybridization of the metallic states around Fermi level with the molecular valence band states. According to previous discussion, the FL step is more intense and lower in energy for strongly adsorbed molecules than for weakly adsorbed (physisorbed), for which it might be completely absent. The step intensity for K-shell excitations additionally depends on the density of p-like states close to FL, arising from both, adsorbate and metal surface. The higher the density and the smaller the energy difference between the adsorbate and metallic levels, which are symmetry-allowed to interact, the greater the height of the FL step. In case of several chemically inequivalent atoms of a certain atom species, more steps can occur. Because of core hole localization, the height of FL step at different K-edges depends on the adsorbate geometry relative to the surface. The spectra of adsorbate atoms near the surface will exhibit more intense FL step than atoms farther away.

Besides the one-electron features, shown on the fig. 3.11, right, other structures arising from *multi-electron* (ME) transitions are present in experimentally observed spectra. The sudden creation of the core hole potential induced by the excitation of the "active" electron may knock one or more of the "passive" electrons into excited states, too. The ME processes thus gradually turn on with the primary resonance, which gives rise to additional *satellite peaks* around the main transition peak in NEXAFS spectrum. In a simple picture, two types of effects can be distinguished. When the excited state is a single (bound) state, the process is called *shake-up*, and when it is a continuum (unbound) state the process is referred to as a *shake-off*. In both processes the total excitation energy is equal to the photon energy and in photoemission spectra the satellites are therefore observed at lower kinetic energy than the main active-electron peak. In general, shake-up structures are peak-like while shake-off structures are step-like or just a smooth background.

3.7   The lineshapes used in fitting NEXAFS spectra

Features in experimental NEXAFS spectra are fitted with diverse lineshapes, chosen according to their physical origin. The intrinsic shape of transition resonance is usually described by the resonant curve of the harmonic oscillator and is correspondingly fitted

by the Lorentzian function:

$$I_L = H \frac{H}{4\left(\frac{E-E_0}{\Gamma}\right)^2 + 1}. \tag{3.30}$$

Here H is the peak maximum intensity, E_0 is the peak position and Γ is the full width at half maximum (FWHM) of the peak. The characteristic width of the resonance is related to the inner-shell hole lifetime by the uncertainty relation $\tau\Gamma \approx \hbar \approx 6.6 \cdot 10^{-16}\,\mathrm{eV\,s}$. For carbon K-shell excitation followed by Auger relaxation the width is typically $\Gamma \sim 0.1\,\mathrm{eV}$, which corresponds to a characteristic lifetime in the $10^{-15} - 10^{-14}\,\mathrm{s}$ range [24, 25].

When additional broadening due to limited experimental resolution, i.e., instrumental width, dominates the natural width of the resonance, the peaks will have Gaussian lineshape, which is given by

$$I_G = H e^{-4\ln 2\left(\frac{E-E_0}{\Gamma}\right)^2}. \tag{3.31}$$

Again H is the peak maximum intensity, E_0 is the peak position and Γ is the FWHM. To be precise, one should always fit the resonances with the convolution of the Gaussian and Lorenzian lineshapes with the same position and height but with different width, yielding Voigt profile:

$$I_V = \int_{-\infty}^{\infty} I_G(E')I_L(E - E')dE'. \tag{3.32}$$

This should particularly be obeyed in the case, when instrumental and lifetime width of the resonance are comparable.

A special issue for fitting are σ^* resonances. As discussed in previous section, their lineshape is in fact a sum of "snapshot" spectra originating from different internuclear distance due to vibration of the molecule. The asymmetric peak profile can be, however, in practice successfully fitted by introducing a variable width in either Gaussian or Lorenzian function:

$$\Gamma = a \cdot E + b, \tag{3.33}$$

where a determines the relative asymmetry of the peak and E is the photon energy near the resonance.

To fit the step-features, two different lineshapes are mostly used. The multielectron step in UPS spectra that coincides with the Lorentz-shaped peak is mathematically constructed by convolution of Lorentz function with the square step at the peak maximum. One obtains the arctan function, which in its normalized form equals

$$I_{F_{step}} = \left[\frac{1}{2} + \frac{1}{\pi}\arctan\left(\frac{E-E_0}{\Gamma/2}\right)\right]. \tag{3.34}$$

Here H refers to the limit height of the step, E_0 to the position and Γ to the FWHM of the step.

In case of fitting the Fermi or vacuum level continuum step, broadening occurs due to limited experimental resolution and because of thermal excitations, contributing $\Gamma = 4.4\,k_BT$ (for room temperature $\Gamma = 25\,\mathrm{meV}$). The step lineshape is thus constructed by the convolution of Gaussian function and square step, yielding the *error function*. By normalization one obtains

$$I_{G_{step}} = H\left[\frac{1}{2} + \frac{1}{2}\mathrm{erf}\left(\frac{E-E_0}{\Gamma/2\sqrt{\ln 2}}\right)\right], \tag{3.35}$$

where H is the limit height of the step, E_0 its position and Γ the FWHM of the step. If the step expresses considerable decay due to decreasing overlap between the initial and final states when passing to higher photon energies, the original function of the step shall be multiplied by the exponential function,

$$
\begin{aligned}
I_{step}^{decay} &= I_{step}, & E \leq E_0 + \Gamma, \\
I_{step}^{decay} &= I_{step}\ e^{-d(E-E_0-\Gamma)}, & E > E_0 + \Gamma,
\end{aligned}
$$

where d is the exponential decay coefficient.

Chapter 4

# The experimental setup and measuring techniques

For the experimental investigation of surfaces and films several complementary diffraction and spectroscopic techniques have been used. In diffraction the structure factors are measured from which one can obtain the information about surface morphology and possibly the geometrical structure. Spectroscopic techniques based on photoemitted electrons on the contrary give the information on electronic structure and (un)occupied electronic states of the studied systems. Photoemission spectra offer element specific chemical analysis with bonding details and valence band shape.

The experimental work presented in this thesis has been performed at the ALOISA/ HASPES beamline of the Elettra Synchrotron, Trieste. The beamline is a part of the TASC laboratories at the INFM-CNR institute.

4.1   ALOISA/HASPES beamline

ALOISA (*Advanced Line for Overlayer, Interface and Surface Analysis*) is a multipurpose beamline for surface science experiments. It was designed to work in a wide spectral range of $100 - 8000\,$eV and hosts two experimental chambers: the first one, (original) Aloisa, is dedicated to X-ray diffraction and X-ray spectroscopy experiments, while the second one, HASPES, additionally offers ultraviolet spectroscopy and scattering of the thermal helium atoms. The outline of the complete beamline is displayed in fig. 4.1. Close to the exit of the synchrotron beam from the storage ring, there is a switching mirror which lets the beam passing directly into the Aloisa chamber or deflects it (when inserted) to the HASPES chamber.

The Aloisa synchrotron radiation (SR) beam is emitted from the U7.2 wiggler / undulator insertion device (ID) of the Elettra sinchrotron. Elettra is a 3rd generation light source, operating at storage ring electron energy of 2 / 2.4 GeV. It provides photon beams in the energy range of $10 - 30000\,$eV with high spectral brilliance of up to 10^{19} photons/s mm^2 mrad^2 0.1%bw by wigglers and undulators. They consist of spatially periodic magnetic field, produced by two series of alternatingly oriented magnets, separated by a user-tunable gap. When the gap is large comparing to the distance of two adjacent magnets in a series, the path of the passing electrons can be well approximated by the sinusoidal curve and the ID is said to operate the *undulator* regime. When the gap
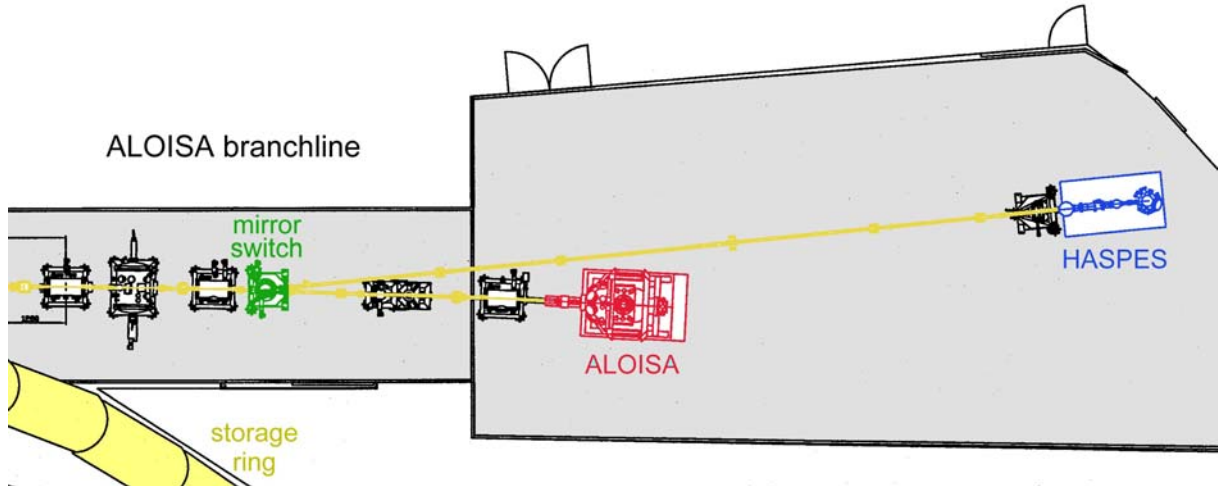
**Figure 4.1:** The outline of the ALOISA/HASPES beamline.

is, on the other hand, comparable to the distance between the magnets in a series, the sinusoidal path becomes heavily distorted (cornered) and the ID operates in the *wiggler* regime. The light produced in each wiggle sums along the direction of the ID axis and becomes the X-ray source of the beamline at the pinhole separating the beamline optics from the storage ring.

By varying the gap size of the Aloisa ID, it can operate as an undulator in the region of high gap values ($\sim 40 - 80$ mm) with low critical[1] beam energy ($100 - 2000$ eV) or as a wiggler in the region of low gap values (~ 20 mm) with high critical beam energy (~ 5000 eV). Fig. 4.2 shows the intensity of the photon beam as a function of the photon energy, obtained for different values of the ID gap. For small gap values the oscillations in the spectrum become very dense resulting in the intensity spectrum similar to the one of the bending magnet. The light is linearly polarized in the plane in which the electrons are wiggled in their trajectory when passing the ID, i.e., in the (horizontal) plane of the synchrotron ring. The linear polarization degree[2] of the light is $\gtrsim 95\%$.

The monochromator of Aloisa covers the full $100-8000$ eV range of photon energy [26]. The main characteristic is the possibility to switch between two types of dispersing systems: a plane mirror plus a grating monochromator (PMGM) for the $100-2000$ eV range and a Si(111) channel-cut crystal for $3-8$ keV range [27]. The two systems lay side by side and they can be inserted onto the optical path by means of a slide mechanism. The PMGM system consists of two plane gratings (with 1200 and 1600 lines/mm), which serve to optimize the monochromator performances in the low energy range, and the mechanism for selecting the grating is the same which shifts the two dispersive systems [28]. The gratings have ≈ 70 Å step height to maximize the reflection for the 1st order diffraction used for energy selection. The monochromatization is then carried out by using the exit slit, which defines the energy window, ΔE, of the passed light. The second dispersive

---

[1] By definition, half of the synchrotron (ID) radiation power is radiated by photons above the critical energy.

[2] The degree of linear polarization or *polarization factor* P in the plane of the electron beam orbit characterizes the intensity or energy density of the electromagnetic field in the orbit plane, relative to the total intensity, $P = \frac{|E^{\parallel}|^2}{|E^{\parallel}|^2 + |E^{\perp}|^2}$. For a complete definition see ref. [17].
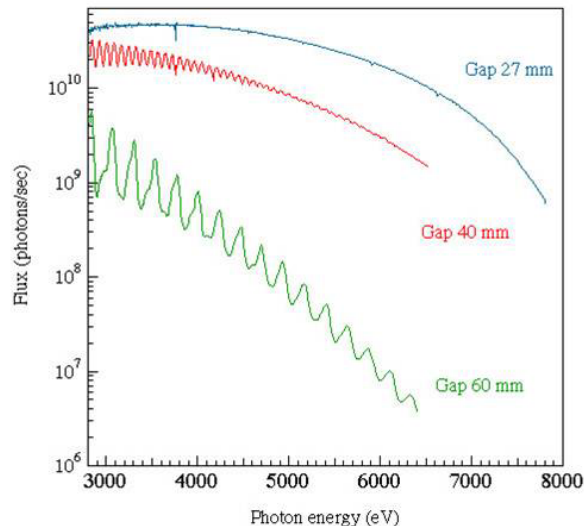
Figure 4.2: The intensity of the photon beam at the exit of the the Aloisa wiggler / undulator ID as a function of the gap value.

element, i.e. channel-cut Si(111) crystal, exploits double diffraction from two surfaces in the gap of a single monocrystal. This way the incident light is monochromatized with very high resolving power, leaving the beam always in the same forward direction during rotation of the crystal. No exit slits are needed because the light, emerging from the channel-cut crystal, already contains a "single" photon energy. The energy resolution of the described monochromator is shown in tab. 4.1.

Beam energy	$100 - 1000\,\text{eV}$	$1000 - 2000\,\text{eV}$	$3000 - 8000\,\text{eV}$
Energy resolution ($\Delta E/E$)	> 10000	4000	7500

Table 4.1: The energy resolution of the Aloisa monochromator.

The complete optical layout of the beamline is sketched in fig. 4.3. The light is collected from the pinhole by a paraboloidal mirror (P1) and is collimated towards the dispersing system. The monochromatic beam is focused at the exit slits (ES) by a second paraboloidal mirror (P2). The diverging beam is re-focused on the sample by a toroidal mirror (RT), producing a spot of approx. $20\,\mu\text{m} \times 150\,\mu\text{m}$. Another paraboloidal mirror (P3) in combination with a plane mirror is used to deviate the beam to the HASPES chamber. It can be inserted manually and deflect the beam by $\approx 6°$. No additional re-focusing mirror is used in this case due to the very long distance of the HASPES chamber from the beamline optics ($14\,\text{m}$). This way a low angular divergence of $< 0.3\,\text{mrad}$ is obtained. The optical layout is in the sagittal focusing (i.e., perpendicular to the scattering plane) configuration to minimize the aberrations in the dispersive plane caused by the slope errors. All the optics is furthermore designed to work in total-reflection condition, i.e., at grazing incidence with deflection angle of $1°$ for P1, P2 and RT. All mirrors have a gold coating to maximize the reflection intensity. Due to the high power density of the "white" beam, generated by the ID, the first paraboloidal mirror, the PMGM and the channel-cut crystal are water cooled. The approximate photon flux through the exit slits

33
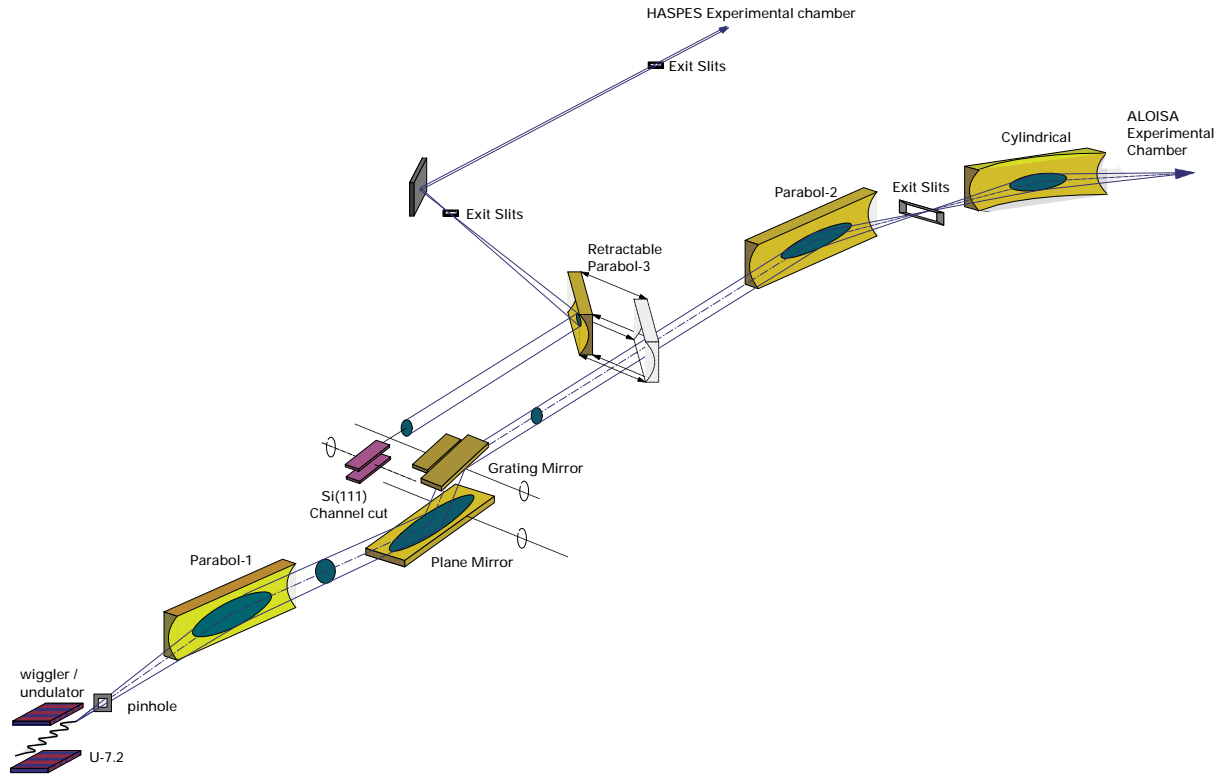
Figure 4.3: Optical lineout of the ALOISA/HASPES beamline.

at $400\,\text{mA}$ of ring current is approximately $2 \cdot 10^{12}\,\text{photons/s/0.1\%bw}$. All movements of the optical elements are available to the beamline user via TCP-IP connection as a service of the Beamline Control System (BCS), a program developed by Elettra technical team.

Besides SR beam, the two experimental chambers are equipped with a few additional (individual) sources. They are listed in tab. 4.2 together with the corresponding experimental techniques. The specific experimental setup of each of the two branchline vacuum chambers is described in the following sections. A photograph of the complete beamline with both experimental chambers is shown in fig. 4.4.

4.2 The experimental setup of the Aloisa chamber

The Aloisa experimental chamber is composed of two parts: a hemispherical void, dedicated to the sample preparation (*preparation chamber*), and a cylindrical void hosting electron analysers and photon detectors for sample investigations (*main chamber*). A sketch of the entire chamber is shown in fig. 4.5. The preparation and main chamber are coupled via large bronze ball bearing and a system of sliding O-rings. This configuration allows the complete rotation of the main chamber (with all detectors) around the SR beam axis, while the preparation chamber stands still. Two differential pumping stages allow the rotation of the main chamber and the frames, maintaining at the same time a constant base pressure of 10^{-11} mbar inside the main chamber.

The preparation chamber is equipped with a MBE cryopanel which hosts four evaporation cells: two Knudsen cells and two electron bombardment evaporators with individual ion gauge for flux control. The cryopanel also holds two quartz microbalances for depo-

vacuum chamber	source	experimental technique
Aloisa	synchrotron X-rays $(100 - 8000\,\mathrm{eV})$	• grazing incidence X-ray diffraction (GIXD) • X-ray reflectivity (XRR)
		• X-ray photoelectron spectroscopy (XPS) • near edge X-ray absorption fine structure (NEXAFS)
	Knudsen cells	molecular beam epitaxy (MBE)
	Ar^+ ion source	surface sputtering
HASPES	thermal He-atoms $(19 - 62\,\mathrm{meV})$	• helium atom scattering (HAS)
	synchrotron X-rays $(100 - 1000\,\mathrm{eV})$	• X-ray photoelectron spectroscopy (XPS) • near edge X-ray absorption fine structure (NEXAFS)
	low energy electrons $(20 - 500\,\mathrm{eV})$	low energy electron diffraction (LEED)
	He UV lamp $(21.22\,\mathrm{eV})$	ultraviolet photoelectron spectroscopy (UPS)
	Knudsen cells	molecular beam epitaxy (MBE)
	Ar^+ ion source $(0 - 3\,\mathrm{keV})$	surface sputtering

Table 4.2: Experimental techniques at Aloisa and HASPES experimental chambers

sition flux calibration. A gas line allows high purity gases to be bled into the chamber. The ion gun for the Ar^+ bombardment enables sample sputtering with the ion energy of up to $3\,\mathrm{keV}$ and the emission current of about $25\,\mathrm{mA}$. A RHEED (*Reflection High Energy Electron Diffraction*) module with electron energy of $15\,\mathrm{keV}$ and the beam impinging to the surface at grazing angle of $4.25°$ is available for checking the surface status *in-situ* during deposition. The preparation chamber is additionally equipped with the sample transfer system and fast entry-lock allowing quick sample exchange.

In the main chamber, the detectors are hosted on two independent frames. A photograph showing the inside of the chamber with the *bimodal* and the *axial* frame is shown in fig. 4.6. The axial frame is mounted at the end of the main chamber and can rotate around the SR beam axis independently from the chamber (see fig. 4.7, right). It hosts five $35\,\mathrm{mm}$ electron analysers with the experimental resolution of $50\,\mathrm{meV}$ and the acceptance angle of $2°$. They are primarily dedicated for the APECS (*Auger Photoelectron Coincidence Spectroscopy*). There is a phosphorus plate with the CCD camera mounted on the axial frame for 2D X-ray reflectivity measurements. The bimodal frame is mounted on the side of the cylindrical main chamber and can rotate around an axis, perpendicular to the SR beam. This axis also rotates around the SR beam together with the main chamber (see fig. 4.7, right). The bimodal frame hosts two $35\,\mathrm{mm}$ electron analysers for angle resolved ($\Delta\varphi \approx 1°$) photoemission (AR-XPS) and photoelectron diffraction (PED) experiments. There are two Si-diodes behind $1\,\mathrm{mm}$ collimators for measuring the total
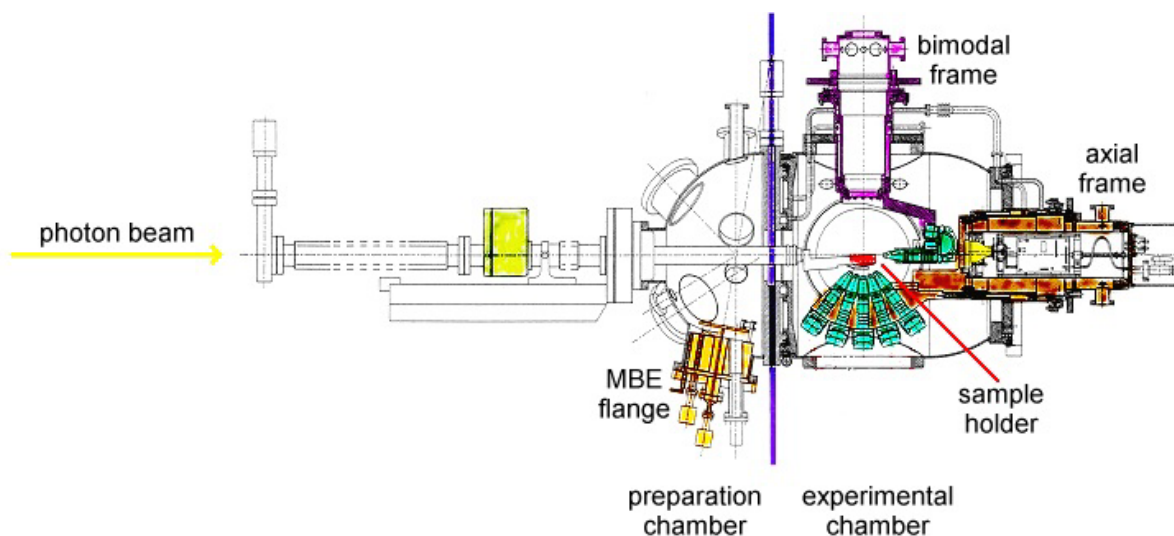
Figure 4.4: A photograph of the ALOISA/HASPES beamline (view towards the synchrotron beam source). The HASPES experimental chamber can be seen in the front and the Aloisa experimental chamber in the back.

current for X-ray diffraction (XRD) and reflectivity (XRR). The bimodal frame additionally hosts two energy-resolved (Peltier-cooled) photodiodes[3] (by Eurisys) operating in single-photon counting mode for X-ray diffraction. They operate in combination with a 12-stage attenuator, thus allowing large dynamical range of the X-rays detection. A wide-angle-acceptance channeltron is mounted on the axis of the bimodal frame, which is used for measuring the partial electron yield in near edge X-ray absorption fine structure (NEXAFS) experiments. The channeltron is equipped in front if its apex with an additional grid, held at adjustable negative potential to repel the low-energy multiple-scattered electrons. This way only high-energy Auger electrons contribute to the partial-yield signal.

The sample is placed onto a six-degree of freedom manipulator which is mounted horizontally into the preparation chamber and can be inserted into the main chamber. The SR beam passes through the whole manipulator and impinges at grazing incidence on the sample. Three rotations of the sample holder allow the sample to be rotated around the synchrotron beam ($R1$) in order to select the desired surface orientation with respect to the photon polarization, the required grazing angle ($R3$) and the azimuthal orientation of the surface symmetry axis with respect to the scattering plane ($R2$). All possible rotations

---

[3]The diodes were recently substituted by a single 66 mm multi-channel plate with 2D array detection.

Figure 4.5: Scheme of the Aloisa chamber.

Figure 4.6: The photograph of the Aloisa main chamber. The SR beam impinges horizontally from the right hand side. The bimodal frame (top) and the axial frame (left/bottom) can be seen.

of the manipulator and the experimental chamber are shown in fig. 4.7. Together with the experimental chamber rotation this allows completely arbitrary configuration between the SR beam, the sample and detectors. All rotations of the manipulator and the main
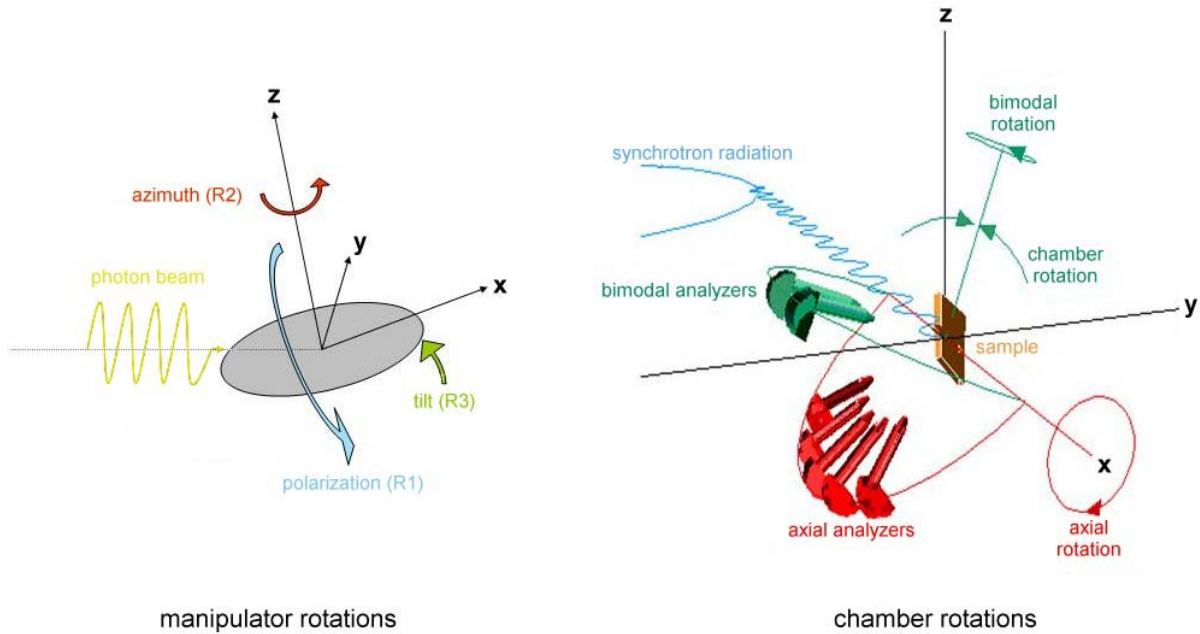
**Figure 4.7:** Sketch of the angular movements available by the manipulator and the experimental chamber.

chamber as well as the translational movement of the manipulator are motorized and computer navigated. The individual rotation ranges and resolutions are listed in the tab. 4.3.

rotating element	rotation axis	extension	resolution
Experimental chamber	SR beam	$\pm120°$	$0.00015°$
Axial frame	SR beam	$\pm120°$	$0.0002°$
Bimodal frame	$\perp$ to the SR beam	$\pm100°$	$0.0002°$
Sample holder: polar angle ($R1$)	SR beam	$\pm185°$	$0.005°$
Sample holder: azimuthal angle ($R2$)	surface normal	$\pm95°$	$0.004°$
Sample holder: grazing angle ($R3$)	$\perp$ to SR beam and surface normal	$-2°$ ... $+10°$	0.004

Table 4.3: The available rotations of the Aloisa manipulator and main chamber, their ranges and resolutions.

The sample holder is equipped with two tungsten filaments, which enables heating of the sample up to 1100 K. Additional gas pipeline enables the liquid nitrogen cooling of the sample down to ~ 150 K. The photograph of the manipulator arm is shown in fig. 4.8. A laboratory-made Labview program has been developed for the data acquisition, detectors control and movements of the experimental chamber and the manipulator.
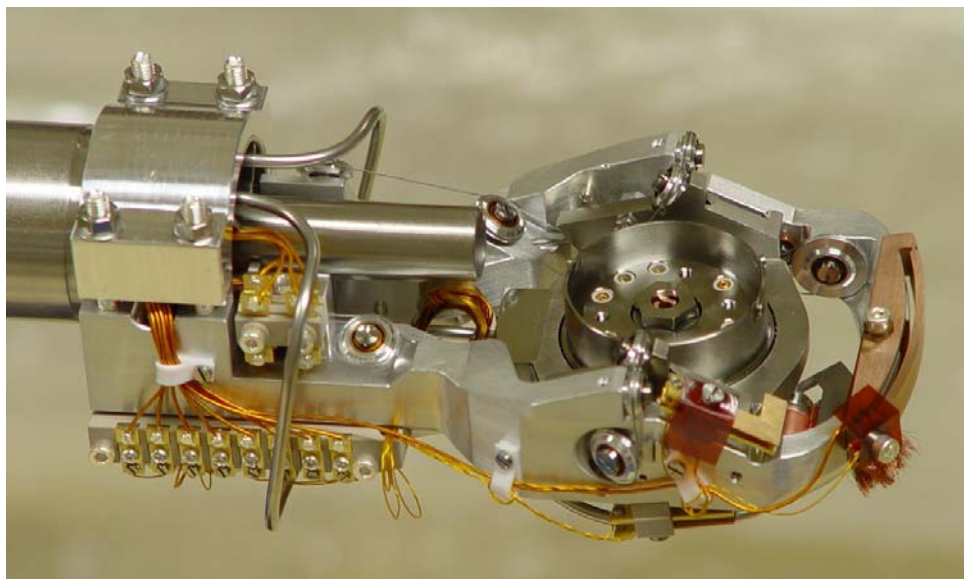
Figure 4.8: The Aloisa manipulator arm (without the sample). A pipeline for the liquid nitrogen cooling can also be seen.

4.3 The experimental setup of the HASPES chamber

The HASPES (*Helium Atom Scattering and Photoelectron Spectroscopy*) vacuum chamber consists of the main upright standing cylindrical void, a prechamber with helium atom source and the helium detection part with quadrupole mass spectrometer. A top-view scheme of the complete apparatus is shown in fig. 4.9. Originally, it operated as a stand-
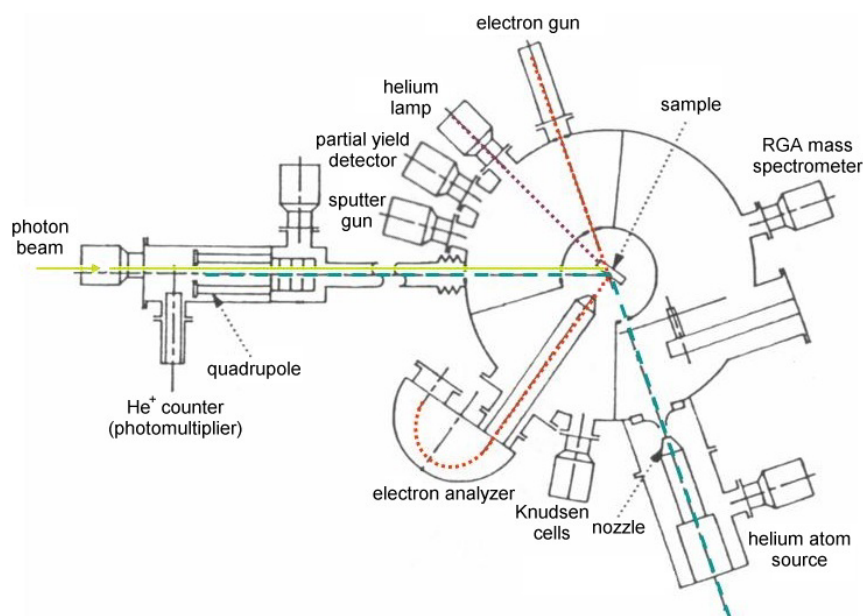

Figure 4.9: The HASPES chamber and the belonging equipment.

alone research chamber for high-resolution He-atom diffraction (HAS) and He energy-loss

spectroscopy (HeELS) [29]. It was attached to the synchrotron in the year of 2003 as a branchline of Aloisa and uses the low-energy monochromatic SR beam in the $120-1000\,\text{eV}$ energy range. The SR beam enters the HASPES chamber through the He detection part, so the beam path coincides with the He scattered beam, but has the opposite direction.

    The main chamber hosts a vertically mounted VG CTPO manipulator with six degrees of freedom and high-precision positioning. The manipulator is mounted on the Omniax translator providing x, y and z translations ($\Delta d = 0.001\,\text{mm}$) and enables three axes of rotation ($\Delta\varphi = 0.005°$). The chamber has a fixed source-sample-detector angle of 110° for HAS, 55° for XPS and 125° for LEED, as can be seen in fig. 4.10, left. The three possible manipulator rotations are presented in the right-hand side of the same figure. By rotating the sample around $R1$ one changes the incidence angle of helium atoms,
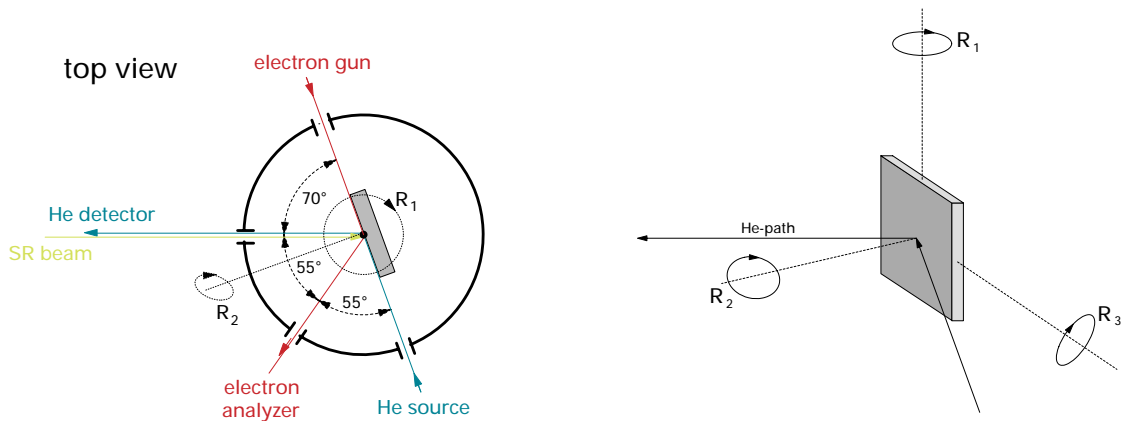
Figure 4.10: HASPES chamber geometry (left) and the manipulator rotations (right).

electron beam and SR beam (see fig. 4.10, left). Rotation around $R2$ varies the angle of the surface symmetry axis with respect to the scattering plane. Tilt rotation ($R3$) allows the sample to incline around a chosen surface axis and therefore enables the acquisition of 2D helium diffraction patterns or 2D valence band mapping (when using photoelectron spectroscopy). The angular range of presented rotations are collected in tab. 4.4. All

incidence angle ($R1$)	$\pm190°$
azimuthal angle ($R2$)	$\pm95°$
grazing angle ($R3$)	$\pm7°$

Table 4.4: The available rotations of the HASPES manipulator.

manipulator rotations are motorized and navigated from the laboratory-made Labview program, which also manages the data acquisition. The manipulator is provided with a thermal link to a small cryostat filled by circulating liquid nitrogen or liquid helium (optional). Together with the tungsten filaments or resistive (ohmic) heating (in case of semiconducting sample) it allows the sample temperature to be maintained in the 100 – 1100 K range.

    The He beam is formed by supersonic expansion from the stagnation chamber into vacuum through a nozzle with $10\,\mu\text{m}$ in diameter, consisting of a standard diaphragm for

electron microscopes. The strong pumping system ensures that the ratio of the stagnation pressure, p_0, inside the nozzle to the background pressure in the beam chamber, p_1, is as high as $p_0/p_1 \sim 10^7$, so that no shock structures occur in the expansion region and a smooth transition from continuum to free-molecular flow takes place a few mm region downstream from the nozzle. The pressure of the He in the stagnation chamber can be set in the $10 - 100$ bar range, defining the flux and the monocromaticity of the He beam. A skimmer with a shape of truncated cone with aperture diameter of 0.5 mm follows the nozzle on a distance of about 25 mm and defines the angular divergence of the beam, which equals $8 \cdot 10^{-6}$ sr. Just downstream from the skimmer, the chopper selects He beam pulses for inelastic scattering measurements. The chopper is followed by another collimator, through which the He beam enters the experimental chamber and presents a cross section of ~ 0.7 mm at the scattering center. The beam energy is selectable between 18.6 and 100 meV by controlling the temperature of the stagnation chamber. It can either be cooled by the attached liquid nitrogen cryostat or heated by the built-in heater. The thermodynamical proceedings of the helium source is thoroughly explained in Appendix A [30].

Scattered He atoms enter the detection chamber through another set of collimators. Neutral atoms are first ionized by the transverse electronic beam and then filtered through the quadrupole mass spectrometer assembly (see fig. 4.9). Electrons in transverse beam have kinetic energy of ~ 100 eV, corresponding to the maximum cross section for the ionization of He atoms, where the ionization efficiency reaches $\sim 10^{-5}$. The ions entering the quadrupole region are then selected according to the desired charge-to-mass ratio, e/m, with an accuracy of 0.05 e.m.u. Finally, the He^+ ions followed by knocked-out electrons are multiplied through a series of 17 dynodes and counted by a computer.

The performance of the presented HAS technique was determined by measuring the diffracted peak width on a perfectly ordered surfaces [29]. The monochromaticity plays a key role in diffraction experiments for structure investigation as well as in inelastic scattering experiments for the determination of surface phonon modes. The concept of *transfer width* has been introduced in order to characterize the resolution of the diffraction instruments. The transfer width is a measure of the instrumental ability to detect surface structures correlated over large distances. In other words, the transfer width is defined as the length at the surface which leads to the instrumental width of the diffraction peaks. For present apparatus, the specular peak reaches the smallest width of 0.135° (FWHM), which is also expected from the geometric characteristics of the apparatus. The contribution to the peak width due to the presence of surface domains or to the dimension of the He wavepackets is estimated to be smaller than 0.05° and the transfer width of the apparatus is found to be 1200 Å.

A differentially pumped helium lamp is fixed on the main chamber to provide ultraviolet radiation of the He I spectral line at 21.22 eV. It is incident at an angle of 50° from above the horizontal scattering plane. In this way the angle of incidence of the radiation does not change substantially when measuring the angle-resolved photoemission spectra by rotating the sample about around $R1$.

A 150 mm high-resolution hemispherical electron analyser is mounted in the scattering plane in the middle of the 110° fixed HAS angle (see fig. 4.10, left). It hosts a 48-segment anode behind two serially-coupled multichannel plates (MCP) and offers an energy resolution of 0.5% of the pass energy, reaching the maximum resolution of 17 meV. The analyser is used for XPS and UPS and has very small acceptance angle ($\sim 0.5°$). Thus,

in combination with the (Leybold) electron gun, also mounted in the scattering plane and emitting the electrons with $10 - 1000\,\text{eV}$ kinetic energy, it offers the angularly well resolved electron detection – LEED technique.

A channeltron is also mounted at an angle of $50°$ from above the horizontal scattering plane for the partial electron yield detection in near edge X-ray absorption fine structure (NEXAFS) experiments. In front if its apex it is equipped with an additional grid, held at adjustable negative potential to repel the low-energy multiple-scattered electrons. This way only high-energy Auger electrons contribute to the partial-yield signal.

The main chamber is furthermore equipped with the liquid-nitrogen cooled cryopanel, hosting three laboratory-made Knudsen evaporation cells. A microbalance for deposition rate control is mounted in the bottom of the vertically inserted manipulator arm. An ion gun for surface cleaning using ionized argon atoms is directed at angle of $50°$ with respect to the scattering plane. The kinetic energy of Ar^+ ions can be varied in the $3\,\text{keV}$ range at the emission current of up to $25\,\text{mA}$. Using the z translation of the manipulator, the sample may be raised by $250\,\text{mm}$ to a level of the vacuum chamber free from internal walls. In this plane the sample may face the flange equipped with fast-entry lock for quick exchange of the sample. A residual gas analysis (RGA) mass spectrometer is attached for easy detection of possible leaks. The chamber base pressure is maintained in the $< 10^{-10}\,\text{mbar}$ range and rises in the $10^{-9}\,\text{mbar}$ range in the presence of the He beam.

4.4 The details about used experimental techniques

In the present section the basics of the experimental techniques used in this thesis are discussed. In case of HAS and NEXAFS, particular properties of the Aloisa and HASPES experimental setup are considered.

4.4.1 Helium Atom Scattering (HAS)

For surface structure determination we employed the helium atom scattering (HAS) technique. Comparing to LEED, RHEED or XRD, HAS is completely nondestructive method, since neutral He atoms are used in the ~ 10 to $100\,\text{meV}$ kinetic energy range ("thermal" atoms). It is a long range (lateral) order probe and is exclusively surface sensitive, because He atoms scatter on the outermost valence electron density. Since He atoms are rigid (spherical) balls without inner rotational and vibrational states, they are very suitable for scattering. Furthermore, they are much less reactive than hydrogen and lighter than other noble gases, so they can excite a single surface vibration mode (phonon). HAS thus offers *in situ* observation of the dynamical surface processes, such as island formation, phase transitions, layer-by-layer thin film growth etc. Besides, thermal He atoms have high cross section for the diffusion scattering and are therefore highly sensitive to the statical (e.g., point-like defects[4]) as well as dynamical disorder (Debye-Waller vibrations).

HAS can efficiently measure both, the structure factor related with the exposed surface structure, and the form factor, describing the position of the scatterers inside the unit cell [31]. The diffraction pattern consists of the signal coherently summed over the area with the diameter of the coherent length ($\sim 1200\,\text{Å}$, see previous section). Details about

---

[4]With the term "point-like defects" we consider a single vacancies, atoms or molecules as well as fluctuations of the single molecular orientation along its polar or azimuthal axis.

He-surface interaction, which consists of an attractive and a repulsive part, can be found in Appendix B. However, for smooth surfaces, i.e., surfaces with low corrugation ζ, where ζ is much smaller than the unit cell, $\zeta \ll a$, the simplest approach to the He-surface interaction is to neglect the attractive (van der Waals) forces and to replace the repulsive part by a *corrugated hard wall, CHW* [30]. The spatial form of such interaction is given by the position of the hard wall, $\zeta(\mathbf{R})$, which corresponds approximately to the locus of the classical turning point for the He atoms of certain kinetic energy. The corrugation of the surface can be expressed by the first term in a Fourier series as:

$$\zeta(\mathbf{R}) = \zeta_0 \left[\cos \frac{2\pi x}{a} + \cos \frac{2\pi y}{b} \right], \tag{4.1}$$

where a and b are the nearest neighbour distances along x and y directions, respectively, and $4\zeta_0$ is the peak-to-valley height of the corrugation. The modulation of the diffracted peaks due to the surface corrugation may be obtained by assuming that all parts of the continuous locus of $\zeta(\mathbf{R})$ contribute equivalently to the diffracted intensity, so that one can make the sum of phase factors over the surface unit cell [32]:

$$I_\mathbf{G} = - \int_{u.c.} \frac{d^2\mathbf{R}}{A_c} e^{-i[\Delta k_z \zeta(\mathbf{R}) + \mathbf{GR}]}, \tag{4.2}$$

where A_c is the surface unit cell, $\mathbf{G}$ the reciprocal lattice vector and Δk_z the perpendicular momentum transfer. By writing the reciprocal lattice vector in the form $\mathbf{G} = (m\frac{2\pi}{a}, n\frac{2\pi}{b})$ and considering eq. (4.1), we obtain

$$I_\mathbf{G} \propto J_{|m|}(\zeta_0 \Delta k_z) J_{|n|}(\zeta_0 \Delta k_z), \tag{4.3}$$

where J_m and J_n are the Bessel function of the m- and n-th order, respectively. The diffracted peak intensities are modulated by the square of the Bessel functions, $J^2(\zeta_0 \Delta k_z)$, which enables the extraction of the information about the surface corrugation ζ_0 from the diffracted peak intensities.

The HAS geometry is described by making use of the kinematic theory of scattering and provides us with the surface structure factor. Monochromatic He atoms impinge on the surface with a wave vector $\mathbf{k} = (\mathbf{K}, k_z)$, where $\mathbf{K}$ and k_z are the momentum parallel and perpendicular to the surface, respectively. In case of elastic scattering the total energy of the single atom is conserved and the parallel momentum changes according to

$$\Delta \mathbf{K} = \mathbf{K_{in}} - \mathbf{K_{out}} = \mathbf{G}. \tag{4.4}$$

Due to the translational symmetry of the surface Bravais lattice, the parallel momentum in elastic scattering process is conserved only to within an additive surface reciprocal lattice vector $\mathbf{G}$, as shown in fig. 4.11. It should be emphasized that here, unlike in the case of the diffraction from the 3D lattices, where the diffraction occurs when the conservation of energy and total momentum is met, the final perpendicular momentum k_z may take continuous values. We therefore refer to as "diffraction rod" rather than diffraction point, where rod is characterized by the parallel momentum $\mathbf{K_{out}}$. The surface diffraction may occur for any value of k_z along the diffraction rod, wherever the energy conservation is satisfied. In other words, there is always diffraction from the 2D Bravais lattice (provided that $|\mathbf{k_{in}}| > |\mathbf{G}|$) since the diffraction rod necessarily crosses the Ewald sphere [33].
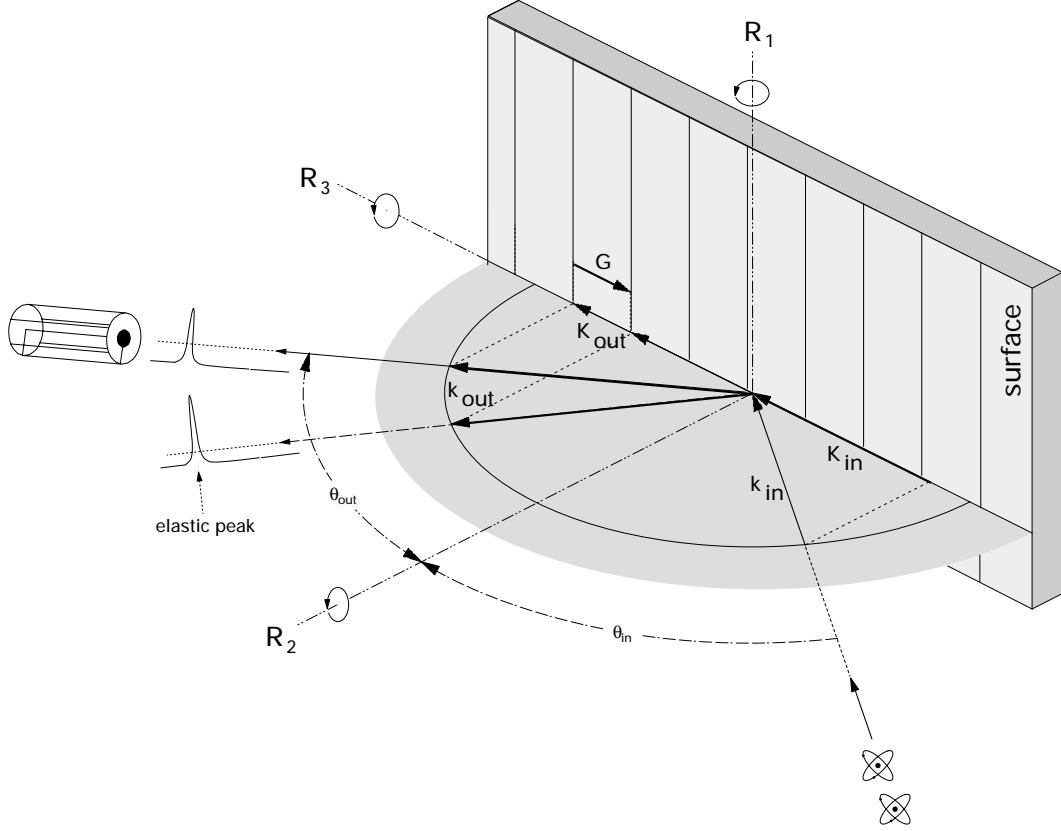
Figure 4.11: Experimental setup of a fixed scattering geometry ($\theta_{in} + \theta_{out} = \theta_{tot} = 110°$) with presented elastic scattering of He atoms. The scattering plane is represented by a shaded circular region and is assumed to be perpendicular to the surface.

The equations describing elastic scattering ($|\mathbf{k_{in}}| = |\mathbf{k_{out}}| = k$) may be expressed in the particular form when considering the existing fixed scattering geometry $\theta_{in} + \theta_{out} = \theta_{tot} = 110°$. The size of the in-plane wave vectors equals

$$
\begin{aligned}
K_{in} &= k \sin(\theta_{tot}/2 + R_1) \quad \text{and} \\
K_{out} &= k \sin(\theta_{tot}/2 - R_1).
\end{aligned}
$$
(4.5)

The size of the parallel momentum transfer is then

$$
\begin{aligned}
\Delta K &= K_{out} - K_{in} \\
&= k \sin(\theta_{tot}/2 - R_1) - k \sin(\theta_{tot}/2 + R_1) \\
&= 2k \sin R_1 \cos(\theta_{tot}/2).
\end{aligned}
$$
(4.6)

Considering this result, one can easily estimate the typical size ξ of the terraces present on the surface from the width of the diffracted peaks. The diffracted peak occurs at $\Delta K = G$. Its width due to the finite size of the terraces is obtained by differentiating eq. (4.6):

$$
\delta G = 2k \cos R_1 \delta R_1 \cos(\theta_{tot}/2).
$$
(4.7)

The typical size of the terraces then equals

$$\xi = \frac{2\pi}{\delta G}. \tag{4.8}$$

Note that the actual width of the diffracted peak, σ_d, is in fact the convolution of the instrumental width of the scattering apparatus, σ_i, and the broadening due to the size of the terraces, δG. An approximation for the size ξ is however simply obtained by subtracting the variances of the actual peak width and the instrumental width, $(\delta G)^2 = \sigma_d^2 - \sigma_i^2$, where $\sigma_i = 0.135°$ (see previous section).

4.4.2 Low-energy Electron Diffraction (LEED)

The diffraction of low-energy electrons is used as the standard technique to check the crystallographic quality of a surface, prepared either as a clean surface, or in connection with ordered adsorbate overlayers [34]. In this experiment a beam of electrons with a primary energy between 20 and 500 eV is incident on the surface and the elastically scattered electrons give rise to diffraction (or Bragg) peaks which are usually imaged as spots on a phosphorous screen. In this energy range, the de Broglie wavelength of the electrons, $\lambda = h/p = h/\sqrt{2mE}$, lies in the range $2.7 - 0.5$ Å which corresponds to the interatomic distances in the crystal (and their surfaces). Electron scattering is surface sensitive only if the electrons have the right energy, since the inelastic mean free path of electrons in a solid depends on the kinetic energy of the electrons. For incident energies in the above mentioned range, strong inelastic scattering caused by plasmon excitations restricts the incoming electrons mean free path to about $5 - 10$ Å, which corresponds to the depth of only a few layers near the surface. In LEED only elastically scattered electrons contribute coherently to the formation of sharp peaks, and these electrons are mostly scattered from the surface of the sample. This makes the LEED surface sensitive.

To understand the essential features of LEED experiment, kinematic theory is sufficient. The condition for the occurrence of an "elastic" Bragg spot is that scattering vector component parallel to the surface, $\mathbf{K} = \mathbf{K_{out}} - \mathbf{K_{in}}$ (see sec. 4.4.1), equals a vector of the 2D surface reciprocal lattice, $\mathbf{G}$. This condition is valid for the limiting case where only the topmost atomic layer is involved in scattering. For the component k_z perpendicular to the surface, no such condition applies. One can therefore attribute to every 2D reciprocal lattice point (h, k) a rod normal to the surface, as shown in fig. 4.12, left. As a contrast, in the 3D diffraction we have discrete reciprocal lattice points in the third dimension rather than rods. In the 2D case, the possible elastically scattered beams ($\mathbf{k_{out}}$) are obtained by Ewald construction. As seen in fig. 4.12, left, the condition $\mathbf{K} = \mathbf{G}$ is fulfilled for every point at which the elastic sphere crosses a reciprocal-lattice rod. In contrast to the 3D scattering in bulk, the occurrence of a Bragg reflection in 2D is not a singular event. In a real LEED experiment, however, the primary electrons penetrate several atomic layers into the solid. The deeper they penetrate, the more scattering events in the z-direction perpendicular to the surface contribute to the LEED pattern. This leads to a modulation of the intensities of the Bragg reflections in comparison with the case of pure 2D scattering. In the Ewald construction one can allow for this situation qualitatively by modulating the rods periodically along z-direction, as shown in fig 4.12, right. In the extreme case of 3D scattering, the thicker regions of the rods become points of the 3D reciprocal lattice. Accordingly, when the Ewald sphere crosses a "thicker" region of the
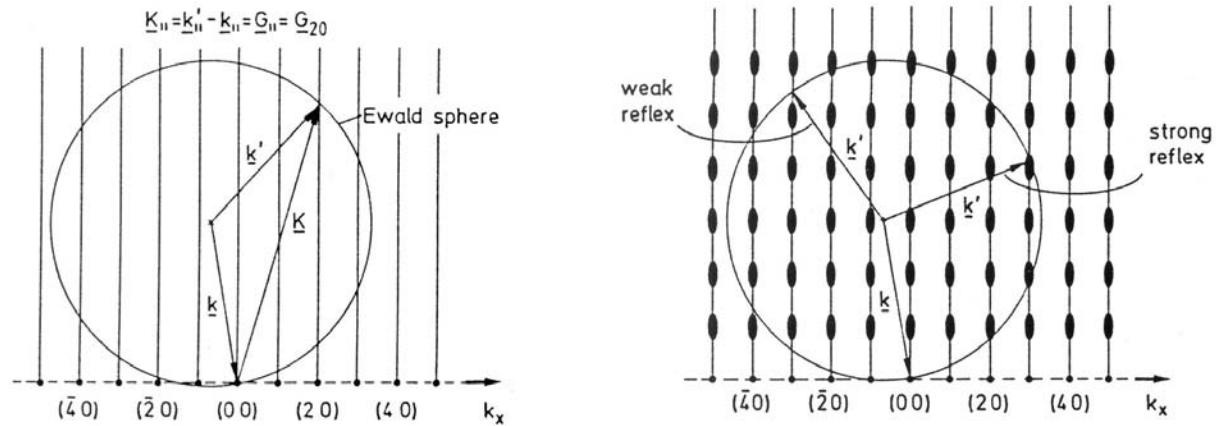
Figure 4.12: Ewald construction for elastic scattering on a 2D surface lattice (left). The scattering condition of the plotted beams is fulfilled for the reciprocal lattice point $(hk) = (20)$, but a number of other reflexes are also possible. Ewald construction for elastic scattering on a quasi-2D surface lattice (right), considering not only topmost lattice plane but also a few underlying planes. Correspondingly the (30) reflex has high intensity, whereas the $(\bar{3}0)$ spot appears weak. [34]

rods, the corresponding Bragg spot has strong intensity, whereas less pronounced regions of the rods give rise to weaker spots. Another important consequence is the following: if the primary energy of the incoming electrons changes, the magnitude of k, i.e., the radius of the Ewald sphere, changes. As k is varied, the Ewald sphere passes successively through stronger and weaker regions of the rods and the intensity of a particular Bragg spot varies periodically. Besides, a LEED spot is never infinitely sharp but exhibits a certain shape with a finite width or even can be split. Spot broadening is usually due to a finite size of islands of ordered atoms as frequently observed in adsorption experiments. The spot's half width is reciprocal to the average lateral size of the islands and the spot's shape contains the information about the statistical distribution of different island sizes.

### 4.4.3 X-ray Spectroscopy (XPS) and UV Spectroscopy (UPS)

The most important and widely used experimental technique giving the information about occupied electronic states is photoemission spectroscopy [34]. The experiment is based on the photoelectric effect, where the solid surface is irradiated by mono-energetic photons and the emitted electrons are detected with respect to their kinetic energy by an electron analyser. When photons in the X-ray spectral range are used the technique is called *X-ray Photoelectron Spectroscopy, XPS*, or *Electron Spectroscopy for Chemical Analysis, ESCA*. With ultraviolet radiation, on the other hand, the technique is called *Ultraviolet Photoemission Spectroscopy, UPS*.

The energy of photons typically used for XPS is up to $\sim 1000\,\mathrm{eV}$. These photons have limited penetrating power in a solid on the order of $1 - 10\,\mu\mathrm{m}$ [35]. Probabilities of electron interaction with matter, however, far exceed those of the photons, so while the path length of the photons is of the order of micrometers, that of the electrons is of the order of tens of Ångströms. Thus, although ionization occurs to a depth of a few micrometers, only those electrons that originate within tens of Ångströms below the solid surfaces can leave the surface without energy loss and contribute to the peaks in the

spectra. The remaining electrons that undergo inelastic processes before emerging, suffer energy loss and increase the spectrum background. It is clear from the above that XPS technique is primarily surface sensitive and has consequently very useful applications in surface and thin film analysis.

The mono-energetic photons interact with atoms in the surface region, causing electrons to be emitted by the photoelectric effect (the quantum-mechanical concept of the photon absorption is discussed in sec. 3.1). The electrons leaving the sample are detected by an electron spectrometer according to their kinetic energy. After ionization, the excited atom relaxes and the vacancy is filled by an electron from a higher level which can lead to either X-ray fluorescence or the radiationless de-excitation process of Auger emission. The mechanism of the XPS as well as the corresponding energy levels are shown in fig. 4.13. The actual kinetic energies of the emitted electrons are given by:
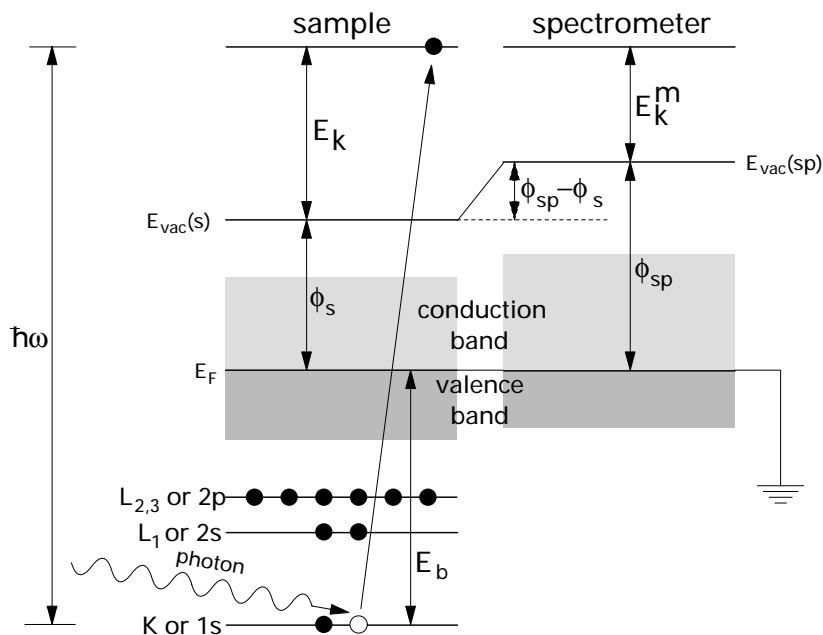
Figure 4.13: The XPS emission process and the influence of the spectrometer work function ϕ_{sp} on photoelectron spectra. The relative energy levels of Fermi level (E_F) and sample work function (ϕ_s) are also shown. E_k is the photoelectron kinetic energy, E_k^m is the kinetic energy of the photoelectron, as measured by the electronic analyser, $\hbar\omega$ is the photon energy and E_b the electron binding energy relative to the Fermi level.

$$E_k = \hbar\omega - E_b - \phi_s, \tag{4.9}$$

where $\hbar\omega$ is the energy of the photon, E_b is the binding energy of the atomic orbital from which the electron originates, and ϕ_s is the sample workfunction. Note that the measured kinetic energy E_k^m of the electrons is smaller by a difference between the spectrometer and sample workfunction, $\phi_{sp} - \phi_s$ (see fig. 4.13).

The kinetic energy of the electron is the experimental quantity measured by the spectrometer, but it is dependent on the photon energy of the X-rays and is therefore not an intrinsic material property. It is the *binding energy* (E_b) of the electron, which identifies the electron specifically, both in terms of its parent element and atomic energy level [36].

It can either be defined relative to the vacuum level or relative to the Fermi level. Since the definition to vacuum level may become impractical due to possible change of material work function in the presence of the adsorbate, the Fermi level is taken in the following discussion as the reference point. Because there is a variety of possible final states of the ions from each atom species, there is a corresponding variety of kinetic energies of the emitted electrons. The photoelectron spectrum accurately reproduces the electronic structure, i.e., occupied electronic states of an element up to the binding energy equal or lower to the photon energy minus the material work function. This way the atom's core levels as well as the valence band are mapped. Since each element has an unique set of binding energies, XPS can be used to identify and determine the concentration of the elements in the surface.

The use of angle-integrating electron analysers gives integrated information about large parts of the reciprocal space, i.e., essentially one obtains the densities of occupied electronic states [34]. In order to investigate the dispersion of electronic bands $E(\mathbf{k})$ and $E(\mathbf{k}_\parallel)$ for bulk and surface states, respectively, a determination of the electron wave vector is necessary. Besides the kinetic energy one thus also needs to know the emission direction. This can be achieved by using electron energy analyser with small angular aperture. Low-energy (UV) photon source is usually used in this case and the method is known as angle-resolved UV photoemission spectroscopy (ARUPS). The essential geometrical parameters in an ARUPS experiment are given in fig. 4.14. The angle of incidence α of
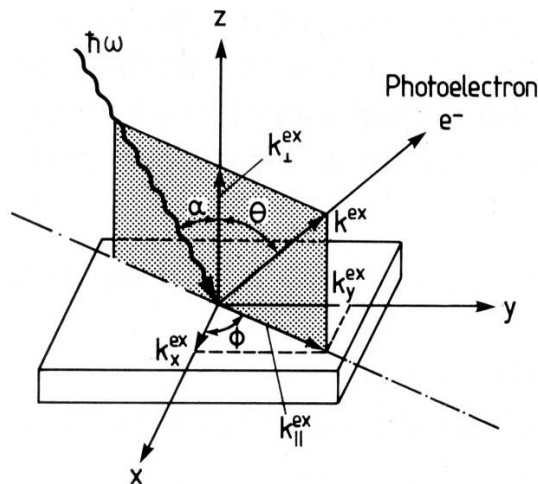

Figure 4.14: Definition of the angles and wave vectors of the incident photon ($\hbar\omega$) and emitted electron e^-.

the photons of energy $\hbar\omega$, their polarization and the plane of incidence, determine the electric field direction and the vector potential **A** of the photoexciting electromagnetic wave with respect to the crystal lattice.

A rigorous theoretical approach to the photoemission process requires full quantum-mechanical treatment of the complete coherent process in which an electron is removed from an occupied state within the solid and deposited at the detector. Theoretical approaches of this kind treat the photoeffect as a one-step process [37, 38]. The less accurate but simpler approach is the so-called three-step model in which the photoemission process is artificially separated into three independent parts [39, 40, 41]: optical excitation of an

electron from an initial into a final electron state within the crystal (fig. 4.15, left), propagation of the excited electron to the surface and the emission of the electron from the solid into the vacuum after transversing the surface (fig. 4.15, right). Although this three steps
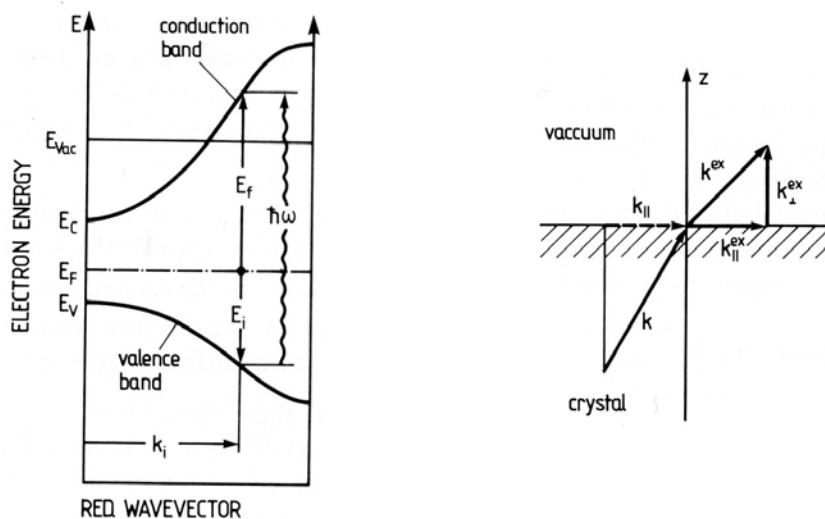
Figure 4.15: Representation of the photoexcitation process in the electronic band scheme $E(\mathbf{k})$ of a semiconductor (left). Only direct transitions with $\mathbf{k_i} \approx \mathbf{k_f}$ are taken into account. The energies of the initial state (E_f) and final state are referred to the Fermi level E_F. Conservation of the wave vector component $\mathbf{k}_\parallel$ (parallel to the surface) upon transmission of the emitted electron through the surface (right).

are in principle not independent of each other, the separate treatment leads to a simple factorization of the corresponding probabilities in the photoemission current of the emitted electrons. The basics of electron excitation by photon absorption has already been discussed in sec. 3.1. Outside the solid on the vacuum side one can only detect electrons whose energy E is above the vacuum energy E_{vac} (fig. 4.15, left) and whose $\mathbf{k}$ vector in the final state is directed outwards from the surface, i.e., $\mathbf{k}_\perp > 0$. The magnitude of the wave vector $\mathbf{k^{ex}}$ of the emitted electrons is determined by

$$k^{ex} = \sqrt{\frac{2mE_{kin}}{\hbar^2}}, \tag{4.10}$$

where E_{kin} is the kinetic energy of the detected electron. The emission direction is described by the angles ϕ and θ. When propagating towards the surface, a large number of electrons undergo inelastic scattering processes: they lose part of their energy E_f by electron-plasmon or electron-phonon scattering. Such electrons contribute to the continuous background in the photoemission spectrum, which is called secondary background. In the third step, transmission of the photoexcited electron through the surface can be considered as the scattering of a Bloch electron wave from the surface-atom potential with translational symmetry parallel, but not normal to the surface. One arrives at the same conclusions when the transmission through the surface is treated by matching the internal Bloch wave functions to free-electron wave functions (in LEED problem) outside on the vacuum side. In any case, because of the 2D translational symmetry, the transmission of the electron through the surface into the vacuum requires conservation of its wave-vector

component parallel to the surface (fig. 4.15, right):

$$\mathbf{k}_{\parallel}^{\mathbf{ex}} = \mathbf{k}_{\parallel} + \mathbf{G}_{\parallel}, \tag{4.11}$$

where $\mathbf{k}$ is the wave vector of the electron inside the crystal. Its component normal to the surface $\mathbf{k}_{\perp}$ is not conserved during transmission through the surface. For the external, electron on the vacuum side, the $k_{\perp}^{ex}$ value is determined by the energy conservation requirement

$$E_{kin} = \frac{\hbar^2 k^{ex^2}}{2m} = \frac{\hbar^2}{2m}(k_{\perp}^{ex^2} + k_{\parallel}^{ex^2}) = E_f - E_{vac}. \tag{4.12}$$

With $\phi_s = E_{vac} - E_F$ as the work function and E_B as the (positive) binding energy referred to the Fermi level E_F (fig. 4.15, left) one obtains eq. (4.9). The wave-vector component parallel to the surface outside the crystal, which is determined from known experimental parameters, can be expressed using eq. (4.9) and (4.12):

$$k_{\parallel}^{ex} = \sqrt{\frac{2m}{\hbar^2}} \sqrt{\hbar\omega - E_b - \phi_s} \sin\theta = \sqrt{\frac{2m}{\hbar^2} E_{kin}} \sin\theta. \tag{4.13}$$

This equation directly yields the internal wave-vector component $k_{\parallel}$ according to parallel-momentum conservation equation (4.11). On the other hand, due to the inner microscopic surface potential V_0, the wave-vector component $k_{\perp}$ of the electron inside the crystal is changed upon transmission through the surface. The outside component is determined by energy conservation according to eq. (4.12) as

$$k_{\perp}^{ex} = \sqrt{\frac{2m}{\hbar^2} E_{kin} - (\mathbf{k}_{\parallel} + \mathbf{G}_{\parallel})^2} = \sqrt{\frac{2m}{\hbar^2} E_{kin}} \cos\theta. \tag{4.14}$$

However, a nearly-free electron (NFE) model is often considered, where the electron kinetic energy relates to k as $E_{kin} = \frac{\hbar^2 k^2}{2m}$.

The measured energy distribution of sharp peaks in the spectra is superimposed on the secondary background, arising from the multiply-scattered electrons. The intensity of the peaks in the photoemission spectra is modulated with the cross-section variations, depending on the element under investigation, the orbital from which the electron is ejected and the energy of the exciting photons. In general, for XPS measurements, the cross-section for photoelectron emission from a given orbital quantum number increases with atomic number for a given series of core levels, such as $1s$, $2p$, etc. The escape depth of the electrons emitted from the atom depends upon their kinetic energy. The escape depth passes through a minimum with increasing kinetic energy and the minimum occurs in the region of 20 to 50 eV. The width of photoemission peaks is determined to a large extent by the lifetime of the core hole (producing homogeneous broadening) and the instrumental resolution. The intrinsic peak width is inversely related to the core hole life time, $\tau \approx \hbar/\Gamma$. Generally it holds that the deeper the core hole, the shorter the lifetime, because core holes are filled by higher lying electrons and for the deeper core holes more de-excitation channels exist that can fill the core hole.

The binding energy of the photoelectrons is an intrinsic material property and does not change with the X-ray source photon energy. However, it exhibit slight variations for a particular element and energy level depending on the exact chemical environment (potential) of the atom (or molecule or ion) and the polarizability of the compound [42].

These *chemical shifts* can be used to identify the chemical state of the materials and have their origin in either initial-state or final-state effects. In the case of initial-state effects, it is the charge on the atom prior to photoemission that plays the major role in the determination of the magnitude of the chemical shift. The electronic configuration in (and around) the atom particularly depends on the oxidation state of the atom [43]. In essence, the more bonds with electronegative atoms that are in place, the greater the positive XPS chemical shift. Final-state effects that occur following photoelectron emission, such as relaxation of electron orbitals, core hole screening and the polarization of surrounding ions are often dominant in influencing the magnitude of the chemical shift. The final state achieved by removing one electron during photoemission corresponds to an ionic state (with a hole in place of the ejected photoelectron) which is not the ground state. The remaining electrons relax and thereby lower the energy of the final state. This type of relaxation occurs regardless of the phase in which atoms or a compound exist. Most of the atomic relaxations result in rearrangement of the outer-shell electrons, making the contribution from the inner-shell electrons (of higher binding) rather small. If the atom is located in a solid, the atomic relaxation can be accompanied by an extra-atomic relaxation, whose nature is determined by the conductivity of the material. In metals[5], valence electrons are free to move from one atom to another and they screen the hole created by photoionization. In insulators, the electrons don't move throughout the material, so the surrounding of the ionized atom gets polarized. The magnitude of the extra-atomic relaxation (as high as $5 - 10\,\mathrm{eV}$) in metals is therefore greater than that of insulators.

These effects result within the high-resolution spectra of individual core levels, giving rise to the fine structure that gives additional information concerning the chemical environment of an atom. The major features in this category are *shake-up* satellites, multiplet splitting and plasmons. As already mentioned in sec. 3.6, shake-up satellites[6] are the multi-electron features, which occur when the outgoing photoelectron simultaneously interacts with a valence electron and excites it to a higher-energy level. The energy of the core electron is then reduced slightly giving a satellite structure a few electron volts lower in the kinetic energy scale (i.e., higher in the binding energy scale) than the core level position. An allied feature is the *shake-off* satellite where the valence electron is ejected from the ion completely. These are usually seen as a broadening of the core level peak or as a contribution to the inelastic background. In the case of inorganic compounds, the dominant factor in the generation of these satellites is due to the final-state effects, such as the screening of the core hole by valence electrons, the relaxation of electron orbitals and the polarization of surrounding species. The multiplet splitting of a photoelectron peak may occur in a compound that has unpaired electrons in the valence band. Such electrons interacts with the remaining unpaired electron in the ionized orbital, and the energy of the state depends on whether the electron spins are aligned parallel or antiparallel to one another. The third type of loss features to be concerned are the plasmon losses, which are specific to clean metal surfaces. They arise when the outgoing electron excites collective oscillations in the conduction band electrons and thus suffers a discrete energy loss (or several losses in multiples of the characteristic plasmon frequency).

---

[5]In most metals there is a positive shift between the elemental form and mono-, di- or trivalent ions.

[6]Shape-up satellites are not very common, but occur for example in the $2p$ spectra of the d-band metals and the bonding to anti-bonding transition of the π molecular orbital ($\pi \rightarrow \pi^*$ transition) brought about by C $1s$ electrons in aromatic organics.

The use of UV light ($h\nu \sim 10 - 40\,\text{eV}$) leads to excitation of valence electrons, and the density of states in the valence band can be obtained in this way. Since valence electrons are involved in chemical bonding, UPS is particularly well-suited to the study of bonding at surfaces. UPS furthermore provides measurements of the work function and band structure of the solid, the surface and adsorbate. The most common laboratory source for UV spectroscopy (besides synchrotron) is the differentially pumped He discharge lamp. Atomic emission lines are extremely sharp allowing the acquisition of the high-resolution spectra, where even small chemical shifts are easily detected. The He I spectral line ($h\nu = 21.22\,\text{eV}$), originating from excitations of the neutral He atoms, is extremely intense and is usually employed with no UV monochromator between lamp and sample. All other spectral lines give rise to minor background only. Depending on the pressure, however, ($1\,\text{mbar}$ for He I and $0.1\,\text{mbar}$ for He II) and discharge current conditions, the He II line at $40.82\,\text{eV}$ can also be used (without a monochromator). The emission originates from excited He$^+$ ions in the discharge. Owing to very high absorption coefficients of the far UV light in all substances and to the very short mean free paths of the photoelectrons, this method is extremely surface sensitive.

4.4.4 Grazing incidence X-ray diffraction (GIXD)

X-ray diffraction is one of the most widely used techniques for studying bulk structure of materials. When X-ray beam impinges on a sample, it is scattered by the electrons of the illuminated region. Coherent electromagnetic field produces scattered field, which brings the information about spatial distribution of the scatterers and gives rise to the intensity maxima (i.e., diffraction peaks) when energy and momentum conservation is met. The position and the intensity of the diffraction peaks give information about the reciprocal space of the crystal structure. Depending on the X-ray energy and material the X-rays penetrate significant distance in the matter (typically in the range of $0.1 - 10\,\text{mm}$), thus the structural information is averaged over a large ensemble of atoms or molecules in the crystal. For studies of bulk materials, X-rays have therefore long been an essential characterization tool.

Bulk X-ray diffraction

In common X-ray diffraction experiment, the intensity and profile of the diffraction peaks are generally measured. When treating three-dimensional crystals, each diffraction peak corresponds to a point of the reciprocal crystal lattice. In the kinematical approximation [44], the diffracted intensity is calculated as the sum of the diffracted signal originating from each atom building the crystal as

$$I(\mathbf{q}) \propto I_0 \left| F(\mathbf{q}) \right|^2 \Gamma_x^2 \Gamma_y^2 \Gamma_z^2, \tag{4.15}$$

where $\mathbf{q}$ is the total exchanged momentum, I_0 is the incident beam intensity and $F(\mathbf{q})$ is the geometrical structure factor of the unit cell. The latest is defined by summing up the diffraction contributions from each of the N atoms within the unit cell

$$F(\mathbf{q}) = \sum_{j=1}^{N} f_j(\mathbf{q}) e^{i\mathbf{q}\cdot\mathbf{r_j}}, \tag{4.16}$$

where $\mathbf{r_j}$ is the spatial position of the j-th atom inside the cell. The term f_j represents the atomic form factor, which is evaluated by

$$f_j(\mathbf{q}) = \int e^{i\mathbf{q}\mathbf{r}} \rho_j(\mathbf{r}) d\mathbf{r}, \tag{4.17}$$

where $\rho_j(\mathbf{r}) = \sum_n \rho_{j,n}$ equals to the sum of the electron density within the j-th atom. The crystal structure factor Γ_i in eq. (4.15) is obtained by summing the signal over N_i unit cells along the i-th direction and is written as

$$\Gamma^2(q_i) = \frac{\sin^2(N_i a_i q_i/2)}{\sin^2(a_i q_i/2)}, \tag{4.18}$$

where a_i and q_i are the i-th component of the crystal lattice vector and the momentum transfer, respectively. For large N a peak in the diffraction intensity accordingly occurs when the momentum transfer $\mathbf{q}$ is equal to the vector of the reciprocal lattice unit of the crystal. In this case $\Gamma_i^2 = N_i^2$, from which immediately follows that the larger the crystal domains, the more intense the diffracted peak. If N_i is large enough ($N_i > 50$), then Γ_i can be approximated by a Gaussian function[7]

$$\Gamma^2(q_i) \approx N_i^2 e^{-\frac{N_i^2(q_i a_i)^2}{\pi}}. \tag{4.19}$$

Diffraction at surfaces in grazing X-ray geometry

By itself the X-ray diffraction technique is far from being a surface-selective probe. Study of surface and overlayer structure with deeply penetrating X-rays is difficult, because of the small ratio between the signal arising from the outermost atomic layers of a crystal and that from the bulk. However, since a refraction index for X-rays in the keV range is slightly lower than unity, the total reflection occurs if beam impinges on the surface at sufficiently small angle, i.e., smaller than the critical angle [45]. In grazing incidence X-ray diffraction we make use of the total reflection which prevents the radiation to reach large depth of the crystal. This way a surface sensitivity of the diffraction is greatly enhanced. In case of total reflection the beam inside the crystal travels as an evanescent wave, with exponentially damped amplitude and effectively illuminates only the surface region of the sample (typically from several tens to few hundreds of Ångströms). For the X-ray energy sufficiently above the ionization edges of the elements in the monitored material, the refraction index can be written in the form

$$\tilde{n} = 1 - \delta + i\beta, \tag{4.20}$$

where $1 - \delta$ represents the real refraction index and β the absorption coefficient. The critical angle is then evaluated using Maxwell relations at the vacuum-material interface [44]

$$\alpha_c = \sqrt{2\delta}. \tag{4.21}$$

For incident angle α_i, where $\alpha_i < \alpha_c$ the penetration depth Λ is given by the equation

$$\Lambda = \frac{1}{2k\sqrt{\alpha_c^2 - \alpha_i^2}}, \tag{4.22}$$

---

[7]The width of this functions corresponds to the width of the diffraction peak; it is equal to $\Delta q_i = 2.35 \frac{\sqrt{2\pi}}{L_i}$ where $L_i = N_i a_i$ is the coherently scattering domain size along the i direction.

where k is the wave vector of the incident light. In the case of metallic and semicon-ducting substrates, this angle usually ranges from 0.25° to 0.40° for X-rays in the keV range [46]. Fig. 4.16 shows the X-ray penetration depth and the portion of the specularly reflected X-ray light as a function of the incidence angle.
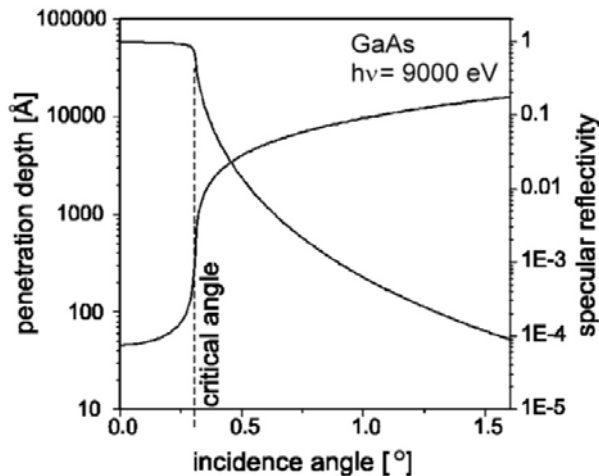
Figure 4.16: The penetration depth and the specular reflectivity of the GaAs crystal as a function of the incidence angle at the photon energy $h\nu = 9000\,\text{eV}$ [47].

When passing the surface, the X-ray beam refracts according to the equation

$$n \cos \alpha_i' = \cos \alpha_i, \tag{4.23}$$

where α_i is the incidence angle on the vacuum side, α_i' the angle between the beam and the surface inside the material and n the (real) refraction index of the material. The amplitude of the evanescent X-ray wave in the material at the same time attenuates as

$$E_t \propto e^{-z/\Lambda}. \tag{4.24}$$

In grazing-incidence diffraction the scattering geometry combines the Bragg condi-tion with the conditions for X-ray total (external) reflection from crystal surfaces. The geometry is presented in fig. 4.17.

The wave which is almost parallel to the surface still has oscillating character and can give rise to Bragg diffraction peaks from periodic structure at the surface. The condition for the in-plane diffraction is described by the Bragg rule:

$$2d \sin \Theta_{\parallel} = m\lambda, \tag{4.25}$$

where m is the integer number, d the period of the surface structure and $2\Theta_{\parallel}$ the diffraction angle between the in-plane components of the initial and final wave vector.

The surface diffraction pattern

In X-ray diffraction besides Bragg points originating from 3D bulk, additional (yet much weaker) diffraction "pattern" appears, arising from the 2D (or nearly 2D) surface struc-ture. In the case of surface-terminated crystal, where the structure of the surface re-gion remains unchanged, *crystal-truncated rods* perpendicular to the surface show up in
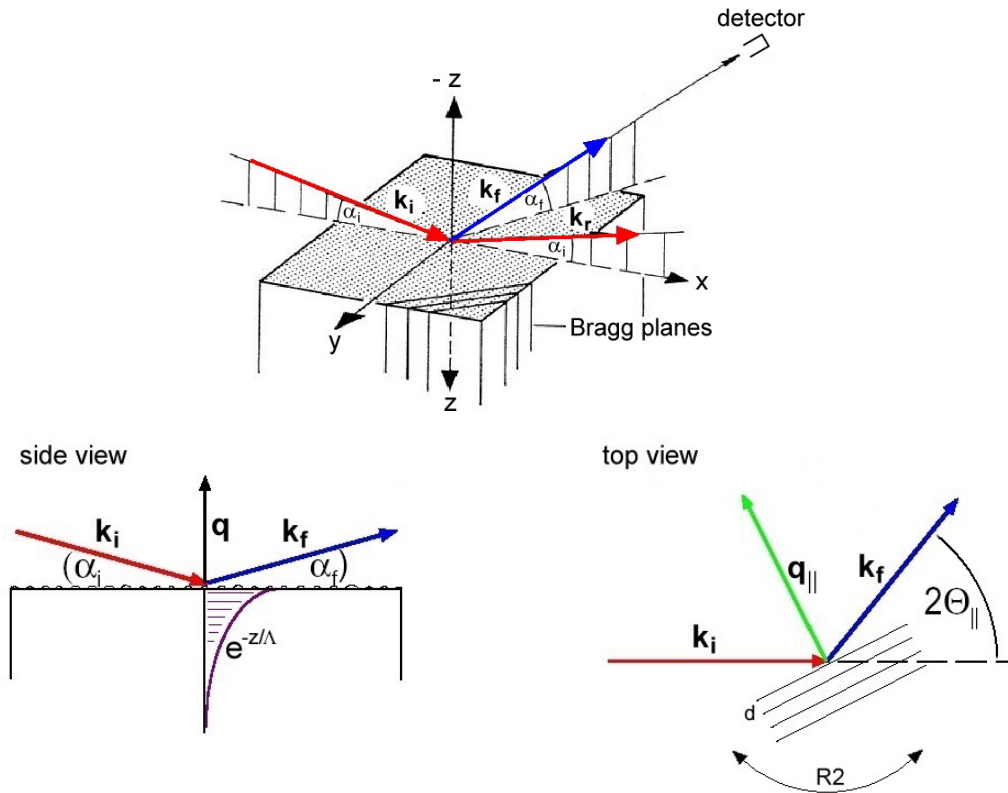
Figure 4.17: The geometry for grazing X-ray diffraction. Here $\mathbf{k_i}$ and $\mathbf{k_f}$ are the wave vectors of the incident and diffracted beam, respectively, and $\mathbf{k_r}$ is the wave vector of the totally reflected beam; α_i is the incident angle of the beam and α_f the exit angle of the diffracted beam. The exchanged momentum is denoted by $\mathbf{q} = \mathbf{k_f} - \mathbf{k_i}$ and its component parallel to the surface by $\mathbf{q}_{\parallel}$. Surface planes are spaced by d and the diffraction angle between the in-plane components of the initial and final wave vectors equals to $2\Theta_{\parallel}$.

the diffraction pattern [48], coinciding with the Bragg points. Since the periodicity in the z-direction ceases at the surface, all k_z momentum vectors are acceptable. A two-dimensional lattice of surface atoms generates a two-dimensional lattice of rods in the reciprocal space, as shown in fig. 4.18.

However, if the surface lateral structure alters comparing to bulk layers, be it either due to relaxation of the surface (because of crystal-cutting) or due to presence of adsorbed species, the resulting diffraction pattern doesn't coincide with the bulk Bragg points any more. By analyzing this pattern it is possible to determine the structure of the surface region. Starting with only one plane (parallel to the surface), the rods, perpendicular to the surface appear in the diffraction pattern. When adding additional planes with the same lateral order, the intensity of the rods becomes modulated (along the rods). By measuring this intensity modulation the so called *rod scan* is performed. This is achieved by varying the perpendicular momentum transfer L while keeping the exchanged parallel momentum $\mathbf{q}_{\parallel}$ fixed to a reciprocal vector of the surface lattice, where the in-plane diffraction condition is met – see eq. (4.25). The period of the intensity maxima along the rods effectively probes the distance between the equivalent parallel planes (i.e., of equal lateral order) and the shape of peaks yields the structure perpendicular to the surface.
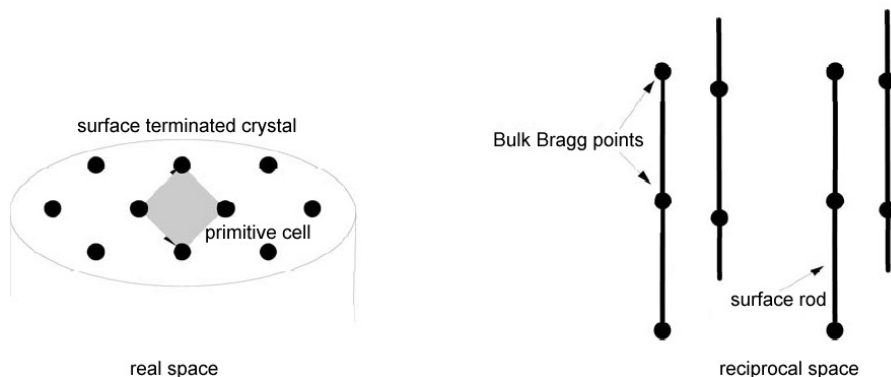
Figure 4.18: Graphic representation of the real and reciprocal space of a surface-terminated crystal. The presence of the 2D surface introduces crystal-truncated rods in the reciprocal space, which are perpendicular to the surface.

The typical intensity of a diffraction peak along a rod is up to 6 orders of magnitude lower than a bulk peak. For this reason a brilliant X-ray source such as synchrotron is required as well as the possibility to work in grazing incidence geometry.

GIXD at the ALOISA beamline

The possibility to work at grazing incidence angle and the high degree of freedom in selecting the diffraction geometry makes Aloisa very suitable to perform the GIXD experiments [49]. Four photon detectors, i.e., two current Si diodes and two energy resolved preamplified Si diodes are mounted on bimodal frame. Current diodes offer a great dynamic range but at the same time rather limited sensitivity. They are used for monitoring bulk diffraction peaks, which are very intense. For surface diffraction peaks the energy resolved diodes are used because of their very high sensitivity. An Al multistage absorber is used to attenuate the beam if measured intensity is too high for the limited dynamics of these diodes.

In performing a diffraction experiment a good control over the direction of crystal axes is obviously required, and a proper alignment of the crystal with respect to the axes of the manipulator rotations has to be made. First of all, it is inevitable to completely eliminate a misalignment between the sample surface and the sample holder plate of the manipulator, on which the sample is mounted. The surface is thus not perfectly perpendicular to the azimuthal axis of the manipulator, giving rise to a precession movement. The acquisition program allows to insert the value of the angle between the sample normal and the azimuthal rotational axis, thereby being able to correct the measurement angles for the precession. The misalignment angle is measured in the preparation chamber, where a laser beam is directed towards the sample surface through the sample window. The specular beam is intercepted through a second window at an exit angle of $90°$ and projected on a screen. The position of the reflected beam is kept fixed on the screen for different azimuthal angles ($R2$, see fig. 4.17, bottom right) by varying the $R1$ and $R3$ values (see fig. 4.7, left). The precession curve is then determined and processed by the acquisition program for the automatic correction. For the orientation of the crystal axis with respect to the chamber angles, the detection of a diffraction peak is required. The simplest way for doing this in the Aloisa chamber is to measure an in-plane peak, i.e., a

diffraction peak arising from the planes perpendicular to the surface. The corresponding experimental geometry is shown in fig. 4.17, bottom right. An adequate photon is first chosen and the sample and detector are positioned in a grazing incident-exit angle configuration. The detector position is fixed at the 2Θ scattering angle, and the azimuthal scan is performed where $R2 = \Theta$ angle is varied until the Bragg condition is reached. As previously discussed, the diffracted intensity of an in-plane peak is very surface sensitive, since the incident beam is exponentially attenuated when propagating into the bulk. The maximum is effectively reached at the critical angle, which means that in fact a real in-plane peak could not be measured and an out-of-plane component of the momentum transfer has to be present in order to have a non-zero peak intensity. By setting the incidence and exit angles at the intensity maximum values, the perpendicular component of the momentum transfer is fixed. The azimuthal scan thus presents a maximum when the parallel component of the momentum transfer equals the reciprocal lattice vector, defined by the distance between the scattering planes. In this way the crystal axis orientation with respect to the chamber and manipulator angles is completely determined.

In the following, the procedure is explained by which the diffracted peaks are further treated. A single diffracted peak profile is first integrated, where the resulting integrated intensity depends not only from the physics of the system but is also affected by the experimental apparatus and geometrical factors used during the measurements. It is crucial to be able to correct the scans in the means of these factors when one wants to compare different diffraction peaks, as in a rodscan measurements. Analytic expression for the required corrections are available in literature for the most diffuse diffractometers [50]. In the case of a non-standard experimental geometry, existing at the Aloisa apparatus, the corrections have to be adequately altered. First the normalization by the photon flux is performed. This is done by taking a set of scans to be compared at the same photon energy to avoid the deviations in the response function of the monochromator. The normalization for the intensity of the beam originated from the synchrotron source is made by reading the ring current at every scan. A further correction for geometrical factors takes into account the variations of volume of the reciprocal space, sampled during a peak detection, due to different geometrical configuration. These variations mainly depend on the way, how the detected rods of the reciprocal lattice are intercepted by the detector during scan and on the shape of the detector active area. A Monte-Carlo simulation program is available for calculating this correction for the Aloisa chamber [51]. The program also takes into account the spatial and energy resolution of the incident beam. The corrections must furthermore be made due to variable size of sample irradiated area. Since the entire illuminated area of the sample is visible by the detector irrespective of the detector position, a correction factor is introduced considering the variable size of the illuminated region when doing azimuthal scans. In order to correctly obtain a structure factor of the system, the polarization factor must also be considered [49].

In a rodscan, a diffraction peak is sampled at variable perpendicular momentum transfer $\mathbf{q}_\perp$ by keeping constant the parallel component $\mathbf{q}_\parallel$. The Aloisa apparatus allows to do this by executing a correlated chamber-bimodal movement for positioning the detector and performing a $R2$ scan. In this way the peak profile is measured by changing only $\mathbf{q}_\perp$ value. Once the crystal axes have been aligned, a separate computer program calculates the angles to be set to sample the desired reciprocal lattice points. The output file, containing a complete set of calculated angles is then read by the acquisition program and the rodscan measurement is performed automatically.

Chapter 5

Pentacene/Au(110)

5.1 Introduction

The property of forming thermally stable and well-ordered films that show high field-effect carrier mobility places pentacene as a model molecule among organic semiconductors [12]. Charge transport properties of π-conjugated molecules such as pentacene are intrinsically correlated with their crystalline structure, degree of orientational order and grain size. A very high room-temperature mobility of charge carriers (holes) in the range of $1\,\mathrm{cm^2/Vs}$ can be achieved in pentacene thin-film transistors, which makes this material a possible inexpensive alternative to amorphous silicon [52]. Understanding the formation of self-assembled pentacene ad-layers on metal substrates would contribute to the fabrication of highly oriented pentacene layers with possible application in electronic devices. Since the charge transfer is dramatically inhibited by increasing the concentration of structural defects, grain boundaries and impurities, the knowledge of the structure and molecular packing in pentacene thin films as well as the growth mechanisms that produce such structure is essential.
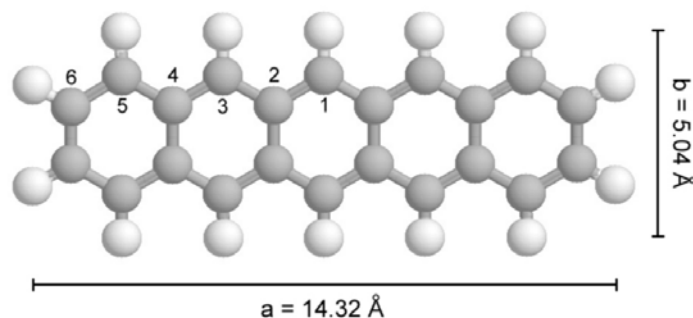
5.1.1 The pentacene molecule

Pentacene ($C_{22}H_{14}$) is an aromatic hydrocarbon belonging to a family of polyacenes, which are made up of a series of aromatic rings (fig. 5.1). The approximate molecule dimensions, i.e., maximal horizontal and vertical distance between hydrogen ions, are $14.21\,\mathrm{\AA} \times 5.04\,\mathrm{\AA}$ [54] and are displayed in fig. 5.2. The molecule contains six symmetrically- and chemically-inequivalent carbon atoms (also shown in fig. 5.2). Chemical diversity of C-atoms within the pentacene may be directly observed in C $1s$ XPS spectra. The core level $1s$ binding energies of isolated molecule were measured in pentacene gas phase and calculated theoretically for an isolated pentacene molecule by M. Alagia and co-workers [53]. Both, experimental and calculated spectra, are displayed in fig. 5.3.

Pentacene molecule possesses a pronounced π-conjugated electronic density concentrated above and below the molecular plane (fig. 5.4). Conjugation is a higher-order bonding interaction between p-orbitals on three or more adjacent atoms in a molecule. It occurs in organic molecules between covalently bound atoms with alternating single and double bonds, e.g., $C = C - C = C - C$. Conjugation effect is at maximum when the axes of the component orbitals are aligned parallel to each other because this allows maximum orbital overlap. This condition is met in planar organic molecules such as polyacenes,
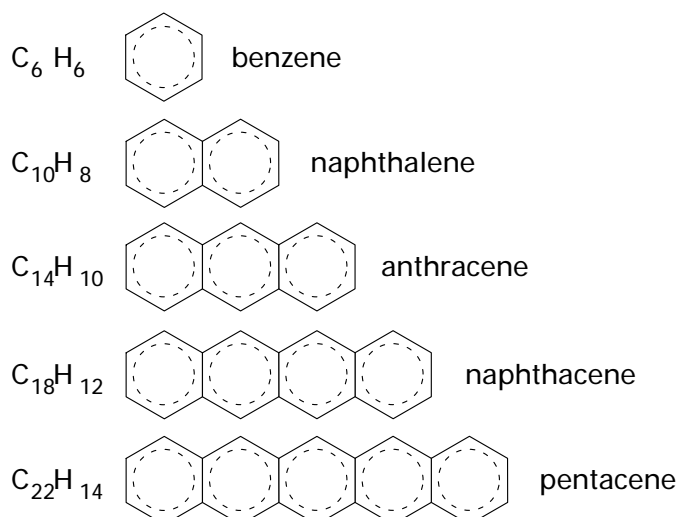
**Figure 5.1:** First five polyacenes.

Figure 5.2: The pentacene molecule and its dimensions. Six chemically- and symmetry-inequivalent carbon atoms are also enumerated.

thus making pentacene a good candidate for conjugation. The orbital overlap leads to delocalization of the π-electrons in an adjacent multiple bond – they are no longer fixed on a particular atom or between a pair of atoms, but are shared throughout the conjugated orbitals (fig. 5.4, right). This decreases the kinetic energy of electrons, which contributes to a lower overall energy and generally results in greater stabilization for the molecule.

In its bulk phase pentacene forms a triclinic structure with a density of $1.32\,\mathrm{g/cm^3}$, where two molecules per unit cell are arranged to form a herringbone configuration (fig. 5.5). The structure of deposited pentacene films can, however, considerably differ from the bulk-like packing which, due to anisotropy of the molecule, directly reflects in film electronic properties. Factors that mostly affect the film structure are substrate temperature, reactivity and morphology. The degree of overlap between pentacene π-conjugated system and substrate charge density dictates molecular charge transport and is consequently responsible for the electronic properties of metal-pentacene interface. By growing in vacuum while the SiO_2 substrate temperature is held close to $70\,\mathrm{K}$ amorphous film is formed which is practically insulating, i.e., with carrier mobility $\mu = 10^{-9}\,\mathrm{cm^2/Vs}$ [55]. As a contrast, when the substrate temperature is kept at room temperature (RT) during
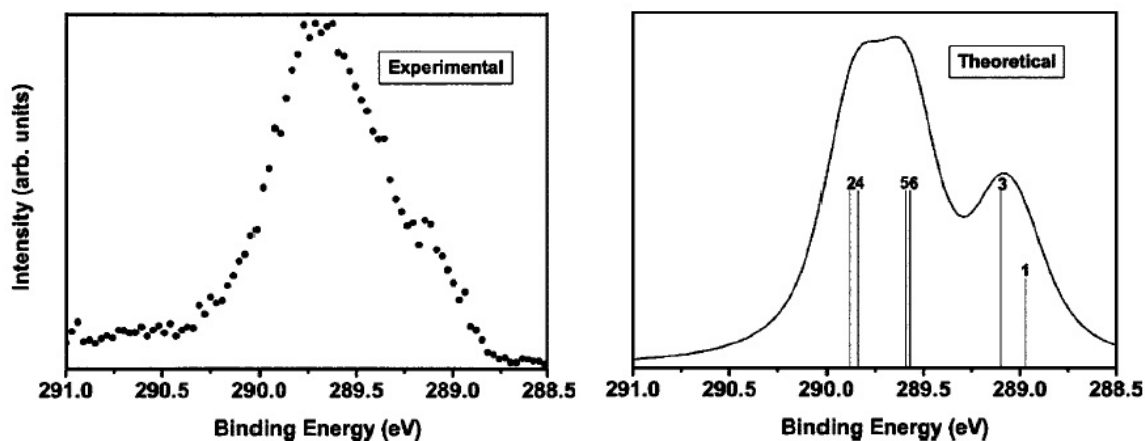
Figure 5.3: Experimental and theoretical X-ray photoemission spectra of the pentacene C $1s$ core-level [53]. Positions of peaks are denoted by vertical bars, which are labeled according to fig. 5.2. The curve of convoluted Voigt shape peaks is then drawn over.
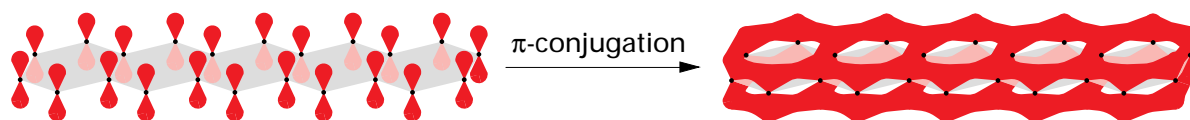
Figure 5.4: Pentacene π-conjugated electronic system. The carbon p-orbitals mix together producing spatially delocalized region of electronic density, which extends over the whole molecule.
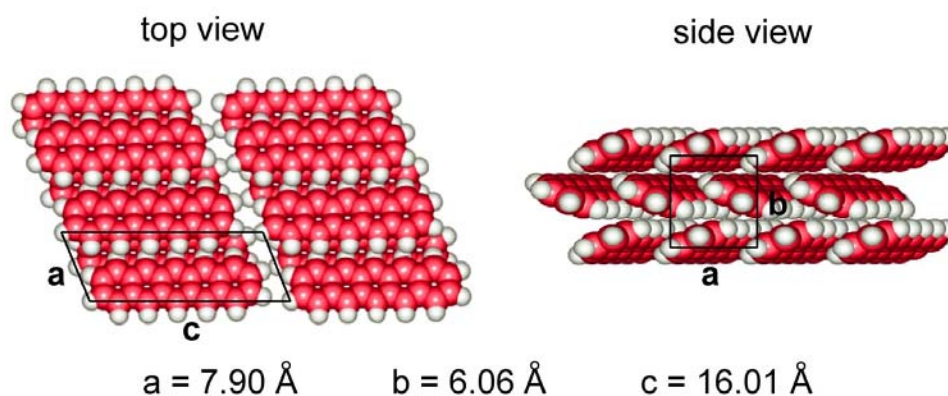

Figure 5.5: Bulk crystalline structure of pentacene. Black rectangles display the bulk unit cell.

deposition, a highly ordered film is formed with the RT hole mobility of $\mu = 0.6\,\mathrm{cm^2/Vs}$. The structure of this film is different than the structure of pentacene bulk crystal and is sometimes referred to as "thin-film phase" [11].

5.1.2   The Au(110) missing row substrate

The (110)-terminated f.c.c. crystals are known to produce critically stable reactive surfaces, which often minimize their free energy by a phase transition to a lower symmetry phase. Accordingly, the Au(110) surface in equilibrium at RT isn't a simple (110)-termination of Au bulk, which would rise as shown on fig. 5.6. Instead it exists in a
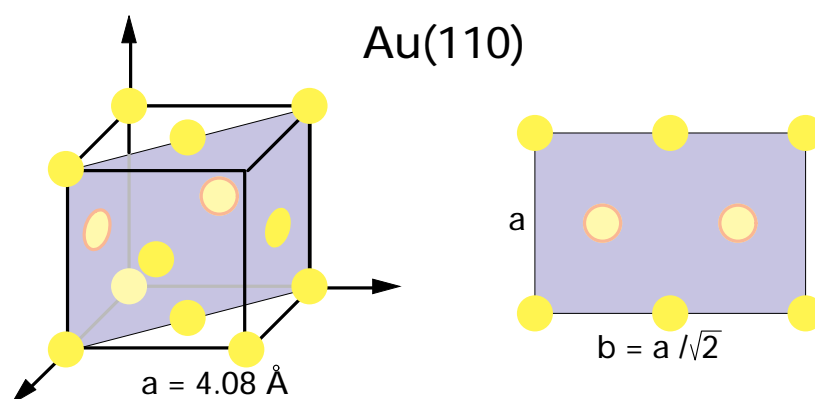
Figure 5.6: Schematical view of unreconstructed Au(110) surface.

(1×2) reconstructed phase with *missing row* (MR) structure where every second close packed row of Au atoms along $(1\bar{1}0)$ is absent. The formation of this phase, where the unreconstructed surface unit cell doubles in the [001] direction, is shown on fig. 5.7. The
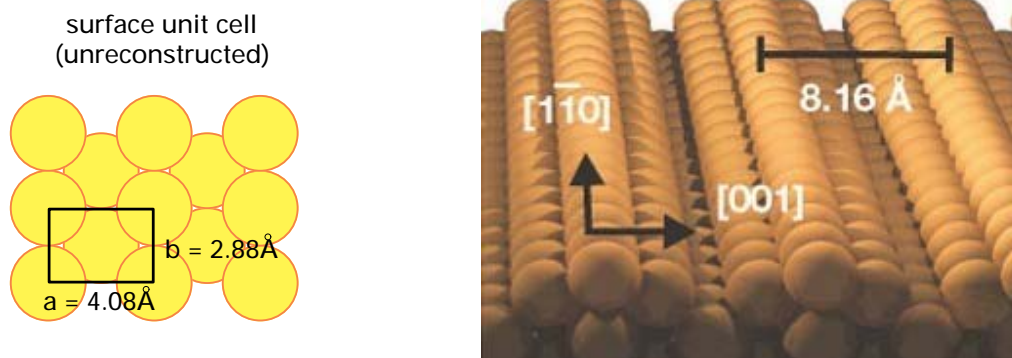
Figure 5.7: The Au(110) (1×1) surface unit cell (left) becomes doubled in missing row structure (right). Surface directions and characteristic distances are also denoted.

$[1\bar{1}0]$ surface direction corresponds to the ΓX direction in the reciprocal space and the [001] direction to the ΓY. By rising the surface temperature, the missing row long range order continuously decreases up to complete disappearance at about $920\,\mathrm{K}$, where the $(1 \times 2) \rightarrow (1 \times 1)$ phase transition occurs [57]. The RT stability of the MR reconstructed Au(110) is partially attributed to the local exposure of (111) microfacets which are energetically more stable over low Miller index surfaces. Despite the increase of the

microscopic surface area, the resulting close-packed surface has lower free energy. It was observed that free energy in case of Au(110) further lowers by surface relaxation. The (1×2) reconstruction is accompanied by approximately 20% contraction in the first interlayer spacing [30].

The MR surface is strongly anisotropic due to the high corrugation of the surface charge density along [001] direction. This corrugation reaches $\sim 1.2\,\text{Å}$ at $10^{-3}\,\text{Å}^{-3}$ iso-electron density [56] which gives the Au(110) surface the unique ability to drive an oriented growth of the thin films. Indeed, substrate influenced ordering of several organic molecules, such as cysteine, sexithiophene, metal-phthalocyanines, perylene tetracarboxylic diimide, pentacene and others has been confirmed on Au(110) [58, 59, 60, 2]. Guaino and co-workers reported that when depositing pentacene on the Au(110) surface, the unidirectional π-stacked molecular rows of pentacene molecules are formed in multilayer film [2]. At the same time, deposited molecules induce a (1×3) surface reconstruction of the substrate in the submonolayer coverage.

The pentacene thin film growth at different substrate temperatures, the molecular orientation in the film and its interaction with Au(110) substrate represent an open issue in the area of organic ad-layers and organic semiconductor device construction. The understanding of the ordering mechanism and molecule orientation in the contact layer with the metal electrode is very important in constructing the electronic devices. It motivated this detailed study performed by HAS, XPS, UPS and NEXAFS experimental techniques.

5.2   Pentacene film structure determination by HAS

The thin film was first investigated with HAS, using liquid nitrogen cooled He beam with the atom kinetic energy of $19\,\text{meV}$ and wave vector $6.3\,\text{Å}^{-1}$. Pentacene molecules were deposited from a Knudsen evaporation cell at temperature around $500\,\text{K}$ which corresponds to the deposition rate of a few monolayers (ML) per hour [63]. The Au(110) surface was cleaned prior to each deposition by sputtering with Ar^+ ions at the energy of $1 - 3\,\text{keV}$. The surface was then thermally annealed by heating up to about $700\,\text{K}$. In this way a well ordered surface was obtained, yielding a diffraction pattern with sharp peaks of the (2×1) reconstructed phase. The width of the specular peak was typically $\sim 0.17°$ which, according to eq. (4.8) in sec. 4.4.1 gives an approximate size of Au terraces of $500\,\text{Å}$.

The pentacene deposition was performed at different substrate temperatures, ranging from RT to $470\,\text{K}$. The molecular growth kinetics on the Au(110) surface was found to change substantially in this temperature range. When depositing the pentacene on the substrate held at $310\,\text{K}$, the intensity of the HAS specular peak decreases monotonously due to increasing surface roughness (fig. 5.8, blue line). There is a slight slow down of this decrease after approximately $250\,\text{s}$ deposition, which points to certain ordering dynamics of the adsorbed molecules. Nevertheless, after approximately $450\,\text{s}$ maximum HAS detectable roughness is achieved since the signal drops to the background level and doesn't recover by further deposition. At higher substrate temperature ($370\,\text{K}$) the ordering of thin film is fast enough relative to the deposition rate, so the surface reflectivity starts to improve after $250\,\text{s}$ of deposition (fig. 5.8, red line). This is a fingerprint of a certain degree of order, where the single uncorrelated molecular patches probably start to
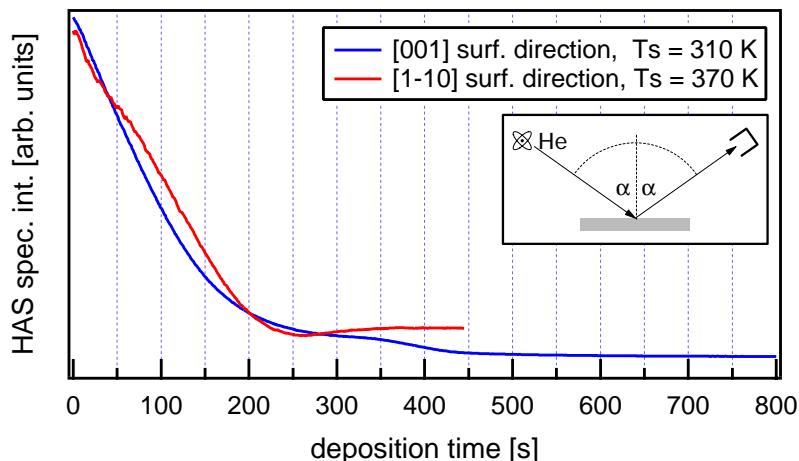
Figure 5.8: The HAS specular intensity during pentacene deposition on Au(110) at two different substrate temperatures.

join together, forming thin film which makes the surface smoother for helium atoms. The reflectivity increase is however rather small and stops after ~ 350 s already, showing that additional molecules don't improve the film smoothness. Due to limited surface diffusion at this substrate temperature the ordering is still quite poor.

The surface morphology was further more thoroughly studied by taking consecutive diffraction patterns during deposition. The evolution of pentacene thin film structure was monitored at the substrate temperature of 470 K by taking scans along [001] surface direction, which corresponds to ΓY direction in reciprocal space. Acquired spectra are shown on fig. 5.9. The horizontal axis has been normalized to the substrate reciprocal lattice units along ΓY and guidelines of sixth order peaks are displayed. At the beginning of deposition the pattern shows the twofold symmetry of the clean Au(110) substrate (bottom of the graph). The structure of thin film evolves continuously through the weakly pronounced threefold stage and ends up with sixfold thin film phase, which was found to be the most stable one and corresponds to the saturation structure at this substrate temperature.

The examination of thin film structure at lower substrate temperature of 420 K shows more structures along ΓY direction. The evolution of the diffraction pattern during pentacene deposition is displayed on fig. 5.10. Here each individual diffraction spectrum was normalized to unity of specular peak. In the early deposition stages we can see the splitting of the one half integer peaks simultaneously with the appearance of the satellites around the specular peak. The gradual shift of the satellite peaks leads to an intermediate sevenfold symmetry followed by a threefold one along the ΓY direction. This suggests that the missing row deterioration is driven by the proliferation of out-of-phase domain walls, that arise from the onset of a correlation between the molecule induced Au substrate defects. The envelope, superimposed over the diffracted peaks in a spectrum (*surface rainbow*[1]), indicates that the fractional peaks of this two symmetries display quite diverse

---

[1]The surface rainbow refers to an overall intensity modulation of the diffraction peaks in the spectra due to finite size of the scattering atoms and their position within the unit cell (i.e., form factor). This modulation enables the extraction of the information about the surface corrugation [61, 62].
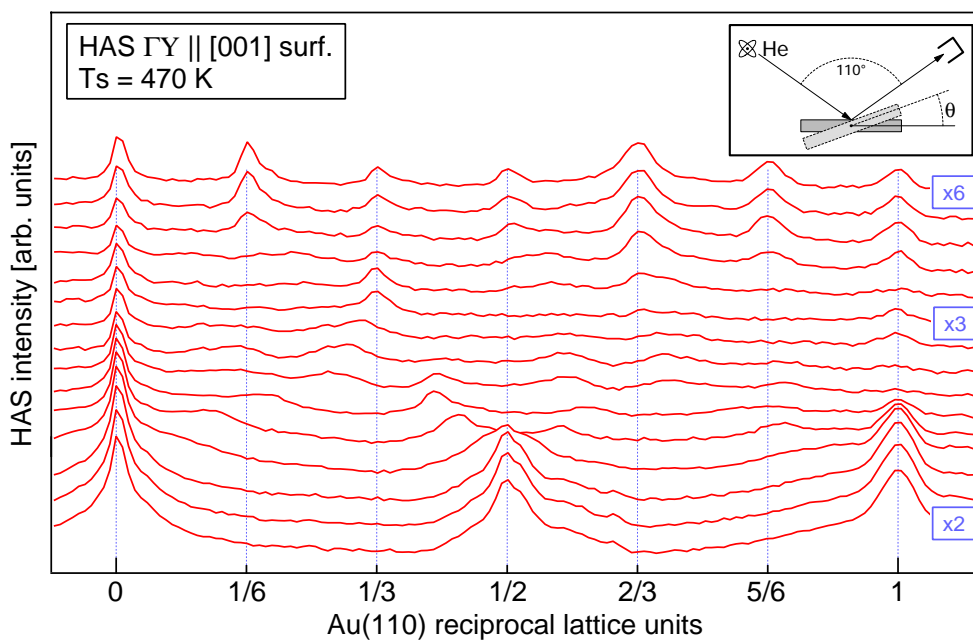
Figure 5.9: HAS angular diffraction scans during deposition at substrate temperature of 470 K. The vertical axis has logarithmic scale.
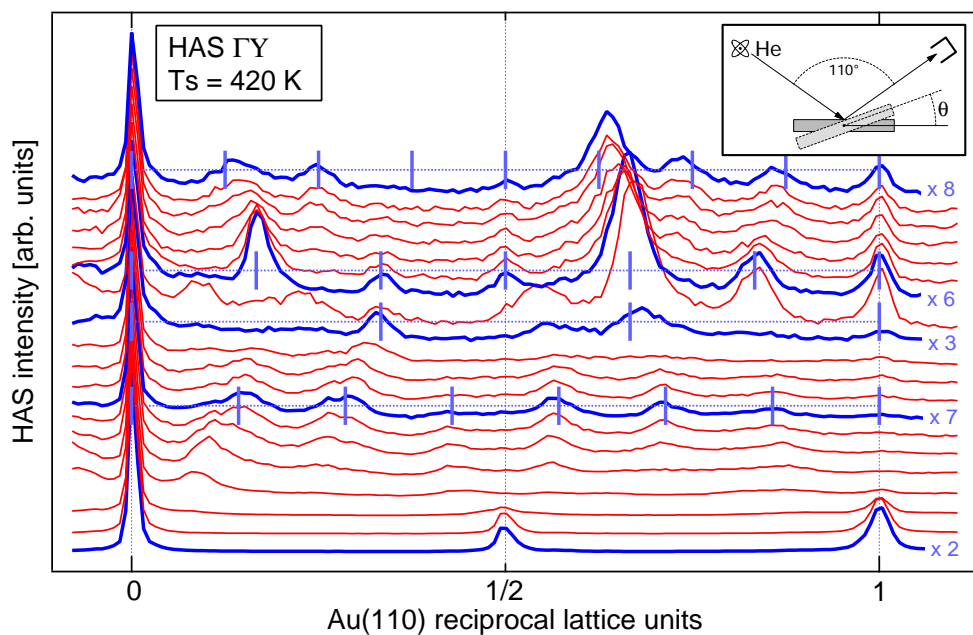

Figure 5.10: The evolution of HAS diffraction spectra during deposition at substrate temperature of 420 K.

intensity ratio to the specular peak than the two phases that follows, i.e., sixfold and eightfold. This large difference in the HAS rainbows points to a different corrugation of the surface charge density in the pentacene phases and could thus be a fingerprint of different molecular orientations.

HAS diffraction patterns were also collected along the ΓX reciprocal direction. The

corrugation along this direction appears by far lower than along the ΓY, as judged from the smaller diffracted peak intensity. The patterns of all symmetry-inequivalent phases along both directions are collected in fig. 5.11. The spectra along ΓX were magnified
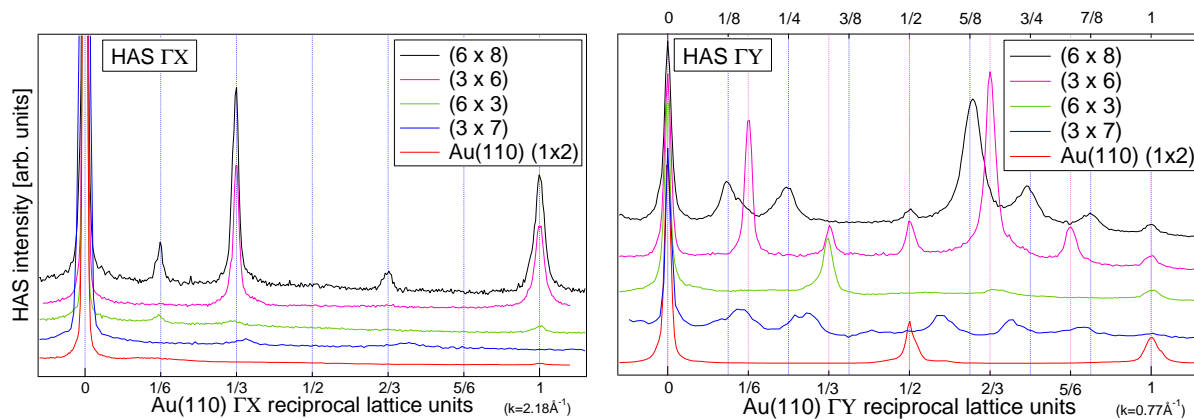

Figure 5.11: Summary of all symmetry phases observed on pentacene/Au(110) along ΓX and ΓY direction.

vertically in order to make the diffracted peaks noticeable. The specular peaks thus greatly exceed vertical size of the figure. HAS diffraction patterns of the (6×8) and (3×6) phases along the ΓX direction were taken at the substrate temperature $170\,\mathrm{K}$ in order to reduce the Debye-Waller attenuation. All patterns along ΓY direction, except the one belonging to (3×7) phase, were taken on the substrate cooled to RT.

The (3×6) phase, represented by the top-most pattern in fig. 5.9, doesn't further evolve upon continued deposition and is thus found to be the saturation coverage of pentacene growth on Au(110) at high temperature, i.e., $470\,\mathrm{K}$. It is the most stable phase of pentacene on this substrate and equals the coverage of 1 ML. It appears that the (3×6) phase could always be recovered by flashing any higher coverage pentacene film (obtained at lower substrate temperatures), e.g. (6×8) structure, to $470\,\mathrm{K}$. This is clearly shown in fig. 5.12, where consecutive HAS patterns have been taken during slow annealing of a ~ 2 ML film grown at $340\,\mathrm{K}$. As can be seen, pentacene self-ordering first leads to the formation of the (6×8) phase at $420\,\mathrm{K}$ which further evolves to (3×6) phase above $470\,\mathrm{K}$ by evaporating the redundant molecules. The diffraction patterns are to scale and their overall intensity decreases by temperature elevation due to Debye-Waller attenuation.

An intermediate conclusion can be made by observing that structure evolution during growth in submonolayer range completely resembles the STM observations. According to Guaino and co-workers [2] the pentacene molecules in the initial stage of growth adsorb between atomic gold rows along $[1\bar{1}0]$ in a head-to-head geometry, consequently inducing a (1×3) surface reconstruction. This is consistent with observed (6×3) structure, which matches the molecular size parallel to $[1\bar{1}0]$ direction, i.e., $6 \times 2.88\,\text{Å} = 17.3\,\text{Å}$. Together with STM observations the model of the structure would be as shown in fig. 5.13, left. Such alignment of molecules yields a very low corrugation of the surface charge density producing faint diffraction peaks, which is further consistent with the observed HAS rainbow in the (6×3) phase along ΓX. The (6×3) structure was, however, not observed during decomposition of higher-coverage phases, pointing to a non-equilibrium nature of this phase. Continuing the deposition at $470K$ irreversibly leads to a highly stable and
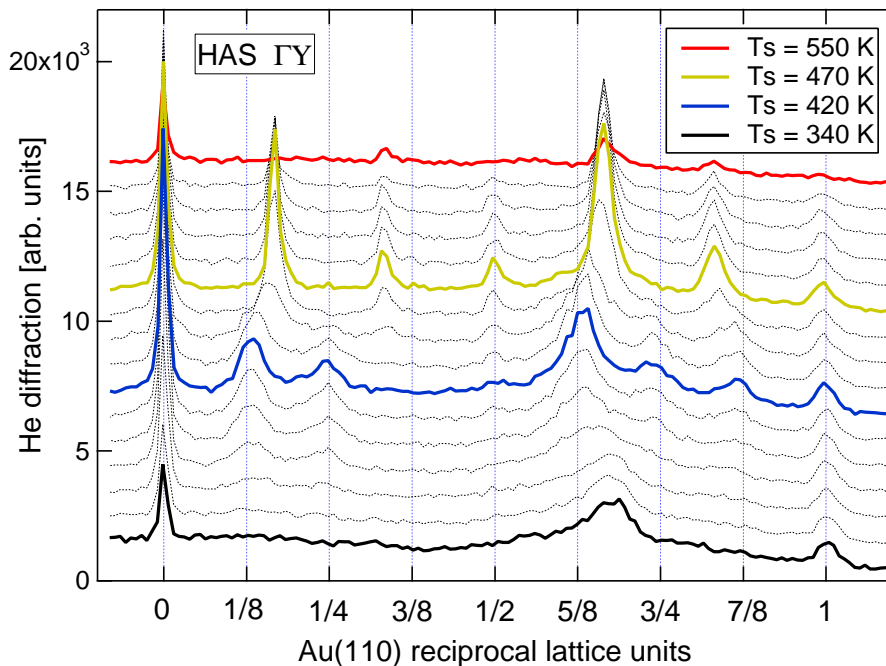
Figure 5.12: HAS diffraction patterns collected consecutively along ΓY during slow surface annealing. The emphasized patterns represent equilibrium stable phases.

well ordered (3×6) phase. This symmetry corresponds to the phase, where molecules were reported to align in side-by-side configuration [2], forming widely spaced $(24.5\,\text{Å})$ chains along $[1\bar{1}0]$. In this case molecules are azimuthally rotated by 90° relative to the direction in (6×3) phase. The corresponding model with one molecule per unit cell is realized in fig. 5.13, right panel.
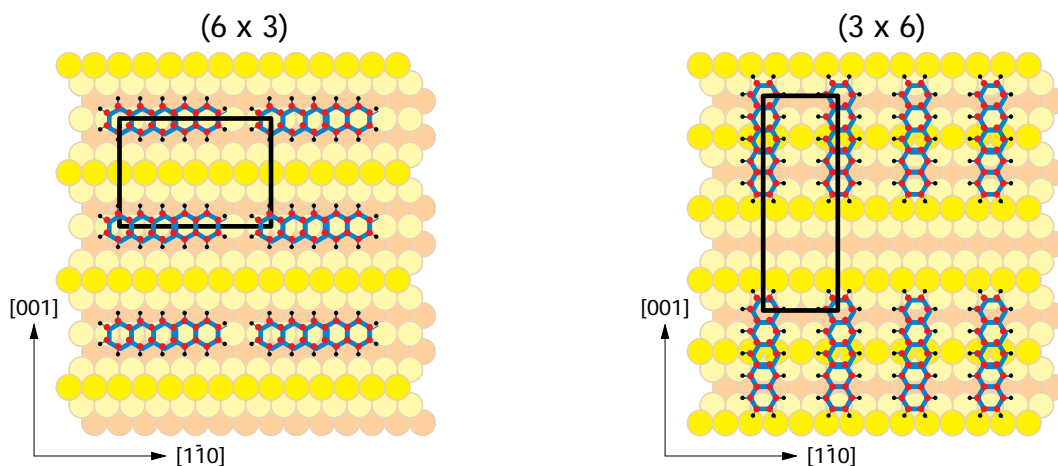
Figure 5.13: The model of (6×3) (left) and (3×6) (right) structure. The unit cell is denoted by a black rectangle. In case of (6×3) structure a possible shallow (1×3) substrate reconstruction is shown.

At RT pentacene deposition, on the other hand, the substrate diffraction pattern rapidly disappears due to the proliferation of pentacene induced defects without yielding any ordered structure. This finding indicates a disordered growth, which is also in agreement with previous observations [2] [64, 65].

The (6×8) phase is found to be the saturation coverage of pentacene thin film on the substrate held at 420 K, since the upper-most diffraction pattern on fig. 5.10 doesn't change upon further deposition. This indicates that no further phases build up beyond the (6×8) at this temperature. It seems that the redundant material either evaporates away or collects in large 3D clusters which have rather small influence on the helium diffraction. This possibilities were examined by measuring the XPS signal of the carbon $1s$ in the next section. Interestingly, the (6×8) phase can also be obtained by continuing the deposition at 420 K on a previously grown (3×6) phase. The fainter and broader (6×8) diffraction pattern was also obtained at the substrate temperature of 370 K. In this case, continuing deposition slowly leads to a decrease of the diffraction pattern intensity without any change of the peak position and width. This behavior is characteristic of a Stranski-Krastanov growth, where uncorrelated 3D pentacene clusters grow on top of the wetting layer (see sec. 2.1). When the substrate temperature was equal to or lower than 370 K, deposition on previously grown (3×6) and (6×8) templates simply leads to the attenuation of the diffraction patterns without modification of their shape due to disordered growth.

Further insight into the morphology of pentacene film was carried out by photoemission analysis.

5.3 X-ray photoemission analysis

We make use of XPS monitoring during deposition to calibrate the total amount of deposited pentacene. The film thickness and the pentacene coverage were determined from intensity variations of the Au $4f_{5/2}$, Au $4f_{7/2}$ and C $1s$ photoelectron peaks. In the following XPS spectra all peaks were fitted by Voigt lineshape, i.e., the convolution of Gaussian and Lorenzian function (see eq. (3.32) in sec. 3.7). The strength of a single XPS peak has been accurately determined by taking the integrated area of the peak instead of taking its height.

The coverage ratio between the (3×6) and (6×8) phase was determined by examining the integrated C $1s$ peak area of both phases (fig. 5.14). XPS spectra were taken with a photon energy of 400 eV and an overall energy resolution of 270 meV. Continuous fit-line obtained by a sum of Voigt function and arctan step is also displayed on the graph. The binding energy scale was calibrated to the energy position of the Au $4f_{7/2}$ peak at 83.9 eV. The peak area ratio of 8:9 was found between the two phases at 1% precision. The same ratio was gained also at 650 eV photon energy. Considering this coverage ratio and the size of the unit cell, corresponding to each phase, i.e., (3×6) and (6×8), respectively, one comes to a result that there are three pentacene molecules per unit cell in the (6×8) phase. No noticeable energy shift was, however, detected between the two peaks, which excludes the possibility of the presence of the second monolayer. By depositing about $10 - 12$ ML at 280 K, on the other hand, which forms a thick (bulk) pentacene film, the C $1s$ peak shifts to higher binding energies by about 0.38 eV relative to its position in (6×8) and (3×6) phases. The shift most likely occurs due to change of work function
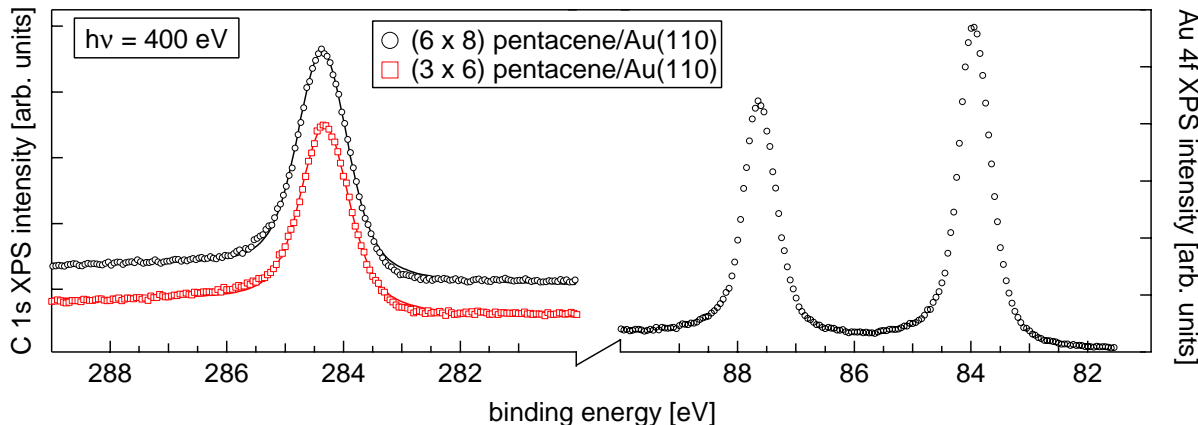
Figure 5.14: The photoelectron peak of C $1s$ core level excitation for (6×8) and (3×6) pentacene phases. The Au $4f_{5/2,7/2}$ doublet (not fitted) is also shown and was used to calibrate the binding energy axis.

because of completely covered Au substrate.

Next we discuss the evolution of the photoemission signal as a function of the pentacene exposure. At a substrate temperature of $370\,K$, the C $1s$ intensity initially increases linearly, whereas after approximately 5 minutes of deposition slope changes (fig. 5.15, left). This is a an indication of first monolayer completion, on which the newly deposited
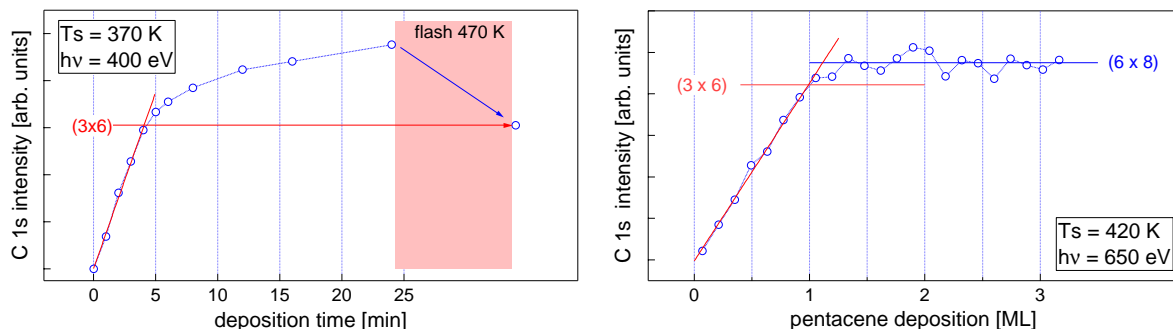

Figure 5.15: Integrated peak intensity of C $1s$ XPS spectra taken during deposition at $T_s = 370\,K$ (left) and $T_s = 420\,K$ (right).

molecules adsorb. The XPS signal thus continues to grow with a decreasing rate, but without clear saturation, indicating that the overall film thickness increases, which is consistent with the previous model of disordered growth at RT. In the submonolayer range at RT, the pentacene molecules easily migrate over the surface producing uniform interface layer, while the subsequently deposited molecules don't order and the amorphous growth takes place. By flashing the thin film up to $470\,K$ the C $1s$ signal drops to the level which exactly coincides with the slope change of the XPS intensity during deposition, indicating that the second and further layer molecules either desorb or get aggregated into 3D islands. The resultant phase exhibits a perfect (3×6) symmetry of the monolayer phase. Linear growth of the C $1s$ signal up to the formation of (3×6) phase where it saturates, was put to evidence also at higher substrate temperature, i.e., $470\,K$. There is

no further increase of the signal pointing out that additionally deposited material doesn't stick to the surface any more, confirming that (3×6) is saturated stable structure at high temperature with 1 ML coverage.

A slightly larger saturation coverage is achieved by depositing on the substrate at temperature 420 K, where the (6×8) phase is formed (fig. 5.15, right). Again the C $1s$ signal is observed to grow linearly up to the intensity, corresponding to the coverage of the (3×6) phase, whereas upon further deposition it grows with a lower rate. This linear increase is associated with the 2D growth of a wetting pentacene layer, whose completion corresponds to the coverage of the (3×6) phase. Additional pentacene deposition, required to form the (6×8) phase, doesn't yield a linear increase of the C $1s$ signal any longer (fig. 5.15, both graphs). We could attribute this effect to the absorption of the additional molecules on top of the first pentacene layer, where the sticking coefficient to incorporate into the wetting layer might be lower than on the uncovered substrate. Another possibility is that the additional pentacene incorporates between the molecules of (3×6) structure thus forming a denser first layer phase. The presence of second layer molecules has already been excluded due to absence of any appreciable core level shift between the two phases (fig. 5.14).

The kinetics of the high density (6×8) phase has been further examined by following a different growth path in the phase diagram. In fig. 5.16 the HAS intensity of the $(0, 1/6)$ diffracted peak is displayed, which represents the order parameter of the (3×6) phase and should disappear in the (6×8) phase. First the saturated (3×6) phase was formed at
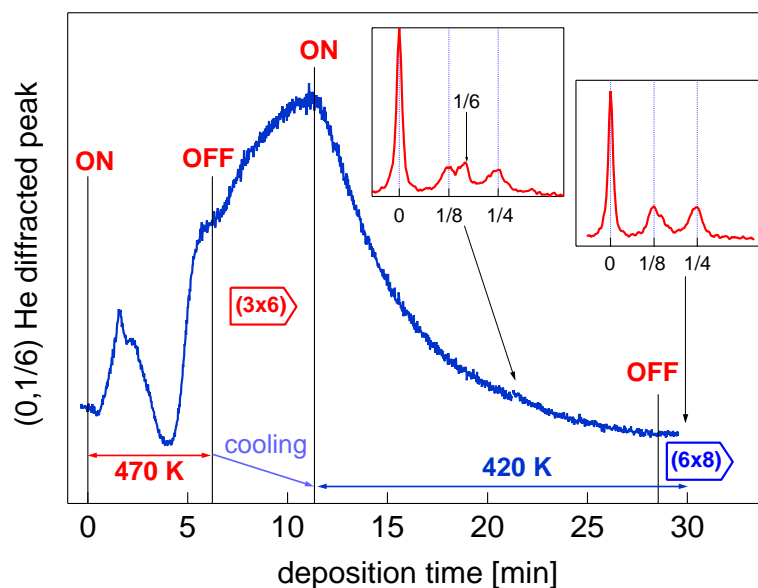
Figure 5.16: HAS intensity of the $(0, 1/6)$ peak during deposition. The deposition at 470 K was stopped after formation of the saturated (3×6) phase at 6 minutes and the substrate was then cooled to 420 K. After additional 16 minutes of deposition a well ordered (6×8) phase was formed. The HAS diffraction patterns are shown for an intermediate and final deposition stage.

470 K which was then used as a template for further pentacene deposition at 420 K. The formation of higher coverage (6×8) phase has then been monitored. The corresponding HAS diffraction patterns are shown in the insets of fig. 5.16. At the intermediate stage

the coexistence of (3×6) and (6×8) phases is observed. Notice that no HAS temporal evolution was observed after continuing the deposition at 420 K indicating the equilibrium growth regime. Upon further pentacene deposition the 1/6 peak decreases continuously until the (6×8) phase is eventually reached.

The deposition time of ~ 17 minutes, needed to obtain the (6×8) phase is remarkably larger than the time required to grow the (3×6) phase (~ 6 minutes). Moreover, this additional exposure is larger than the total exposure required to grow the (6×8) phase starting with the clean substrate, e.g., deposition in fig. 5.15, right. If the (6×8) phase was a simple extension of the (3×6) phase by means of condensating a portion of molecules on top of it, the total exposure should be roughly independent from the procedure to prepare the underneath (3×6) phase. Considering that the pentacene exposure required to form the (6×8) phase depends on the history of deposition and that optimal (3×6) phase cannot be formed at 420 K, we conclude that the (6×8) is as well a monolayer phase that has denser pentacene packing compared to (3×6) phase. The formation of the high density (6×8) phase from the pre-deposited (3×6) phase is inhibited by kinetic limitations, dependent on the exact path. The structural defects were found to be essential for additional pentacene incorporation into (3×6) phase.

We now summarize all observed structures of pentacene on Au(110) in the phase diagram, shown on fig. 5.17.
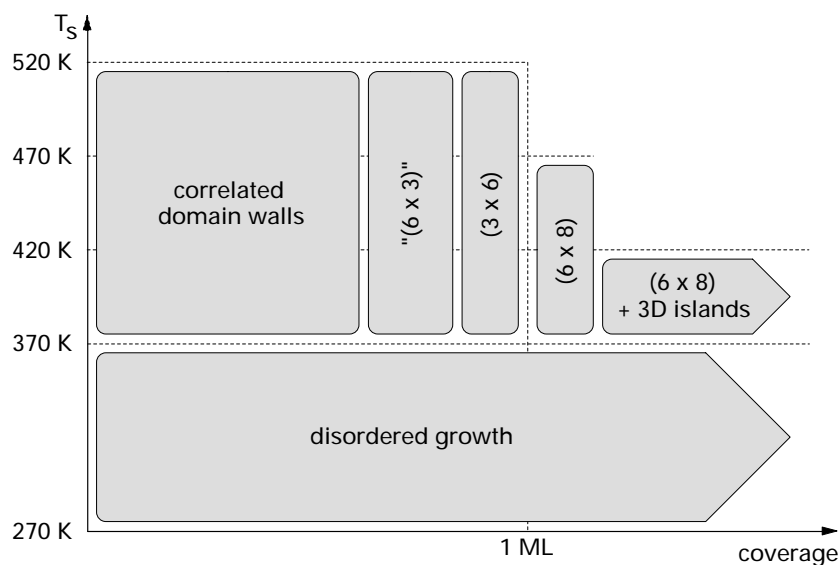
Figure 5.17: Phase diagram of pentacene structures in Au(110) surface.

In conclusion we observe that pentacene molecules grown on the substrate with temperature of 420 K and higher don't form a multilayer film. In fact, no C $1s$ signal increase is observed upon further pentacene deposition after the (6×8) phase is formed and there is no chemical shift of the XPS peak. The (6×8) phase was found to have approximately 9:8 greater coverage than the (3×6) and contains three molecules per unit cell. Since the (6×8) phase is packed closer than (3×6) phase, it is hard to realize its model without tilting certain portion of the adsorbed molecules. The actual spatial orientation of molecules is further deduced from the X-ray absorption signal (NEXAFS).

5.4 Molecular orientation study from NEXAFS

As discussed in details in chapter 3, NEXAFS measurements are most helpful in determining the molecular bond orientation relative to the direction of the X-ray polarization vector. By tuning the photon energy across specific absorption edge, one excites the electrons of a chosen atomic species into the unoccupied molecular states. NEXAFS thus at the same time effectively maps the unoccupied molecular states. The absorption signal is measured as an electron yield, collected by the wide angle channeltron detector, placed above the illuminated sample. The grid in front of the channeltron was polarized to $-200\,\text{V}$ in order to reject the low energy electrons. This way partial yield was measured with high-pass filter, which is known to increase surface sensitivity of the absorption measurements.

The acquired NEXAFS spectra were appropriately normalized to exclude all possible artefacts. Beginning with the X-ray source, because of decaying synchrotron current and due to specific nature of the monochromator, normalization to the actual photon flux at monochromator exit (I_0) was performed. To cancel out the intensity variations due to geometry specific sample illumination as well as detector field of view variations at different angles, NEXAFS spectrum was additionally normalized with the spectrum acquired on clean Au(110) in the same conditions. Furthermore a careful tuning to the accurate photon energy was made. Its exact value was determined from the calibration to gas absorption resonances in CO, observing the C $1s \to \pi^*$ transition at $287.40\,\text{eV}$ [66]. All NEXAFS spectra presented in this thesis were treated according to described procedure.

Analysis of NEXAFS spectra

Fig. 5.18 shows the NEXAFS spectrum of the (6×8) film grown at $420\,\text{K}$. It exhibits all the features that will be met later in this chapter and was therefore chosen to present them. The energy resolution was $\sim 0.1\,\text{eV}$. A good agreement with the pentacene gas-phase NEXAFS spectra can generally be noted, with some variations in the relative intensity of the resonances. The only qualitative difference is that the peak at $287\,\text{eV}$ is not present in the spectrum of the pentacene thin film. This happens due to selection rules and will be discussed later.

The resulting best fit of the experimental spectrum, performed with the multicomponent function, is denoted by continuous red curve. The individual components are displayed in the bottom of the figure. At the low-energy part of the spectrum two peaks occur at 284 and $285.8\,\text{eV}$, respectively, belonging to the C $1s \to$ LUMO and LUMO+1 transition. The multicomponent nature of the π^* resonances partly originate in inequivalent C $1s$ initial states due to 6 inequivalent carbon atoms within the pentacene molecule (see fig. 5.3). Theoretically predicted energy positions of the transitions from the individual C $1s$ states are denoted by vertical bars on fig. 5.19 [53]. In practice, the nearest peaks blend together due to natural width of the resonances and because of additional broadening due to finite experimental resolution. For this reason the two multicomponent peaks were successfully fitted by a sum of three and two Gaussian peaks, respectively (see eq. (3.31) on page 29), which are shown in the bottom of fig. 5.18.

In the high-energy part of the spectrum, at 294 and $301\,\text{eV}$ two broad features are observed. They are both located above the ionization potential which makes them belonging to transitions to unbound states. However, according to discussion in sec. 3.6,
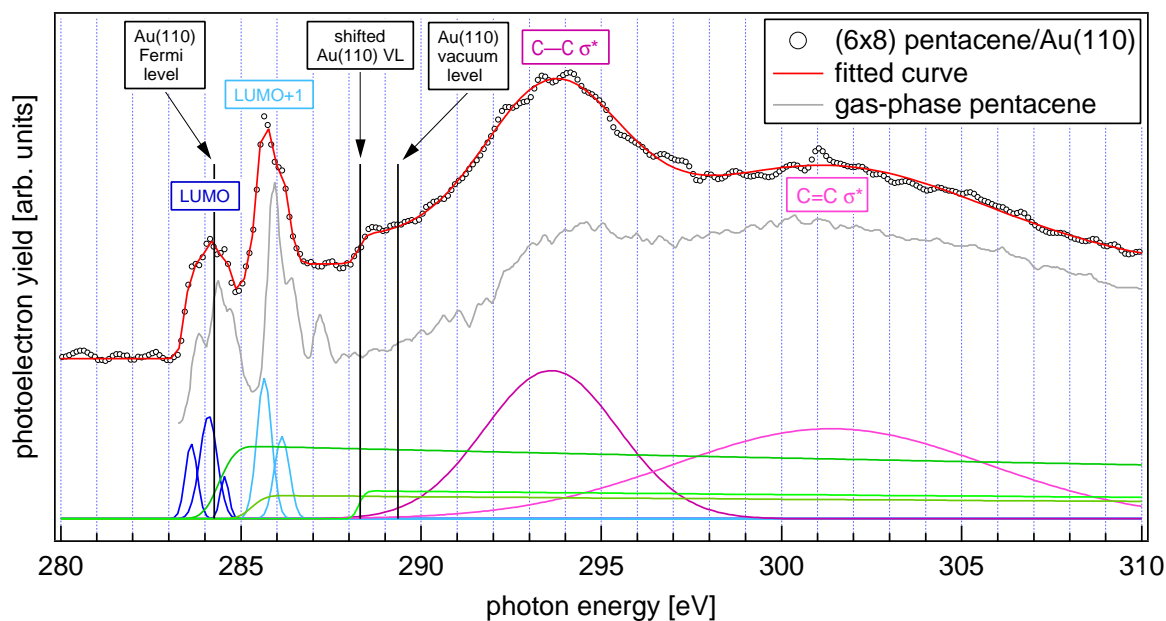
Figure 5.18: The NEXAFS spectra of (6×8) pentacene/Au(110). Under the fitted curve there is the decomposition to individual components of the spectra.
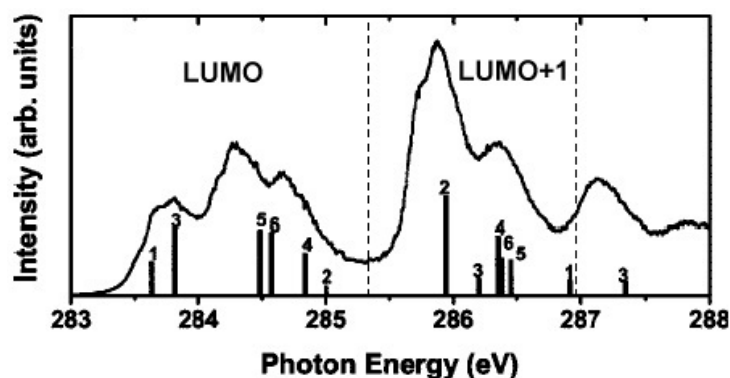

Figure 5.19: Calculated and measured positions of the C $1s \rightarrow$ LUMO and LUMO+1 resonances from six chemically inequivalent carbon atoms. The enumeration is in accordance with fig. 5.2. Above the bars there is an experimental NEXAFS spectrum of pentacene gas-phase [53].

page 26, this two peaks stem from the transition to quasi-bound σ^* molecular states. The low-energy peak corresponds to the transition to C−C and the high-energy one to C=C molecular orbitals. Due to unexpressed asymmetry, both resonances were well fitted by simple Gaussian lineshape leaving all fitting parameters free. A small shift of σ^* resonances to lower energy indicates a slight lengthening of C−C bonds in the pentacene molecule and occurs due to interaction with the substrate.

For easier characterization of the step features, three black guidelines were put on the graph. From the XPS spectra that were taken on the pentacene covered substrate, we determined the exact position of the C $1s$ binding energy relative to the Fermi level. Correspondingly, the first guideline is put at the value of $h\nu = 284.3$ eV. This photon

energy is theoretically sufficient to excite the carbon $1s$ electrons in the substrate empty states above the Fermi level. Considering the work function of Au(110) surface to be $\phi = 5.1\,\text{eV}$ [67], the vacuum level (VL) guideline is placed at 289.4 eV, as discussed in sec. 3.6 on page 27. There is, however, no feature in the NEXAFS spectra at this energy. The metal work function is obviously altered in the presence of adsorbate, which means that we don't have a simple case of metal-adsorbate junction where vacuum levels of substrate and adsorbate coincide as shown in fig. 5.20, left. It was shown that the substrate
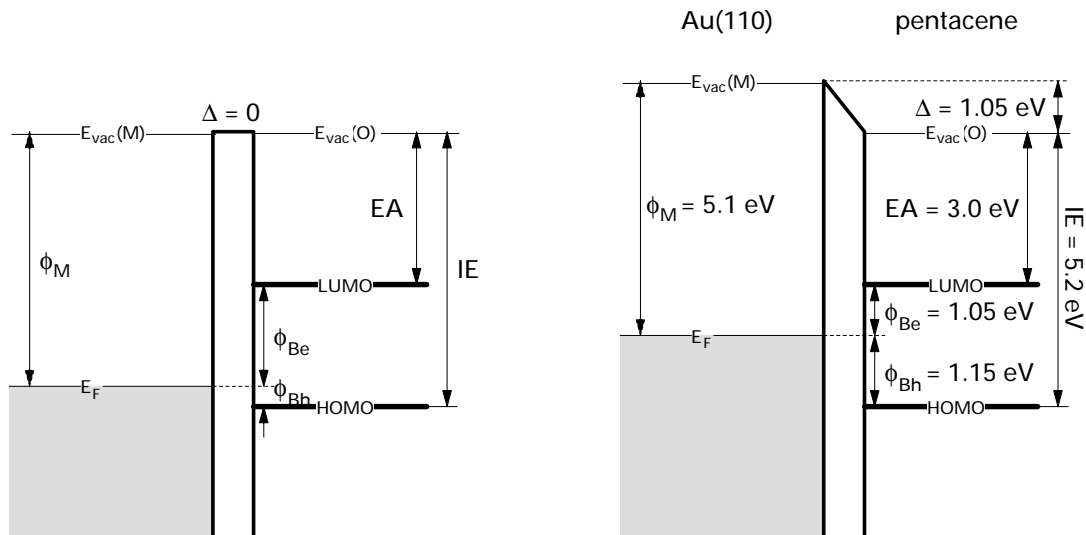
Figure 5.20: Schematic of an organic-metal interface level diagram without (left) and with (right) an interface dipole barrier Δ. EA stays for the electron affinity, while the electron and hole barriers are denoted by ϕ_{Be} and ϕ_{Bh}, respectively. $E_{vac}(M)$ and $E_{vac}(O)$ are the metal and organic vacuum levels. Values in the case of pentacene/Au(110) are displayed on the right hand sketch.

dipole contribution becomes substantially modified in the presence of large adsorbate species such as conjugated organic molecules [10]. Due to overlapping of molecule and substrate electron density, the repulsion occurs leading to compression of the electron tails, which gives rise of an interface dipole barrier (Δ). This correspondingly lifts the VL of the metal and at the same time lowers the effective metal work function[2] by the same difference Δ (fig. 5.20, right). The third guide line is thus set up so that it coincides with the VL step in the spectrum, which is of light green color in fig. 5.18. Its position for fitting with error function (eq. (3.35) on page 29) was left as a free fit parameter. This way the Au(110) work function shift of $\Delta = 1.05\,\text{eV}$ is obtained. Interestingly, this value is in perfect agreement with the result of Koch and co-workers, who obtained the same value for the pentacene thin film deposited on the amorphous Au [68]. The width of the VL step was also left as a free parameter, for which the fit yields 0.12 eV. The value matches previously stated experimental resolution.

---

[2]The height of the interface electron barrier (ϕ_{Be}) is thus no more a simple difference between the metal work function (ϕ_M) and the electron affinity (AF) of the organic solid (fig. 5.20, left). This is an important consequence which needs to be considered in production of organic electronic devices. Analogously, the hole barrier (ϕ_{Bh}) isn't just a difference between the ionization energy (IE) of the organic material and the metal work function. Here IE of the organic material is taken to be IE $= E_{vac}(O) - E_{HOMO}$.

By closer inspection of NEXAFS pattern in fig. 5.18 one notes that the background level is raised after first and second π^* resonances, i.e., at $285\,\mathrm{eV}$ and $287\,\mathrm{eV}$. This occurs because of multielectron excitations (ME) that become possible after crossing the level of each individual π^* resonance by increasing the photon energy. The possibility for ME excitations in fact grows proportionally to the resonance integral with upper limit equal to photon energy (see sec. 3.6 on page 28). For this reason an error function was used in fitting, representing the integral of Gaussian function. Each of two steps had its energy position locked to the position of adequate resonance. The step width was also made equal to the width of the corresponding resonance.

Being familiar with the typical features of pentacene/Au(110) NEXAFS spectrum we can now observe how they depend on the surface structure and the X-ray incident angle. We make use of the linear dichroism of π^* and σ^* resonances, described in sec. 3.4, to exploit the molecular orientation of the pentacene in (3×6) and (6×8) phases. As a source the linearly polarized synchrotron light is used. The following measurements were performed on the Aloisa experimental chamber.

NEXAFS angular dependence of (3×6) phase

In the experiment, NEXAFS spectra with grazing incidence X-rays were acquired as a function of angle (α) between the photon polarization vector and the surface plane, as displayed in fig. 5.21, left. The azimuthal angle ϕ of the grazing incident X-rays with respect to the Au(110) substrate was varied as well (fig. 5.21, right).
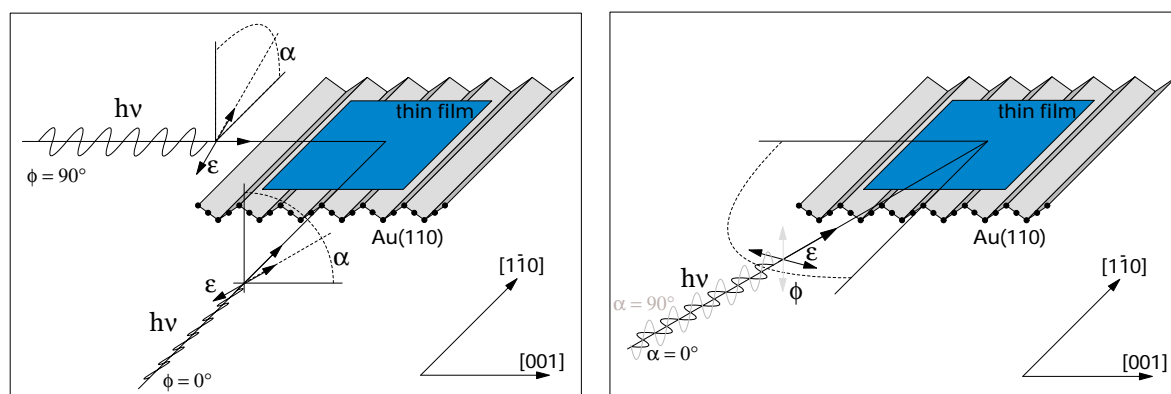
Figure 5.21: The experimental geometries for acquisition of pentacene/Au(110) NEXAFS spectra. The angle of X-ray polarization relative to the surface plane (left) and the azimuthal angle of the incident X-rays on Au(110) substrate (right).

For $\alpha = 0°$ the polarization vector ϵ lies in the surface plane. The X-rays are in this case said to be *s*-polarized. For $\alpha = 90°$ the polarization vector ϵ lies (almost) perpendicular to the surface plane and the X-ray light is termed as *p*-polarized. The azimuthal scans were made with both X-ray polarizations.

Fig. 5.22 shows NEXAFS spectra taken as a function of angle α on (3×6) phase. The grazing incident beam was parallel to [001] and [1$\bar{1}$0] surface direction, respectively. The experimental resolution was $\sim 0.15\,\mathrm{eV}$. For both incident directions of X-rays a strong dichroism of π^* and σ^* resonances can be immediately seen, pointing to high orientational
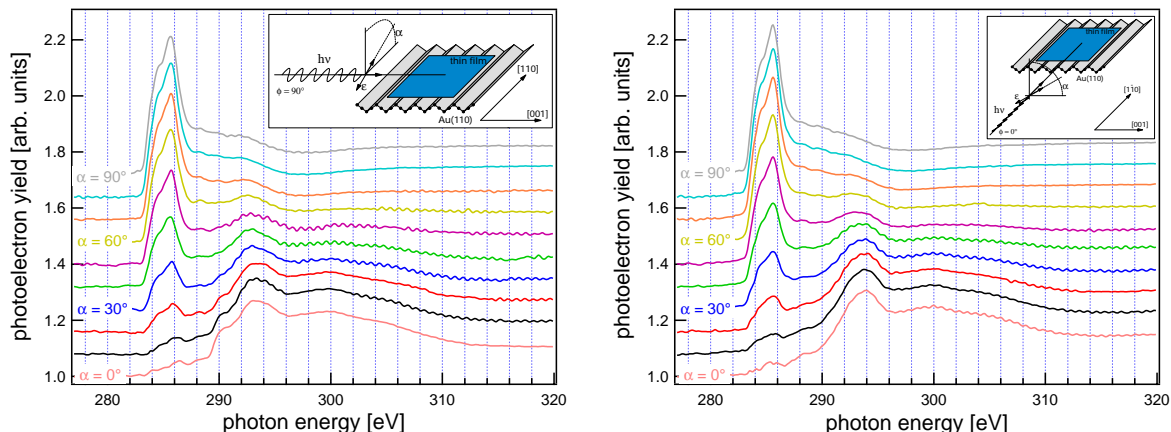
Figure 5.22: NEXAFS spectra on (3×6) pentacene/Au(110) acquired by varying the angle α. Incident photon beam is parallel to the [001] surface direction.

order of the adsorbed molecules. The π^* resonances disappear almost completely when X-ray polarization angle reaches $\alpha = 0°$. On contrary, the two σ^* resonances are at their maximum when $\alpha = 0°$. This angular dependence is characteristic for molecules lying flat on the surface, i.e., molecular plane is parallel to the surface plane. The LUMO and LUMO+1 peaks are not resolved as well as in fig. 5.18, which indicates strong interaction of π^* states with the substrate states involving the hybridization. The small intensity of π^* resonances that remain also at $\alpha = 0°$ can be attributed to a minute portion of molecules, that are adsorbed at steps or defect sites in a tilted configuration, and due to a small distortion of the π^* states because of the presence of the substrate. Other possibilities for non-zero intensity, such as out-of-plane distortion of the originally planar molecule [70], were neglected.

The tilt of the adsorbed molecules was precisely determined by extracting the π^* and σ^* peak intensities. Each π^* peak was fitted by two Gaussian components, whereas the σ^* peaks were fitted by a single component. The peak intensities are shown as a function of angle α in fig. 5.23, left panel. By fitting with functions (3.25) and (3.26) introduced in sec. 3.5, the tilt angle of $0° \pm 0.5°$ is obtained. The corresponding surface model is shown in fig. 5.23, right panel.

We may conclude that the pentacene molecules in the phase with (3×6) symmetry are orientationally well ordered and lie perfectly flat on the surface. They lie with the long molecular axis oriented along the [001] direction (sixfold periodicity) and are aligned side-by-side into long chains, extending parallel to the $[1 - 10]$ direction (threefold periodicity). Molecules adsorb so that they maximize the overlap of the molecular π orbitals and the π-like orbitals of the surface metal atoms (π-bound molecules). Strong interaction with the substrate causes a small hybridization of the involved molecular states. The observed angular behavior of π^* and σ^* resonances is consistent with the results, obtained by applying the selection rules on the symmetry character of calculated pentacene molecular orbitals. The calculation of orbitals was performed by K. Lee and J. Yu [69] and is discussed together with the particular selection rules for pentacene in the following section.
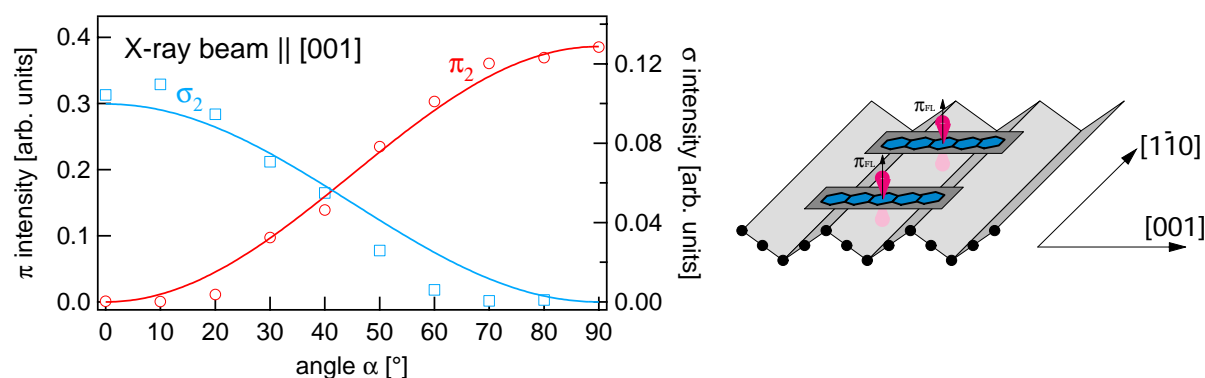
Figure 5.23: The intensity of π^* and σ^* resonances while photon beam is along [001] direction (left). Fit yields the absolute tilt of the molecular plane relative to the substrate to be $0° \pm 0.5°$ for both photon directions. The realization of the model for the (3×6) phase (right).

Transition selection rules for pentacene

The isolated planar molecule of pentacene possesses a D_{2h} symmetry. The coordinate system is placed with the x-axis parallel to the longest molecular axis and the z-coordinate axis perpendicular to the molecular plane, as shown on fig. 5.24. Because the photon
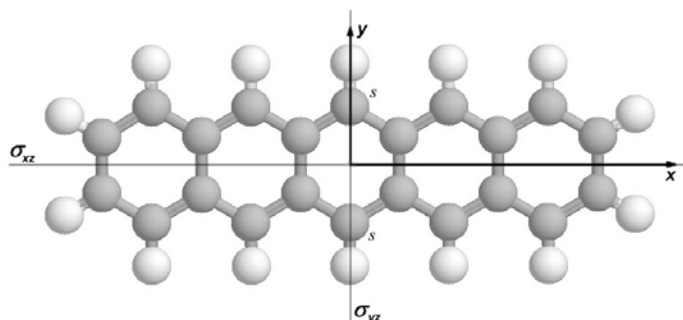
Figure 5.24: The pentacene molecule placed in coordinate system and the two mirror planes σ_{xz} and σ_{yz}.

polarization vector is antisymmetric in just one direction, we are only interested in symmetry operation of reflection through the plane. The characters of point group D_{2h} for this operation together with the corresponding basis functions are shown in tab. 5.1. Each pentacene molecular orbital belongs to the symmetry of one of the basis functions (right column in tab. 5.1) and transforms as the corresponding irreducible representation. To denote the relating electronic state, capital letters are used (left column in tab. 5.1), while the involved orbitals are denoted by small letters.

The isosurface plots of the pentacene molecular orbitals according to K. Lee and J. Yu [69] are depicted on fig. 5.25. The positive and negative phase of the wavefunctions are visualized by blue and red color, respectively. We focus on unoccupied orbitals, i.e., LUMOs, for being the only possible candidates for final electronic states.

According to selection rules, discussed in sec. 3.3, the transition is allowed if the

D_{2h}	σ_{xy}	σ_{xz}	σ_{yz}	basis f.
A_g	1	1	1	x^2, y^2, z^2
A_{1g}	1	-1	-1	xy
A_{2g}	-1	1	-1	xz
A_{3g}	-1	-1	1	yz
B_u	-1	-1	-1	xyz
B_{1u}	-1	1	1	z
B_{2u}	1	-1	1	y
B_{3u}	1	1	-1	x

Table 5.1: The table of selected characters for the point group D_{2h} and the corresponding basis functions.
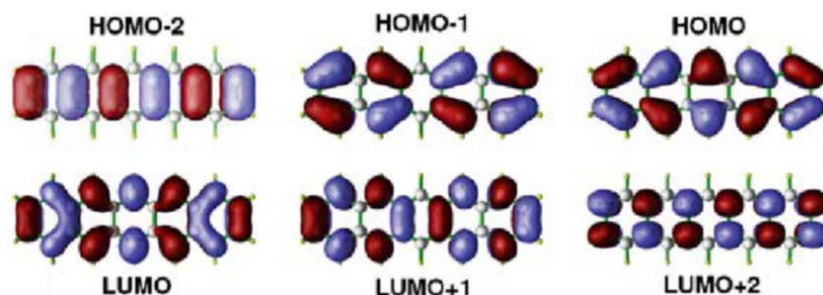
Figure 5.25: The electronic density of the last three filled (HOMOs) and the first three unfilled (LUMOs) pentacene molecular orbitals.

following triple product is totally symmetric:

$$\Gamma(MO) \times \Gamma(\mu) \times \Gamma(C1s) = \text{sym.} \tag{5.1}$$
$$\Downarrow$$
$$\langle MO | \mu | C1s \rangle \neq 0 \qquad \Rightarrow \qquad \text{allowed transition}$$

To evaluate the direct product one must also know how the photon and the atomic initial state transform in the basis of D_{2h} point group.

Considering $\boldsymbol{\mu} = e\mathbf{r}$, the individual component of the dipole moment operator $\boldsymbol{\mu}$ has the same symmetry as the basis functions x, y and z, respectively. Their parity, i.e., the character upon reflection through all three planes, are shown in tab. 5.2. In the case of linearly polarized X-ray light with the polarization vector along one of the coordinate axes, only one component from the dipole operator $\boldsymbol{\mu}$ remains. The dot product $\boldsymbol{\epsilon} \cdot \boldsymbol{\mu}$ for exclusive polarization along ϵ_x, ϵ_z and ϵ_y yields μ_x, μ_y and μ_z, respectively, for which the corresponding characters read as lines in tab. 5.2

Before determining the symmetry of initial state C $1s$ orbital, it must be stressed that the irreducible representations within the PGOM holds only for the symmetry operations defined with respect to the coordinate system, placed in the molecular center of symmetry with the coordinate axes pointing along molecular symmetry directions. The symmetry of the localized C $1s$ orbital of the individual excited atom must, however, be

$$\Gamma(\mu) \quad = \quad \begin{array}{c|ccc} & \sigma_{xy} & \sigma_{xz} & \sigma_{yz} \\ \hline \Gamma(\mu_x) & 1 & 1 & -1 \\ \Gamma(\mu_y) & 1 & -1 & 1 \\ \Gamma(\mu_z) & -1 & 1 & 1 \end{array} \quad \sim \quad \begin{array}{c} B_{3u} \\ B_{2u} \\ B_{1u} \end{array}$$

Table 5.2: The symmetry of the dipole operator μ on the reflection through the planes σ_{xy}, σ_{xz} and σ_{yz}. On the right side there are the irreducible representations to which each component belongs. The $\sim$ sign should here read as "transforms as".

inspected separately. It depends on the position of an individual carbon atom relative to the molecular symmetry directions which are related with electron final state.

The symmetries for the individual carbon atoms in the coordinate system and the symmetry operations of the molecule can be inferred from fig. 5.24, if there is no molecular bending (due to the presence of a substrate or other molecules). The $1s$ orbitals from all carbon atoms within the molecule are symmetric on the reflection through the molecular plane, i.e., xy. There are two atoms, s, that possess additional symmetry on the reflection through the plane yz. The C $1s$ symmetry properties of all carbon atoms are collected in tab. 5.3.

|	σ_{xy}	σ_{xz}	σ_{yz}
s	1	/	1
other	1	/	/

Table 5.3: Symmetry properties of carbon atoms in pentacene molecule. The "/" sign means that atom has no symmetry to that operation.

We can now examine if the individual transition C $1s \to$ MO is allowed. The lowest lying excitations are expected to belong to the transition C $1s \to$ LUMO, which is of π^*-type and possesses B_{1u} symmetry. We calculate the direct product from eq. (5.1) by multiplying the characters of B_{1u} orbital (from tab. 5.1), the characters of all three X-ray light polarizations (tab. 5.2) and the characters for both groups of atoms with inequivalent symmetry properties, s and *other*, (tab. 5.3):

$$
\begin{array}{c}
\quad\quad\quad \langle\text{MO}| \quad\quad\quad \mu \quad\quad\quad |C1s\rangle \\[4pt]
\begin{array}{c}
\sigma_{xy}: \\ \sigma_{xz}: \\ \sigma_{yz}:
\end{array}
\left\|
\begin{array}{c|ccc|cc}
B_{1u} & \epsilon_x, & \epsilon_y, & \epsilon_z & \text{other}, & s \\
\hline
-1 & 1 & 1 & -1 & 1 & 1 \\
1 & 1 & -1 & 1 & / & / \\
1 & -1 & 1 & 1 & / & 1
\end{array}
\right\|
=
\left\|
\begin{array}{ccc}
\Gamma^o_{\epsilon_x},\Gamma^s_{\epsilon_x} & \Gamma^o_{\epsilon_y},\Gamma^s_{\epsilon_y} & \Gamma^o_{\epsilon_z},\Gamma^s_{\epsilon_z} \\
\hline
-1,-1 & -1,-1 & 1,\ 1 \\
/,\ / & /,\ / & /,\ / \\
/,-1 & /\ \ 1 & /,\ 1
\end{array}
\right\|
\end{array}
\quad (5.2)
$$

The transition is forbidden if the resulting parity is *odd*. For the transition to be allowed, the triple product (i.e. *all* product components) can thus only be of *even* or no symmetry. For X-ray polarization parallel to x- or y-axis, the eq. (5.2) yields odd product parity, since first component in all four columns $\Gamma^o_{\epsilon_x}, \Gamma^s_{\epsilon_x}, \Gamma^o_{\epsilon_y}$ and $\Gamma^s_{\epsilon_y}$ is odd. This means that the transition $C1s \to$ LUMO for X-ray polarizations along x- and y-axis is forbidden. However, when the X-ray polarization points along z-axis, the product is of even parity

for all atoms, since all three components in each column, $\Gamma^o_{\epsilon_z}$ and $\Gamma^s_{\epsilon_z}$, have either even or no parity. For p-polarized X-rays, i.e., perpendicular to the molecular plane, the π^*-transition is thus allowed (fig. 5.26).
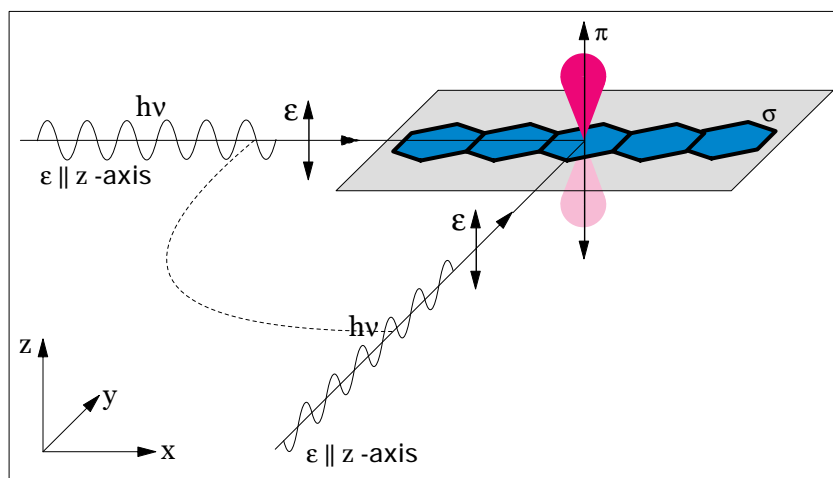
Figure 5.26: When X-ray polarization vector lies perpendicular to the molecular plane, π^* resonances are allowed.

The selection rules are not much different in the case of transition to LUMO+1 orbital, shown on fig. 5.25, which has B_{2g} symmetry. The triple product again yields allowed transitions only when X-ray polarization points along z-axis – as seen in column $\Gamma^o_{\epsilon_z}$ from equation (5.3).

$$
\begin{array}{c}
\sigma_{xy}: \\
\sigma_{xz}: \\
\sigma_{yz}:
\end{array}
\left\|
\begin{array}{c|ccc|cc}
B_{2g} & \epsilon_x, & \epsilon_y, & \epsilon_z & \text{other}, & s \\
\hline
-1 & 1 & 1 & -1 & 1 & 1 \\
1 & 1 & -1 & 1 & / & / \\
-1 & -1 & 1 & 1 & / & 1
\end{array}
\right\|
=
\left\|
\begin{array}{ccc}
\Gamma^o_{\epsilon_x},\Gamma^s_{\epsilon_x} & \Gamma^o_{\epsilon_y},\Gamma^s_{\epsilon_y} & \Gamma^o_{\epsilon_z},\Gamma^s_{\epsilon_z} \\
\hline
-1,-1 & -1,-1 & 1,\ 1 \\
/,\ / & /,\ / & /,\ / \\
/,\ 1 & /,-1 & /,-1
\end{array}
\right\|
\quad (5.3)
$$

However, the transition is forbidden for the two s atoms, lying on the places with higher symmetry. Theoretically the signal should thus be attenuated by factor 20/22 which could be hardly seen in the experiment.

It is interesting to check also transition to LUMO+2 orbital, which features the σ^* transition character and is thus opposite to the angular dependence of the two predecessors, LUMO and LUMO+1. The pentacene LUMO+2 orbital has B_{1g} symmetry which prohibits completely the transitions, when the X-rays are z-polarized:

$$
\begin{array}{c}
\sigma_{xy}: \\
\sigma_{xz}: \\
\sigma_{yz}:
\end{array}
\left\|
\begin{array}{c|ccc|cc}
B_{1g} & \epsilon_x, & \epsilon_y, & \epsilon_z & \text{other}, & s \\
\hline
1 & 1 & 1 & -1 & 1 & 1 \\
-1 & 1 & -1 & 1 & / & / \\
-1 & -1 & 1 & 1 & / & 1
\end{array}
\right\|
=
\left\|
\begin{array}{ccc}
\Gamma^o_{\epsilon_x},\Gamma^s_{\epsilon_x} & \Gamma^o_{\epsilon_y},\Gamma^s_{\epsilon_y} & \Gamma^o_{\epsilon_z},\Gamma^s_{\epsilon_z} \\
\hline
1,\ 1 & 1,\ 1 & -1,-1 \\
/,\ / & /,\ / & /,\ / \\
/,\ 1 & /,-1 & /,-1
\end{array}
\right\|
\quad (5.4)
$$

There are indeed no significant peaks between LUMO+2 and first σ resonance in the experimental spectra in fig. 5.22 in case of p-polarized X-rays. The transition is allowed for other two polarizations of X-rays, i.e., x and y, with the exception of s atoms, when photon is y-polarized (column $\Gamma^s_{\epsilon_y}$). One can in fact notice a really small feature at

286.4 eV in fig. 5.22, arising when angle α approaches zero, that could be attributed to transition to LUMO+2.

The transitions to "quasi-bound" molecular states above VL, that show σ^* character, can not be inspected in similar way, because no theoretical data about their symmetry was found. We can at this point infer their symmetry properties from the angular behavior in experimental NEXAFS spectra. In fig. 5.22 both σ^* resonances are at their maximum when angle α is equal to zero. The transition thus occurs when X-rays are s-polarized, as displayed in fig. 5.27. Comparing to the π^* resonances, this finding suggests the opposite
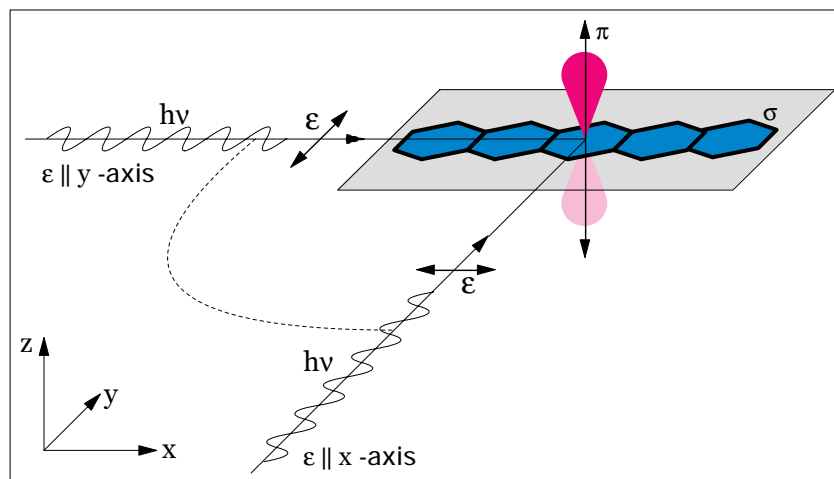

Figure 5.27: When X-ray polarization vector lies in the molecular plane, σ^* resonances are allowed.

parity for reflection through the xy-plane. The selection-rule equation would in this case write as

$$
\begin{array}{c|c|ccc|cc}
\sigma^* & \epsilon_x, & \epsilon_y, & \epsilon_z & \text{other}, & \text{s} \\
\hline
\sigma_{xy}: & 1 & 1 & 1 & -1 & 1 & 1 \\
\sigma_{xz}: & ? & 1 & -1 & 1 & / & / \\
\sigma_{yz}: & ? & -1 & 1 & 1 & / & 1
\end{array}
=
\begin{array}{ccc}
\Gamma^o_{\epsilon_x},\Gamma^s_{\epsilon_x} & \Gamma^o_{\epsilon_y},\Gamma^s_{\epsilon_y} & \Gamma^o_{\epsilon_z},\Gamma^s_{\epsilon_z} \\
\hline
1, \ 1 & 1, \ 1 & -1,-1 \\
?, \ ? & ?, \ ? & ?, \ ? \\
?, \ ? & ?, \ ? & ?, \ ?
\end{array} . \tag{5.5}
$$

The present discussion predicts clear results for D_{2h} symmetry of the molecule. We must however mention the possibility that the pentacene molecule could slightly bend along its longer axis in the presence of the substrate or other nearby molecules, as shows fig. 5.28. In this case the C_{2v} symmetry is attributed to the pentacene molecule, denoting the same symmetry as the water molecule has. The only direction along which the molecule now becomes intrinsically non-symmetric is the z-axis, i.e., perpendicularly to the plane of the unperturbed molecule. As the X-ray polarization vector rotates in the xz-plane of the molecular coordinate system, one can thus not expect such strong dichroism as in case of non-bent molecule. Nevertheless, the π^* resonances in the NEXAFS spectra of the (3×6) phase in fig. 5.22 vanishes almost completely, indicating that the pentacene molecule is only minimally bent.
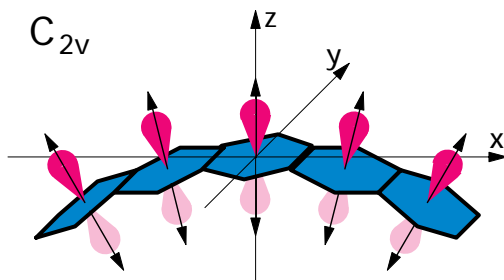
Figure 5.28: Pentacene molecule bend along longer axis has C_{2h} symmetry. The benzene π-systems are not parallel to each other any more.

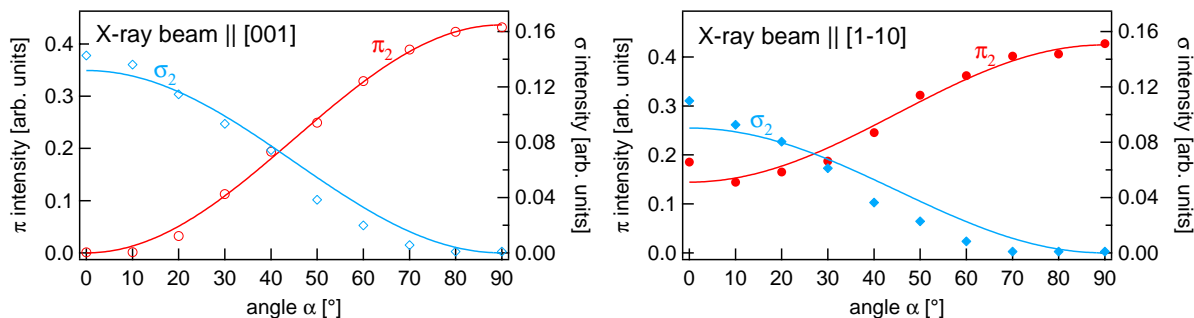### NEXAFS angular dependence of (6×8) phase

NEXAFS measurements at different polar angles α were also taken on the more dense (6×8) phase. The photon beam impinging at grazing incidence was pointed along [001] and [$1\bar{1}0$] surface directions, respectively. The acquired spectra are shown in fig. 5.29. An
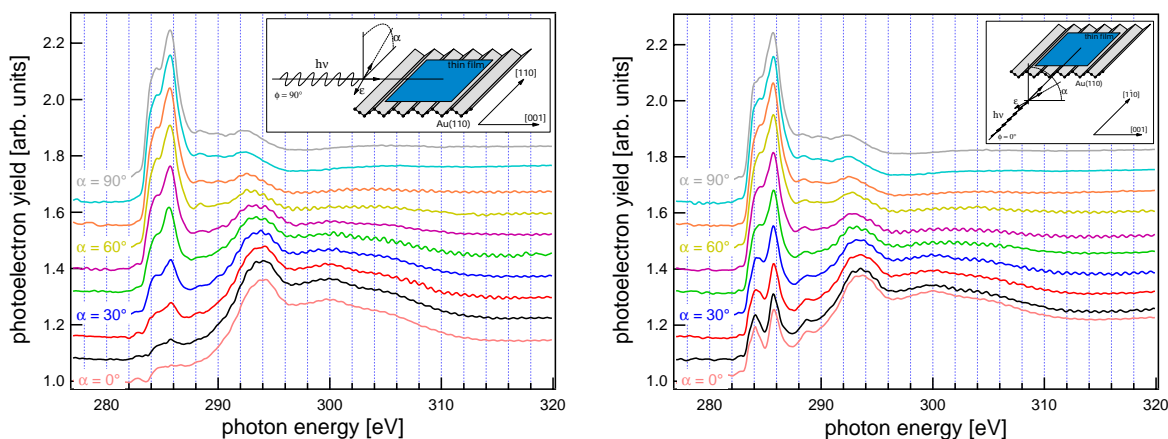
Figure 5.29: NEXAFS spectra on (6×8) pentacene/Au(110) acquired by varying the angle α. Incident photon beam is parallel to the [001] (left) and [$1\bar{1}0$] surface direction (right), respectively.

apparent difference can be noticed between the left and the right panel, as well as when comparing the right panel to the spectra of the (3×6) phase in fig. 5.22. When the beam is parallel to the [001] direction the observed angular dependence is very similar to that of the (3×6) phase. The π^* peak intensity goes to zero for $\alpha = 0°$ (s-polarization) and σ^* peak reaches maximum. On the other hand, when the beam is parallel to [$1\bar{1}0$] direction, the π^* resonances don't vanish when α approaches zero.

We get a closer insight by extracting the π^* and σ^* signal from both sequences of the spectra in fig. 5.29. The intensities of the π_2^* and σ_2^* peaks are displayed as a function of polar angle α in fig. 5.30. The π^* peaks were again fitted with two and the σ^* peaks with a single Gaussian component. The left panel in fig. 5.30 resembles well the behavior in the (3×6) phase (see fig. 5.23), indicating that the flat-lying molecules observed in the (3×6) phase are present also in the (6×8) phase. When the beam is parallel to

Figure 5.30: Angular dependence of the π^* and σ^* intensity during NEXAFS polar scan. Note that the π_2^* intensity doesn't vanish when $\alpha = 0°$ and the photon beam is parallel to the $[1\bar{1}0]$ direction, pointing to a presence of another molecular species with different adsorption geometry.

the $[1\bar{1}0]$ direction, however, the π^* signal doesn't vanish at $\alpha = 0°$ (see fig. 5.30, right panel), indicating the existence of another population of differently oriented molecules on the surface[3]. The pentacene molecules in the (6×8) phase coexist in two (or more) inequivalent adsorption geometries, where the additional molecules stand upright, i.e., with the molecular plane perpendicular to the surface and parallel to the $[1\bar{1}0]$ direction. We bare in mind that the (6×8) phase is only slightly denser than the (3×6) phase, so we model this phase as the (3×6) plus the additional pentacene molecules. Considering that the intensity of π^* peaks goes to zero when the beam is parallel to the $[001]$ direction, the additional molecules are only tilted in one direction, i.e., $[001]$. When the beam is parallel to the $[1\bar{1}0]$ direction, the maximum of the π^* intensity remains at $\alpha = 90°$ evidencing that the flat-lying molecules remains the majority population of the molecules present on the surface. The ratio of the π^* intensities at $\alpha = 90°$ and $\alpha = 0°$ is approximately 2.5:1 (see fig. 5.30, right panel) and reflects the ratio between the majority and minority molecular population, i.e., between flat-lying (FL) and up-standing (US) molecules. We recall the XPS data of the C $1s$ quantitative analysis, which reveals 3 molecules per unit cell, and conclude that there is one US molecule per every two FL. The excess ratio of the NEXAFS signal from the FL molecules, i.e., 2.5:1 ratio instead of 2:1, might indicate that a portion of the surface is still covered with the (3×6) phase and the (6×8) phase is not yet fully saturated. Alternatively, a deviation from the 2:1 ratio could also be attributed to the possibility, that the US molecules are not perfectly perpendicular to the surface but are tilted at some angle close to $90°$.

As deduced from the sharp diffracted peaks in the HAS spectra, the (6×8) phase is also well ordered over large areas. In combination with the NEXAFS results we may conclude that the US pentacene molecules line up head-to-head along the $[1\bar{1}0]$ direction. Accordingly, we introduce a simple geometrical model of the unit cell[4] which is shown in fig. 5.31.

---

[3]The non-zero tilt of a single population of the molecules would cause a maximum of π^* peak intensity to occur at some different angle and can therefore be excluded.

[4]For the present model, when the beam is parallel to the $[1\bar{1}0]$ direction, the expected intensity of the σ^* signal at $\alpha = 90°$ is one half of the maximum value at $\alpha = 0°$. The reason for signal drop to zero (see right hand panel in fig. 5.30) can be addressed to the ill-conditioned fit in the high-energy part of the NEXAFS spectrum, where the overlap of π^* multi-electron step, vacuum level step and σ^* peaks occurs.
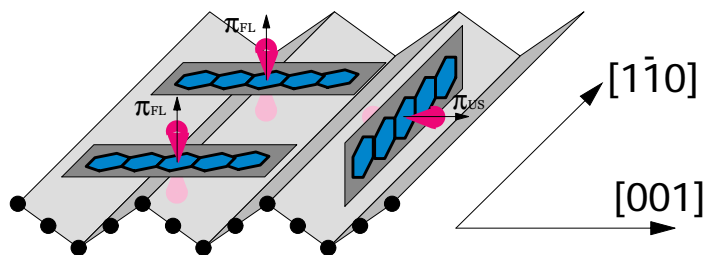
Figure 5.31: Geometrical model of differently oriented pentacene molecules in (6×8) phase. The directions of the π^* electronic system are denoted with arrows.

By inspecting the spectra in the right hand-panel of the fig. 5.29, one notices that the two π^* peaks are in fact much better resolved when $\alpha = 0°$ (note also the good resemblance of the spectrum at $\alpha = 0°$ with the gas-phase spectrum in fig. 5.18). At this azimuth angle of the incident beam, the signal of π^* resonances arises entirely from the US molecules. Well separated π^* peaks indicate that the molecular interaction with the substrate is relatively weaker, so the molecular states are accordingly less affected by the interaction with the substrate valence electrons.

Azimuthal scans with s-polarized X-rays have been also acquired on both, (3×6) and (6×8) structure, shown in fig. 5.32. The corresponding scan geometry is displayed in
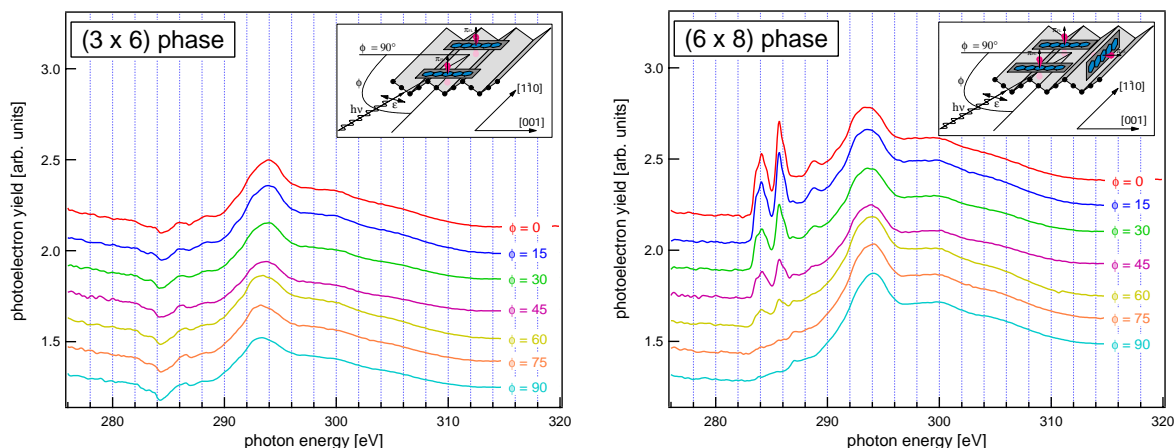
Figure 5.32: The NEXAFS spectra during azimuthal scan with s-polarized X-rays taken on (3×6) phase (left) and on (6×8) pentacene/Au(110) phase (right).

the figure insets. No azimuthal dependence of the π^* intensity can be seen in the left panel, referring to the (3×6) phase, again witnessing only flat-lying molecules to be present in this phase. A small σ^* peak intensity variation of $\approx 10\%$ at 293 eV most likely occurs due to the transition from $1s$ orbitals of the two s carbon atoms lying on high symmetry sites. Namely, this transition is forbidden when the X-ray polarization vector is parallel to the shorter molecular axis (when $\phi = 90°$). In the right panel, corresponding to the (6×8) phase, the dichroism of two well resolved π^* peaks is observed, evidencing very good azimuthal order of the US molecules with the π^* electronic system parallel to the surface and oriented along the [001] direction. There is a faint peak observed at

287 eV, which increases with growing azimuthal angle ϕ. The peak was clearly seen in the NEXAFS spectrum of the gas phase pentacene (see gray curve in fig. 5.18). Energetically it corresponds to the transition $C1s \rightarrow$ LUMO+2, which is of σ^* nature. Surprisingly, the resonance is not seen in the azimuthal scan of the (3×6) phase, which means that it originates from the US pentacene molecules. Apparently the LUMO+2 state of the FL molecules is hybridized much stronger with the substrate and is thus altered to a degree, where no dichroism is detected. This is another evidence of rather strong bonding of the FL molecules to the substrate.

In conclusion we observe that pentacene molecules form two different stable monolayer phases on the Au(110) substrate. The high-temperature equilibrium phase ($T > 470$ K) with (3×6) periodicity contains a single population of well-ordered molecules lying perfectly flat on the Au(110) substrate. Pentacene molecules are oriented with their longest axis along the [001] direction, whereas they line up side-by-side forming long chains along [$1\bar{1}0$] direction, as shown in the model in fig. 5.33, left. Relatively strong interaction with
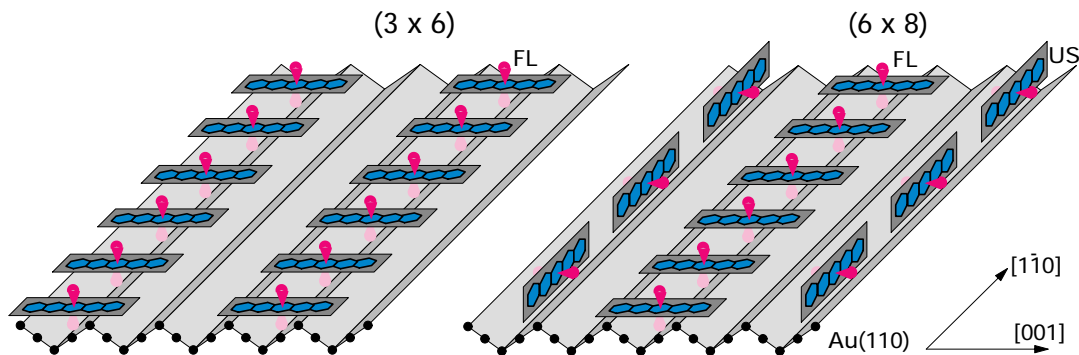
Figure 5.33: The model of the pentacene molecular chains along [$1\bar{1}0$] direction in the (3×6) phase (left) and the "nanorails" in the (6×8) phase.

the substrate occurs due to the overlap of the Au surface states with the π^* molecular electronic system, which consequently considerably hybridizes low-lying molecular states. At moderately lower temperature ($T \approx 420$ K), on the other hand, a stable (6×8) phase forms where three molecules per unit cell are observed with two different geometrical orientations. The chains, extending along the [$1\bar{1}0$] direction of the flat-lying side-by-side oriented pentacene molecules are preserved in the (6×8) phase, but their spacing increases. There is an additional population of the up-standing molecules arranged head-to-head along [$1\bar{1}0$] direction, forming "nanorails". We find 3 molecules per unit cell with 2 flat-lying and one up-standing. Well resolved non-hybridized π^* states are attributed to the up-standing molecules, which interact much weaker with the substrate than flat-lying, thus retaining their electronic states almost intact.

Recently, some preliminary scanning tunneling microscope (STM) images of both pentacene phases were acquired in collaboration with the SSR group [71]. As can be seen in fig. 5.34, the STM images are in good accordance with the presented models for the (3×6) and (6×8) phase. They clearly reveal that both phases contain same chains of side-by-side packed molecules along the [$1\bar{1}0$] direction. Interestingly, in the STM images, the (6×8) phase appears less dense than the (3×6) due to longer periodicity. However, faint STM signal is detected alongside the (6×8) flat-lying molecules evidencing
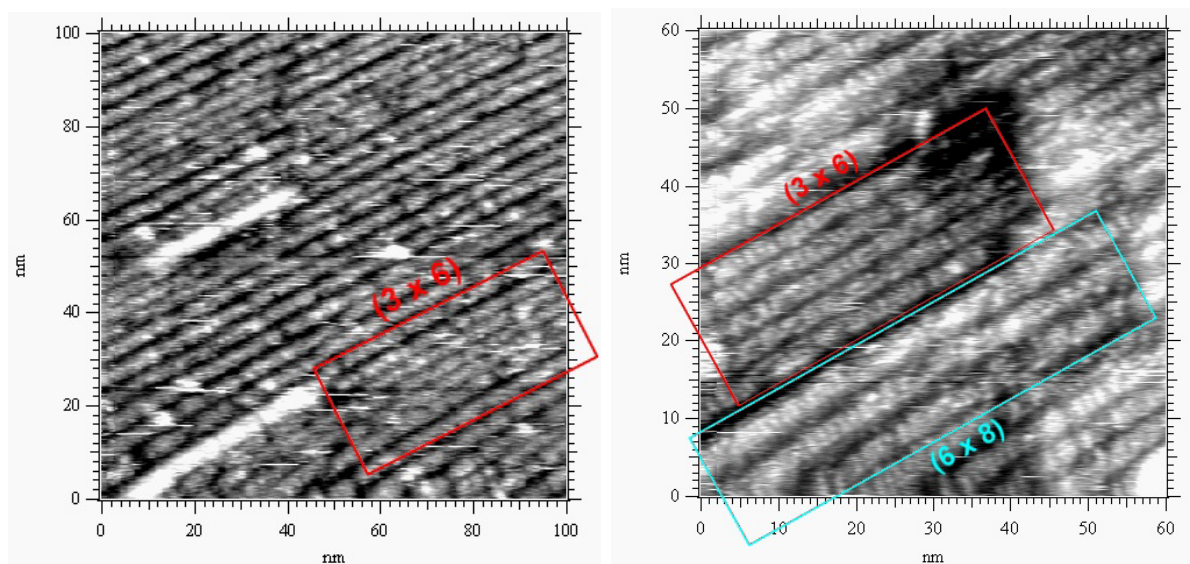
Figure 5.34: STM images of the (3×6) and (6×8) phase of pentacene/Au(110).

the presence of additional up-standing molecules aside. The detection of this molecules is hindered by the molecular vibrations and due to low electron density in the hydrogen orbitals at the molecular flank.

Chapter 6

CuPc/Au(110)

6.1 Introduction

The semiconducting properties and the high thermal and chemical stability of metal phthalocyanines (M-Pcs) has in recent years sponsored the emergence of several new technological applications. The M-Pcs have been successfully used in photovoltaic devices, photodetectors, organic transistors, organic electroluminescence devices and sensors [72]. The possibility of choosing the host metal atom gives a certain degree of freedom in tailoring the molecular properties, such as electronic structure (HOMO and LUMO orbitals), molecular spin in ground state etc. M-Pcs have been observed to grow and form two dimensional films on a number of ordered as well as amorphous substrates. In the low-coverage range, the orientation of the M-Pc molecules can be driven by a proper choice of a reactive substrate. When metal surfaces are considered, the delocalization of π-orbitals in the aromatic rings of M-Pc is expected to favor a flat-lying adsorption geometry. One expects the driving force for molecule adsorption on metals to be the maximization of the contact area with the substrate. In fact, a flat growth of the first organic layers was observed for a few M-Pcs on several metals, e.g., CuPc/Au(100) [74], CuPc/Au(111) [75], CuPc/Al(100) [76], SnPc/Ag(111) [77], NiPc/Cu(100) [78] and others. The orientation of the molecules was found to be affected by the surface roughness [79] and the adsorption at the step edges on Au(111) was demonstrated to effectively change the azimuthal orientation of CuPc molecules on narrow terraces. This indicates the possibility of exploiting highly corrugated crystal surfaces to drive the orientation of a growing overlayer on an otherwise poorly interacting substrate. The molecular orientation and the degree of crystalline order reached during deposition crucially determines the transport properties of thin organic films, so it is essential to obtain an accurate control over the relevant growth conditions.

6.1.1 CuPc molecule

Among the phthalocyanines, copper phthalocyanine (CuPc) has been the most studied compound because of its stability and extensive use in the dye industry. Thanks to its semiconducting properties, CuPc is commonly used as a hole injection layer in organic light emitting diodes (OLEDs). Among small-molecule-based photovoltaic devices, CuPc-cell was reported to have the highest power conversion efficiency of 3.6% [72].

CuPc molecule (shown in fig. 6.1) consists of conjugated aromatic macrocycles, i.e.,

four pyrrolic and four benzene rings, where the central copper atom is surrounded by four nitrogen atoms. It is a planar molecule with D_{4h} symmetry. The molecular "diameter"
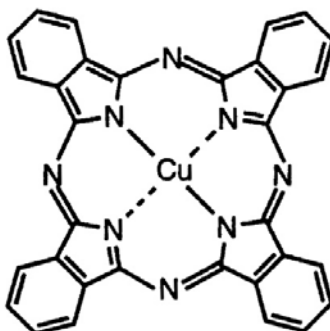
Figure 6.1: The molecule of copper phthalocyanine.

is approx. 13.8 Å with the copper-nitrogen distance of 1.98 Å [80]. High decomposition temperature 680 K [81] makes the material suitable for thermal vacuum deposition. For CuPc thin films, high mobility in the $0.01 - 0.02 \, cm^2/Vs$ range was achieved by employing elevated substrate temperature during deposition, which affected directly the morphology of the film [3].

In phthalocyanines, polymorphism is a common phenomenon. This is because the intermolecular forces between phthalocyanine molecules are relatively weak and a variety of molecular stacking arrangements of similar interaction energies are possible. It turned out that the variation of molecular stacking in the solid state has a profound influence on the electro- and photo-conductivity too. Five polymorphs, namely the α-, β-, γ-, δ- and ϵ-form of CuPc are known [82], all expressing optical dichroism. Whereas α-, γ-, δ- and ϵ-CuPc are metastable, the β-CuPc is thermodynamically stable polymorph and is obtained directly from synthesis or recrystallization from other metastable polymorphs. The stacking arrangements of CuPc molecules in the α- and β-polymorphs are depicted in fig. 6.2.
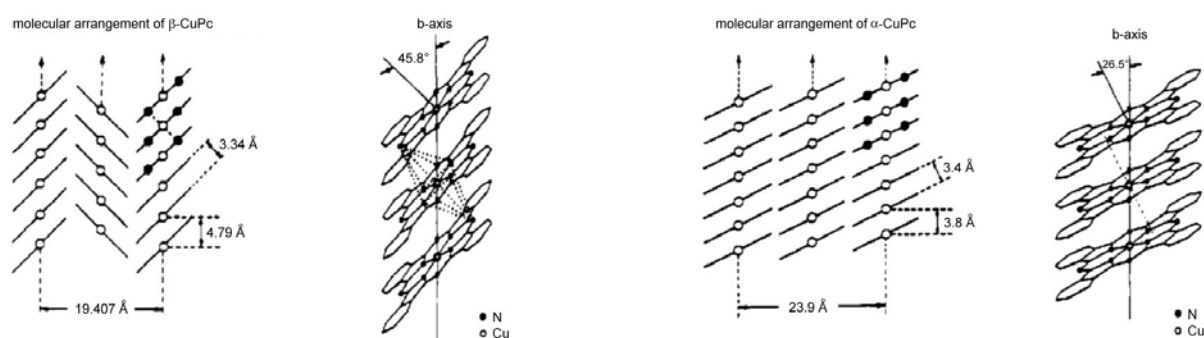
Figure 6.2: Polymorphism in CuPc: the stable β-phase crystallizes in herring-bone structure (left) whereas metastable α-phase exhibits simple planar stacking (right) [82].

The CuPc structure in thin films was in some cases observed to resemble the structure of bulk CuPc crystals. It was shown by X-ray diffraction analysis that the as-deposited

thin film of CuPc on Si/SiO$_2$ adopts the stable β-phase structure. The CuPc molecular planes are oriented edge on with respect to the substrate and the film is highly ordered [3]. In contrast, the deposition of CuPc on well ordered Cu(100) surface produces a crystalline film consisting of oriented crystallites with growth planes inclined to the substrate plane [83]. Moreover, the exposed growth plane does not correspond to a plane in the bulk crystal structures of CuPc. The role of particular substrate morphology on film growth was demonstrated by Peisert et al. [84]. While the CuPc molecules in the film generally stand up on polycrystallinic technical substrates, they supposedly lie flat on the single crystalline Au(110) surface. In the following sections, the CuPc molecular order and alignment on Au(110) is thoroughly studied.

6.2 Film structure determination by HAS and LEED

The structure and order of the CuPc monolayer phase has been addressed by simultaneous HAS and LEED diffraction experiments [73]. HAS intensity has been collected with a beam energy $E_{He} = 19.6$ meV, wavelength $\lambda_{He} = 1.02$ Å and energy resolution $\Delta E/E \approx 0.02$. LEED pattern has been acquired with the electron kinetic energy of 200 eV.

The HAS and LEED diffraction scans as a function of polar angle have been collected during CuPc deposition on Au(110) held at 340 K. The substrate surface has been azimuthally oriented with the [001] direction in the scattering plane (corresponding to ΓY direction in reciprocal space) to reveal the structural evolution of the system across the missing-row direction of the surface (for the Au(110) missing-row surface structure refer to sec. 5.1.2). The scans are shown in fig. 6.3 and 6.4, respectively.
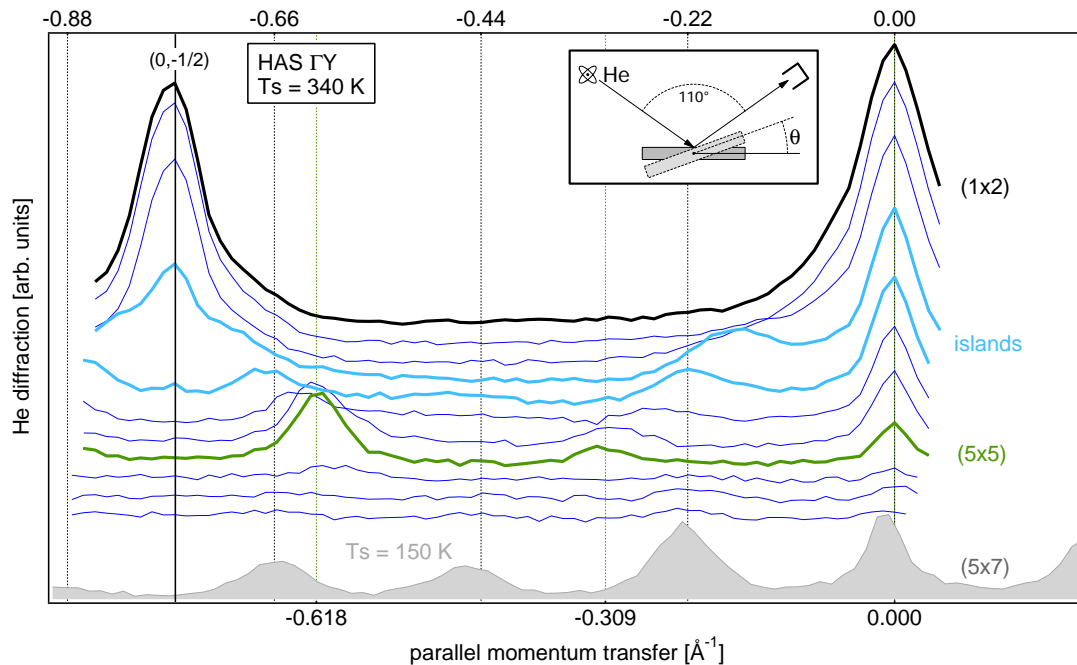
Figure 6.3: Consecutive HAS diffraction patterns acquired along surface ΓY direction during CuPc deposition on Au(110). The energy of the He atoms is 19.6 eV.
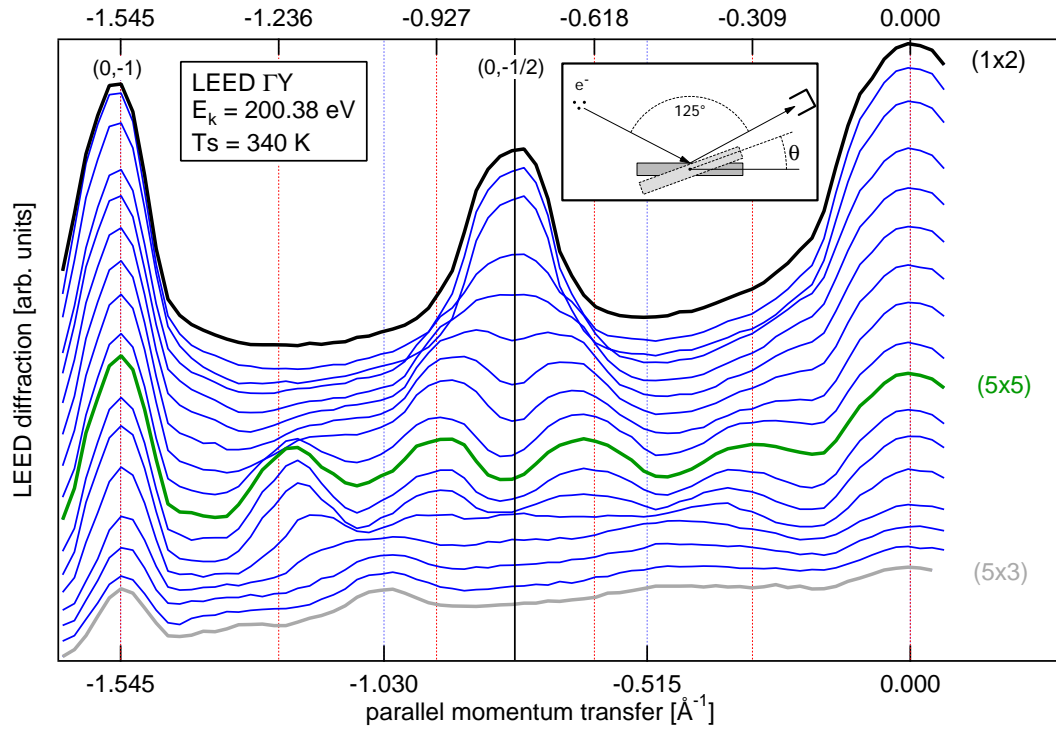
Figure 6.4: Consecutive LEED diffraction patterns acquired along surface ΓY direction during CuPc deposition on Au(110). The energy of electrons was 200 eV.

Both diffraction techniques probe the surface, yet the helium scattering is only sensitive to the outermost valence charge distribution and hence probes the topmost layer structure, whereas the low-energy electrons of 200 eV kinetic energy penetrate deeper inside the solid and effectively probe the Au substrate structure as well. The first scans in both figures have been taken on clean Au(110) substrate, exhibiting characteristic two-fold missing-row periodicity. The CuPc organic layer starts to grow from the second scan on. Initially, the clean Au surface displays well ordered terraces extending over 250 Å as judged from the widths of the integer and half-integer diffraction peaks at 1.54 Å^{-1} and 0.77 Å^{-1}, respectively. The deposition rate has been kept small, i.e., about 0.1 ML/scan to prevent the out-of-equilibrium evolution of the diffraction pattern within a single scan. In the initial deposition stage both, HAS and LEED diffraction scans display similar periodicity. The half-integer peak splits into two symmetrically displaced side peaks which upon further CuPc deposition gradually shift away from the half-integer position up to the 5-fold periodicity, showing up at close to 2/3 ML. The observed half-integer peak reduction and decomposition into a central narrow spike and two well pronounced satellites aside indicates the formation of terraces of opposite (i.e., antiphase) missing-row order of similar size and separation. On the (1×2) reconstructed Au(110) surface, the missing-row order becomes inverted by introduction of a pair of monoatomic steps along the [001] direction. The schematical model of the resulting terraced surface is shown in fig. 6.5. At the same time the specular peak develops a satellite peak at smaller values of exchanged parallel momentum, indicating the presence of a stepped surface. For present scattering geometry the specularly reflected He atoms ($\Delta k_{\perp} = 2k_{He} \cos 55° = 7.07$ Å^{-1}) from terraces separated by monoatomic steps ($h_{Au(110)} = 1.41$ Å) scatter in
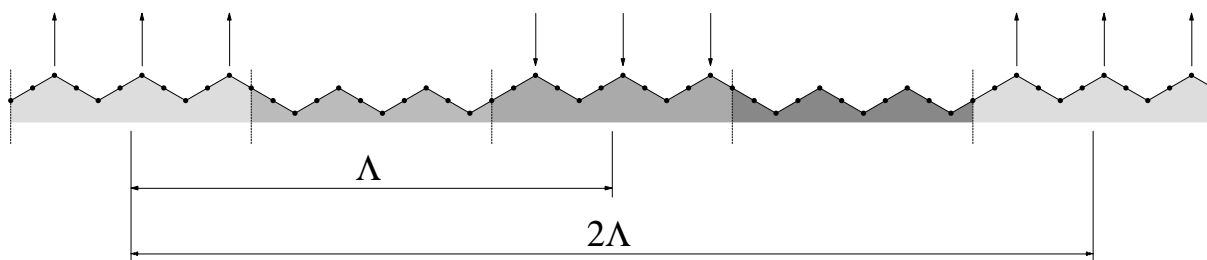
Figure 6.5: The schematical model of terrace formation upon introducing pairs of monoatomic steps on the Au(110) surface. The up- and down-directed arrows denote the missing-row and the anti-phase missing-row order.

nearly destructive interference ($\phi = \Delta k_\perp h_{Au(110)} \approx (2n + 1)\pi$), thus being very sensitive to the proliferation of the monoatomic steps. One may also note that the distance of the (1×2) satellite from the reciprocal lattice vector $G_{(1 \times 2)}$ is twice the distance of the specular satellite. This is expected for a surface with up-down correlated steps, since for specular peak the period equals to Λ, whereas for the (1×2) missing-row order a period is doubled to 2Λ (see fig. 6.5). Note that when the terraces upon increasing density of steps shrink to a minimum possible size, the surface results in the 5-fold periodicity.

From the profile evolution of the specular and the half-integer diffraction peak, we may conclude that CuPc molecules locally induce the proliferation of the monoatomic steps, which are spatially correlated and form flat terraces of unperturbed (1×2) missing row order separated by monoatomic steps. The (decreasing) size of the islands may be inferred from specular and half-integer peak satellites, which move away from the parent peaks and eventually reach the positions of the 5-fold reconstructed ordered phase. The density of monoatomic steps, measured by the satellite peak positions therefore scales with the increasing CuPc coverage and we may argue that along [001] direction there is an effective repulsive interaction among the induced Au steps which are decorated by the adsorbed CuPc molecules. Interestingly, both HAS and LEED show identical diffraction structures up to the (5×5) phase, indicating that the overlayer and the Au substrate share the same translational symmetry.

This phase has been previously identified by LEED [5] as a (5×5) structure where 5-fold periodicity along the $[1\bar{1}0]$ direction (corresponding to size of 14.4 Å) closely matches the lateral size of the CuPc molecule (13.8 Å). This indicates, that the organic molecules effectively line up into long chains along the $[1\bar{1}0]$ direction, where a significant inter-chain correlation is essential for the 2D 5-fold long-range order to be established.

Upon further CuPc deposition at room temperature, HAS and LEED data start to display significant differences. LEED pattern along the [100] direction ends up in a 3-fold phase, where a CuPc monolayer coverage is presumably reached. It is recognized as a saturation coverage, since it remains unchanged at higher coverages. On the other hand, beyond the (5×5) phase the HAS diffraction pattern shows no diffraction peaks in correspondence to the 3-fold periodicity seen by LEED. Moreover, the integer order peaks are extremely faint, indicating that surface is essentially disordered. A 7-fold overlayer periodicity is however observed at a slightly lower coverage and is only seen when the substrate is brought down to 150 K, because "soft" organic layer exhibits pronounced vibrations and high Debye-Waller attenuation of HAS signal.

During the morphology evolution all diffraction peaks surprisingly continue to show the narrow peak profiles along ΓX direction, evidencing a nearly one-dimensional character of proliferated defects (i.e., along the [1$\bar{1}$0] direction). The He diffraction patterns, evidencing 5-fold periodicity along the ΓX and the corresponding 7-fold periodicity along the ΓY direction are shown in fig. 6.6. The 5-fold periodicity along ΓX in fact shows up
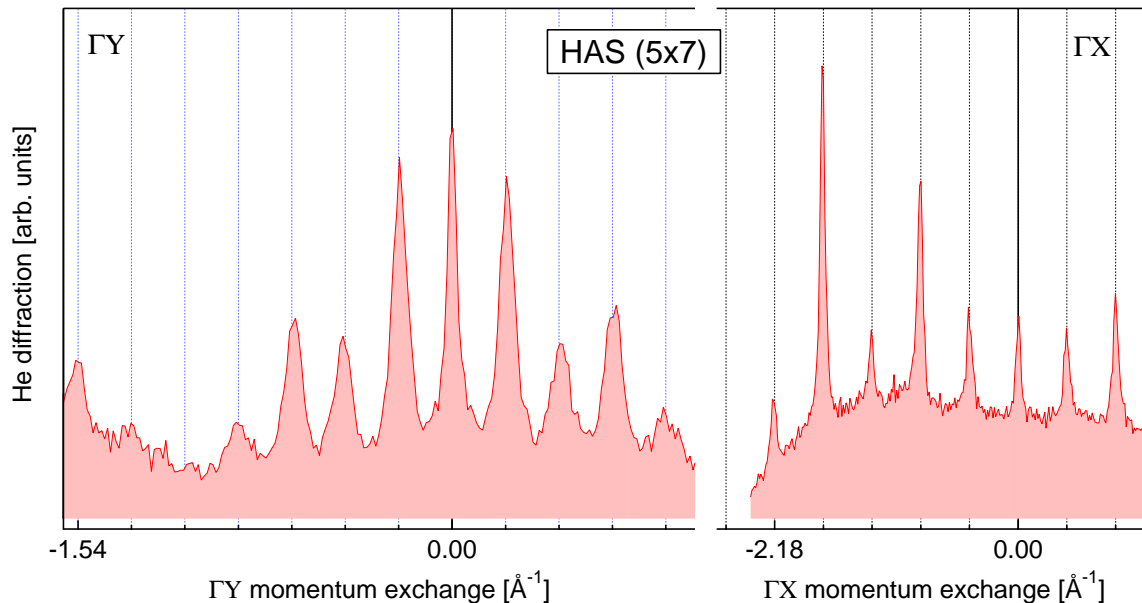

Figure 6.6: The He diffraction patterns of the (5×7) phase taken at low substrate temperature (150 K) along ΓY (left) and ΓX direction (right).

already in the submonolayer coverage, close to the formation of the (5×5) phase.

Considering the probing depth of each of the two diffraction techniques, i.e., HAS and LEED, we may conclude that the 7-fold periodicity observed by HAS reflects the overlayer structure, whereas the 3-fold periodicity of LEED pattern mainly arises from the Au substrate. By measuring the 7th order peak profile we observe that the mean domain size exceeds 120 Å.

6.3 XPS and NEXAFS study of CuPc film

XPS spectrum of the C $1s$ core level has been collected for a 3 Å CuPc film (as estimated from the quartz microbalance) which nominally corresponds to the coverage of one monolayer. The spectrum is shown in fig. 6.7. For this coverage the RHEED and GIXD yield a 3-fold periodicity along the [001] direction, which is in agreement with the LEED observation of a (5×3) phase by Evangelista et al. [5], and we can assume that the CuPc molecules are all in contact with the Au substrate. In this case we expect that any effect due to the molecule-substrate interaction should show up in the XPS spectra. The XPS spectrum presented in fig. 6.7 displays two main peaks, arising from chemically inequivalent carbon atoms in pyrrolic (labeled $C3$) and benzene rings ($C1$), as well as a shake-up satellite ($S3$) stemming from the HOMO-LUMO transition in the molecule [85, 86, 87]. A more detailed analysis reveals the presence of other two components,
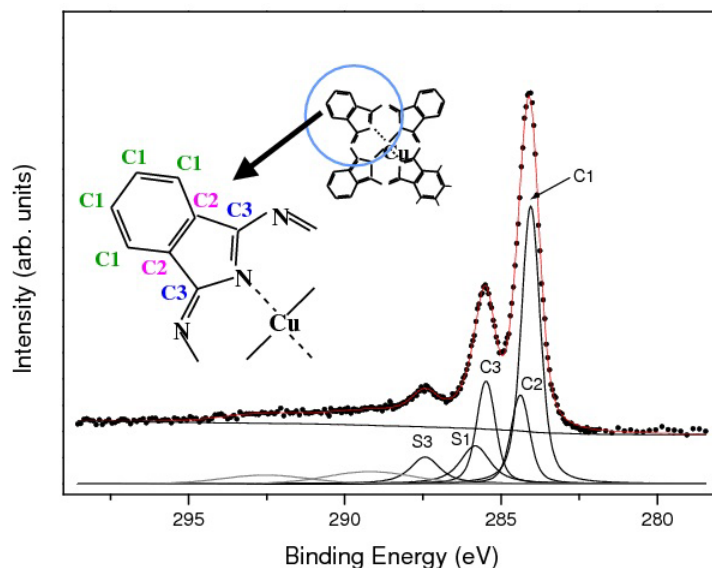
Figure 6.7: X-ray photoemission spectrum of the C $1s$ core level at the mono-layer CuPc coverage taken with the photon energy of $500\,eV$. Experimental points (markers) have been fit to multicomponent spectrum (full line). Different components belonging to chemically different C atoms within the CuPc molecule are also shown and denoted. Inset: the real-space model of the CuPc molecule with the central Cu atom surrounded by four nitrogens. Left hand side of the inset is a magnified quadrant of the CuPc molecule. The carbon atoms belonging to the benzene ($C1$) and pyrrolic ($C2$ and $C3$) ring are denoted.

labeled $S1$ and $C2$. The component $S1$ on the high binding energy side of the pyrrolic carbon $C3$ is recognized as the shake-up satellite of the benzene $C1$ atoms [88, 89, 90], whereas the highest binding energy shake-up satellite $S3$ originates from the pyrrolic $C3$ atoms. The fifth component $C2$ might be attributed to inequivalent carbon atoms in the benzene rings, but recent density-functional calculations for the similar PbPc molecule have shown that energy shift between the inequivalent benzene atoms is much smaller than the observed $C1 - C3$ splitting. The $C2$ component has been rather attributed to the vibrational coupling with the $C - H$ stretching mode [90].

In the present case, the observed spectrum is indeed quite similar to the photoemission structures observed for the bulk-like CuPc, so it seems that the substrate does not affect the molecular electronic structure in a dramatic way, thus suggesting only a weak interaction of CuPc molecules with the substrate, at least when compared to other substrates such as Al [91] or Si [87].

To gain information on the molecular orientation, the Cu $L_{2,3}$ X-ray absorption edge was investigated. The absorption spectrum is composed of a main line (commonly called white line) and some satellites as already observed experimentally on other substrates [78, 87] and recently calculated by a density-functional approach [92]. These calculations demonstrate that the white line corresponds to an atomic-like transition from the Cu $2p$ to an empty state, which is mainly of Cu $3d_{x^2-y^2}$ character and whose orbitals lie in the molecular plane. This transition is thus strongly enhanced when the radiation electric field vector lies in the molecular plane and absent when electric field vector is perpendicular to the molecular plane. The polar angular dependence of the L_3 white line has therefore

been used to determine the molecular orientation at the surface. The intensity of the L_3 white line as a function of the polar angle for a CuPc coverage corresponding to the monolayer phase is shown in fig. 6.8. Every point represents the integrated peak intensity
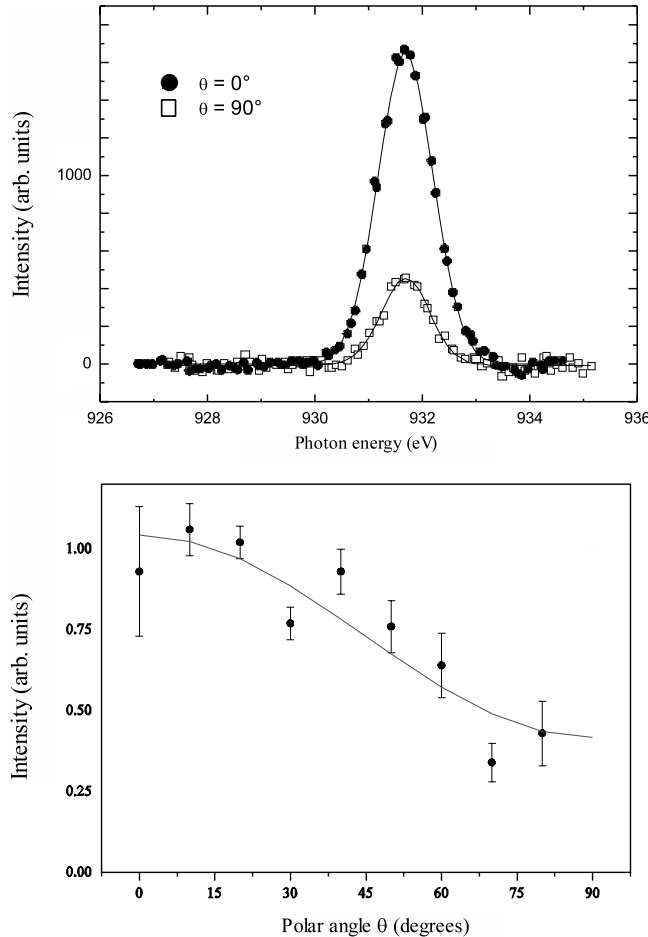
Figure 6.8: Normalized Cu L_3 X-ray absorption spectrum (NEXAFS) as a function of the photon energy taken for two different polar angles θ (upper panel). The integrated NEXAFS intensity (markers) as a function of θ for the monolayer (5×3) CuPc/Au(110) surface (lower panel). The best fit (full line) yields the molecular tilt angle from the surface to be $\gamma = 32° \pm 3°$.

after the normalization procedure, described in sec. 5.4. In the model used to interpret the data we also consider the incidence angle α of the light (which was kept fixed to $7°$) and the orientation of the molecules with respect to the [001] surface direction (the azimuthal angle ϕ). The overall normalized intensity, accounting for these contributions, can be written as

$$
\begin{aligned}
I_p &\propto 1 - |\mathbf{N} \cdot \boldsymbol{\epsilon}|^2 \\
&\propto 1 - |\sin\gamma\sin\phi\sin\alpha + \sin\gamma\cos\phi\cos\theta + \cos\gamma\sin\theta\cos\alpha|^2,
\end{aligned}
\tag{6.1}
$$

where $\mathbf{N}$ is a unit vector normal to the molecular plane and γ is the angle between the

molecular plane and the substrate surface. Here the 2-fold symmetry of the substrate must be taken into account; in particular, for the chosen reference frame, NEXAFS data have been collected for $\phi = \pm 90°$, so that the former expression becomes:

$$I_p \propto 1 - |\sin\gamma\sin\alpha + \cos\gamma\sin\theta\cos\alpha|^2. \tag{6.2}$$

In this equation only the amplitude and γ angle are free fitting parameters. The best fit to the experimental points, shown in the lower panel in fig. 6.8, yields the molecular tilt angle to be $\gamma = 32° \pm 3°$. Since the reconstructed Au surface effectively exposes (111) microfacets tilted by 35° to the (110) surface plane (geometrical consideration), the 32° molecular tilt indicates that CuPc molecules indeed favor adsorption parallel to the (111) surface, as reported for example by Fritz et al. [75]. The realization of a possible adsorption model is shown in fig. 6.9, left.
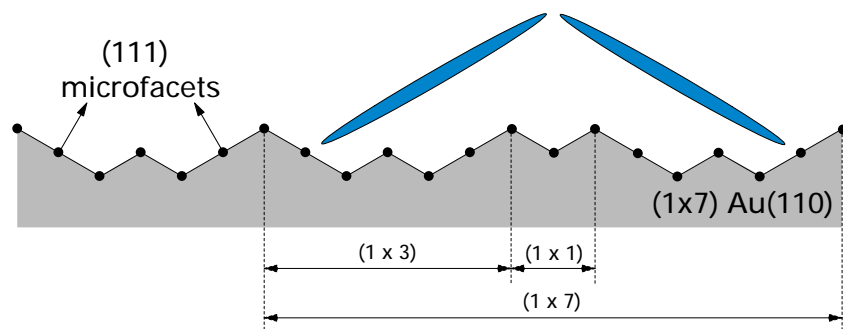

Figure 6.9: Schematical model of the CuPc possible adsorption geometry on the shallow-(3×1) reconstructed Au(110) substrate.

6.4 GIXD substrate structure analysis

The structure of the Au(110) substrate has been determined by a grazing incidence X-ray diffraction study of the monolayer CuPc phase. The GIXD measurements have been performed according to procedure, described in sec. 4.4.4. Fig. 6.10 shows the $(0, 5/3)$ in-plane reflection as a function of the parallel momentum transfer, expressed in units of $q_2 = \frac{2\pi}{a_2}$, where a_2 equals to the length of unit cell of the unreconstructed (1×1) Au(110) surface along the [001] direction (see sec. 5.1.2). The notation used for indicating the X-ray reflections is referred to the unit cell depicted in the inset of fig. 6.10. The inverse of the peak width yields a 170 Å spatial extension of the average domain with 3-fold symmetry along [001] direction, whereas the same analysis performed on the $(0, 3/2)$ reflection on a clean missing-row reconstructed Au surface yields an (1×2) domain size of 740 Å.

The real space structure of the (1×3) unit cell of the reconstructed Au substrate has been analysed by measuring the out-of-plane X-ray diffraction peaks. Six non-equivalent rod-scans (292 reflections in total) along the [010] direction have been acquired, both on bulk and reconstruction peaks. Fig. 6.11 shows the integrated diffraction peak intensities as a function of the vertical momentum transfer ("rod scans") and the corresponding best-fit calculated curves, obtained with the numerical "ROD" simulation program [93]. In this program the positions of the atoms within the unit cell are varied as fitting parameters. No overlayer molecules have been included in the numerical calculations and
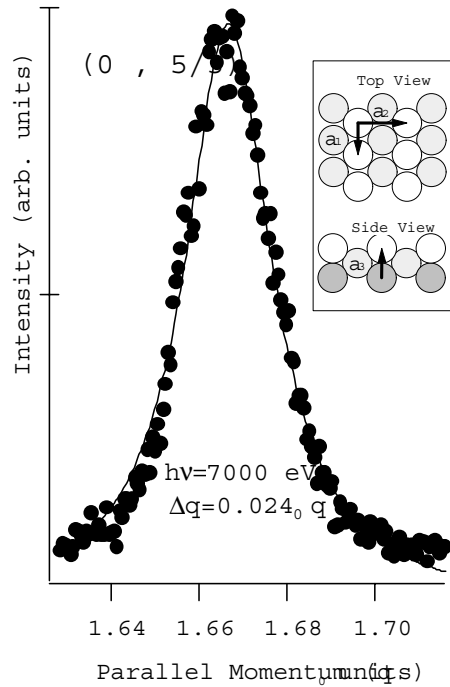
Figure 6.10: In-plane X-ray surface diffraction peak, characteristic of the (5×3) CuPc monolayer phase taken with the photon energy of 7000 eV (markers). The full line is a best fit Lorentzian curve, yielding a peak width $\Delta q = 0.024q_0$, where q_0 is the reciprocal lattice unit vector, corresponding to $(2\pi/a_2)$. The resulting 3-fold order correlation length exceeds 170 Å. Inset: Au(110) unreconstructed unit cell; a_1 and a_2 are the surface unit vectors of the unreconstructed surface along the $[1\bar{1}0]$ and [001] directions, respectively, and a_3 is twice the (110) interplanar distance. The vector lengths are $a_1 = a_3 = 2.88$ Å and $a_2 = 4.08$ Å.

only the position of the Au substrate atoms has been varied in the fitting procedure. This approximation is based on two evidences: first, as indicated by LEED and HAS, the 3-fold periodicity mainly arises from a substrate distortion, whose atoms have an atomic scattering factor much larger than that of the low Z atoms, which mainly constitute the CuPc molecules. Second, the absence of 3-fold periodicity in the HAS patterns along $[1\bar{1}0]$ direction (ΓY), which is only sensitive to the outermost surface charge density, implies a strongly disordered overlayer[1], i.e., no coherent contribution to the X-ray diffraction due to CuPc molecules is expected in the 3-fold pattern.

The best fit results are summarized in fig. 6.12 and tab. 6.1. Filled markers in fig. 6.12 indicate the "shallow" Au (1×3) reconstructed unit cell, where two $[1\bar{1}0]$ Au rows out of three along the [001] are missing. The other possible missing row 3-fold substrate reconstruction was also considered, where the central atomic row (number 3 in fig. 6.12) is also missing, exposing two (111) micro-facets within the unit cell. The $(0, 3)$ rodscan data and the simulations for the two types of unrelaxed (1×3) unit cells are reported in fig. 6.13. It is evident that the shallow cell reproduces the experimental data much better. Moreover the best fit parameters obtained for the "deep" (1×3) unit cell yield a poor quality fit, which also results in unphysical cell distortions.

---

[1]It can not be excluded that the lack of diffraction peaks in HAS pattern partly reflect also the Debye-Waller attenuation due to the RMS displacements of the organic molecules.
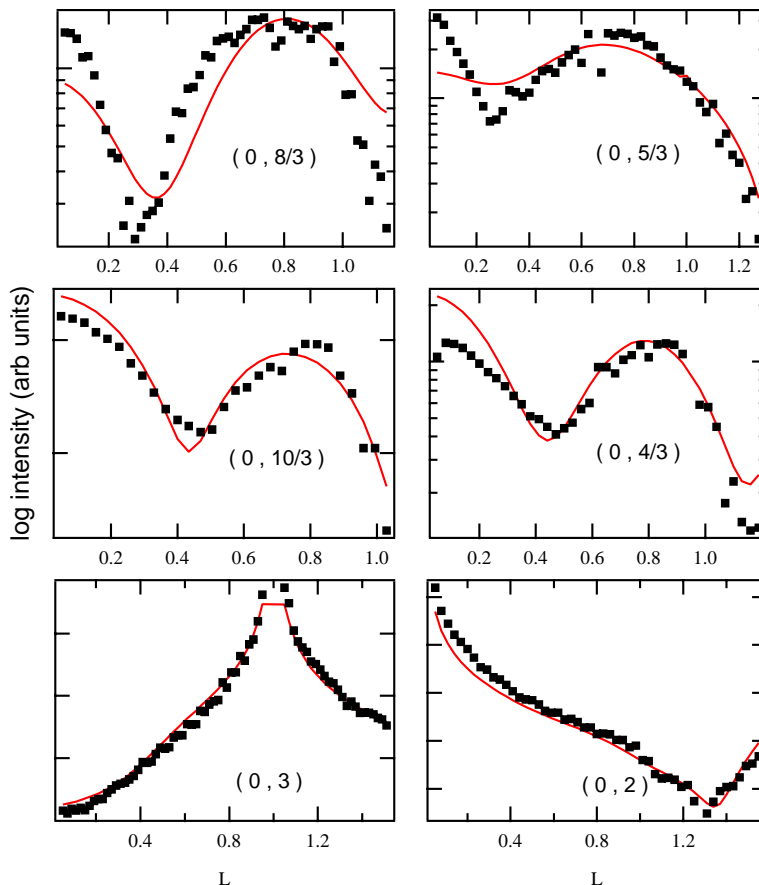
Figure 6.11: Six non-equivalent rod-scan analysis of the out of plane GIXD for the (5×3) CuPc structure. L denotes the perpendicular momentum transfer in units of $(2\pi/a_3)$. Each experimental point (markers) is obtained as an angle integrated intensity of a single diffraction peak at a given L. Full line is the best overall fit to the experimental data obtained with the "ROD" simulation program [93], by assuming the "shallow" Au(110) (1×3) reconstructed unit cell. The structural best fit parameters are given in tab. 6.1.

The displacements of the single atoms of the shallow (1×3) unit cell obtained from the best fit to all 6 non-equivalent X-ray rod scans are displayed in tab. 6.1. An asymmetrical relaxation of the substrate unit cell is required for the best fit. As a consequence, the fitting curve has been obtained by an incoherent sum of two 180° azimuthally rotated unit cells.

The shallow (1×3) unit cell may be viewed as a pair of up-down correlated monoatomic steps, containing a local (1×1) unit, whereas the deep (1×3) unit cell is a pair of up-down correlated steps made of (111) micro-facets [94]. The fact that the shallow (1×3) Au reconstruction is preferred in presence of CuPc molecules is quite interesting since, on a clean Au(110) surface, the deep (1×3) reconstruction is expected to be more favorable [95]. This hierarchy of the energy of Au(110) surface defects is experimentally confirmed, since (1×3) step type has been observed to dominate over the (1×1) type at the Au(110) roughening transition, which takes place by proliferation of monoatomic steps [96]. CuPc deposition on Au(111) has also been reported to favor molecular alignment along the pre-
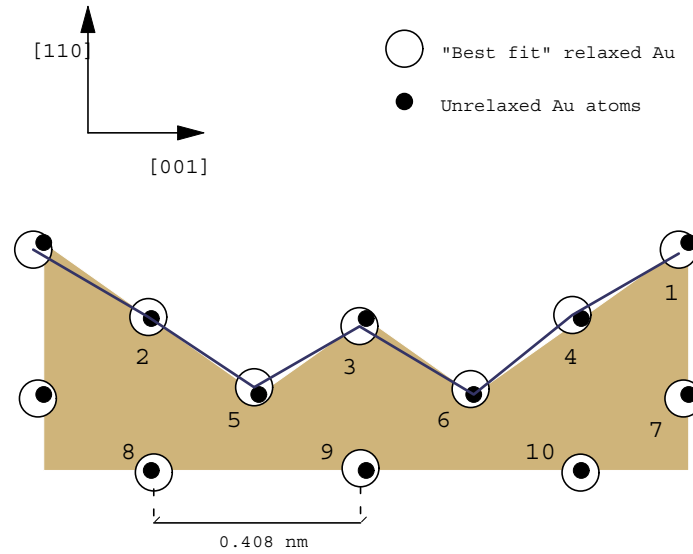
Figure 6.12: Schematic representation of the unrelaxed (filled markers) and best fit (open circles) atomic positions of he "shallow" Au(110) (1×3) reconstructed unit cell (in scale). The same atom indexing is used in tab. 6.1.

Atom index	In-plane displacement [Å]	Out of plane displacement [Å]
1	-0.19	-0.13
2	-0.06	0.03
3	-0.13	-0.14
4	-0.17	0.07
5	-0.09	0.13
6	-0.06	0.10
7	-0.10	-0.08
8	0.05	-0.04
9	-0.11	0.04
10	-0.01	-0.04

Table 6.1: Atomic displacements from the ideal bulk position of the Au atoms in the shallow (1×3) unit cell. Displacements are given with an accuracy of ± 0.03 Å. The atom indexes correspond to labeling in fig. 6.12.

existing monoatomic steps [97]. On the bare Au(110) surface monoatomic steps mainly extend along the $[1\bar{1}0]$ direction [96, 98] so it may not be surprising that CuPc molecules, not only align along the $[1\bar{1}0]$ direction, but also induce a particular substrate reconstruction in which the (1×3) unit cell is formed by an up-down correlated pair of monoatomic steps along $[1\bar{1}0]$.

The NEXAFS measurements at the Cu L_{23} edge as a function of polar and azimuthal orientation demonstrate that the CuPc molecules lie along the (1×3) Au(110) troughs, tilted by 32° from the surface. This finding is further consistent with the observed asymmetric relaxation of the Au(110) shallow (1×3) unit cell. In fact, in both NEXAFS
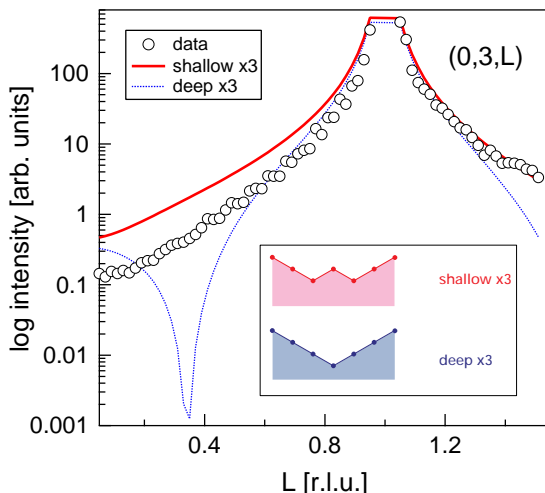
Figure 6.13: $(0,3)$ integer order rod scan of the (5×3) CuPc monolayer phase. The simulated intensity for both, the unrelaxed "shallow" (full line) and unrelaxed "deep" (dotted line) (1×3) reconstructions is shown for comparison. A sketch of the structure of the two models along the [001] direction is also shown.

and GIXD analysis an incoherent sum of the two equivalent molecular tilt angles, and substrate unit cell relaxations, produced the best fit to the experimental data.

We conclude the chapter by observing that in CuPc monolayer phase a "shallow" 3-fold reconstruction of the Au(110) surface takes place, where only three outermost layers of the substrate are involved. The geometrical relaxations of the Au atoms within the (1×3) unit cell have been also determined. Significant inward and sideward atomic displacements have been found with a broken reflection symmetry across the missing row, consistent with the fact that CuPc molecules lie tilted within the Au troughs. Indeed, polarization dependent NEXAFS measurements of the CuPc molecular orientation evidence that molecules lie with molecular plane along the $[1\bar{1}0]$ direction and are tilted by $32°$ from the surface (110) plane (see model in fig. 6.9, right). Although little evidence of molecule-substrate interaction could be observed in the XPS measurements of the carbon $1s$ core level spectrum, the type of induced (1×3) Au(110) substrate unit cell suggests a rather strong CuPc overlayer coupling to the substrate reconstruction. This finding is also in agreement with the formation of interface states in the system valence band, which was reported to show up at the early deposition stage of CuPc [5].

Chapter 7

PTCDA/Ge(001)

7.1 Introduction

The PTCDA crystal has one of the highest reported carrier mobility amongst organic semi-conductors, which exceeds $1\,cm^2/Vs$ along stacking direction in well ordered films [99], thus making this material a promising candidate in constructing the organic molecular based electronic devices. Due to PTCDA molecular symmetry, bulk crystals show high anisotropies in their physical properties, and the carrier mobility falls in the region of $10^{-5} - 10^{-4}\,cm^2/Vs$ in the direction perpendicular to the stacking direction [100]. The efficiency of carrier injection at the interface with the substrate highly depends on the orientation and geometry of the adsorbed molecules in the interface layer, as well as on their orientation and packing in the subsequent organic layers. Observations of PTCDA growth on noble metal surfaces, such as Au(111) [101], have shown strong temperature dependence of molecular ordering in the adlayer. The low-temperature adsorbed molecules form well ordered multilayers, where the interface layer grows in a preferred orientation with respect to the substrate due to the weak, but nevertheless significant interaction between the film and the substrate lattice. Moreover, strong temperature dependence of the charge carrier mobility in the PTCDA overlayer has been observed [7], indicating that growth morphology at various substrate temperatures might drive the film electronic properties, representing a challenge of highest interest for any technological application. The lack of experimental data in growth of PTCDA on semiconductors, especially germanium, is one of the motivations to study in detail the PTCDA films on Ge(001) surface.

7.1.1 The PTCDA molecule

PTCDA (3,4,9,10-perylene-tetracarboxylic-dianhydride, $C_{24}H_8O_6$) is a perylene derivative, obtained by attaching one anhydride functional group at each side of the perylene molecule, as shows fig. 7.1. The natural division of the molecule into the perylene core and the two anhydride functional groups turns out to be quite practical, especially when concerning with the spectroscopic observations of the C $1s$ and O $1s$ levels. Although the PTCDA molecule contains seven chemically inequivalent carbon atoms, usually only those from the perylene core and those from the anhydride groups will be taken into account. PTCDA is a planar organic molecule whose ionic dimensions are respectively $a = 6.79\,Å$ and $b = 11.47\,Å$ (fig. 7.2) and van der Waals radii of $9.2\,Å$ and $14.2\,Å$, respectively [102]. Due to the planar shape, it possesses pronounced π-conjugated electronic system, which
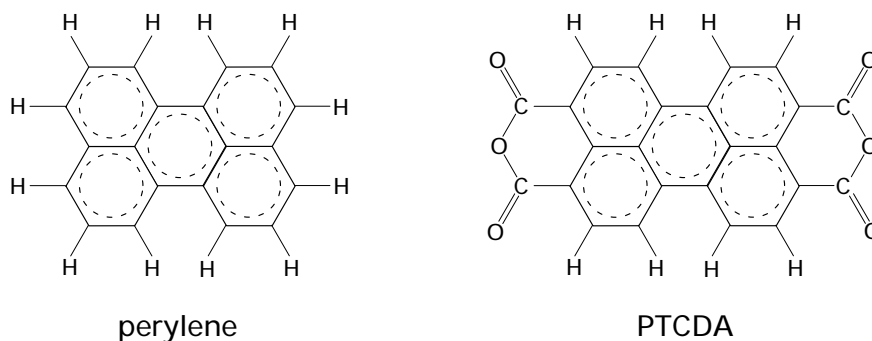
Figure 7.1: The perylene (left) and PTCDA molecule (right).
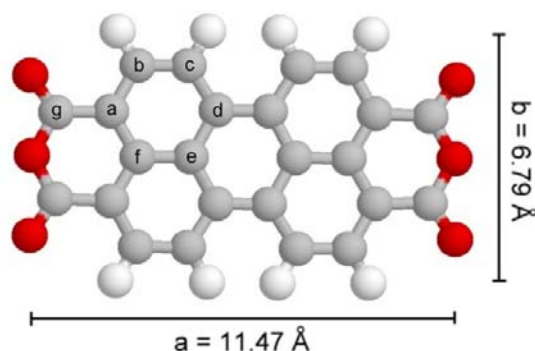
Figure 7.2: The PTCDA molecule and its ionic dimensions. Seven chemically inequivalent carbon atoms are labeled with letters from a to f.

extends out of the molecular plane, similarly as in the pentacene molecule (see fig. 5.4). The corresponding molecular orbitals are essentially localized on the perylene core of the molecule. Bulk PTCDA crystallizes in stacked (102) molecular sheets, each plane containing interlocking molecules in a herringbone structure stabilized by dispersive van der Waals forces and electrostatic interaction between molecular quadrupole moment. Two monoclinic polymorphs have been observed, which are referred to as α- and β-phase (fig 7.3). The in-plane unit cell contains 2 molecules almost perpendicular to each other, with the corresponding parameters $a = 3.74$ Å, $b = 11.96$ Å, $c = 17.34$ Å, $\beta = 98.8°$ for α- and $a = 3.87$ Å, $b = 19.30$ Å, $c = 10.77$ Å, $\beta = 83.6°$ for β-phase, respectively [103]. At RT the interlayer distance along the (102) direction is $d_\alpha = 3.22$ Å and $d_\beta = 3.25$ Å, respectively for the α- and β-phase [104]. The unique planar molecular stacking along the (102) direction in the bulk crystal structure indicates the presence of significant π-interactions between these layers which additionally stabilize thin films. The π-π orbital overlap is furthermore held responsible for high conductivity along the stacking direction [7].

It is known from photoemission and NEXAFS measurements that PTCDA molecules bond strongly on the reactive metallic (i.e. sp metals or d metals with partially filled d bands) or semiconductor surfaces. The molecules may simultaneously be bound in various orientations at sites where they impinge on the surface or may even partially dis-
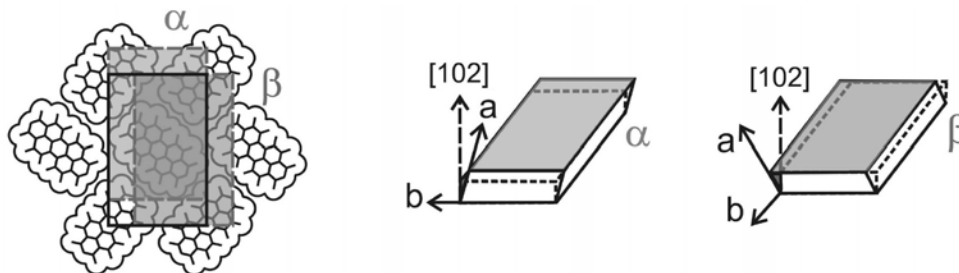
Figure 7.3: The herringbone structure of (102) PTCDA molecular sheet with the unit cell denoted by black rectangle. Two possibilities of unit cell stacking in the subsequent (102) layer are denoted by shaded rectangles and correspond to α- and β-phase, respectively.

sociate [105]. Due to high reactivity, the molecule frequently adsorbs with the anhydride group and no lateral order is usually found. On the other hand, on more inert substrates, such as Ag(111), large well ordered domains occur, since the molecules are highly mobile on this surface, thus being able to diffuse over large distances in order to form ordered overlayers. The molecular arrangement in the adlayer is similar to the one in the (102) plane of a PTCDA bulk crystal and the molecules adsorb in a flat-lying geometry, i.e., with molecular plane parallel to the surface. The hybrid orbitals form mainly between the molecular π-system and substrate orbitals, producing a covalent (chemisorptive) bond, with the highest occupied orbital (HOMO) and the lowest unoccupied π-orbital (LUMO) being most strongly involved.

7.1.2 The Ge(001) substrate

Most of the work on PTCDA films reported in literature is made on Si(111), Si(001) or on hydrogen passivated silicon. In the present work, the Ge(001) substrate was chosen which can easily be prepared clean in UHV and is expected to have similar electronic properties to those of silicon. The Ge(001) surface at room temperature is reconstructed to a lower symmetry so the substrate driven morphology is expected.

Germanium crystallizes in a diamond structure (fig. 7.4, left), which is equivalent to two f.c.c. lattices shifted along unit cell's diagonal by a quarter of its length. The (001) surface unit cell is shown in fig. 7.4, right, with its size equal to $a_s = a/\sqrt{2} = 4.00\,\text{Å}$ In equilibrium, Ge(001) surface is not a simple (001) bulk termination with the unsaturated bonds of the top most Ge atoms. Every atom appearing on the surface looses two nearest neighbours, leaving two reactive free bonds dangling out of the surface. The covalent bonding in semiconductors results in high tendency of binding of neighbouring atoms, making the unreconstructed and unrelaxed (001) surface rather unstable. The surface free energy is minimized by the configuration, which reduces the number of broken bonds per atom. In fact, adjacent atom pairing in dimers is one of the possible reconstructions by which the surface energy is lowered. The energy, involved in the formation of buckled dimers, is quite high, i.e., $\approx 1\,\text{eV}$ per bond [106]. The resulting doubling of the surface periodicity along the $[1\bar{1}0]$ direction caused by dimerization at RT leads to (2×1) surface reconstruction, as is sketched in fig. 7.5. It is important to note that (2×1) long range

103
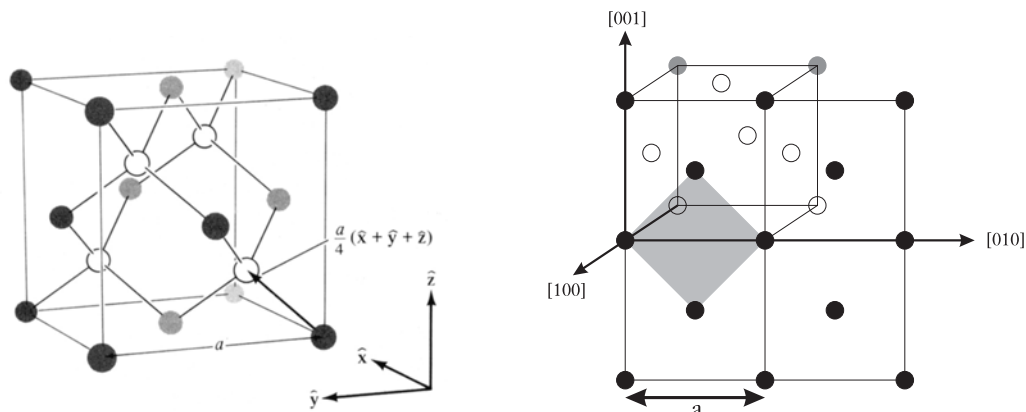
Figure 7.4: Diamond structure of Ge-crystal (left), lattice constant equals $a = 5.66\,\text{Å}$. The model of unreconstructed Ge(001) surface with dashed unit cell of size $a_s = 4.00\,\text{Å}$ (right).
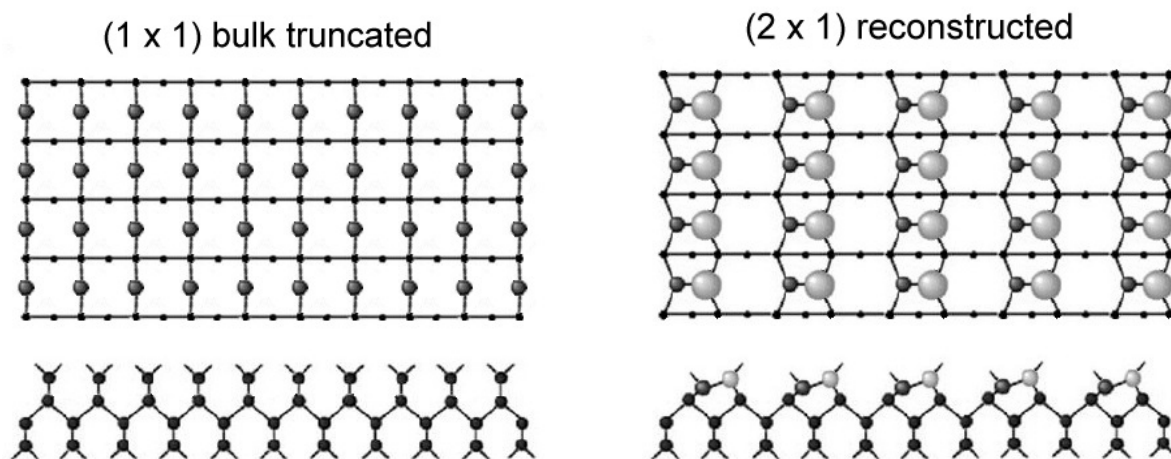
Figure 7.5: Top- and side-view illustrations of the unreconstructed Ge(001) (left) and (2×1) reconstructed phase, composed of buckled dimers (right).

order is established if the dimer formation is coherent. In fact, above $955\,\text{K}$ the dimer long range order breaks down and the order-disorder type phase transition occurs.

The equivalent rows in (2×1) periodicity structure at RT, that produce diffraction pattern with lowest exchanged momentum, are therefore spaced by $4.00\,\text{Å}$ and $8.00\,\text{Å}$, corresponding to $0.79\,\text{Å}^{-1}$ and $1.57\,\text{Å}^{-1}$ inverse lattice constants, respectively. Since the square symmetry, i.e., C_4 of the (001) surfaces implies that there exist two types of equivalent domains, rotated by 90° relative to each other, the resulting diffraction pattern is a simple superposition of the respective contributions, exhibiting peak at $1.57\,\text{Å}^{-1}$ along both mutually perpendicular surface directions.

At low temperature, i.e., below $220\,\text{K}$, an order-disorder type reversible phase transition to lower $c(4 \times 2)$ symmetry phase takes place. The resulting anti-ferromagnetic like structure, obtained by antisymmetrical pairing of the up-down neighbouring dimers,

lowers the energy for only $\approx 0.1\,\mathrm{eV}$ per atom [106]. Fig. 7.6 shows the realization of the surface with the corresponding 2D diffraction pattern. The two by 90° mutually rotated
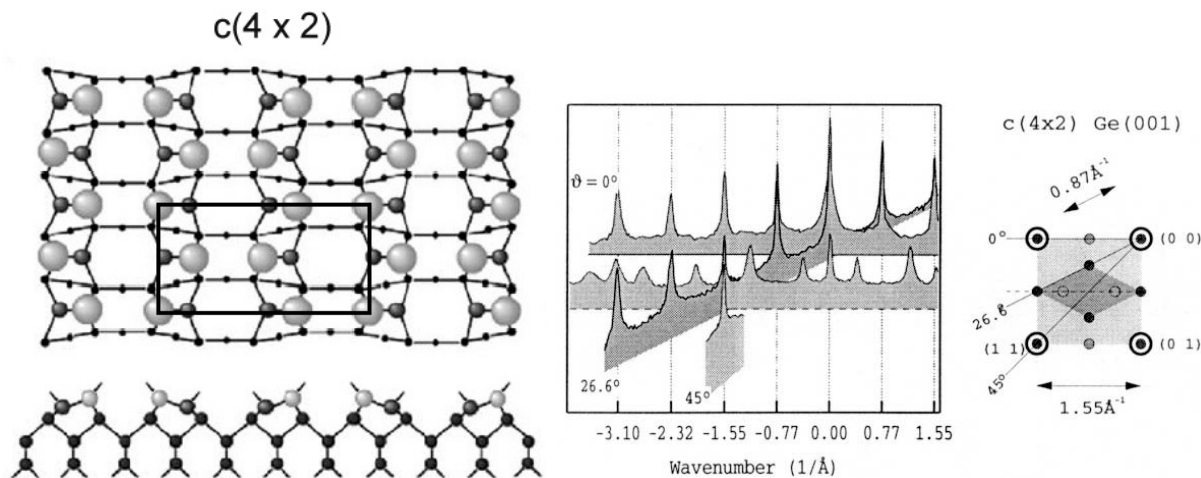
Figure 7.6: A top- and side view of the $c(4 \times 2)$ reconstructed surface with antiferromagnetically buckled Ge dimers (left) and the corresponding 2D HAS diffraction pattern (right). The surface unit cell is represented by the black rectangle.

domains result in the superposition of the $c(4 \times 2)$ and $c(2 \times 4)$ structures, producing a diffraction pattern along the principal surface axes equal to that of (2×2) reconstructed surface.

The reconstruction of Ge(001) surface further causes a significant core-level shift, which is nicely observed by XPS [107]. In the core level photoemission, the dimer-atom contribution from the surface atoms can be seen as a shoulder in the high-kinetic-energy side of the spectra, as shown in fig. 7.7. The spectra taken from the clean Ge(001) (2×1) reconstructed surface at RT are decomposed into same shaped components corresponding to $3d_{3/2}$ and $3d_{5/2}$ spin-orbit doublets. For the purposes in this thesis, the fitting of the photoemission spectrum is satisfactory with a bulk component and a single surface component[1] shifted by $0.49\,\mathrm{eV}$, as displayed in fig. 7.7. The strength of the surface component is very useful in determining the relative surface coverage with the adsorbate, which chemically bounds to the surface. The adsorbate effectively substitutes the subsequent layer of Ge atoms thus causing the surface components to alter or even disappear completely. This was in fact observed in the case of PTCDA adsorbate.

7.2 HAS characterization

The Ge (001) substrate was cleaned before each deposition by Ar^+ ion bombardment with the energy of ions varying from 0.5 to $3\,\mathrm{keV}$. The surface was subsequently thermally annealed by heating up to around $1000\,\mathrm{K}$. This way a well ordered surface was obtained

---

[1]In fact two surface components, shifted by $0.23\,\mathrm{eV}$ and $0.60\,\mathrm{eV}$ relative to the bulk one are present [107]. This convolution is fully consistent with the asymmetric-dimer reconstruction model of this surface, where the $S2$ (low BE) component is assigned to the up atoms and the $S1$ component to the down atoms.
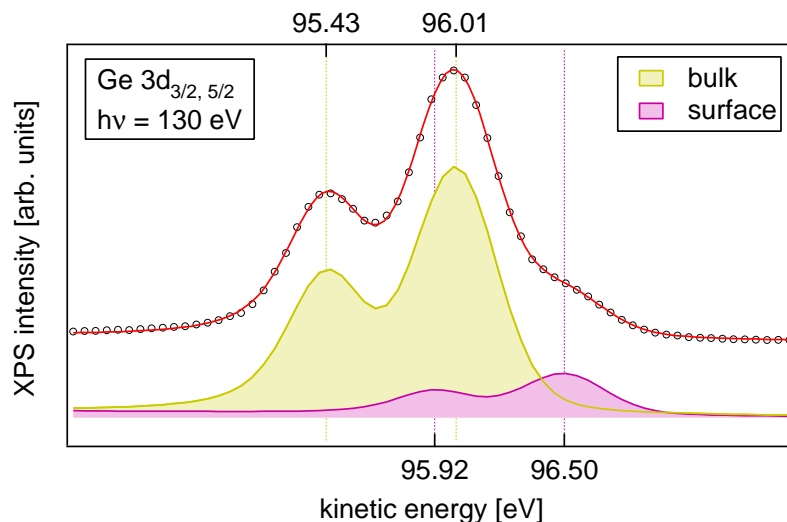
Figure 7.7: The XPS spectrum of clean (2×1) reconstructed Ge(001) surface at RT. The bulk and surface contributions represented by two shadowed doublets are displayed under the experimental XPS spectrum.

with the stepless domain size of approx. 1000 Å, as follows from the specular peak width according to eq. (4.8) in sec. 4.4.1. The PTCDA was evaporated from the laboratory-made Knudsen cell with power feedback controlled temperature and a mechanical shutter. The cell was heated to ≈ 670 K, which corresponds to a typical deposition rate of $\sim$ 0.1 ML/min.

The evolution of HAS surface reflectivity was observed by monitoring the intensity of the HAS specular peak during PTCDA deposition. The kinetic energy of He atoms was 19 meV and the wave vector $k = 6.3\,\text{Å}^{-1}$. Fig. 7.8 features HAS specular reflectivity evolution at various substrate temperatures, ranging from 170 to 450 K. The lowest curve in fig. 7.8 shows monotonic decrease of HAS specular intensity at 170 K (LT), which points to a gradual increase of disorder on the surface. The low substrate temperature and consequently reduced thermal energy does not allow for extensive molecule migration and thus limits the overlayer ordering. It appears that the randomly distributed molecules can adopt various adsorption geometries which further inhibits the formation of the long range order in the overlayer. With increasing PTCDA coverage, the molecules with non-uniform adsorption geometry act as large uncorrelated defects, making the coherent part of HAS intensity to disappear completely after ~ 300 s. The left over diffuse background originates almost exclusively from the diffuse scattering of He atoms. The specular intensity doesn't recover at any later deposition stage, indicating continuous disordered growth. Film order was further inspected by taking the angular HAS diffraction pattern after 30 minutes of PTCDA deposition. It is represented by the black curve in fig. 7.9, left.

The presence of strong inelastic background and the absence of any diffraction peak makes clear that the LT deposited PTCDA overlayer doesn't exhibit any long range order. The order is not established even upon consecutive flashing (fig. 7.9, left), indicating that LT grown PTCDA overlayer remains stable even when heating to RT.

When depositing on the substrate at temperature of 350 K and higher, the initial
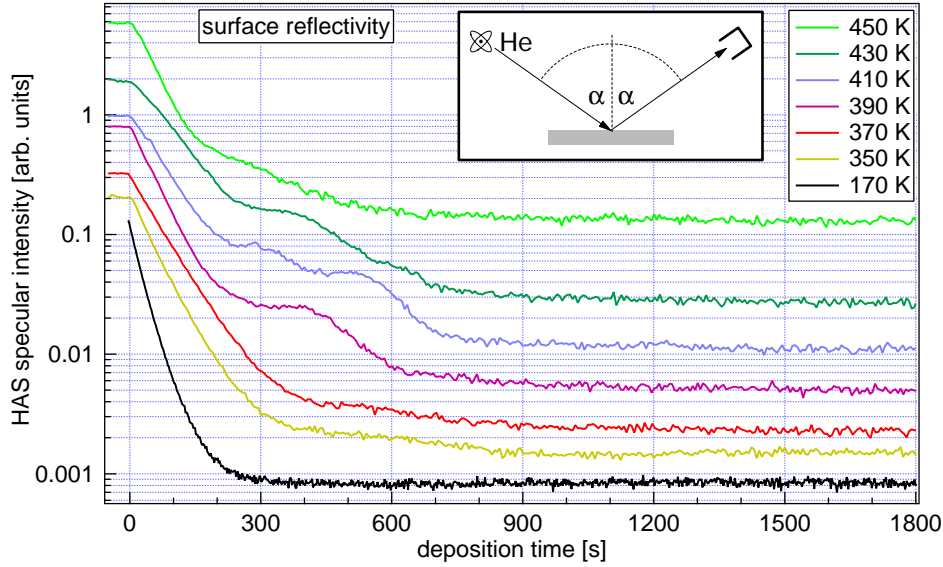
Figure 7.8: The surface reflectivity for He atoms during deposition of PTCDA at different substrate temperatures.
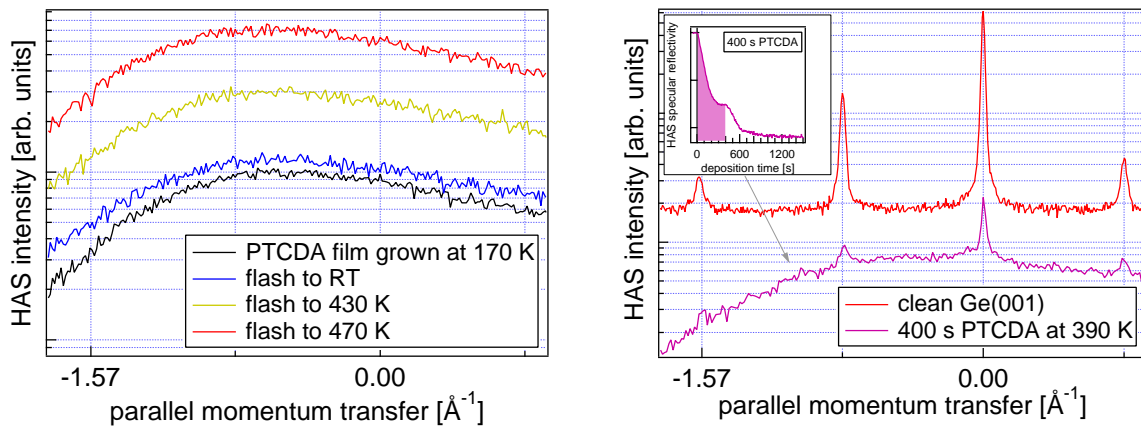
Figure 7.9: HAS diffraction pattern along [001] direction after 30 minutes of PTCDA deposition at 170 K and after consecutive flashes (left). Diffraction pattern of clean Ge substrate and after 400 s of PTCDA deposition at 390 K (right).

HAS specular intensity decreases similarly as at LT, whereas close to the completion of the monolayer, the decrease slows down or even stops, indicating a significant ordering of the organic film. In fact in the $350 - 430\,\text{K}$ region, a rather pronounced shoulder appears in the HAS specular intensity after 400 s of deposition, indicating that substantial ordering of PTCDA molecules takes place. The shoulder intensity depends on the substrate temperature and so does the degree of ordering. HAS diffraction pattern, acquired at the deposition stage where the shoulder occurs in the 390 K spectrum (after 400 s of deposition), still shows a weak Ge(001) diffraction pattern but with quite narrow peaks.

This fact evidences that a part of Ge substrate is still uncovered and its long range order correlation is preserved regardless of the presence of the organic overlayer. A possible interpretation is that the randomly deposited PTCDA molecules can migrate over the surface and order into three-dimensional (3D) aggregates, leaving partly uncovered regions of Ge in between. Nevertheless, upon further deposition the Ge substrate is eventually fully covered also for higher substrate temperatures and in the organic overlayer no ordered structure is built up.

We may conclude HAS analysis by finding that PTCDA film growth at LT is quite uniform since it is kinetically limited in reaching the RT morphology, which consists of large uncorrelated 3D PTCDA islands and poorly covered intermediate regions. The LT growth produces amorphous film with no long range order present.

7.3 XPS analysis

Further spectroscopical analysis of the PTCDA thin films facilitates a closer insight into the growth mechanism. The XPS spectra of the O $1s$ signal were collected in real time during PTCDA deposition on the Ge substrate held at $190\,\mathrm{K}$, shown in fig. 7.10, left. The X-rays at $650\,\mathrm{eV}$ were incident grazingly at $84°$, thus stronger illuminating the region
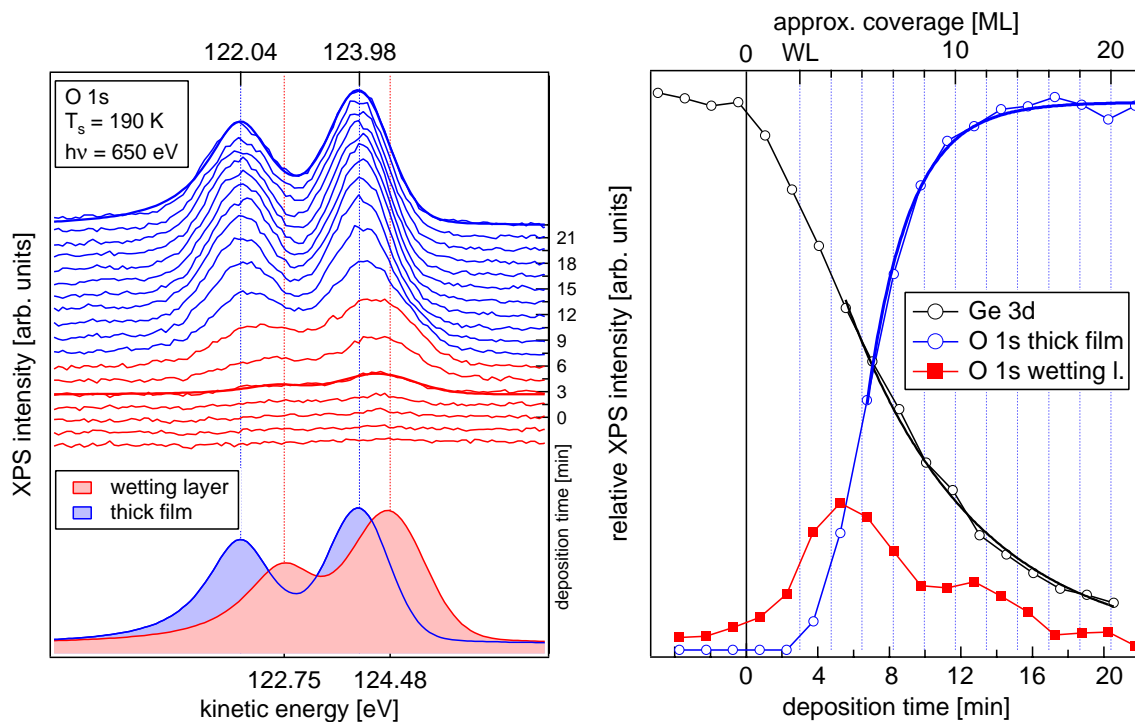
Figure 7.10: Evolution of the two O $1s$ components during LT PTCDA deposition (left). Relative XPS intensity of Ge $3d$, O $1s$ wetting layer and O $1s$ thick film component (right).

close to the surface due to total reflection condition. The photoelectrons were collected at $29°$ from the sample normal. The overall intensity increases with the PTCDA coverage and eventually saturates when the film thickness exceeds the inelastic mean free path for

the electrons at $\sim 120\,\text{eV}$. The topmost spectrum may thus be regarded as the saturation photoemission spectrum of the thick PTCDA film. The two components correspond to the two chemically inequivalent oxygen sites within the PTCDA molecule (see fig. 7.2). The actual 1:2 stoichiometric intensity ratio is well resembled by fitting the two resonances with a doublet of Voigt peaks. An energy shift of the two oxygen components can be noticed in the initial stages of deposition, pointing to a rather strong molecule-substrate interaction. The oxygen peaks start to show up at the kinetic energies of $122.75\,\text{eV}$ and $124.48\,\text{eV}$, and then gradually shift towards lower binding energy by $0.5\,\text{eV}$ and $0.7\,\text{eV}$, respectively. At the beginning of the deposition, the signal arises from the interface layer of PTCDA, which covers the Ge surface – wetting layer. The XPS spectra where the wetting layer doublet dominates the bulk one are for the sake of clarity of different colour. All spectra in the deposition sequence were fitted by two doublets with locked energy position (shown at the bottom of fig. 7.10), while leaving the ratio between the two contributions as a free fit parameter. Results of the oxygen fit as well as the intensity of the substrate Ge $3d$ XPS resonance are summarized in the fig. 7.10, right. The wetting-layer signal reaches its maximum intensity after 5 minutes of deposition. This coincides well with the time, at which the HAS coherent signal disappears (see fig. 7.8, black curve), indicating a completion of the wetting layer. The thick film O $1s$ component, however, grows continuously until it reaches its saturation level after approximately 16 minutes. The saturation occurs because the film thickness exceeds the mean free path of the O $1s$ photoelectrons.

The wetting layer thickness and PTCDA coverage can be deduced from the intensity of the WL and thick film O $1s$ signal as well as from the attenuation of the Ge $3d$ signal. We first observe the attenuation of Ge $3d$ photoemission peak (black curve in the right panel in fig. 7.10). Due to high energy of X-rays ($h\nu = 650\,\text{eV}$), one can assume that the substrate is uniformly illuminated deep into the bulk region and that the photon flux attenuation because of deposited PTCDA film is negligible. The energy of photoelectrons is $h\nu - E_{\text{Ge}3d} \approx 650\,\text{eV} - 30\,\text{eV} = 620\,\text{eV}$ and the corresponding inelastic mean free path (IMFP), obtained from the IMFP Grapher [108], equals $\lambda_{620\,\text{eV}} = 26.7\,\text{Å}$. For the density of the overlayer, the PTCDA bulk value was taken, $\rho = 1.7\,\text{g/cm}^3$ [109], [99]. The fit of Ge $3d$ intensity with the function $I = I_0 \cdot e^{-d/\lambda}$ yields the mean growth rate value of $R \approx 3.7\,\text{Å/min} = 1.15\,\text{ML/min}$, where bulk value of interlayer distance $d = 3.22\,\text{Å}$ was considered and ML corresponds to the PTCDA bulk monolayer along the stacking direction.

Next we try to estimate the WL thickness from a simple model, where the substrate is completely covered with 1 area unit of wetting layer. Yet before its completion, the second layer starts to fill, reaching X area units after certain deposition time, as shown in fig. 7.11. The signal, originating from the wetting layer is proportional to the exposed area $(1 - X)$ and the area X, which is attenuated by the subsequent layer of thickness h as follows:

$$I_{surf} = (1 - X) + X \cdot e^{-h/\lambda}. \tag{7.1}$$

The thickness h of the overgrown layer is here assumed to be equal to wetting layer thickness. The result, in fact, doesn't change up to the first order, if the subsequent layer was n-times thinner and had n-times larger area. For example, if PTCDA molecules in a single layer were lying flat instead of standing up, this ratio would be approximately 4. The signal of the overgrown layer is further simply proportional to X. By dividing
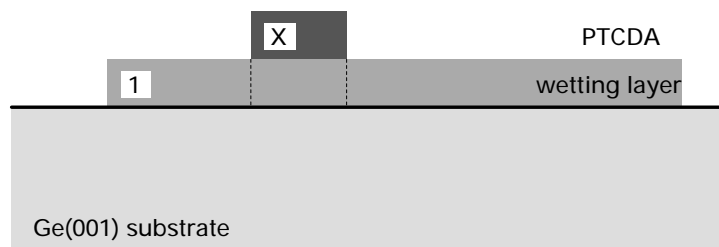
Figure 7.11: Model of covering Ge substrate with wetting and subsequent layer.

eq. (7.1) with $I_{thick} = X$ we get

$$X = \frac{1}{1 + I_{surf}/I_{thick} - e^{-h/\lambda}}. \tag{7.2}$$

Since the thickness of the overgrown layer and the amount of material in the WL are correlated, the equation is solved by iteration. For the thickness of the overgrown layer we initially take the bulk interlayer distance $h = d = 3.22\,\text{Å}$. The value of IMFP for O 1s photoelectrons with energy $650\,\text{eV} - 543\,\text{eV} = 107\,\text{eV}$ is again obtained from the IMFP grapher and equals $\lambda_{107\,\text{eV}} = 11.1\,\text{Å}$. After depositing 5.5 minutes, where both intensities are equal (fig. 7.10, right), we get the first iteration value of X to be 0.80. The actual amount of deposited material is then $1 + 0.80 = 1.8\,\text{WL}$ and the amount needed to complete (only) wetting layer is deposited in $5.5/1.8 \approx 3$ minutes. Comparing this result with the rate value, determined from the attenuation of the Ge 3d signal, we estimate the thickness of the wetting layer to be $11.3\,\text{Å}$. After repeating the iteration four times we may eventually summarize:

$$\left.\begin{array}{l} d(1\,\text{WL}) = 12.8\,\text{Å} \\ d(1\,\text{ML}) = 3.2\,\text{Å} \end{array}\right\} \quad 1\,\text{WL} = 4\,\text{ML}.$$

Interestingly, this value is close to the thickness of a monolayer, consistent of randomly oriented PTCDA molecules. The average of the cosine over the entire polar angle θ yields $\bar{h} = \overline{\cos\theta}|_0^{\pi/2} = \pi/4 \approx 0.79$. Taking the van der Waals length of the PTCDA molecule multiplied by this value we get $11.2\,\text{Å}$, suggesting that the PTCDA molecules are indeed randomly oriented in the wetting layer. According to the wetting layer thickness an upper scale was added aposteriori to the right hand graph in fig. 7.10 as a guideline, illustrating the approximate coverage in the bulk monolayers.

For comparison with the value obtained from the Ge signal attenuation, the deposition rate was also determined from the O 1s thick film signal alone. The amount which contributes to the signal intensity is (at LT) ever growing, but eventually starts to screen its own photoelectron yield when the thickness exceeds the IMFP of electrons. For this reason the fitting of the curve is carried out with the function $I = I_0(1 - e^{d/\lambda})$, yielding slightly higher rate of $R \approx 1.46\,\text{ML/min}$.

The XPS pattern of C 1s level was acquired at high PTCDA coverage on the substrate at 160 K (LT) and 300 K (RT) and is shown on fig. 7.12. The major peak at binding energy 284.84 eV is observed and is assigned to the perylene core carbon atoms. Smaller peak at higher binding energy of 288.59 eV further corresponds to the carbons in anhydride

groups, reflecting approximately the stoichiometric ratio 5:1. For the RT spectrum a shift of 0.2 eV towards lower binding energies is observed indicating molecular interaction with the substrate and / or different molecular orientation. The interface layer C 1s core level shift is smaller than that of O 1s, suggesting that oxygen levels are more strongly involved in binding to the substrate, possibly reflecting the tilted geometry of the adsorbed molecules.
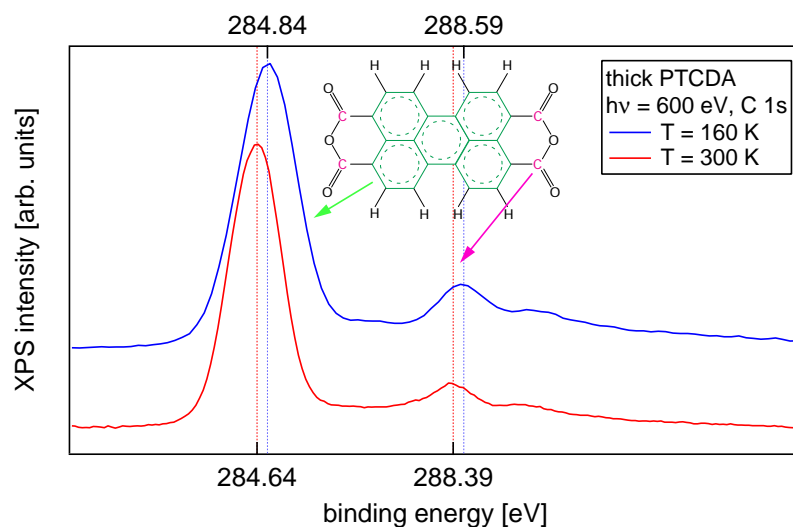
Figure 7.12: XPS spectrum of C 1s for high PTCDA coverage at LT (blue curve) and RT (red curve). Surface sensitivity was enhanced by grazing incidence of X-rays, $\theta = 7°$

.

The evolution of the O 1s signal was also measured for the growth at various substrate temperatures. Different growth morphology can be inferred from the correspondence of the XPS intensity and the HAS specular reflectivity, shown in fig. 7.13. Lower graph shows the integrated O 1s photoemission intensity during PTCDA deposition for three different substrate temperatures. For the deposition at 300 K (RT), the Ge 3d surface signal, normalized to the bulk Ge 3d component is also displayed (see page 105). In the upper panel there are the corresponding specular HAS intensities, plotted on the same time scale as the underlying XPS spectra. For the LT deposition the O 1s signal increases continuously without clear saturation indicating the uniform film growth.

For the substrate held at 300 K (RT), the O 1s intensity increases more slowly and saturates after ≈ 800 s, yet at the significantly lower value, indicating that part of the PTCDA molecules have aggregated into large 3D islands. The drop of relative Ge 3d surface signal, which arises from the dimer atoms in the (2 × 1) reconstructed surface and is proportional to the part of the unaffected surface, coincides closely with the loss of coherent HAS intensity (annotated by the black arrow), evidencing the completion of the wetting layer. The loss of the signal originating from the (2 × 1) reconstructed surface further indicates that the dimers become significantly altered (or even opened) which points to a rather strong interaction with the PTCDA film. The surface signal was obtained by fitting the Ge 3$d_{3/2}$ and 3$d_{5/2}$ doublet with bulk and surface contribution, shown in fig. 7.7. To cancel out the increasing attenuation due to the growing film, the
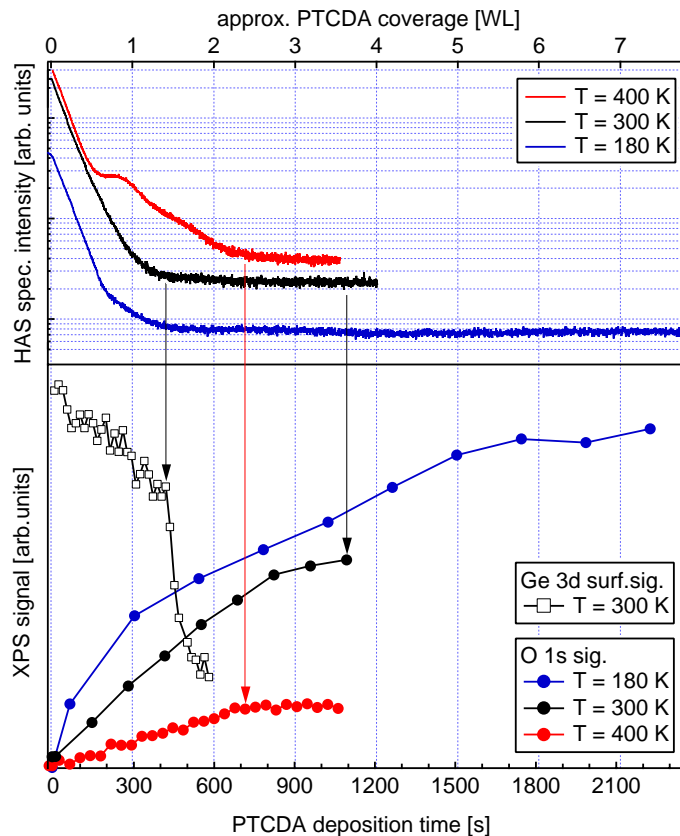
Figure 7.13: The intensity of O 1*s* and surface Ge 3*d* signal with the corresponding HAS specular reflectivity during PTCDA deposition. The left black arrow points out the coincidence of Ge 3*d* surface signal drop with the saturation of HAS signal. The other two arrows indicate the inflection point where the O 1*s* intensities saturate and the passage to invariant film morphology takes place.

surface intensity was normalized to the bulk Ge 3*d* signal.

The effect of 3D aggregation is even more evident for the high temperature deposition (HT), where the substrate was maintained at 400 K. The PTCDA deposition rate was equal at all substrate temperatures, which enables to compare the saturation times and the slope of the O 1*s* XPS intensity growth. At HT, the O 1*s* signal grows even slower and saturates already after ~ 700 s. The saturation intensity is even lower than at RT, indicating that no more than a single wetting layer effectively covers the substrate. The photoemission and HAS saturation occur simultaneously, showing that formation of large 3D islands sets-in right after the completion of the wetting layer.

We conclude the XPS analysis by observing that during PTCDA deposition the wetting layer is formed on Ge(001) surface, with the thickness equivalent to about 4 PTCDA bulk monolayers. At LT the uniform thick film growth takes place, whereas at RT and higher temperatures the coverage saturates with the completion of the single (wetting) layer. Additionally deposited molecules aggregate into large 3D islands and don't form any subsequent layer.

7.4 Valence band study with UPS

We next focus on the VB analysis of the PTCDA/Ge(001) film. UPS spectra were acquired with a single channel 150 mm hemispherical analyser where the electron pass energy (E_p) was chosen to match the approximate natural width of the Fermi step $(\sim 4k_BT)$. The experimental resolution of photoelectron detection, which equals $0.5\% E_p$, was ≈ 70 meV. Helium discharge lamp with non-polarized light was used as a source. In its emission spectrum, the He I line dominates with the photon energy $h\nu = 21.22$ eV. The contribution of He II photons at 40.8 eV was negligible.

The UPS technique was first employed to measure the system work function and its possible change due to the presence of the PTCDA. A fixed bias of 10 V was applied on the sample to assure that all photoelectrons are detected. The work function was then determined from the photoelectron cut-off edge position in the biased VB spectra. Fig. 7.14 shows valence band photoemission from clean Ge substrate and the nearby metallic clip of the sample holder. E_F of then clean Ge(001) coincides with the top of the
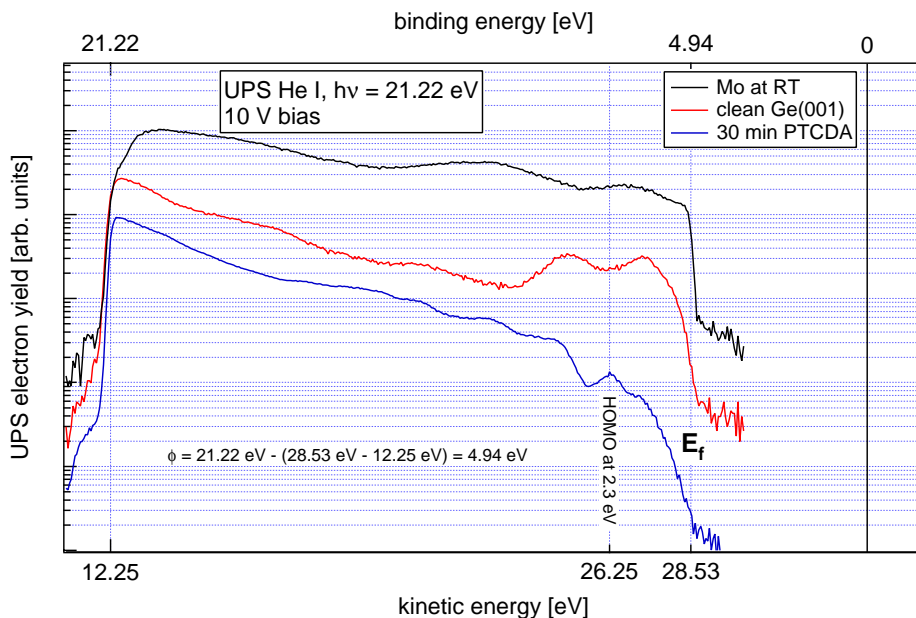
Figure 7.14: The determination of workfunction.

filled VB as expected for the p-type semiconductor. The calculated work function is found to be 4.94 eV. The spectrum of PTCDA covered Ge doesn't terminate so steeply, but the cut-off effectively remains at the same energy. We conclude that no dipole barrier Δ occurs and summarize the electronic levels of Ge and PTCDA [112] in fig. 7.15. No detectable change of workfunction, i.e., dipole barrier (Δ) between the surface and adsorbate was found during PTCDA deposition.

Next a sequence of UPS spectra was taken during PTCDA deposition at two substrate temperatures, 170 K and 300 K (RT), displayed in fig. 7.16. All spectra are shown as a function of binding energy (BE) relative to the Fermi level. On the right-hand side of each sequence there is a corresponding HAS specular intensity plotted on logarithmic scale versus vertical coverage axis. The PCTDA coverage is scaled in wetting layer (WL)
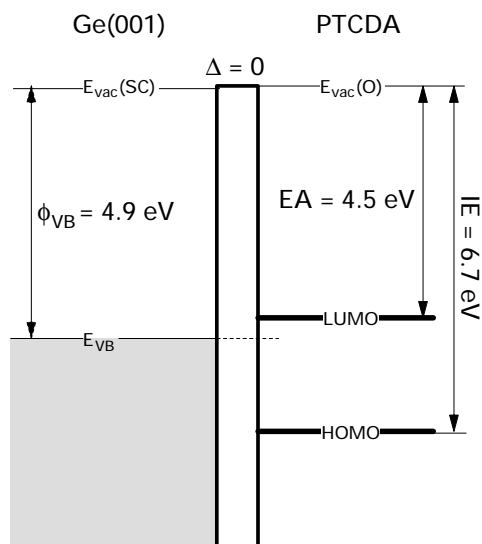
Figure 7.15: The schematics of the PTCDA and Ge(001) electronic levels.
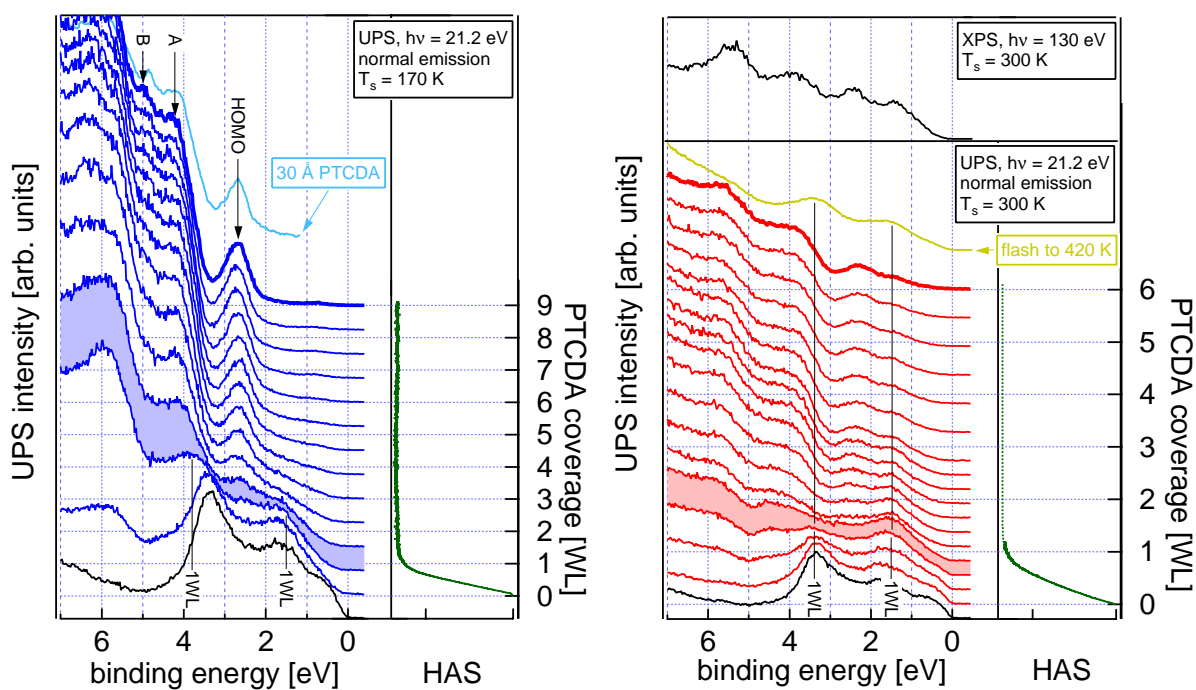
Figure 7.16: The sequence of UV photoemission spectra, taken during PTCDA deposition on the Ge(001) substrate at 170 K (left) and on the substrate at RT (right). Helium discharge source was used with the photon energy 21.22 eV. The corresponding HAS specular intensity and approximate coverage is shown on the vertical right axis of each graph.

units, where HAS elastic reflectivity signal vanishes.

Left panel of fig. 7.16 shows the evolution of VB spectra during LT PTCDA growth, starting with the spectrum of clean Ge(001) and ending with the saturated spectrum of thick PTCDA film. The two germanium peaks at 3.4 eV and 1.6 eV disappear rapidly after the completion of wetting layer. At the same time the PTCDA features turn up and saturate shortly after 2 WL equivalent thickness, keeping the spectra almost unchanged upon further deposition. At coverages where the adsorbate components dominate, the lowest lying peak at 2.6 eV corresponds to the highest occupied molecular state (HOMO) [110]. The next strong, yet weakly pronounced peak A appears at 4.2 eV and represents a composition of at least $4-5$ underlying molecular orbitals. Another composed peak B follows at 5.0 eV and belong to the next group of molecular orbitals. Moreover, the saturation spectrum (emphasized blue line) resembles well the spectrum reported in the literature [111] (light blue line), taken on 30 Å thick PTCDA film with the photon energy of $h\nu = 22$ eV. Angular dependence examination of the thick film doesn't give any appreciable dispersion of the HOMO peak. The thick film peaks show up at around second monolayer of coverage and stay fixed in energy for all remaining time of the deposition. For lower coverages, however, the molecular states occur at altered binding energies. At 1 WL coverage HOMO peak appears at 1.5 eV and peak A at 3.8 eV. They shift towards higher binding energy when going to thicker layers, indicating that only the first (wetting) layer exhibits strong interaction of the PTCDA molecular states with the substrate.

For the deposition on substrate held at 300 K (RT), the spectral evolution is quite different. While at LT deposition the bulk-like saturation spectrum is achieved after 2 or 3 WL, at RT this doesn't happen even after the coverage of 6 WL equivalent. The overall shape of the RT saturated spectra resembles closely the one at 1.5 ML grown at LT. This is another indication that PTCDA morphology at RT consists of a wetting layer plus large 3D islands, with the main part of the UPS signal arising from the single layer present. In fact, the peak at 1.5 eV, which belongs to the HOMO states of the wetting layer, and the peak A at 3.8 eV remain always present at RT growth. Additionally, the photoelectron yield in the low binding energy region (< 1 eV), corresponding to the Ge substrate states, fades away very slowly, evidencing that the substrate is much less effective covered in RT than in LT growth. The yellow curve above the sequence points out that the substrate signal actually recovers already after short flash to 420 K, due to fusion of 3D clusters into even larger 3D aggregates, accompanied by partial uncovering of the surface. The VB spectrum was also acquired with the photon energy $h\nu = 130$ eV on the substrate at 300 K (RT), covered with thick PTCDA film. Displayed on the top of the right panel in fig. 7.16 it reveals the presence of HOMO states belonging to both, wetting layer and thick film.

We conclude the UPS and XPS analysis by noting that for the wetting layer a significant interaction of the organic molecules with the substrate takes place. It is accompanied by strong electronic level rearrangement, which produces the (0.5 eV) shift of O $1s$ level and substantial shift of HOMO components of the wetting layer comparing to those in bulk like PTCDA. For growth at LT, the uniform film morphology is present with practically unperturbed molecular film valence band occurring already after 2 WLs of coverage. The morphology of RT and HT grown films on the other hand consists of large 3D islands and only partly covered wetting layer, whose signal in valence band remains present even at several WLs of PTCDA deposited.

7.5 NEXAFS study of molecular orientation

Further insight into the adsorption geometry and orientational order of the PTCDA film on Ge(001) was gained by measuring a series of NEXAFS absorption spectra. In particular we have measured the X-ray absorption across the K-edge of carbon atoms. All spectra were normalized to the incident photon flux by division with the absorption signal on the clean Ge(001) substrate. The accurate photon energy was calibrated to the gas absorption resonances in CO. Spectra were further normalized to unity in the lower energy range just before the first resonance, so the strengths of transitions at different absorption geometries are to scale.

A typical NEXAFS spectrum of thick PTCDA/Ge(001) film, grown at LT is shown in fig. 7.17. The absorption spectrum has been acquired at grazing incidence angle $\theta = 8°$. For comparison, PTCDA K-edge absorption spectrum of 10 ML PTCDA film on H-
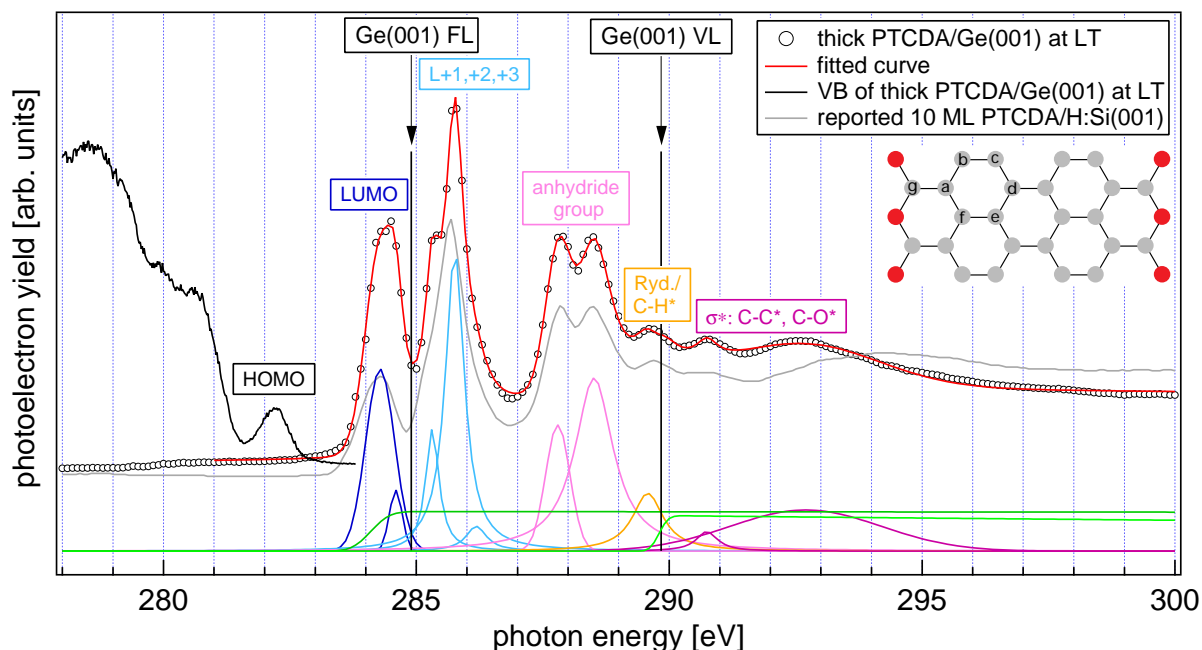
Figure 7.17: The NEXAFS spectra of thick PTCDA/Au(110) at LT. Under the fitted curve there is the decomposition to individual components of the spectra.

passivated Si(001) substrate is also displayed [113]. It is evident, that LT grown thick PTCDA film resembles all principal absorption features of the 10 ML film on H : Si(001), confirming that the vast majority deposited molecules remain chemically intact when grown on Ge(001). Fermi level (FL) as determined from the XPS measurements is also put on the graph. The energy of the vacuum level (VL) was determined by considering the system work function (4.94 eV).

The overall spectrum was fitted with the multicomponent function and the resulting best fit, composed of a sum of all individual components is represented by the continuum (red) line. The two low-energy π^* peaks are composed of several blend-together resonances, so they were fitted with a Gaussian profile, leaving its width as a free fitting parameter. According to ref. [110], the first double peak in the spectrum, occurring

at 284.5 eV, corresponds to the transitions from C 1s levels of the perylene core atoms ($a, c \rightarrow$ LUMO) and ($b, d \rightarrow$ LUMO), respectively. Notice that this transition falls below the Ge(001) Fermi level, which is a consequence of carbon atomic levels rearrangement due to the presence of C 1s core hole. The strongest resonance, located at 285.5 eV, belongs to transitions ($e, f \rightarrow$ L1, L2), ($c \rightarrow$ L1, L2) and ($a, d \rightarrow$ L3, L4). The actual fit was performed with three components. The following doublet close to 288 eV refers to the transition from carbon atoms in the PTCDA anhydride groups ($f \rightarrow$ LUMO) and ($f \rightarrow$ L1, L2, L3). They were fitted with two Gaussian components, both widths were left as free fitting parameters. The energetic difference between this doublet at 288 eV and the first LUMO peak at 284.5 eV is in agreement with the XPS measurements, shown in fig. 7.12, where the separation between the C 1s binding energy of the atoms in the carbonyl group and those from the perylene core equals 3.75 eV. A weak resonance, which follows just below the vacuum level of the system at 289.8 eV, corresponds to transitions to closely spaced atomic Rydberg states and to the C $-$ H* molecular states. The energetic position of vacuum level (VL) was obtained by summing the Fermi level energy with the value of pre-determined work function. The two broad peaks at 290.8 and 292.5 eV further refers to the quasi-bound C $-$ O* and C $-$ C* σ^* states. The widths of the Gaussian fitting peaks were left free for the fit. The absorption spectrum was further fitted with two continuum steps. The first one at 284.1 eV represents the multi-electron excitations, which gradually turn on along with the LUMO resonance. The step was fitted with its position and width locked to the values of the corresponding LUMO peak. The second step is introduced by the transitions to the continuum states above the vacuum level, so it was fitted with the position locked to the VL. The step width was locked to the experimental resolution (~ 0.12 eV).

Polarization dependent NEXAFS

PTCDA is a highly symmetric organic molecule belonging to the same symmetry group as pentacene, i.e., D_{2h}. Fig. 7.18 shows C 1s NEXAFS spectra of thick PTCDA film (≥ 5 ML) deposited at two different substrate temperatures, 170 K (LT) and 300 K (RT), for three different polar angles θ. With $\theta = 8°$ the photon polarization vector is almost completely p-polarized, whereas for $\theta = 80°$ the photon polarization lies almost parallel to the surface, i.e., s-polarized. The spectrum at $\theta = 8°$ has a good resemblance to the reported PTCDA NEXAFS spectra obtained with p-polarized X-rays on well-ordered multilayer films with flat-lying molecules [114]. Strong dichroism is observed in the series of the spectra of film grown at low substrate temperature (left panel). For p-polarized photons, sharp π^* resonances occur on the low energy side of the core-level absorption spectra (between 283 and 290 eV photon energy). For the detailed analysis of allowed and forbidden transitions considering selection rules and orbital symmetry we refer to the sec. 5.4. However, the symmetries of the involved destination molecular orbitals are summarized in tab. 7.5. All transition resonances in the $283 - 290$ eV range dominate the absorption spectra for the p-polarized light and nearly disappear for the s-polarization. On the other hand, the high energy tail (above 294 eV) stems from the transitions into molecular quasi-bound σ^* states and is at its maximum for the s-polarized photons. All this findings are consistent only with an uniform PTCDA film growth where the deposited molecules are orientationally well ordered and possess flat lying geometry, i.e., the molecular plane is parallel to the substrate.
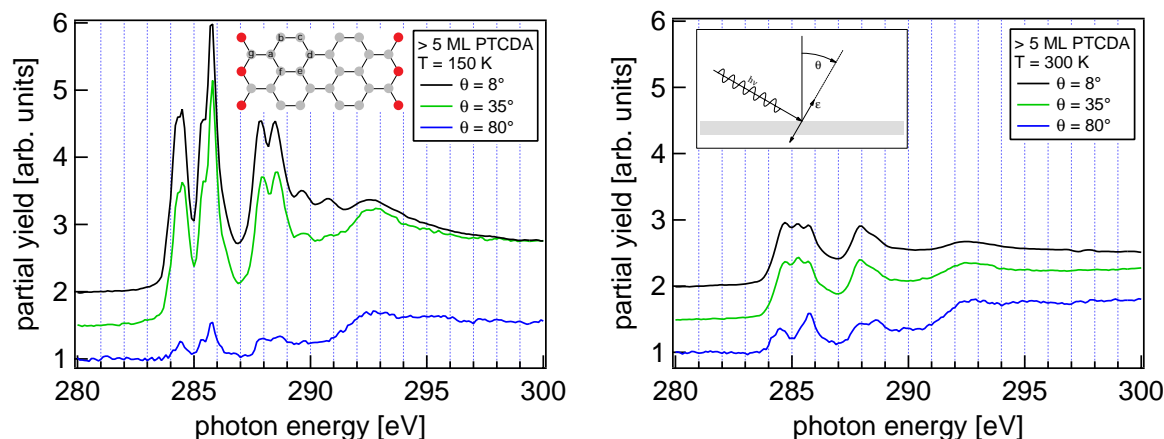
Figure 7.18: Linear dichroism of the C 1s NEXAFS for thick PTCDA film grown on substrate at 150 K (left) and 300 K (right). The spectra were vertically shifted for the sake of clarity.

mol. orb.	symmetry
LUMO	B_{2g}
LUMO+1	B_{1u}
+2	B_{3g}
+3	B_{1u}
+4	A_u

Table 7.1: The symmetries of first few PTCDA molecular orbitals.

When comparing LT spectra with the RT ones, shown in fig. 7.18, right, almost no shape change is noticed in RT spectra pointing to a quite different growth morphology. A slight energy shift (≈ 0.2 eV) of the two dominant peaks can be observed in the low energy part of the absorption edge. A new feature is also present, located at 284.7 eV (just in between the two major peaks of the LT spectrum, which are suppressed for the RT film), evidencing the contribution from the exposed PTCDA wetting layer which apparently interacts strongly with the substrate. A similar NEXAFS spectrum was reported for a monolayer PTCDA film on Ag(111) [110]. In fact all peaks in the $283 - 290$ eV region are heavily affected, indicating that the interaction with the substrate occurs via perylene ring as well as through the anhydride groups. The lack of the linear dichroism in the C $1s \rightarrow \pi^*$ transition may also be attributed to the strong hybridization of the PTCDA molecular states with the Ge(001) substrate. Alternatively, the deficient linear dichroism indicates that for the RT grown film no significant orientational order is present in the film morphology.

We therefore conclude that on the substrate at RT, the wetting layer and 3D PTCDA islands form, which are uncorrelated and randomly oriented, resulting in poor overall orientational order. Interestingly, for the RT spectrum at $\theta = 80°$, a fairly good resemblance with the spectrum of the thick LT grown film can be observed. This witnesses that a portion of 3D islands is built up of the molecules, oriented with their plane perpendicular to

the surface which exhibit rather weak interaction with the substrate via anhydride group. Only flat lying molecules of the wetting layer interact strongly with the Ge(001) substrate, whereas upward oriented molecules show nearly bulk like spectroscopic behavior.

Layer resolved NEXAFS

The PTCDA NEXAFS spectra is next analysed as a function of film thickness. The amount of deposited material is measured in the units of interface layer equivalent, i.e., for substrate at LT 1 WL is approximately required for the HAS coherent signal to disappear. It was shown in the sections 7.2 and 7.3 that at this stage the substrate is completely covered since no diffraction from the Ge(001) beneath can be detected, which coincides with the disappearance of the surface component from the Ge $3d$ XPS peak profile. Layer resolved NEXAFS spectra with p-polarized X-rays ($\theta = 8°$) for LT and RT growth are shown in the fig. 7.19.
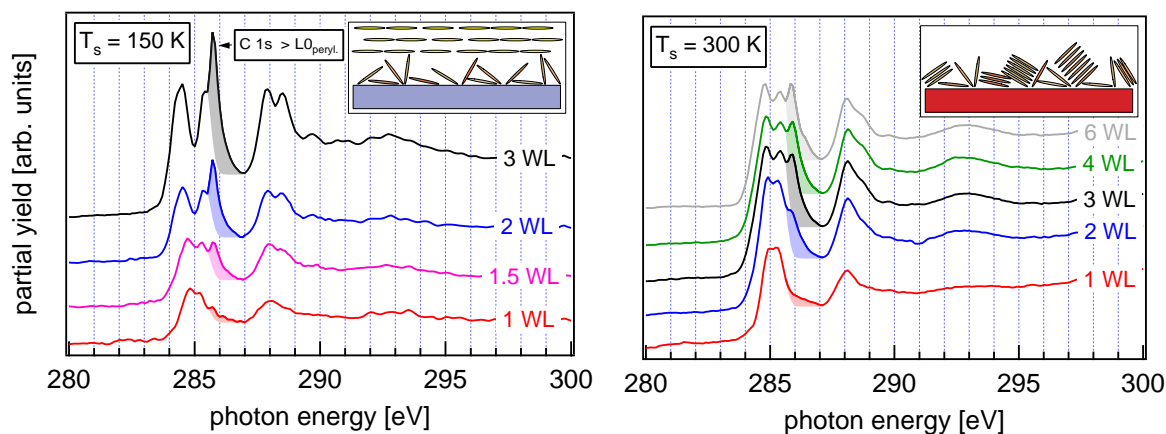
Figure 7.19: C $1s$ NEXAFS spectra of different PTCDA coverages in the units of interface layers for growth at 170 K (left) and 300 K (right).

For the 1 WL thick film grown at LT, the NEXAFS spectrum differs substantially from the thick film. Only single peaks can be observed in the NEXAFS spectrum for the C $1s \rightarrow$ LUMO transition for atoms in the perylene ring and in the anhydride group, respectively. The loss of fine structure in the NEXAFS spectrum of 1 WL film indicates that strong hybridization of the molecular states with the substrate occurs for the WL. Additional shift of the strongest π^* resonance towards lower energy with respect to its position in the bulk spectrum is a clear fingerprint, that the chemical state of PTCDA in the monolayer is quite different from that in bulk state. A similar analysis for PTCDA on Ag(111) and Ag(110) was made by Y. Zou et al. [110].

The 2 WL film, on the other hand, already shows all spectral features found in the NEXAFS spectra of the thicker PTCDA film, indicating that the second layer is quite unperturbed, with well ordered flat lying molecular geometry. There is practically no difference in the spectra of 1 WL film grown at LT and RT. Only single transitions from the perylene core carbon atoms and the anhydride group can be observed. This points to no significant difference in the wetting layer morphology for the RT and LT grown films.

Major differences in the RT film growth start to show up at the coverages beyond the wetting layer of the deposited material. In fact, for $2-3$ WL film the RT spectra saturate, showing an invariant film morphology which is quite similar to the spectrum of the 1.5 WL film grown at LT. The wetting layer features, however, continue to dominate the RT spectra for further PTCDA deposition. Interestingly, if additional 2 WL of PTCDA are deposited at 140 K on the previously grown 5 WL film at RT, the unperturbed flat lying geometry spectrum shows up, indicating that reduced diffusion and ordering dynamics of PTCDA molecules at LT again produce the uniform growth with flat lying molecules.

A more detailed NEXAFS analysis of the C $1s \rightarrow \pi^*$ linear dichroism as a function of film thickness is displayed in the left and center panel of fig. 7.20, respectively for the 1 WL and 2 WL films grown at LT. Whereas in 1 WL film almost no angular dependence
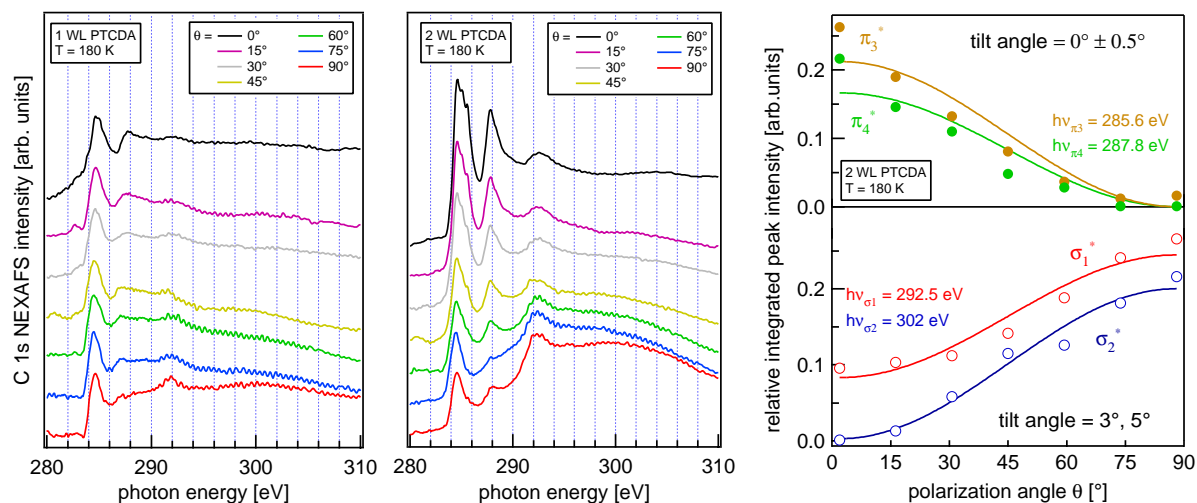
Figure 7.20: C $1s$ linear dichroism of interface layer (left) and 2 WL film (center) grown on LT substrate. The relative intensity of π^* and σ^* resonances on 2 WL film for different polarization angles θ (right)

of the π^* resonances is observed, it is rather strong in the 2 WL film due to exhibited second layer NEXAFS contribution. The absence of linear dichroism in the π^* absorption transitions in the wetting layer can be attributed to the strong hybridization of molecular orbitals with Ge(001) surface states, or it may simply reflect the fact that in the WL no preferred adsorption geometry of the PTCDA molecules exists, thus leaving the molecules without the orientational order. The symmetry of the LUMO states becomes significantly altered, resulting in the break down of the linear dichroism present at the unperturbed molecular absorption. We can not exclude the possibility, however, that the molecules in the wetting layer are randomly oriented (or even partially dissociated) thus lacking the orientational order and consequently contributing no angular dependence to the observed NEXAFS spectra.

All the 2 WL spectra were fitted with the components, introduced in the fig. 7.17, to extract the quantitative angular dependence of the transition resonance strengths. The resulting peak intensities of the two dominant π^* peaks and both present σ^* peaks are given in the right hand panel of fig. 7.20. The intensities were fitted with the corresponding

functions, given by the equations (3.27) and (3.27) in sec. 3.5, respectively. The best fit values for the molecular tilt angle ($\sim 0°$) are also displayed. The values yield a perfectly flat geometry of molecules in the second PTCDA monolayer, indicating the formation of orientational order with molecular π-stacking along the growth direction which is preserved for subsequently deposited monolayers.

The PTCDA growth hence forms an interface layer, whose morphology doesn't depend on the substrate temperature in the $140 - 300\,\mathrm{K}$ range. The disordered initial layer acts as a passivation layer, which leads to the formation of 3D islands for coverage beyond 1 WL for RT deposition and growth of orientationally ordered multilayer film at LT. Such a passivation of Ge dangling bonds by the initial layer is sufficient to prevent the additionally deposited molecules from interacting with the surface, allowing the diffusion of molecules, which eventually build the temperature-conditioned morphology. The ordering of the material deposited after 1 WL deposited was shown to depend crucially on the temperature of the substrate and is not affected by the morphology present in the template. The stability of the multilayer film morphology (5 WL) was furthermore proven to sustain temperatures as high as $370\,\mathrm{K}$, still featuring UPS and NEXAFS linear dichroism as observed for the LT thick film.

Chapter 8

Conclusions

In the present work three organic/inorganic heterosystems have been studied, namely pentacene/Au(110), CuPc/Au(110) and PTCDA/Ge(001). Formation of interface layer, film growth and ordering, strength of film interaction with the substrate and molecular orientation in the film have been inspected by making use of several complementary diffraction and spectroscopic experimental techniques. Structural order and periodicity of the substrate and overlayer were probed by helium atom scattering, diffraction of low energy electrons and grazing incidence X-ray diffraction. The strength of interaction with the substrate has been traced with X-ray and ultraviolet photoemission spectroscopy and the molecular orientation was determined with angle resolved X-ray absorption near atomic edges.

The morphology of thin film has been expectedly most affected on the reactive semi-conducting substrate, where the structure of the interface layer of PTCDA/Ge(001) is completely disordered, irrespective of the temperature. Rather large core-level shifts of carbon and oxygen $1s$ level ($\approx 0.5\,\mathrm{eV}$) as well as displaced and distorted HOMO levels with respect to (unperturbed) PTCDA crystal indicate significant substrate-film interaction. The thickness of the interface layer has interestingly been found to match closely the longest axis of the PTCDA molecule. The disorder of the template layer, however, doesn't prevent the subsequent film growth from being orientationally perfectly ordered, when maintaining the growth temperature of the substrate below $150\,\mathrm{K}$. In this case the PTCDA molecules lie flat on the otherwise disordered interface layer, with the molecular planes parallel to the substrate. The observed low-temperature orientational ordering and the formation of uniform film successfully explains the anomalous PTCDA/Si conducting properties, reported by Forrest et al. [7], where higher conductivity was measured when the film was grown at lower temperature (see fig. 1.3). The low-temperature film morphology remains preserved even when bringing the substrate up to room temperature. One could say that the interface layer acts as the passivation layer enabling ordered subsequent growth. Notwithstanding, no long range order has been put to evidence by helium atom scattering at any growth temperature. No layer growth formation has furthermore been observed upon subsequent deposition at and above the room temperature, where large randomly oriented 3D PTCDA islands form, causing poor overall film orientational order.

The CuPc, on the other hand, forms well ordered long molecular chains along the missing row reconstructed Au(110) troughs even at slightly elevated temperature, i.e., at $340\,\mathrm{K}$. Although much less reactive than semiconducting Ge surface exposing dangling-bonds, the Au(110) surface classifies as moderately reactive metallic surface. With exposed (111)

microfacets tilted by 35° from the (110) plane it represents a very suitable substrate to drive oriented growth of the adsorbed molecules. The adsorbed CuPc molecules have been observed to locally induce a proliferation of Au(110) monoatomic steps which at the same time drive the molecular alignment in long CuPc chains along the [1$\bar{1}$0] surface direction. A nearly one-dimensional character of the substrate defect proliferation has been observed. The parallel CuPc chains are excellently correlated along the [1$\bar{1}$0] surface direction (ΓX) and exhibit well pronounced 5-fold periodicity (along the same direction), which establishes in the early growth stages already. The exposed structure during CuPc deposition as seen by HAS evolves from the initial (1×2) of the clean Au substrate, passing the intermediate (5×5) and ending up with the (5×7) periodicity. Interestingly, the low-energy electron diffraction also passes the (5×5) intermediate structure but effectively ends up with the phase of the (5×3) periodicity. Considering the probing depth of the two techniques, HAS reflects the 7-fold periodicity of the CuPc film, whereas LEED reveals the 3-fold periodicity of the underlying Au substrate. The CuPc molecules in the (5×7) phase have been observed to lie tilted by 32° from the substrate plane and are organized in correlated chains along the [1$\bar{1}$0] surface direction. Although CuPc adsorbs rather weakly on the Au(110) substrate as deduced from a good resemblance of the carbon core-level photoemission spectrum with the bulk one, the present molecules induce (1×3) reconstruction of the Au substrate, enlarging the (111) facets thus lowering the surface energy. As determined by the grazing incidence X-ray diffraction, the Au surface exhibits "shallow" 3-fold missing-row reconstruction, with asymmetric relaxation of the Au unit cell due to interaction with CuPc molecules. The best fit revealed that unit cell relaxation results in the significant inward and sideward atomic displacements.

A crucial temperature dependence of growth has been observed in the pentacene/ Au(110) system. A phase diagram has been introduced, showing one transient and two monolayer ordered phases at saturation coverages taking place on the substrate held at different temperatures. Whereas under 370 K a disordered growth of the pentacene has been evidenced, above 470 K an equilibrium (3×6) saturation phase show up at the monolayer coverage. In the initial growth stage a metastable (6×3) phase starts to show up, which is then overwhelmed by the (3×6) phase. At slightly lower substrate temperature, i.e., between 370 and 420 K, the (3×6) monolayer phase further evolve to the phase with (6×8) structure, reaching the saturation at $\approx 12\%$ higher coverage. The excess material upon further deposition collects in the large 3D islands which coexist with the present (6×8) phase. No core-level shift of the carbon $1s$ level has been observed whatsoever, witnessing rather weak interaction of the adlayer with the substrate. The molecular alignment in the two saturation phases has been probed by NEXAFS and the complete structure has been revealed in combination with HAS and XPS data. In the equilibrium (3×6) phase, the pentacene molecules lie flat on the Au(110) surface with the long molecular axis oriented along the [001] direction. Molecules are aligned side-by-side into long chains extending parallel to the [1$\bar{1}$0] direction. In the denser (6×8) phase, the pentacene molecules appear in two different adsorption geometries. Between each two flat lying chains of the (3×6) phase, another chain of edge-on oriented molecules inserts, thus increasing the unit cell along the [001] direction. The molecules in the upright chains line up head-by-head along the [1$\bar{1}$0] direction with the molecular plane normal to the surface, forming extended correlated "nano-rails". The electronic structure of the edge-on molecules has been observed to be less hybridized with the substrate electronic states, indicating an almost negligible interaction of these molecules with the substrate (as a

contrast flat-lying ones).

It has been shown that highly-ordered self-assembled organic monolayers can be produced when suitable molecules and substrates are chosen and the preparation conditions are optimized. The role of bonding to the substrate has also been demonstrated to substantially affect the quality of the organic films. The realization of organic/inorganic systems with particular molecular geometry opens a way to tailor the new optical and electrical properties of the organic thin films, which may be referred to as surface "nano-architecture" and which will continue to be of high research interest also in the future.

Appendix A

Helium source

The He beam source consists of a nozzle aligned with a hollow truncated cone, i.e., skimmer to "skim off" all those molecules not directed along the beam axis in order to minimize the disturbances of the reflected molecules with the beam. This type of arrangement is shown in fig. A.1. The Knudsen number[1] of such source is less than unity, and the mass
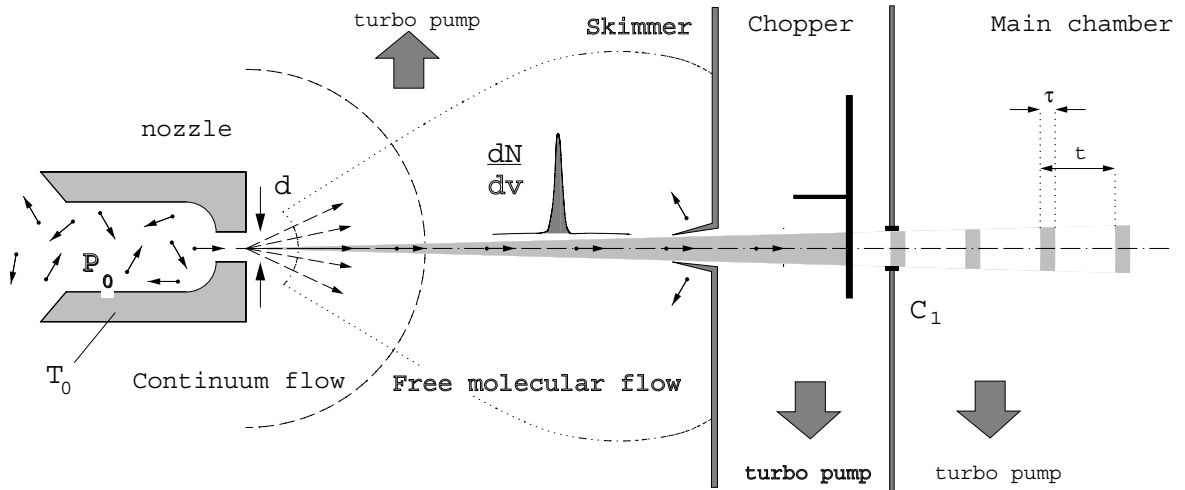
Figure A.1: Schematic diagram of the He beam source. The He pressure in the stagnation chamber is denoted by p_0 and the nozzle temperature with T_0. Nozzle diameter $d = 5\,\mu$m. The gating and repetition time of the He pulses for inelastic scattering experiments is denoted by τ and t, respectively.

flow through the nozzle is substantial. The gas expands adiabatically from a high pressure stagnation chamber (p_0) through the nozzle into the vacuum chamber with base pressure p_1. As the gas expands into the lower pressure region, lower gas densities result with increasing distance from the nozzle, the collision rate between the particle decreases, and eventually a transition from the continuum flow in the nozzle into a free-molecular-flow takes place. Because of the high flow through the nozzle there is a net mass transport into the beam direction and this involves the conversion of the total enthalpy into a beam

---

[1] The Knudsen number is a ratio of the gas mean-free-path to source diameter, $K_n = \lambda/d$.

translational energy. As a result, the gas is cooled during the expansion through the nozzle and the velocity distribution of the atoms in the beam becomes centered around the mean translational velocity v_1. The velocity spread is characterized by the beam "temperature" T which is much smaller than the nozzle temperature T_0. In this way rather narrow velocity distribution and high beam fluxes are obtained.

Since neither the pressure nor the volume are constant during the beam expansion, the conserving quantity is enthalpy, h, rather than the internal energy. In the continuum flow regime the expansion is considered to be adiabatic[2], where $T = T_0(p_1/p_0)^{(\kappa-1)/\kappa}$ and $\kappa = c_p/c_v$. We can write

$$h_1 - h_0 + \frac{v_1 - v_0}{2} = 0. \tag{A.1}$$

In the stagnation chamber the center of mass is obviously at rest, $v_0 = 0$, and for the enthalpy we may write $dh = c_p dT$. For the final velocity v_1 we obtain

$$v_1 = \sqrt{2(h_0 - h_1)} = \sqrt{\int_T^{T_0} c_p dT'}. \tag{A.2}$$

Assuming that in the required temperature range the c_p does not change substantially, the final velocity becomes

$$v_1 = \sqrt{2c_p(T_0 - T)} \approx \sqrt{2c_p T_0}, \tag{A.3}$$

which is a function of the source temperature T_0 only. The beam temperature decreases strongly and the asymptotic final velocity is reached very soon, i.e., at a distance of a few nozzle diameters [44]. Similarly, the collision rate between the atoms in the beam becomes negligible and the transition from the continuum to molecular flow occurs. Due to negligible collision rate, the velocity $\mathbf{v}$ of an isolated molecule in the beam is "frozen" in a sense that neither the direction nor the velocity changes as the atom propagates along the beam path. The velocity distribution may be well approximated [115] with a Maxwellian distribution around the v_1 with the temperature T:

$$f(v) = n \left(\frac{m}{2\pi k_B T} \right)^{\frac{3}{2}} e^{-\frac{1}{2}m \frac{(v_\parallel - v_1)^2 + v_\perp^2}{k_B T}} \tag{A.4}$$

If the pressure ratio between the base pressure in the expansion chamber and the pressure in the stagnation chamber, p_1/p_0, exceeds a certain value $p_1/p_0 \geq G$, where $G = \left(\frac{\kappa+1}{2} \right)^{\kappa/(\kappa-1)}$, the gas expands supersonically through the nozzle. Here we considered that the sound velocity decreases with the decreasing temperature of the gas as $v_s = \sqrt{\frac{\kappa k_B T}{m}}$. The supersonic velocity is often given in terms of Mach number, $M = v/v_s$, i.e., the ratio of the mean particle velocity and local velocity of the sound A.2.

---

[2]The gas is taken to be ideal and the flux is supposed to be fast with respect to the characteristic diffusion processes.
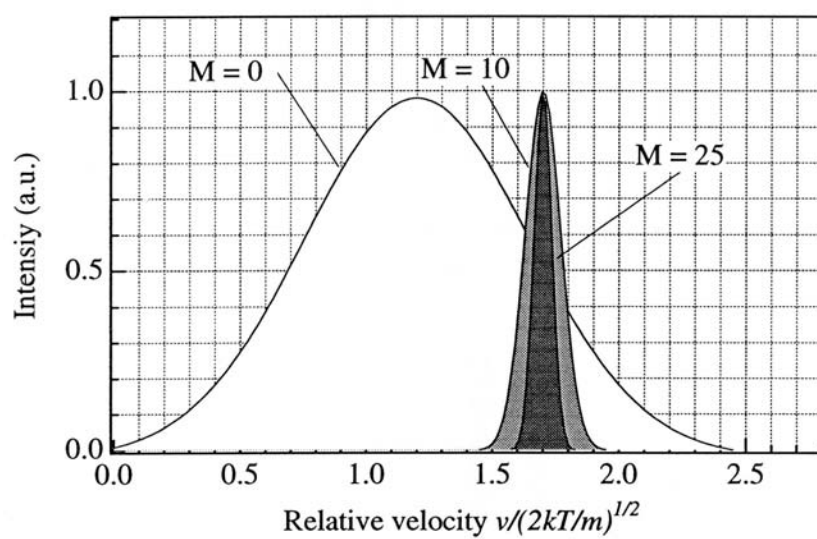
Figure A.2: The He beam velocity distributions for the different final velocities, expressed in Mach number ($M = 0, 10, 25$). The $M = 0$ curve is that of the effusive (thermal) sources. [115, 44]

129

Appendix B

Interaction of He with the surface

The interaction of neutral He atoms with the surface atoms and surface-adsorbed species generally consists of the repulsive and attractive contribution. The repulsive part arises from the overlap of the atom and surface electronic density whereas the attractive part has its origin in the van der Waals dispersion forces.

The attractive interaction is based on the correlated charge fluctuations of both participants, i.e., mutually induced dipole moments, and is rather weak, so the electronic picture of the participants essentially remains unchanged [117]. It can be described by the potential energy of the induced dipole in the electric field of the primary dipole. The first dipole, $\mathbf{p_1}$, arised from the charge fluctuation causes in the point of the second particle at the distance r the electric field $\mathbf{E} \approx \mathbf{p_1}/r^3$. The dipole moment induced in the second particle equals $\mathbf{p_2} = \alpha \mathbf{p_1}/r^3$, where α is the polarizability of the particle. The pair potential of the second dipole in the field of the first one is then $V \propto 1/r^6$, which leads to a well-known van der Waals potential [116]:

$$V_{\text{vdW}}(r) = \frac{C_6}{r^6},$$ (B.1)

where C_6 is the strength of the interaction.

In case of He scattering [118], the van der Waals interaction arises because of correlation between the He atom electrons and those of the upper few layers in the substrate. In semiclassical terms this corresponds to the formation of an image dipole in the substrate in response to the instantaneous dipole moment of the He atom, as shown in fig. B.1, left. The atom dipole fluctuation at large distance z interacts with its mirror image in the surface and the corresponding potential is obtained by summing-up the pairwise contributions. The summation goes first over all atoms in one layer of the substrate and then over several layers, yielding

$$V_{attr} = -\frac{C_3}{z^3},$$ (B.2)

where C_3 is defined by the Lifshitz formula [119]

$$C_3 = \frac{\hbar}{4\pi} \int_0^\infty \frac{\epsilon(i\omega) - 1}{\epsilon(i\omega) + 1} \, \alpha_{He}(i\omega) d\omega.$$ (B.3)

Here ϵ is the dielectric function of the surface and α_{He} the polarizability of the He atoms. Improvements of eq. (B.2) have been obtained by considering inhomogeneous charge distribution and higher multipolar charge fluctuations [120], which contribute to the attractive potential higher order terms like $-C_4/z^4$, $-C_5/z^5$ etc. However, while C_3 can be
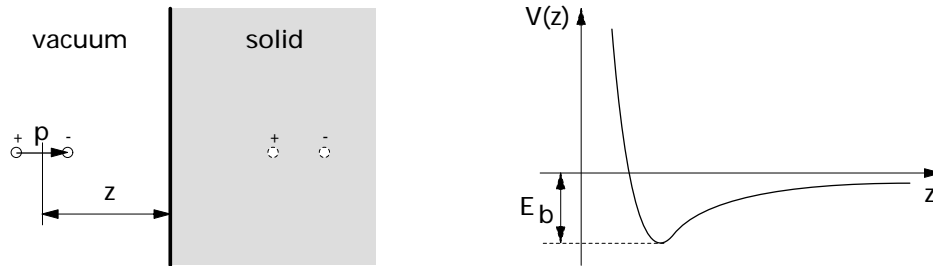
Figure B.1: Model of dipole interaction with the metal surface (left) and the corresponding potential curve (right).

quite accurately evaluated using eq. (B.3), or by direct measurements, where the $\epsilon(\omega)$ and $\alpha(\omega)$ can be both measured independently in an optical experiment, the higher order corrections to $-C_3/z^3$ are neither directly measurable, nor easy to evaluate.

The repulsion part in the interaction arises from the overlap of the electronic functions of the molecule and the substrate (Pauli principle). The problem was studied by Zaremba and Kohn [121] and later by Harris and Liebsch [122] within the Hartree-Fock approximation, which is, however, beyond the scope of this thesis. In practice, the laterally averaged repulsive He-surface potential is proportional to the electronic density close to the surface and can be well approximated by

$$V_{rep} \propto \rho_e z \propto U_{rep}\, e^{-\beta z}, \tag{B.4}$$

which is consistent with a pairwise summation of the Yukawa potential $U_\kappa e^{-\beta r}/r$ over a monoatomic top layer.

We get a complete He-surface potential by summation of the V_{attr} and V_{rep}, yielding a common shape of the physisorption potential, which is shown in fig. B.1, right. In the limit, where $\beta \to \infty$, the *hard-wall* model is obtained, which is discussed in sec. 4.4.1.

Appendix C

The list of related publications and public presentations

Pentacene/Au(110)

- G. Bavdek, D. Cvetko, L. Floreano, A. Cossaro and A. Morgante: *The structure of "nano-rails" in the pentacene/*Au(110) *thin film*, "New materials at the nanometric scale", 2nd Workshop of the INTERREG IIIA SLO-ITA project, Trieste, October 23-24 2006

- G. Bavdek, D. Cvetko, L. Floreano, A. Cossaro and A. Morgante: *NEXAFS study of pentacene/*Au(110) *thin film*, 5th Symposium of Science and Technology of Nanomaterials in Slovenia, Ljubljana, September 20-21 2006

- L. Floreano, A. Cossaro, D. Cvetko, G. Bavdek and A. Morgante: *Phase Diagram of Pentacene Growth on* Au(110), J. Phys. Chem. B **110** (2006) 4908

- L. Floreano, G. Bavdek, A. Cossaro, F. Bruno, D. Cvetko and A. Morgante: *Pentacene Nanorails on the* Au(110) *Surface*, ECOSS 24, Paris, September 4-8 2006

- L. Floreano, A. Cossaro, D. Cvetko, G. Bavdek, K. Bučar and A. Morgante: *Comensurated phases of pentacene grown on the missing row* (1×2)-Au(110) *surface*, ECOSS 23, Berlin, September 4-9 2005

CuPc/Au(110)

- L. Floreano, A. Cossaro, F. Bruno, A. Verdini, A. Morgante, G. Bavdek, D. Cvetko, A. Ruocco and F. Evangelista: *Structural study of the Cu-Pc/*Au(110) *interface by XAS, XRD,* He *and electron diffraction*, The European Materials Research Society Fall Meeting, Warsaw, September 5-9 2005

- A. Cossaro, D. Cvetko, G. Bavdek, F. Bruno, L. Floreano, A. Verdini, A. Morgante, F. Evangelista and A. Ruocco: *Structural study of thin copper phthalocyanine (CuPc) films on* Au(110), 16th International Vacuum Congress, Venice, June 28 - July 2 2004

- A. Morgante, A. Cossaro, D. Cvetko, G. Bavdek, L. Floreano, R. Gotter, F. Evangelista and A. Ruocco: *CuPhtalocyanine*-Au(110) *interface formation*, 20th General Conference of the Condensed Matter Division of the European Physical Society, Prague, July 19-23 2004

- A. Cossaro, D. Cvetko, G. Bavdek, L. Floreano, R. Gotter, A. Morgante, F. Evangelista and A. Ruocco: *Copper-Phthalocyanine Induced Reconstruction of* Au(110), J. Phys. Chem. B **108** (2004) 14671

PTCDA/Ge(001)

- G. Bavdek: *Morfologija in elektronska struktura tankega organskega filma PTCDA/* Ge(001), Vakuumska znanost i tehnika - 12. Međunarodni sastanak, Trakošćan, 18. maja 2005

- G. Bavdek: *Raziskave morfologije in elektronske strukture tankih organskih filmov*, 4. Konferenca fizikov v osnovnih raziskavah, Cerkno, 12. november 2004

- D. Cvetko, G. Bavdek, A. Cossaro, L. Floreano, R. Hudej, G. Bratina and A. Morgante: *Structural and Electronic Properties of Thin PTCDA Films on* Ge(001), 12th Elettra Users' Meeting, Miramare - Trieste, October 26-27 2004

Dodatek D

Razširjeni povzetek v slovenščini

Uvod

V zadnjem desetletju vse več organskih materialov uspešno prodira na področje polprevodniških, senzorskih in fotovoltaičnih naprav. Zaradi nizke cene postajajo obetavna zamenjava za silicij kot aktivni material v polprevodniških elementih. Ker je mobilnost nosilcev naboja v organskih polprevodnikih dosti manjša od mobilnosti v tradicionalnih anorganskih polprevodnikih (Si, Ge, GaAs), organski materiali v polprevodniških elementih, ki zahtevajo veliko stikalno hitrost, sicer niso uporabni. So pa organski materiali nenadomestljivi npr. pri izdelavi elementov, ki ne dopuščajo visokotemperaturne obdelave ($T \approx 360\,°C$); takšni so npr. upogljivi tekočekristalni zasloni, ki imajo za osnovo tanko plastično folijo.

Medmolekulska interakcija v organskih materialih temelji v glavnem na šibkih van der Waalsovih silah, ki so odgovorne za sorazmerno majhno mobilnost nosilcev naboja (med 10^{-5} in $10^{-4}\,\mathrm{cm^2/Vs}$). Razdalja med sosednjimi molekulami je pogosto prevelika, da bi omogočala dobro prekrivanje molekulskih elektronskih stanj in s tem dobro prevodnost. V neurejenih filmih tako poteka prenos naboja v glavnem s preskoki (angl. *hopping*) nosilcev med lokaliziranimi stanji na molekulah. Velike organske molekule z dobro izraženim π-elektronskim sistemom, ki se razteza preko (skoraj) celotne molekulske ravnine, pa se lahko med seboj močno povezujejo prav s $\pi - \pi^*$ interakcijo. Ta posredno vpliva na smer preferenčnega zlaganja molekul, kar privede do velike prevodnosti vzdolž smeri zlaganja ($1 - 10\,\mathrm{cm^2/Vs}$). Primerjava prevodnosti tankih filmov pentacena z različno ureditvijo molekul na substratu SiO_2 je prikazana na sl. 1.1 (str. 2). Očitno je s primernim nadzorom parametrov rasti mogoče tvoriti dobro urejene filme s tehnološko uporabnimi električnimi lastnostmi.

Izdelavo dobrih polprevodniških elementov dodatno omejuje slaba prevodnost na stiku organskega materiala s kovinsko elektrodo. Če se struktura organske plasti v prisotnosti kovine lokalno spremeni, pride do nastanka strukturnih mej, kjer je transport nosilcev naboja drastično zmanjšan. Velikost zrn z enako strukturo je tako lahko zelo različna, kadar organski material naparevamo npr. na čisti SiO_2 ali očiščen Au, kot kaže sl. 1.2 na str. 3. Poznavanje strukture organskega filma v stiku s kovino ali anorganskim polprevodnikom je zato pri izdelavi visokokvalitetnih polprevodniških elementov ključnega pomena.

V disertaciji se osredotočam na način rasti in urejevanja tankih filmov na kovinskih in polprevodniških substratih pri različnih temperaturah. Z več komplementarnimi tehnikami sem raziskoval orientacijo molekul in strukturo stične plasti ter celotnega

tankega filma, naparjenega z metodo organske molekulske epitaksije (OMBE) v pogojih ultravisokega vakuuma.

Eksperimentalna postavitev

Meritve sem v celoti opravil na žarkovni liniji ALOISA/HASPES, ki je ena izmed linij na sinhrotronu Elettra v Trstu in pripada laboratorijem TASC italijanskega INFM-CNR. Linija je namenjena raziskavam površin in tankih filmov in je opremljena s širokim spektrom uklonskih in spektroskopskih eksperimentalnih tehnik, ki jih gostita dve eksperimentalni postaji – Aloisa in HASPES. Skica linije s postavitvijo obeh eksperimentalnih postaj je prikazana na sl. 4.1 (str. 32). Žarkovna linija je zasnovana tako, da uporablja sinhrotronsko svetlobo v območju energije $100 - 8000\,\text{eV}$. Za dobro enobarvnost X-žarkov poskrbi monokromator, ki za pokritje tako velikega energijskega območja uporablja dva disperzijska elementa. Prvi je sestavljen iz dveh vzporednih zrcal, od katerih ima eden na svoji površini vrezane ekvidistantne brazde, ki predstavlja mrežico. Namenjen je monokromatizaciji svetlobe v nizkem energijskem območju $(100 - 2000\,\text{eV})$, kar dosežemo s sočasno uporabo izhodne reže, ki iz dispergirane "mavrice" izreže svetlobo z izbrano energijo oz. energijskim intervalom. Dosežena ločljivost $(\Delta E / E)$ je v tem primeru večja od 10000. Drugi disperzijski element je silicijev monokristal z vrezano režo, v kateri sta izpostavljeni dve popolnoma vzporedni ploskvi. Za monokromatizacijo svetlobe v tem primeru izkoriščamo dvojni uklon svetlobe na ravninah (111) obeh delov kristala. Enobarven žarek svetlobe z ločljivostjo, večjo od 7500, zapusti silicijev kristal vzporedno z vpadnim žarkom. Tok fotonov skozi izstopno režo je pri elektronskem toku $400\,\text{mA}$ v obroču sinhrotrona približno enak $2 \cdot 10^{12}$ fotonov/s/0.1%bw.

Optična postavitev linije je skicirana na sl. 4.3 (str. 34). Ko svetloba zapusti sinhrotronski obroč najprej prečka kolimator, nato pa jo parabolično zrcalo (P1) izostri na disperzijski sistem. Enobarvni žarek je z drugim paraboličnim zrcalom (P2) izostren na izhodno režo (ES). Divergentni žarek je v eksperimentalno postajo Aloisa ponovno fokusiran s toroidnim zrcalom (RT). Dodatno parabolično zrcalo (P3) lahko v kombinaciji z ravnim zrcalom usmeri sinhrotronski žarek v eksperimentalno postajo HASPES, ki je od optičnega sistema oddaljena $14\,\text{m}$, zato uporaba dodatnega zbiralnega zrcala ni potrebna. Vsa zrcala so prevlečena z zlatom, celotna optična pot žarkovne linije pa je izpeljana v pogoju popolnega odboja, s čimer so karseda zmanjšane izgube zaradi absorpcije svetlobe v optičnih elementih. Kljub temu so prvo parabolično zrcalo in oba disperzijska elementa, na katere pada "bel" žarek, vodno hlajeni. Vsi premiki optičnih elementov so avtomatizirani in krmiljeni z računalnikom. Fotografija celotne žarkovne linije-dvojčka je prikazana na sl. 4.4 (str. 36).

Eksperimentalna postaja Aloisa je sestavljena iz predkomore, ki je namenjena pripravi in predhodni karakterizaciji vzorca, in glavne merilne komore, opremljene z več vrstami detektorjev. Skica postaje je prikazana na sl. 4.5 (str. 37). V predkomori so nameščene štiri izparilne celice, ki so opremljene s kvarčnimi tehtnicami za merjenje hitrosti naparevanja. Čiščenje vzorca omogoča nameščena Ar^+ ionska puška z nastavljivo energijo ionov $(1 - 3\,\text{keV})$. Na okvir predkomore je nameščen tudi modul za uklon visokoenergijskih elektronov (RHEED), ki omogoča *in-situ* opazovajne stanja površine med naparevanjem filmov ali čiščenjem z Ar^+ bombardiranjem. Poseben sistem ventilov omogoča hitro izmenjavo vzorcev brez vdora atmosferskega pritiska v predkomoro. V glavni komori, ki se s pomočjo diferencialno črpanih ležajev lahko vrti okrog osi žarka, so detektorji nameščeni

na bimodalno in aksialno ogrodje, ki se vsako lahko vrti okrog svoje osi neodvisno od vrtenja komore (sl. 4.7, desno, str. 38). Dva 35 mm elektronska analizatorja sta namenjena kotno ločljivi fotoelektronski spektroskopiji (AR-XPS) in uklonu fotoelektronov (PED). V zadnjem obdobju sta bila nadomeščena z 2D kotno in energijsko ločljivim detektorjem. Dve silijevi diodi, opremljeni z 1-milimetrskimi kolimatorji, sta namenjeni detekciji skupnega fotonskega toka pri merjenju uklona in reflektivnosti X-žarkov (XRD, XRR). Dve dodatni energijsko-ločljivi diodi, ki delujeta v načinu detekcije posameznih fotonov, sta prav tako namenjeni merjenju uklona X-žarkov. Elektronski pomnoževalni detektor (channeltron), ki sprejema elektrone iz širokega prostorskega kota, je namenjen merjenju absorpcije X-žarkov v bližini atomskih absorpcijskij robov (NEXAFS). Ta ima pred svojim ustjem nameščeno mrežico s konstantnim negativnim potencialom, ki odbije nizkoenergijske večkrat sipane elektrone. K detektiranemu fotoemisijskemu signalu tako prispevajo le visokoenergijski Augerjevi elektroni. Vzorec je pritrjen na manipulator s šestimi prostostnimi stopnjami, ki je nameščen vodoravno v predkomoro in ga je mogoče vstaviti v merilno komoro. Tri neodvisne rotacije so prikazane na sl. 4.7, levo (str. 38). Vsi premiki manipulatorja so motorizirani in krmiljeni z računalnikom. Držalo vzorca (glej sl. 4.8, str. 39) je opremljeno z dvema volframovima nitkama, ki omogočata segrevanje vzorca do 1100 K. Dodaten kriostat, v katerega je mogoče preko kapilar dovajati tekoč dušik, omogoča hlajenje vzorca do ~ 150 K. Sistem turbočrpalk vzdržuje v eksperimentalni komori tlak v območju 10^{-10} mbar. Za zajem podatkov, nastavljanje detektorjev ter premikanje delov komore in manipulatorja je bil razvit računalniški program v programskem jeziku Labview.

Eksperimentalna postaja HASPES je namenjena samostojnemu opazovanju površin s sipanjem atomov helija (HAS) in opazovanju površinskih nihanj s spektroskopijo neelastično sipanih atomov helija (HeELS). Omogoča tudi hkratno osvetlitev površine s sinhrotronskim žarkom in pripadajočo fotoelektronsko spektroskopijo, pri čemer izkorišča nizkoenergijsko fotonsko območje monokromatorja $(120 - 1000\,\text{eV})$. Sinhrotronska svetloba vstopa skozi predel komore, namenjen detekciji atomov He, in ima nasprotno smer od smeri žarka helija. Skica postaje je prikazana na sl. 4.9 (str. 39). Glavna komora je opremljena z navpično postavljenim manipulatorjem s šestimi prostostnimi stopnjami in z visokonatančnim pozicioniranjem $(\Delta d = 0.001\,\text{mm}, \Delta\varphi = 0.005°)$. Komora ima fiksni sipalni kot 105° med izvirom He, vzorcem in detektorjem He. Eksperimentalna geometrija je skupaj s tremi neodvisnimi rotacijami manipulatorja prikazana na sl. 4.10 (str. 40). Vse tri rotacije manipulatorja so motorizirane in krmiljene z računalnikom. Manipulator je opremljen z volframovimi nitkami in kriostatom s tekočim dušikom, kar omogoča nastavitev temperature vzorca v širokem obsegu $100 - 1000$ K.

Helijev žarek nastane z nadzvočnim razširjanjem He iz zadrževalne komore v vakuum skozi 10-mikronsko šobo. Močnan črpalni sistem na vakuumski strani omogoča zvezni prehod iz Brownovega gibanja v molekulski tok brez pojava udarnih valov. Sistem kolimatorjev omeji žarek atomov He na nizko divergenco $(8 \cdot 10^{-6}\,\text{sr.})$, ki na površini vzorca "osvetli" območje s premerom ~ 0.7 mm. Energijo žarka je s segrevanjem ali hlajenjem zadrževalne komore mogoče nastaviti v območju $19 - 100$ meV. Sipani atomi helija nato vstopijo v detekcijski del, ki nevtralne atome najprej ionizira, nato pa iz curka z masnim spektrometrom izlušči samo ione He$^+$. Te na koncu zazna fotopomnoževalka, prešteje pa računalnik. Instrumentalna širina aparata, ki je definirana kot širina zrcalnega uklonskega vrha na idealno ravni površini, je 0,135°. Ker je v praksi mogoče izmeriti že razširitev vrhov za $\sim 0,01°$, lahko z opisanim aparatom na površini opazujemo strukture do velikosti

1200 Å.

Na komoro je dodatno nameščena še razelektritvena helijeva luč, pri kateri v sevalnem spektru prevladuje spektralna črta He I z energijo 21.22 eV. Elektrone, izbite bodisi z UV svetlobo bodisi s sinhrotronskimi X-žarki, zazna 150 mm hemisferični analizator, ki je nameščen na simetrali fiksnega 110° sipalnega kota za HAS. Opremljen je z 48-segmentno anodo, ki ima pred seboj dve zaporedno postavljeni večkanalni ploščici (MCP). Največja energijska ločljivost elektronskega analizatorja je 17 meV. Analizator ima zelo majhen kot zaznave vpadnih elektronov ($\sim 0,5°$), zato v kombinaciji z elektronsko puško, ki je prav tako nameščena v sipalni ravnini in oddaja elektrone s kinetično energijo $10 - 1000$ eV, ponuja tudi tehniko uklona nizkoenergijskih elektronov (LEED). Za detekcijo fotoelektronov pri merjenju absorpcije X-žarkov (NEXAFS) je komora opremljena s širokokotnim elektronskim detektorjem (channeltron) z visokopasovnim filtrom. Komora je opremljena s sistemom za čiščenje vzorca z ionskim (Ar^+) bombardiranjem, naparilnimi celicami in kvarčno mikrotehtnico za kalibracijo hitrosti nanašanja. Dodaten sistem ventilov omogoča hitro izmenjavo vzorca brez odpiranja komore. Zmogljiv črpalni sistem vzdržuje v eksperimentalni komori tlak v območju 10^{-10} mbar.

Pentacen/Au(110)

Sposobnost formiranja dobro urejenih tankih filmov z veliko mobilnostjo nosilcev naboja uvršča pentacen kot vzorčno molekulo med organski polprevodniki [12]. Kristalna struktura, stopnja orientacijske urejenosti in velikost zrn odločilno vplivajo na električne transportne lastnosti tankih slojev, sestavljenih iz π-konjugiranih molekul, kakršna je pentacen. Razumevanje nastanka takšnih tankih slojev, ki se na kristalografsko dobro definiranih kovinskih substratih pogosto samouredijo, je zato ključnega pomena pri proizvodnji organskih polprevodniških elementov.

Pentacen je aromatični ogljikovodik iz družine poliacenov. Molekula pentacena je planarna in je sestavljena iz petih benzenovih obročev, povezanih v verigo (sl. 5.2, str. 60). Ima dobro izražen π-konjugiran elektronski sistem, ki se razteza nad in pod molekulsko ravnino in izvira iz povezovanja ogljikovih p-atomskih orbital. π-elektronski sistem igra odločilno vlogo pri medsebojni vezavi molekul pentacena, ki se v kristalu uredijo v strukturo ribje kosti, v tankih filmih pa je struktura praviloma povsem drugačna. Glede na to, kako so molekule v plasti pentacena medsebojno orientirane, se lahko mobilnost nosilcev naboja v takšni plasti spremeni tudi za 9 velikostnih razredov.

Ob uporabi močno nagubanih površin in zadosti močni interakciji filma s substratom lahko pričakujemo, da bo struktura substrata do določene mere narekovala orientacijo adsorbiranih molekul in s tem pogojevala tudi strukturo filma. Površina Au(110) je v primerjavi z ostalimi prehodnimi kovinami dokaj inertna. Pri sobni temperaturi nastopa v (1×2) rekonstruirani fazi z manjkajočimi vrstami, kjer manjka vsaka druga vrsta atomov zlata vzdolž smeri [$1\bar{1}0$] (sl. 5.7, str. 62). Zaradi sorazmerno močne nagubanosti (≈ 3 Å med ioni izpostavljenih plasti) je površina Au(110) primerna izbira za študij adsorpcije organskih molekul in strukture, v katero se le-te pri adsorpciji uredijo.

Strukturo v tankem filmu pentacena sem določil z uporabo tehnike sipanja termičnih atomov helija (HAS) z energijo 19 eV in valovnim vektorjem $6,3$ Å^{-1}. Molekule pentacena so bile na površino naparjene iz Knudsnove izparilne celice pri temperaturi okrog 500 K, pri čemer je hitrost naparevanja znašala nekaj monoplasti na uro. Površina Au(110) je bila pred nanosom najprej očiščena z bombardiranjem z ioni Ar^+, ki so imeli energijo

$1 - 3\,\mathrm{keV}$, in nato termično urejena s segrevanjem do $700\,\mathrm{K}$.

Pentacen sem nanašal na Au(110) substrat pri temperaturah med $293\,\mathrm{K}$ in $470\,\mathrm{K}$. Z *in-situ* opazovanjem strukture naparjene organske plasti s sipanjem helijevih atomov je bil sestavljen fazni diagram, prikazan na sl. 5.17 (str. 71). Med tem ko je pri temperaturi substrata pod $370\,\mathrm{K}$ rast pentacena na Au(110) popolnoma neurejena, nastaneta pri višjih temperaturah dve dobro urejeni stabilni fazi. Pri naparevanju na substrat s temperaturo $470\,\mathrm{K}$ nastane pri pokritosti približno ene monoplasti urejena faza s periodičnostjo (3×6). Meritev fotoelektronske emisije je pokazala, da nadaljnje naparevanje pentacena ne privede do nastanka druge (ali kasnejših) monoplasti in da je pokritost 1 monoplasti pri tej temperaturi saturacijska. Ob naparevanju pentacena pri nekoliko nižji temperaturi substrata ($420\,\mathrm{K}$), se razvoj struktur na površini ne zaustavi pri fazi (3×6), ampak pri fazi (6×8), ki nastopi pri $\sim 12\%$ večji pokritosti, kar je bilo določeno z merjenjem fotoelektronske emisije med naparevanjem. Tudi ta pokritost je (pri tej temperaturi) saturacijska, saj fotoemisijski signal C $1s$ ob nadaljnjem naparevanju ne raste več. Faza (6×8) je prav tako sestavljena iz ene monoplasti, ki pa je gosteje zložena kot faza (3×6).

Orientacijo molekul v tankem filmu pentacena sem določil z opazovanjem absorpcije X-žarkov v bližini atomskih absorpcijskih robov (NEXAFS). Molekula pentacena je planarna, zato se pri absorpciji rentgenske svetlobe pojavi izrazita kotna odvisnost. Pri tem so odločilne simetrijske lastnosti začetnega in končnega elektronskega stanja ter kot med simetrijskimi osmi molekule in smerjo električnega polja rentgenske svetlobe. Prehodi iz atomskega stanja C $1s$ v najnižjo (LUMO) in drugo najnižjo (LUMO+1) nezasedeno molekulsko orbitalo pentacena s π-simetrijo so dovoljeni, če je električno polje X-žarkov *pravokotno* na molekulsko ravnino. Obratno pa so prehodi iz atomskega stanja C $1s$ v kvazi-vezani σ^*-stanji, ki pripadata vezema C – C in C = C, dovoljeni, kadar je električno polje X-žarkov *vzporedno* z molekulsko ravnino. Karakterističen absorpcijski spekter molekulskega filma pentacena, v katerem absorpcijski vrhovi pripadajo ustreznim (omenjenim) prehodom, je prikazan na sl. 5.18 (str. 73). Absorpcijo X-žarkov sem torej opazoval v odvisnosti polarnega kota α med vektorjem električnega polja X-žarkov in površino substrata ter azimutnega kota ϕ med smerjo vpada X-žarkov in atomskimi vrstami na površini Au(110), kot kaže sl. 5.21 (str. 75).

Absorpcijski spektri, ki pripadajo ravnovesni fazi s periodičnostjo (3×6), izkazujejo izrazito kotno odvisnost (sl. 5.22, str. 76), kar kaže na odlično orientacijsko urejenost molekul pentacena v organskem filmu. S prilagajanjem intenzitete π^* in σ^* resonanc sem ugotovil, da je kot med molekulskimi ravnivami in površino substrata enak $0° \pm 0.5°$ (sl. 5.23, str. 77). Molekule v fazi (3×6) torej ležijo vzporedno s površino, pri čemer je daljša os molekule orientirana pravokotno glede na atomske vrste zlata na površini Au(110). Molekule se med seboj bočno stikajo, s čimer tvorijo dolge verige, ki se raztezajo vzdolž smeri $[1\bar{1}0]$. Model takšnega tankega filma je prikazan na sl. 5.33, levo (str. 85). Zaradi dobrega prekrivanja površinskih stanj zlata s π^* elektronskim sistemom molekule je interakcija filma s substratom relativno močna, kar privede do hibridizacije nizko ležečih molekulskih stanj.

Faza (6×8) izkazuje drugačno kotno odvisnost absorpcijskih spektrov, ki nedvoumno kažejo na prisotnost molekul v več različnih adsorpcijskih geometrijah (sl. 5.29, str. 82). Kadar žarek vpada na površino vzporedno s smerjo $[001]$, je absorpcijski spekter skoraj enak tistemu pri fazi (3×6), kar pomeni, da so dolge verige bočno staknjenih molekul, vzporednih s površino, še vedno prisotne. Ko pa žarek vpada vzporedno s smerjo $[1\bar{1}0]$, signal, ki izvira iz prehodov v molekulska stanja π^*, ne pade na nič niti v primeru, ko

je električno polje X-žarkov povsem vzporedno s površino (sl. 5.30, str. 83). Opaženo obnašanje intenzitet uspešno opiše model, v katerem na vsaki dve ležeči molekuli pentacena stoji tretja molekula pokonci, t.j. z molekulsko ravnino pravokotno na površino substrata. Upoštevajoč velikost osnovne celice (6×8) in zastopanost populacij ležečih in pokonci stoječih molekul (2:1) sem vpeljal model, prikazan na sl. 5.33 (str. 85). V njem se razdalja med verigami bočno staknjenih molekul iz faze (3×6) poveča, mednje pa se vrine nova vrsta pokonci stoječih molekul, ki se med seboj stikajo vzdolžno. Dobro ločena nehibridizirana molekulska stanja π^* v absorpcijskem spektru pri $\alpha = 0$ in $\phi = 0$ kažejo, da pokonci stoječe molekule v primerjavi z ležečimi s substratom interagirajo precej šibkeje, pri tem pa ostanejo njihova elektronska stanja skoraj nespremenjena.

CuPc/Au(110)

Kovinski ftalocianini so bili v zadnjih letih uspešno uporabljeni v fotovoltaičnih napravah, fotodetektorjih, organskih tranzistorjih, svetlečih diodah in senzorjih. Možnost izbire središčnega kovinskega atoma dopušča nekaj svobode pri izbiranju molekulskih lastnosti, kot je npr. elektronska struktura, molekulski spin v osnovnem stanju itd. Zaradi svoje stabilnosti in razširjene uporabe v industriji barv je med najbolje raziskanimi ftalocianini *bakrov ftalocianin*, CuPc. Molekula je sestavljena iz konjugiranih makroobročev, in sicer štirih piroličnih in štirih benzenovih, pri čemer je središčni bakrov atom obkrožen s štirimi atomi dušika (sl. 6.1, str. 88). Molekula je planarna in ima izven molekulske ravnine dobro izražene delokalizirane π-orbitale. Zaradi šibkih medmolekulskih sil je polimorfizem pri ftalocianinih prej pravilo kot izjema. Najstabilnejša je kristalna faza β-CuPc, v kateri so molekule urejene v obliki ribje kosti, kot je prikazano na sl. 6.2, levo (str.88). Ista faza je bila opažena tudi pri adsorpciji molekul CuPc na SiO_2 [3]. Pri nanašanju na kovinske površine je zaradi delokaliziranosti π-orbital v kovinskih ftalocianinih pričakovati, da se bodo molekule na substrat pretežno vezale z molekulsko ravnino, vzporedno s površino substrata. Ker zavisi orientacija molekul od hrapavosti površine, bi z izbiro dovolj močno nagubane površine lahko povzročili usmerjeno rast tankega filma na sicer slabo interagirajočem substratu. V tem smislu je površina Au(110), ki je zmerno reaktivna in ima izpostavljene (111) mikropovršine, nagnjene za 35° glede na (110) ravnino, obetaven kandidat. Molekulska orientacija in stopnja kristalinične urejenosti pri nanašanju na substrat odločilno določata transportne lastnosti tankih organskih filmov, zato je natančen nadzor ustreznih parametrov rasti ključen.

Urejenost in strukturo monoplastnega filma CuPc sem opazoval sočasno s sipanjem atomov helija (HAS) in nizkoenergijskih elektronov (LEED). Energija atomov helija je bila $19,6$ meV, energija elektronov pa 200 eV. Uklonski vzorci so bili zajeti kot funkcija polarnega kota (glej sl. 4.11 na str. 44) med naparevanjem CuPc na Au(110) pri temperaturi substrata 340 K. Hitrost naparevanja CuPc je znašala približno $0,1$ monoplast/ukl.vzorec. Substrat je bil azimutno orientiran tako, da je bila v sipalni ravnini površinska smer [001], ki v recipročnem prostoru ustreza smeri ΓY. Razvoj strukture na površini poteka pri opazovanju s sipanjem atomov helija od začetne strukture substrata (1×2) preko vmesne strukture (5×5) pri pokritosti $\sim 2/3$ monoplasti do končne (5×7) pri pokritosti ene monoplasti (sl. 6.3, str. 89). Slednja je zaradi Debye-Wallerjevega pojava opazna šele, ko je substrat ohlajen na nizko temperaturo (< 170 K). Sosledje uklonskih vzorcev, narejenih z nizkoenergijskimi elektroni, prav tako najprej pokaže (1×2) strukturo substrata in se nato preko vmesne periodičnosti (5×5) presenetljivo konča pri strukturi s periodičnostjo

(5×3) (sl. 6.4, str. 90). Kljub temu da z obema tehnikama opazujemo strukturo površine, je uklon helijevih atomov občutljiv le na skrajno zunanjo (valenčno) elektronsko gostoto in je zato z njim moč opazovati le izpostavljeno plast. Nizkoenergijski elektroni z energijo 200 eV pa prodrejo globlje in v resnici dajo (pretežno) tudi informacijo o strukturi Au substrata. Do faze s periodičnostjo (5×5) imata torej film in substrat enako strukturo. Dekompozicija polštevnega uklonskega vrha v središčno ostro špico in v dva dobro izražena satelitska vrhova kaže na nastanek teras z nasprotno fazo manjkajočih vrst. Na (1×2) rekonstruirani površini Au(110) se faza manjkajočih vrst obrne z uvedbo para enoatomskih stopnic vzdolž smeri [001]. Shematični model nastale terasaste površine je prikazan na sl. 6.5 (str. 91). Iz razvoja zrcalnega in pol-števnega vrha med naparevanjem lahko zaključimo, da adsorbirane molekule CuPc lokalno povzročijo proliferacijo Au(110) monoatomskih stopnic, ki sočasno vpliva na usmerjeno rast CuPc molekul v dolge verige vzdolž površinske smeri [1$\bar{1}$0], t.j. vzdolž brazd na površini z manjkajočimi vrstami. Proliferacija defektov na površini ima pri tem skoraj enodimenzionalni značaj, saj med naparevanjem vsi uklonski vrhovi presenetljivo ohranjajo zelo majhno širino vzdolž smeri ΓX. Vzporedne verige CuPc so torej vzdolž smeri [1$\bar{1}$0] odlično korelirane že od zgodnejših stopenj nanosa naprej.

Fotoelektronski spekter C 1s, posnet na tankem filmu CuPc, se ne razlikuje dosti od spektra, zajetega na kristalu CuPc, kar kaže na nespremenjeno elektronsko strukturo molekule in s tem na sorazmerno šibko interakcijo filma s substratom. Orientacija molekul je bila določena z opazovanjem absorpcije X-žarkov v bližini absorpcijskega roba L_3 atomov Cu. Absorpcija se močno poveča, kadar leži električno polje vpadajočih X-žarkov v molekulski ravnini, in je praktično ni v primeru, ko je električno polje pravokotno na ravnino molekule. Intenziteta absorpcije v odvisnosti od kota med električnim poljem in molekulsko ravnino je za fazo (5×7) skupaj z opazovanim resonančnim vrhom prikazana na sl. 6.8 (str. 94). V modelu za prilagajanje krivulji intenzitete sem upošteval, da so molekule CuPc na površini prisotne v dveh domenah, kar je prikazano na sl. 6.9 (str. 95). Naklon molekul v fazi (5×7) je, sledeč rezultatu prilagajanja, 32° glede na ravnino substrata.

Kljub opaženi šibki interakciji filma s substratom molekule CuPc na površini inducirajo rekonstrukcijo substrata v strukturo (1×3). Natančna lega atomov v vrhnji plasti Au substrata je bila določena z metodo uklona X-žarkov, ki vpadajo na površino pod zelo majhnim kotom, t.j. skoraj vzporedno s površino (GIXD). Pri tej metodi spreminjamo izmenjano gibalno količino v smeri pravokotno na površino, pri čemer ohranjamo v ravnini izmenjano gibalno količino konstantno. Na ta način je mogoče natančno določiti lego atomov v urejeni vrhnji plasti substrata. Na površini prisotne organske molekule zaradi majhnega Z (števila elektronov) k sipanemu signalu iz substrata ne prispevajo praktično nič, saj ima slednji bistveno večji atomski sipalni faktor od atomov v organskih molekulah. S pomočjo simulacijskega programa [93], ki ima za prilagoditveni parameter lego atomov znotraj osnovne celice, sem določil lego atomov in s tem tip (1×3) rekonstrukcije. Struktura (1×3) plitvo rekonstruiranega substrata z asimetrično relaksirano osnovno celico je prikazana na sl. 6.12, relativni premiki atomov pa so zbrani v tabeli 6.1 na str. 98.

PTCDA/Ge(001)

Kristal 3,4,9,10-perilen-dianhidrid-tetrakarboksilne kisline (PTCDA) ima med organskimi polprevodniki eno največjih izmerjenih mobilnosti nosilcev naboja, ki presega $1\,\mathrm{cm^2/Vs}$ vzdolž smeri zlaganja molekul [99]. Ta lastnost pomeni nesporno prednost PTCDA pri izbiri aktivnega materiala za izdelavo organskih polprevodnikov.

Molekula PTCDA je derivat perilena, ki ima na vsaki strani vezano eno anhidridno skupino. Zaradi planarne oblike ima molekula PTCDA izražen π-konjugiran elektronski sistem, ki se razteza izven molekulske ravnine podobno kot pri molekuli pentacena. Omenjeni elektronski sistem je tudi odgovoren, da se molekule PTCDA vežejo v kristal v obliki tankih (102) lističev, znotraj katerih so molekule urejene v strukturo ribje kosti, kot je prikazano na sl. 7.3 (str. 103). Močna anizotropija molekule se izraža tudi v anizotropiji fizikalnih lastnosti kristala PTCDA. Mobilnost nosilcev naboja tako pade v območje $10^{-5} - 10^{-4}\,\mathrm{cm^2/Vs}$ v smeri pravokotno na smer zlaganja molekul. Učinkovitost vbrizgavanja nosilcev naboja na stiku substrata z organskim polprevodnikom je še en parameter, ki vpliva na kvaliteto polprevodniškega elementa. Poznavanje orientacije molekul v takšnih heterostikih je zato ključno. V literaturi je že bilo objavljeno, da tvorijo molekule PTCDA pri naparevanju na substrat z nizko temperaturo ($< 170\,\mathrm{K}$) dobro urejene plasti s preferenčno orientacijo molekul [7]. Opaženo je bilo tudi, da je mobilnost nosilcev naboja močno odvisna od temperature substrata, pri kateri je bil na njem rasčen film, kar kaže na to, da ima morfologija rasti ključno vlogo pri določanju električnih lastnosti organskega filma. Zaradi pomanjkanja eksperimentalnih podatkov o rasti PTCDA na polprevodniških substratih, še posebej na germaniju, sem za pričujočo študijo izbral substrat Ge(001).

Površina Ge(001) pri sobni temperaturi rekonstruira v strukturo (2×1), pri temperaturi nižji od $220\,\mathrm{K}$ pa ima simetrijo $c(4 \times 2)$. Omenjeni strukturi, v katerih so na površini izpostavljeni sorazmerno reaktivni germanijevi dimeri, sta prikazani na sl. 7.5 in 7.6 (str. 104 in 105). Takšna površina je v primerjavi s površino Au(110) precej bolj reaktivna in hkrati dovolj nagubana, da bi lahko povzročila usmerjeno rast naparjenih tankih plasti.

Morebitno urejenost tankega filma na dolg doseg sem ugotavljal z opazovanjem sipanja atomov helija (HAS). Površina je bila pred vsakim nanosom očiščena z ionskim bombardiranjem z ioni $\mathrm{Ar^+}$ in naknadno termično urejena s segrevanjem do $\sim 1000\,\mathrm{K}$. Na ta način so na površini nastale domenske terase s tipično velikostjo $\sim 1000\,\text{Å}$, kar je bilo moč sklepati iz širine zrcalnega vrha ob upoštevanju enačbe (4.8). PTCDA je bil na površino naparjen iz Knudsenove celice, segrete do temperature $\sim 670\,\mathrm{K}$, s tipično hitrostjo nanašanja $\sim 0,1\,\mathrm{monoplast/min}$. Energija atomov helija je bila $19\,\mathrm{meV}$, valovni vektor pa $6,3\,\text{Å}^{-1}$.

Naparevanje PTCDA na substrat pri nizki temperaturi ($170\,\mathrm{K}$) povzroči monotono padanje intenzitete zrcalnega vrha do končne (najnižje) vrednosti, kar kaže na odsotnost kakršnekoli urejene strukture dolgega dosega. Padanje intenzitete zrcalnega vrha pa se ob naparevanju pri temperaturi $350\,\mathrm{K}$ ali višji po približno $400\,\mathrm{s}$ zaustavi oz. upočasni, kar kaže na precejšnjo stopnjo urejevanja PTCDA filma. Glede na to, da je na tej stopnji nanosa uklonski vzorec Ge substrata še vedno opazen in da se širina uklonskih vrhov ni povečala, je moč sklepati, da je del površine Ge še vedno odkrit in da se red dolgega dosega na njem ni porušil. Do tega pride, ker se PTCDA molekule zaradi velike mobilnosti na Ge substratu pri višjih temperaturah združujejo v 3D kapljice, pri čemer ostane del površine substrata nepokrit. Popolna pokritost substrata je v tem primeru dosežena kasneje kot

pri nizki temperaturi, kjer je film kinetično omejen in se molekule PTCDA ne morejo svobodno premikati po površini.

Natančnejši vpogled v mehanizem rasti PTCDA filma omogoča fotoemisijska spektroskopija (XPS). Sorazmerno močan premik kisikovih $1s$ vrhov (~ 0.5 in $\sim 0.7\,eV$) v omočitveni plasti glede na debel PTCDA film (sl. 7.10, str. 108) kaže, da omočitvena plast v primerjavi z višje ležečimi plastmi PTCDA močno interagira s substratom. Signal O $1s$ končno saturira, ko postane debelina filma enaka povprečni prosti poti fotoelektronov v filmu. Z opazovanjem fotoemisijskega signala iz omočitvene plasti, iz debelega filma in iz substrata dobimo rezultat, da je debelina stične plasti približno štirikrat večja od kasnejših monoplasti PTCDA. Debelina stične plasti hkrati presenetljivo dobro ustreza dolžini daljše molekulske osi. Opazovanje fotoemisijske intenzitete O $1s$ med naparevanjem PTCDA pri sobni temperaturi pokaže, da v tem primeru PTCDA tvori le omočitveno plast in ne tvori višjih plasti. Preostali naparjeni material se pri tem zbere v velike 3D otoke.

Razliko med morfologijo PTCDA filma pri nizki in sobni temperaturi lepo pokaže tudi ultraviolična spektroskopija. Za izvor UV svetlobe sem uporabil helijevo razelektritvenao luč, pri kateri v sevalnem spektru prevladuje spektralna črta He I z energijo $21.22\,eV$. Med naparevanjem PTCDA pri nizki temperaturi iz fotoelektronskega spektra germanijeva vrhova izgineta sočasno z zaključitvijo nastanka omočitvene plasti. V istem trenutku pričnejo v spektru rasti vrhovi, ki pripadajo višje ležečim zasedenim elektronskim stanjem (HOMO, HOMO-1...) debelega filma PTCDA in saturirajo že po naparjenih dveh omočitvenih plasteh materiala. Razvoj fotoelektronskega spektra med naparevanjem PTCDA na substrat pri sobni temperaturi se precej razlikuje od nizkotemperaturnega. Spekter ne saturira in je še pri količini materiala, ki ustreza šestim omočitvenim plastem, podoben nizkotemperaturnemu spektru pri pokritosti približno $1,5$ omočitvene plasti. Premik in slabša izraženost vrhov v spektru visokotemperaturnega filma glede na spekter nizkotemperaturnega filma priča o prisotnosti novih elektronskih stanj, ki so nastala s hibridizacijo elektronskih stanj substrata in PTCDA filma. To opažanje je v skladu s prejšnjim zaključkom, da PTCDA na Ge(001) pri sobni temperaturi tvori le omočitveno plast, preostali material pa se zbira v velikih 3D otokih.

Opazovanje absorpcije X-žarkov v bližini ogljikovega absorpcijskega roba razkrije orientacijo molekul v tankem filmu PTCDA. Ker je molekula PTCDA planarna in ker imajo vse opažene resonance do energije fotonov $289\,eV$ π-značaj, so le-te v absorpcijskem spektru najmočnejše, kadar je vektor električnega polja X-žarkov pravokoten na molekulsko ravnino. Tipičen absorpcijski spekter debelega PTCDA filma, naparjenega na Ge(001) substrat pri nizki temperaturi, je skupaj z razlago posameznih vrhov, ki nastopajo v spektru, prikazan na sl. 7.17 (str. 116). Absorpcija X-žarkov v debelem filmu PTCDA, naparjenem na substrat pri nizki temperaturi, pokaže močno kotno odvisnost (sl. 7.18, str. 118), kar kaže na to, da je film homogen in odlično orientacijsko urejen. Ker so π^*-resonance najmočnejše, kadar je vektor električnega polja vpadle svetlobe pravokoten na površino, in prepovedane, kadar je ta vzporeden s površino, je moč sklepati, da so molekule PTCDA orientirane z molekulsko ravnino vzporedno s površino substrata. Za razliko od nizkotemperaturnega filma izkazuje absorpcijski spekter debelega PTCDA filma, naparjenega na substrat pri sobni temperaturi, neprimerno manjšo kotno odvisnost, kar kaže na povsem drugačno morfologijo filma. Vsi vrhovi, ki so v nizkotemperaturnem spektru izraziti, imajo pri filmu, naparjenem pri sobni temperaturi, precej spremenjeno obliko, kar pomeni, da molekule PTCDA močno interagirajo s susbstratom tako preko perilenskega

jedra kot tudi preko anhidridnih funkcionalnih skupin. Odsotnost kotne odvisnosti lahko po eni strani kaže na to, da so molekulska stanja PTCDA močno hibridizirana in/ali pa film v resnici ne premore opaznejše orientacijske urejenosti. Takšen film sestavljajo 3D otoki PTCDA, ki so nekorelirani in naključno orientirani. Ne glede na to, ali je bil film raščen pri nizki ali pri sobni temperaturi substrata, pa sipanje atomov helija ne pokaže urejenosti filma na dolg doseg.

Razvoju orientacijske urejenosti filma lahko natančneje sledimo z opazovanjem absorpcijskega spektra na več različnih stopnjah nanosa. Pri pokritosti ene monoplasti sta absorpcijska spektra pri naparevanju na substrat pri sobni in nizki temperaturi praktično enaka, kar kaže na zelo podobno morfologijo pripadajočih filmov (sl. 7.19, str. 119). Večja razlika v morfologiji se pokaže šele pri višjih stopnjah nanosa. Naparevanje pri nizki temperaturi tako kaže praktično vse značilnosti debelega filma že od pokritosti dveh omočitvenih plasti naprej. PTCDA film, raščen pri sobni temperaturi, pa ne razvije izrazitejših absorpcijskih vrhov niti pri večjih pokritostih, ohrani pa značilnosti spektra omočitvene plasti.

Medtem ko absorpcijski spekter omočitvene plasti PTCDA ne kaže praktično nobene kotne odvisnosti (sl. 7.20, str. 120), pa to ne velja za PTCDA film debeline 2 omočitvene plasti, ki je bil naparjen na substrat pri nizki temperaturi. Opaženo orientacijsko urejevanje molekul v PTCDA filmu pri nizki temperaturi uspešno pojasni tudi anomalno obnašanje prevodnosti filma PTCDA/Si, ki jo je objavil Forrest s sodelavci [7] (glej sl. 1.3 na str. 5). Prilagajanje krivulje intenzitam π^* vrhov v odvisnosti od polarnega kota pokaže, da molekule PTCDA v plasteh filma od omočitvene plasti naprej ležijo z molekulsko ravnino popolnoma vzporedno s površino substrata. Neurejena stična plast, zanimivo, ne prepreči nadaljnje rasti orientacijsko urejenih plasti PTCDA na Ge(001) substratu pri nizki temperaturi. Odlična orientacijska urejenost takšnega filma se ne poruši niti v primeru, ko substrat segrejemo do sobne temperature. Lahko bi rekli, da igra omočitvena plast vlogo pasivacijske plasti in s tem omogoča urejeno nadaljnjo rast filma.

Zaključek

V tej disertaciji sem pokazal, da je z ustrezno izbiro substrata in organskega materiala mogoče spreminjati jakost interakcije molekulskga filma s površino, kar odločilno vpliva na ureditveno strukturo naparjene plasti. Izpostavil sem, da igra pri kvaliteti tankega filma ključno vlogo način vezave organskih molekul s substratom. Realizacija organsko/anorganskih heterosistemov s posebno molekulsko geometrijo odpira pot za izdelavo tankih organskih filmov s po meri izbranimi optičnimi in električnimi lastnostmi, čemur bi lahko rekli "nano-arhitektura". Ta bo znanstveno in tehnološko nedvomno zelo zanimiva tudi v prihodnosti.

Bibliography

[1] C.1. Dimitrakopoulos and D. J. Mascaro, IBM J. Res. & Dev. **45** (2001) 11

[2] Ph. Guaino, D. Carty, G. Hughes, O. McDonald and A. A. Cafolla, App. Phys. Lett. **85** (2004) 2777

[3] Z. Bao, A. J. Lovinger and A. Dodabalapur, Appl. Phys. Lett. **69** (1996) 3066

[4] P. H. Lippel, R. J. Wilson, M. D. Miller, Ch. Wöll and S. Chiang, Phys. Rev. Lett. **62** (1989) 171

[5] F. Evangelista, A. Ruocco, V. Corradini, M. P. Donzello, C. Mariani and M. G. Betti, Surf. Sci. **531** (2003) 123

[6] Y. Hirose, S. R. Forrest and A. Kahn, Phys. Rev. B **52** (1995) 14040

[7] S. R. Forrest, Chem. Rev. **97** (1997) 1793

[8] G. Witte and C. Wöll, J. Mater. Res. **19** (2004) 1889

[9] IUPAC: Definitions And Terminology, 2001,
`http://www.iupac.org/reports/2001/colloid_2001/manual_of_s_and_t/node16.html`

[10] I. G. Hill, A. Rajagopal, A. Kahn and Y. Hu, App. Phys. Lett. **73** (1998) 662

[11] C. D. Dimitrakopoulos, A. R. Brown and A. Pomp, J. Appl. Phys. **80** (1996) 2501

[12] R. Ruiz, D. Choudhary, B. Nickel, T. Toccoli, K. Chang, A. C. Mayer, P. Clancy, J. M. Blakely, R. L. Headrick, S. Iannotta and G. G. Malliaras, Chem. Mater. **16** (2004) 4497

[13] V. Marinković: *Mejne površine*, NTF of University of Ljubljana, 1999

[14] J. A. Venables, G. D. T. Spiller and M. Hanbucken, Rep. Prog. Phys. **47** (1984) 399

[15] J. Krug, Adv. Phys. **46** (1997) 139

[16] F. Schreiber, Phys. Stat. Sol. (a) **201** (2004) 1037

[17] J. Stöhr: *NEXAFS Spectroscopy*, Springer-Verlag, Berlin Heidelberg (1992)

[18] J. D. Jackson: *Classical Electrodynamics*, Wiley, New York (1962)

[19] J. I. Steinfeld: *Molecules and Radiation*, Dover Publications, Inc., New York (1985)

[20] P. Hofmann: *Lecture Notes on Surface Science*, Århus University, Århus, Denmark (2000)

[21] D. N. Blauch: *Molecular Orbital Theory*, 2001,
`http://www.chm.davidson.edu/ChemistryApplets/MolecularOrbitals/`

[22] S. M. Condren: *Molecular Structure and Bonding*, 1999,
`http://www.cbu.edu/~mcondren/c422c3-p2_05.ppt`

[23] D. C. Harris, M. D. Bertolucci: *Symmetry And Spectroscopy*, Oxford University Press (1978), New York

[24] T. X. Carroll, N. Berrah, J. Bozek, J. Hahne, E. Kukk, L. J. Sæthre and T. D. Thomas, Phys. Rev. A **59** (1999) 3386

[25] M. Coville, T. D. Thomas, Phys. Rev. A **43** (1991) 6053

[26] E. Busetto, A. Lausi and S. Bernstotff, Rev. Sci. Instrum. **66** (1995) 2078

[27] L. Floreano, G. Naletto, D. Cvetko, R. Gotter, M. Malvezzi, L. Marassi, A. Morgante, A. Santaniello, A. Verdini, F. Tommasini and G. Tondello, Rev. Sci. Instrum. **70** (1999) 3855

[28] G. Naletto and G. Tondello, Pure Appl. Opt. **1** (1992) 347

[29] D. Cvetko, A. Lausi, A. Morgante, F. Tommasini, K. C. Prince and M. Sastry, Meas. Sci. Technol. **3** (1992) 997

[30] D. Cvetko: *Structure and Order of* (110) *f.c.c. Surfaces Studied by He Atom Scattering*, Master's thesis, Ljubljana (1993)

[31] H. N. Yang, G. C. Wang, T. M. Lu: *Diffraction From Rough Surfaces and Dynamic Growth Fronts*, World Scientific (1993)

[32] A. C. Levi and H. Suhl, Surf. Sci. **88** (1979) 221

[33] F. Tommasini, **31** (1981) 647

[34] H. Lüth: *Surfaces and Interfaces of Solid Materials*, Springer (1998) Heidelberg

[35] J. F. Moulder, W. F. Stickle, P. E. Sobol and K. D. Bomben: *Handbook of X-ray Photoelectron Spectroscopy*, Physical Electronics, Inc. (1992) Eden Prairie, Minnesota, USA

[36] J. F. Watts: *An introduction to surface analysis by XPS and AES*, Wiley (2003) West Sussex, England

[37] A. Einstein, Ann. Phys. **17** (1905) 132

[38] I. Adawi, Phys. Rev. **134** (1964) A 788

[39] B. Feuerbacher and R. F. Willis, J. Phys. C **9** (1976) 169

[40] H. Puff, Phys. Status Solidi **1** (1961) 636

[41] C. N. Berglung and W. E. Spicer, Phys. Rev. **136** (1964) A1030

[42] J. M. Walls and R. Smith: *Surface science techniques*, Pergamon (1994), Oxford, England

[43] K. W. Kolasinski: *Surface science: foundations of catalysis and nanoscience*, Wiley (2001) West Sussex, England

[44] D. P. Woodruff and T. A. Delchar: *Modern Techniques of Surface Science*, Cambridge University Presss (199), Cambridge, England

[45] G. H. Vineyard, Phys. Rev. B **26** (1982) 4146

[46] G. Lim, W. Parrish, C. Ortiz, M. Bellotto and M. Hart, J. Mater. Res. **2** (1987) 471

[47] S. Stepanov: *Grazing-Incidence X-Ray Diffraction*, Illinios Institute of Technology, BioCAT at the Advanced Photon Source, Argonne National Lab, 9700 S. Cass Ave., Bldg.435, Argonne, IL 60439

[48] I. K. Robinson, Phys. Rev. B **33** (1986) 3830

[49] A. Cossaro: *Structural investigation of thin films: from metal heterostructures to metal-organic systems*, PhD thesis, Trieste (2004)

[50] E. Vlieg, J. Appl. Cryst **30** (1997) 532

[51] F. Bruno, not published

[52] J. E. Northrup, Phys. Rev. B **66** (2002) 121404

[53] M. Alagia, C. Baldacchini, M. G. Betti, F. Bussolotti, V. Carravetta, U. Ekström, C. Mariani and S. Stranges, J. Chem. Phys. **122** (2005) 124305

[54] R. G. Endres, C. Y. Fong, L. H. Yang, G. Witte and Ch. Wöll, Comp. Mat. Sci. **29** (2004) 362

[55] C. D. Dimitrakopoulos and P. R. L. Malenfant, Adv. Mater. **15** (2002) 99

[56] P. Cortona, M. G. Dondi, D. Cvetko, A. Lausi, A. Morgante, K. C. Prince and F. Tommasini, Phys. Rev. B **47** (1993) 6705

[57] M. Sturmat, R. Koch and K. H. Rieder, Phys. Rev. Lett. **77** (1996) 5071

[58] A. Kühnle, L. M. Molina, T. R. Linderoth, B. Hammer and F. Besenbacher, Phys. Rev. Lett **93** (2004) 086101

[59] C. E. Heiner, J. Dreyer, I. V. Hertel, N. Koch, H.-H. Ritze, W. Widdra and B. Winter, Appl. Phys. Lett. **87** (2005) 093501

[60] O. Guillermet, A. Glachant, M. Mossoyan and J.C. Mossoyan, J. Phys. IV France **132** (2006) 77

[61] U. Garibaldi, A. C. Levi, R. Spadacini and G. E. Tommei, Jpn. J. Appl. Phys. **2** (1974) 549

[62] G. Boato, P. Cantini, U. Garibaldi, A. C. Levi, L. Mattera, R. Spadacini and G. E. Tommei, J. Phys. C, **6** (1973) L394

[63] L. Floreano, A. Cossaro, D. Cvetko, G. Bavdek and A. Morgante, J. Phys. Chem. B **110** (2006) 4908

[64] C. Menozzi, V. Corradini, M. Cavallini, F. Biscarini, M. G. Betti and C. Mariani, Thin Solid Films **428** (2003) 227

[65] V. Corradini, C. Menozzi, M. Cavallini, F. Biscarini, M. G. Betti and C. Mariani, Surf. Sci. **532-535** (2003) 249

[66] L. Floreano, G. Naletto, D. Cvetko, R. Gotter, M. Malvezzi, L. Marassi, A. Morgante, A. Santaniello, G.Tondello, A. Verdini and F. Tommasini, Rev. Sci. Instrum. **70** (1999) 3855

[67] T. Quast, R. Bellmann, B. Winter, J. Gatzke and I. V. Hertelb, J. Appl. Phys. **83** (1998) 1642

[68] N. Koch, A. Kahn, J. Ghijsen, J. J. Pireaux, J. Schwartz, R. L. Johnson and A. Elschner App. Phys. Lett **82** (2003) 70

[69] K. Lee and J. Yu, Surf. Sci. **589** (2005) 8

[70] C. Mainka, P. S. Bagus, A. Schertel, T. Strunskus, M. Grunze and Ch. Wöll, Surf. Sci. **341** (1995) L1055

[71] C. Africh, C. Blasetti and F. Esch: *Surface Structure and Reactivity Group*, TASC-INFM Laboratory, Trieste (2006)

[72] Z. T. Liu, H. S. Kwok and A. B. Djurišić, J. Phys. D: Appl. Phys. **37** (2004) 678

[73] A. Cossaro, D. Cvetko, G. Bavdek, L. Floreano, R. Gotter, A. Morgante, F. Evangelista and A. Ruocco, J. Phys. Chem. B **108** (2004) 14671

[74] K. T. Park, A. Millerm K. Klier, R. L. Opila and J. E. Rowe, Surf. Sci. **529** (2003) L285

[75] T. Fritz, M. Hara, W. Knoll and H. Sasabe, Mol. Cryst. Liq. Cryst. **253** (1994) 269

[76] A. Ruocco, M. P. Donzello, F. Evangelista and G. Stefani, Phys. Rev. B **67** (2003) 155408

[77] M. Lackinger and M. Hietschild, Surf. Sci. **520** (2002) L619

[78] G. Dufour, C. Poncey, F. Rochet, H. Roulet, S. Iacobucci, M. Sacchi, F. Yubero, N. Motta, M. N. Piancastelli, A. Sgarlata and M. J. DeCrescenzi, J. Electron. Spectrosc. Relat. Phenom. **76** (1995) 219

[79] M. Nakamura, Y. Morita, Y. Mori, A. Ishitani and H. Tokumoto, J. Vac. Sci. Technol. B **14** (1996) 1109

[80] M. -S. Liao and S. Scheinera, J. Chem. Phys **114** (2001) 9780

[81] V. Mastryukova, C. Ruana, M. Finka, Z. Wangb and R. Pachterb, J. Mol. Struct. **556** (2000) 225

[82] K. Y. Law, Chem. Rev. **93** (1993) 449

[83] J. C. Buchholz and G. A. Somorjai, J. Chem. Phys. **66** (1977) 573

[84] H. Peisert, T. Schwieger, J. M. Auerhammer, M. Knupfer, M. S. Golden and J. Fink, J. Appl. Phys. **90** (2001) 466

[85] L. Ottaviano, L. Lozzi, F. Ramondo, P. Picozzi and S. Santuzzi, J. Electron. Spectrosc. Relat. Phenom. **105** (1999) 145

[86] L. Giovanelli, H. Von Schenck, M. Sinner-Hettenbach, N. Papagergiou, M. Göthelid and G. Le Lay, Surf. Sci. **486** (2001) 55

[87] G. Dufour, C. Poncey, F. Rochet, H. Roulet, M. Sacchi, M. De Santis and M. De Crescenzi, Surf. Sci. **319** (1994) 251

[88] Y. Niwa, H. Kobayashi and T. Tsuchiya, J. Chem. Phys. **60** (1974) 799

[89] H. Peisert, M. Knupfer and J. Fink, J. Surf. Sci. **515** (2002) 491

[90] N. Papageorgiou, Y. Ferro, E. Salomon, A. Allouche, J. M. Layet, L. Giovanelli and G. Le Lay, Phys. Rev. B **68** (2003) 235105

[91] A. Ruocco, F. Evangelista, A. Attili, M. P. Donzello, M. G. Betti, L. Giovanelli and R. Gotter, J. Electron. Spectrosc. Relat. Phenom. **137-140** (2004) 165

[92] S. Carniato, Y. Luo and H. Ågren, Phys. Rev. B **63** (2001) 085105

[93] E. Vlieg, J. Appl. Crystallogr. **33** (2000) 401, the software is freely distributed at `http://www.esrf.fr/UsersAndScience/Experiments/TBS/SciSoft`

[94] M. Bernasconi and E. Tosatti, Surf. Sci. Rep. **17** (1993) 363

[95] M. Garofalo, E. Tosatti and F. Ercolessi, Surf. Sci. **188** (1987) 321

[96] D. Cvetko, A. Lausi, A. Morgante, F. Tommasini and K. C. Prince, Surf. Sci. **269/270** (1992) 68

[97] I. Chizhov, G. Scoles and A. Kahn, Langmuir **16** (2000) 4358

[98] I. Vilfan and J. Villain, Surf. Sci. **199** (1988) 165

[99] S. R. Forrest, M. L. Kaplan and P. H. Schmidt, J. Appl. Phys. **55** (1984) 1492

[100] J. R. Ostrick, A. Dodabalapur, L. Torsi, A. J. Lovinger, E. W. Kwock, T. M. Miller, M. Galvin, M. Berggren and H. E. Katz, J. Appl. Phys **81** (1997) 6804

[101] P. Fenter, P. E. Burrows, P. Eisenberger and S. R. Forrest, J. Cryst. Growth **152** (1995) 65

[102] K. Glöckler, C. Seidel, A. Soukopp, M. Sokolowski, E. Umbach, M. Böhringer, R. Berndt and W.-D. Schneider, Surf. Sci **405** (1998) 1

[103] B. Krause, A. C. Dürr, K. A. Ritley, F. Schreiber, H. Dosch and D. Smilgies, Appl. Surf. Sci **175** (2001) 332

[104] B. Krause, A. C. Dürr, F. Schreiber, H. Dosch and O. H. Seeck, Surf. Sci. **572** (2004) 385

[105] E. Umbach, K. Glöckler and M. Sokolowsky, Surf. Sci. **402-404** (1998) 20

[106] S. D. Kevan, Phys. Rev. B **32** (1985) 2344

[107] G. L. Lay, J. Kanski, P. O. Nilsson, U. O. Karlsson and K. Hricovini, Phys. Rev. B **45** (1992) 6692

[108] P. J. Cumpson, M. P. Seah and G. Quintana: *Inelastic Mean Free Path Grapher*, 1997, `http://www.lasurface.com/xps/imfpgrapher.php`

[109] Y. Azuma, K. Iwasawa, T. Kurihara, K. K. Okudaira, Y. Harada and N. Ueno J. Appl. Phys. **91** (2002) 5024

[110] Y. Zou, L. Kilian, A. Schöll, Th. Schmidt, R. Fink and E. Umbach, Surf. Sci. **600** (2006) 1240

[111] H. Yamane, S. Kera, K. K. Okudaira, D. Yoshimura, K. Seki and N. Ueno, Phys. Rev. B **68** (2003) 033102

[112] J. Xue and S. R. Forrest, Phys. Rev. B **69** (2004) 245322

[113] J. B. Gustafsson, E. Moons, S. M. Widstrand and L. S. O. Johansson, Surf. Sci. **572** (2004) 23

[114] J. Taborski, P. Väterlein, H. Dietz, U. Zimmermann and E. Umbach, J. Electron. Spectrosc. Relat. Phenom. **75** (1995) 129

[115] D. R. Miller: *Atomic and Molecular Beam Methods*, Vol. textbf1, Ed G. Scoles et al., Oxford University Press (1988), Oxford, England

[116] D. Lovrić and B. Gumhalter, Phys. Rev. B **38** (1988) 10323

[117] J. F. Annett and P. M. Echenique, Phys. Rev. B **34** (1986) 6853

[118] J. Harris and A. Liebsch, Phys. Rev. Lett. **59** (1982) 341

[119] B. N. J. Persson and P. Apell, Phys. Rev. B **27** (1983) 6058

[120] I. E. Dzyaloshinskii, E. M. Lifshitz and L. P. Pitaevskii, Adv. Phys. **10** (1961) 165

[121] E. Zaremba and W. Kohn, Phys. Rev. B **15** (1977) 1769

[122] J. Harris and A. Liebsch, J. Phys. C **15** (1982) 2275

Acknowledgments

Statement / Izjava

I hearby state that the present thesis is a result of my autonomus research work.

Izjavljam, da je ta disertacija rezultat mojega samostojnega raziskovalnega dela.

<div align="right">Gregor Bavdek</div>

Kranj, 13. november 2006